![Queen Mary University of London logo]

3D Printing of Teeth from X-Ray Microtomography for the Purpose of Research and Training

Alexander Jon Cresswell-Boyes

BSc, MSc.

A thesis submitted in fulfilment of the requirement for the degree of *Doctor of Philosophy* in the Institute of

Dentistry, Barts and the London School of Medicine and Dentistry, Queen Mary University of London.

September 2020

66352 Words

Statement of Originality

I, **Alexander Jon Cresswell-Boyes**, confirm that the research included within this thesis is my own work or that where it has been carried out in collaboration with or supported by others, that this is duly acknowledged below, and my contribution indicated. Previously published material is also acknowledged below.

I attest that I have exercised reasonable care to ensure that the work is original and does not to the best of my knowledge break any UK law, infringe any third party's copyright or other Intellectual Property Right, or contain any confidential material. I accept that the College has the right to use plagiarism detection software to check the electronic version of the thesis. I confirm that this thesis has not been previously submitted for the award of a degree by this or any other university. The copyright of this thesis rests with the author and no quotation from it or information derived from it may be published without the prior written consent of the author.

Signature: A. J. Cresswell-Boyes

Date: 02.09.20

Details of publications (reproduced publications found in Appendix D):

1. Cresswell-Boyes, A. J., Barber, A. H., Mills, D., Tatla, A., & Davis, G. R. (2018). Approaches to 3D Printing Teeth from X-Ray Microtomography. Journal of Microscopy, 272(3), 207-212.

2. Cresswell-Boyes, A. J., Mills, D., Davis, G. R., & Boyde, A. (2018). L2 Bone Quality in Osteoporosis: BIOMED 1 Revisited. Orthopaedic Proceedings: a supplement to The Bone & Joint Journal, 100-B(Supplement 14), 76.

Details of conference publications:

1. Cresswell-Boyes, A.J., Barber, A.H., Mills, D., Tatla, A., & Davis, G.R. (2017, 07-08 September). Approaches to 3D Printing of Teeth from X-Ray Microtomography. Paper presented at the ToScA, Portsmouth, UK.

2. Cresswell-Boyes, A.J., Barber, A.H., Tatla, A., Mills, D., & Davis, G.R. (2018, 24-28 July). 3D Printing Artificial Teeth Using X-Ray Microtomography Techniques. Paper presented at the IADR, London, UK.

3. Cresswell-Boyes, A.J., Barber, A.H., Tatla, A., Mills, D., & Davis, G.R. (2018a, 10-12 September). Evaluating 3D Printing Software Using X-Ray Microtomography. Paper presented at the ToScA, Warwick, UK.

4. Cresswell-Boyes, A.J., Barber, A.H., Tatla, A., Mills, D., & Davis, G.R. (2018b, 20-22 September). Understanding the Difficulties in Using Artificial Teeth for Pre-Clinical Teaching. Paper presented at the ICDO, Rome, Italy.

5. Cresswell-Boyes, A.J., Mills, D., Davis, G.R., & Boyde, A. (2018, 25-28 September). L2 Bone Quality in Osteoporosis: BIOMED 1 Revisited. Paper presented at the EORS, Galway, Ireland.

6. Cresswell-Boyes, A.J. (2019, 16 April). 3D Printing Artificial Teeth (Dannedd Argraffu Artiffisial 3D): How to achieve a functional teaching aid. Paper presented at the ASEiD, Cardiff, UK.

7. Cresswell-Boyes, A.J., Mills, D., Davis, G.R., & Boyde, A. (2019, 01-04 July). 3D Visualisation of Bone Quality in Osteoporosis. Paper presented at the MMC, Manchester, UK.

8. Cresswell-Boyes, A.J., Barber, A.H., Krishnamoorthy, M., & Davis, G.R. (2019, 21-23 August). 3D Printing Teeth – How to achieve a functional teaching aid. Paper presented at ADEE, Berlin, Germany.

9. Cresswell-Boyes, A.J., Barber, A.H., Krishnamoorthy, M., Mills, D., & Davis, G.R. (2019, 21-23 August). Investigating the Required Forces to Cut Extracted and Artificial Teeth. Paper presented at BSODR, Leeds, UK.

10. Cresswell-Boyes, A.J., Mills, D., Davis, G.R., & Boyde, A. (2019, 01-04 September). 3D Printing for Visualisation of Bone Quality in Osteoporosis. Paper presented at the BRS, Cardiff, UK.

11. Cresswell-Boyes, A.J., Barber, A.H., Krishnamoorthy, M., & Davis, G.R. (2019, 12-13 September). Digitising Dental Education: From X-ray microtomography to 3D printing and virtual reality. Paper presented at ToScA, Southampton, UK.

12. Cresswell-Boyes, A.J. (2020, 6 March). Additive Manufacturing of Synthetic Teeth for Teaching. Paper presented at Digital Dentistry, London, UK.

13. Cresswell-Boyes, A.J., Barber, A.H., Krishnamoorthy, M., Mills, D., & Davis, G.R. (2020, 9 March). 3D Printing Teeth for Research and Teaching. Paper presented at STEM for Britain, London, UK.

Details of collaboration:

Acknowledgements

There were stages throughout the PhD that writing and submitting a thesis seemed an impossible and daunting task, and to this day, I am still in disbelief that my ridiculous ramblings could produce this work. However, this was not solely the work of a lone mad researcher, and therefore would like to give my undying gratitude to the following:

Firstly, my eternal thanks to my lead supervisor **Prof. Graham Davis**, for the opportunity, support, vast knowledge and numerous tea breaks. Our long discussions (sometimes about research) will be what I take away from this project. I would also like to express my sincere gratitude to my second supervisor **Prof. Asa Barber** for the continuous support of my PhD study and related research, for his motivation and immense knowledge, as well as his resilience to my bombardment of emails over the years. I thank you both for your patience, and your abilities to help translate my lunacy into legible English.

Besides my supervisors, I would like to thank my "unofficial" supervisor, **Dr David Mills**, for his insightful comments and encouragement, your guidance and knowledge on how to destroy things (for science) is something I wish to impart onto young researchers in the future. My sincere thanks also go to **Prof. Alan Boyde**, who provided me with numerous opportunities, and who gave me access to his laboratory and research facilities, your extensive knowledge and worldly views (typically over a pint) have given me aspirations for the future. A special thanks must also go to **Prof. Helen Liversidge**, for whom I am most grateful for the opportunities you provided and your ability to "convince" students and staff to complete a questionnaire.

To **Prof. Robert Hill**, **Prof. Mangala Patel**, **Dr David Gillam**, **Dr Peter Tomlins** and **Dr Swati Nehete** my thanks for your insightful comments, long discussions

"To absent friends."

Abstract

Within dental education, there is a distinct need for hands-on pre-clinical training before a patient's treatment is carried out for the first time. A combination of extracted teeth and artificial teeth (typodonts) are widely used. However, the availability of extracted teeth is low, and there is a dissatisfaction amongst undergraduate dental students that these artificial teeth do not look and feel like extracted teeth.

This project aimed to produce an artificial tooth that looks and feels like an extracted tooth, utilising images collected from X-ray microtomography (XMT) and manufacturing techniques of three-dimensional (3D) printing. As well as to establish differences between extracted and artificial teeth from a haptic point of view.

Extracted human teeth were imaged using high-contrast XMT. A method was developed to convert reconstructed XMT images into a 3D printing file format (STL). A technique was also developed to measure the forces imposed on the tooth from a dental handpiece, with forces being measured during the cutting process.

Models were 3D printed to high accuracy from the original reconstructed XMT images. From the simulated 'haptic' feedback experiment, it was shown that commercially available artificial teeth required more force to cut compared to extracted teeth. The composites that were designed and printed closely resembled this force needed to cut, compared to artificial teeth. These teeth were provided to qualified dentists and undergraduate dental students. Feedback from them showed a promising basis for future development.

To conclude, this project has investigated the consensus that dental students are unhappy with current commercially available teeth and has developed a force measuring technique to quantify this difficulty in cutting. Through material development, materials

that required a similar cutting force were produced. This project provides the basis for future development in producing more accurate dental simulants for teaching and training.

Table of Contents

List of Figures

List of Tables

List of Abbreviations

2D	Two-dimensional			Attenuated Total Reflectance
3D	Three-Dimensional		GF	Glass Flake
ABS	Acrylonitrile Butadiene Styrene		HAp	Hydroxyapatite
ADEE	Association for Dental Education in Europe		H_V	Vicker's Hardness
AR	Augmented Reality		ISO	International Organization for Standardization
ASCII	American Standard Code for Information Interchange		K_C	Fracture Toughness
ASTM	American Society for Testing and Materials		K_{ifr}	Fracture Resistance
BAG	Bioactive Glass		LAC	Linear Attenuation Coefficient
BSE	Back-Scattered Electrons		PBL	Problem-Based Learning
CAD	Computer-Aided Design		PC	Polycarbonate
CAL	Computer-Aided Learning		PGMA	Poly(glycidyl methacrylate)
CAM	Computer-Aided Manufacturing		PLA	Polylactic Acid
CBCT	Cone-Beam Computed Tomography		PMMA	Poly(methyl methacrylate)
CCD	Charge-Coupled Detector		PVA	Polyvinyl Alcohol
CEJ	Cementoenamel Junction		QMUL	Queen Mary University of London
CHAp	Carbonated Hydroxyapatite		Ra	Surface Roughness
CNC	Computer Numerical Control		ROI	Region of Interest
CT	Computed Tomography		SBME	Simulation-Based Medical Education
DEJ	Dentinoenamel Junction		SD	Standard Deviation
DICOM	Digital Imaging and Communications in Medicine		SEM	Scanning Electron Microscopy
DLP	Direct Light Processing		SLA	Stereolithography
$\bar{E}$	Elastic Modulus		SLS	Selective Laser Sintering
FDM	Fused Deposition Modelling		STL	Stereolithography (file format) or Standard Triangle Language
FFF	Fused Filament Fabrication		TEL	Technology Enhanced Learning
FM	Fluormica Glass		TDI	Time-Delay Integration
FPS	Frames per Second		TMJ	Temporomandibular Joint
FTIR-ATR	Fourier-Transform Infrared Spectroscopy-		UV	Ultraviolet
			VR	Virtual Reality
			XMT	X-Ray Microtomography
			XRD	X-Ray Diffraction

Chapter 1

Introduction and Background

1.1 Background

There is a distinct need for hands-on pre-clinical training in dental education before a patient's treatment is carried out for the first time (Qualtrough *et al.*, 1999). Over the years, multiple techniques have been used to help teach students the anatomy of the oral cavity as well as procedures to combat common oral diseases. Traditionally, anatomy and procedures are taught using a mixture of extracted and artificial teeth; however, despite this dual approach, extracted teeth are seen as the 'gold standard' when creating a simulated environment for students to learn (Dummer, 1991).

Extracted teeth, for many years, were exclusively used within undergraduate teaching, however, as oral health has improved in recent years, the number of extractions has decreased, meaning the availability of extracted teeth has been limited. Other disadvantages include the possibility of cross-infection, being potentially infectious to students and the anatomical variability of extracted teeth meaning valid assessment for students is not uniform (Tchorz *et al.*, 2015).

Artificial teeth (typodonts) are commonly used as a teaching and simulation aid for standard procedures; these teeth are typically made from opaque or transparent resins. They have distinguishable enamel, dentine, pulp and root canals through the use of different materials or colours (Nassri *et al.*, 2008). The advantages of these artificial teeth are: they do not have the risk of infection, are available in large quantities, allow for validated assessment through uniformity and can be modified to offer anatomical

challenges (Al-Sudani & Basudan, 2016; Bitter *et al.*, 2016). More recently, these typodonts have been three-dimensionally (3D) printed for simulation-based medical education (SBME) offering new advantages over the traditional manufacturing techniques (San Diego *et al.*, 2013; O'Brien *et al.*, 2016; Höhne *et al.*, 2020).

Despite these advantages, studies have shown that students perceive these typodonts as 'unsatisfactory', due to their physical characteristics, making them difficult to practise on when compared to natural tissue. Although students' perceptions of artificial teeth are negative, students have been noted to recognise the advantage of using typodonts over extracted teeth. They, therefore, have suggested improving current commercial products, by changing the mechanical properties such as hardness, to reflect that of natural tissues (Abu Eid *et al.*, 2013; Al-Sudani & Basudan, 2016).

1.2 Aims and Objectives

This study aims to produce an artificial tooth through 3D printing that looks and 'feels' like natural tissue to recreate a realistic simulation for undergraduate dental students to learn and practise clinical treatments.

− Measure the mechanical properties of both extracted and commercial artificial teeth, to establish a method in which the tactile feedback can be measured when cutting the teeth.

− Using X-ray microtomography (XMT) techniques to collect high-resolution datasets of natural teeth, to develop a method to convert these datasets into modifiable virtual 3D models.

− Investigate current 3D printing technologies and evaluate these methods to find a suitable workflow in printing XMT datasets.

– Develop materials that can mimic the mechanical or tactile response of natural teeth when cutting, ensuring the materials are suitable for 3D printing.

– Evaluate students' perceptions of the developed 3D printed teeth and their suitability for pre-clinical teaching and training.

1.3 Rationale and Clinical Significance

With the lack of uniform assessment seen with extracted teeth, artificial teeth offer valid assessments; however, as established, students do not favour current commercial typodonts. Therefore, this study hypothesises that the 3D printed teeth will have improved mechanical properties compared with existing commercial artificial teeth. With the more realistic 'feel' to the 3D printed teeth, the assumption is that students would favour the developed 3D printed typodonts over commercial alternatives, allowing students to repeat procedures within a safe, realistic simulated environment.

1.4 Thesis Structure

The thesis is divided into nine chapters, with each chapter formatted to the specification as outlined by the Research Degrees Office at Queen Mary University of London (QMUL). Data that has been published previously or in publication is noted at the beginning of each chapter. Any data or figures that have been reproduced from other sources has been highlighted and permission obtained.

Chapter 1 provides a brief background and introduction to the study, complete with aim, objectives and rationale for the work undertaken. Chapter 2 is the literature review, which is divided into four sections: dental anatomy, dental education, X-ray microscopy and 3D printing. Chapter 3 is an overview of common methodologies and techniques used throughout the project. Chapters 4, 5, 6, 7 and 8 represent the results and discussion obtained throughout the project, with each chapter focussing on an individual aspect of

the study, with its own introduction and material and methods for each chapter. Chapter 9 is a general conclusion, an overall summary of each conclusion in Chapters 4, 5, 6, 7 and 8, with a section focussing on future recommendations. Appendices have been added to support the data and conclusions presented within this thesis.

Chapter 2

Literature Review

This chapter introduces the current literature about dental education in the UK, in particular, present and novel ways of teaching dental anatomy to undergraduate students. The advantages and disadvantages of teaching methods are explored along with ways in which dental education can be improved (Section 2.2). Section 2.1 is a brief introduction to the anatomy of the tooth and its mechanical properties. Section 2.3 investigates the role of X-ray microscopy and how current techniques have been used in dental research. Section 2.4 focuses on current additive manufacturing techniques, with a brief review of how 3D printing has been used in anatomy teaching.

2.1 Tooth Structure and Properties

Teeth are hard bone-like structures located within the maxilla (upper jaw) and mandible (lower jaw) that are surrounded coronally by gingival tissue. They are responsible for aesthetics, cutting, and mastication, as well as aiding in phonetics and communication (Nanci, 2012). Humans have two sets of teeth, a deciduous dentition of 20 teeth and a permanent dentition of 32 teeth (Lacruz *et al.*, 2017). Three anatomical sections make up teeth: crown, neck, and root (Figure 2.1). The crown is the visible and functional part of the tooth, located above the gum. The root is embedded within the gum and the alveolar bone, fixed via the periodontal membrane. The neck represents the middle part of the tooth, the supportive structure between the crown and root.

Regarding the composition, each tooth comprises of mineralised and unmineralised tissues. The mineralised tissues include; enamel, dentine and cementum,

with the inner structure of the tooth being made up of unmineralised oral tissue known as the pulp (Avery & Chiego, 2006; Nanci, 2012).
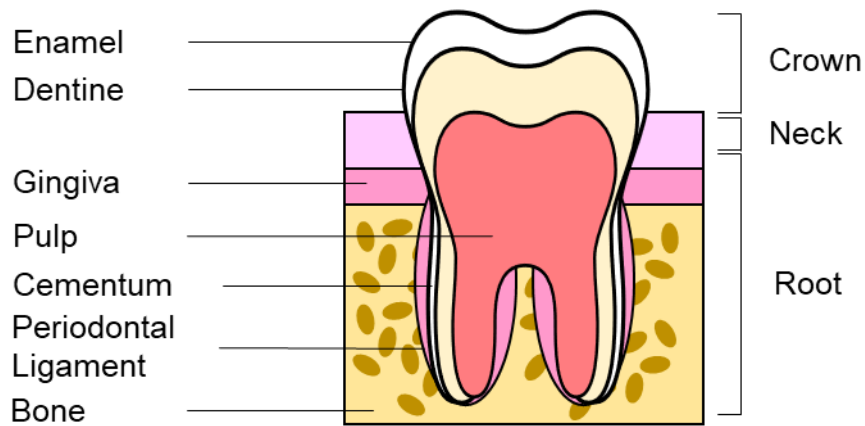
Figure 2.1: The basic anatomy of a human tooth. Teeth are comprised of enamel, dentine, pulp, and cementum. Adapted from Lacruz *et al.* (2017).

2.1.1   Enamel

Enamel is an acellular structure that covers the exposed surface of the tooth, formed from apoptosed ameloblasts, as the tooth erupts (Kondo *et al.*, 2001; Musson, 2010). Enamel is one of the most mineralised tissue, and hardest material found in the body comprising of approximately 96 wt. % mineral, 2-4 wt. % water and 1-2 wt. % organic matrix (Nanci, 2012; Schmitz *et al.*, 2014). The mineral contains non-stoichiometric, impure hydroxyapatite (HAp) crystallites, with a similar density to pure HAp (Boyde, 1989). Many studies have reported that HAp in the enamel can incorporate; sodium, magnesium, hydrogen, phosphate, and carbonate into its lattice (Trautz *et al.*, 1953; Elliott *et al.*, 1994; Elliott *et al.*, 1997; Robinson *et al.*, 2000; Elliott *et al.*, 2005; Moradian-Oldak & Paine, 2010). Arranged into prisms, the HAp crystallites, are perpendicular to the dentinoenamel junction (DEJ) and the enamel surface (Boyde, 1964). This prismatic arrangement allows for efficient packing of crystallites, maximising their strength and bendability, enhancing wear resistance (Boyde, 2007). A single prism

contains approximately thousands of crystallites (Simmer *et al.*, 2012; Uskokovic, 2012). According to Elliott *et al.* (1994), crystallite orientation is parallel to the long axis of the prism. In particular to human enamel, the majority of the prisms are arc-shaped and have a 'keyhole' pattern in transverse section, with a head and a tail region (Boyde, 1964). Although biologically classed as 'dead', enamel is permeable, allowing ion exchange between the enamel and oral cavity, to ions present in saliva which aid in remineralisation. Despite its ion exchange, enamel is highly susceptible to demineralisation and once lost to wear or caries, the enamel cannot be replaced, due to the absence of cellular activity (Musson, 2010; Nanci, 2012).

2.1.2   Dentine

The second structure of the tooth structure is dentine which makes up much of the tooth and is divided into two types according to its location, coronal and root dentine. Coronal dentine is located under the enamel, and root dentine is situated between the pulp chamber and the cementum. Dentine is an avascular, hard, connective tissue which consists of type I collagenous fibres and an apatite mineral phase. These components are responsible for providing strength and rigidity to the dentine, while its tubular nature offers flexibility. This flexibility is required to support the enamel, especially during mastication (Kinney *et al.*, 1999; Musson, 2010; Nanci, 2012). Dentine is synthesised and maintained by odontoblasts, which produce different forms of dentine depending on the cell's age. Dentine's composition is either primary, secondary, or tertiary. The most abundant is the primary dentine; this material is rapidly produced up until root formation, at which point secondary dentine is subsequently created and at a slower rate. A tubular structure, due to the mode of its deposition, dentine tubules contain the odontoblast process, collagen fibrils, peritubular dentine, and a complex mixture of proteins (Linde & Goldberg, 1993; Nanci, 2012). Within the crown, the tubules extend from the DEJ to the odontoblast layer, making dentine a permeable structure, similar to enamel (Musson,

2010; Nanci, 2012). After root formation, the odontoblasts continue to place secondary dentine at a significantly lower rate resulting in a smaller pulp chamber. Secondary dentine's structure is less regular compared to that of primary dentine; however, the tubules are continuous (Linde & Goldberg, 1993; Nanci, 2012). Tertiary dentine is formed in response to trauma such as dental caries, by odontoblasts below the site of injury to help protect the underlying soft tissue (Lesot *et al.*, 1994; D'Souza *et al.*, 1995). The morphology of tertiary dentine is often irregular, with reduced permeability due to the reduction of the tubular structure and continuity (Tziafas *et al.*, 2000; Musson, 2010).

2.1.3   Pulp

The dental pulp centred within the core of the tooth is made up of soft connective tissues with the essential functions to form, repair, and nourish the dentine. A heterogeneous cell population of fibroblasts, these cells secrete an extracellular matrix, composed primarily of type I and III collagenous fibrils responsible for providing structural integrity (Tsukamoto *et al.*, 1992; Goldberg & Smith, 2004; Killough *et al.*, 2009). Additionally, present in the pulp is a network of capillaries and nervous tissue (plexus of Raschkow), which provides nutritive and sensory support to the dentine-pulp complex (Goldberg & Smith, 2004; Musson, 2010).

2.1.4   Cementum

Cementum is a hard-mineralised connective tissue, which is attached to the root and categorised into three types; acellular afibrillar, acellular extrinsic fibre, and cellular intrinsic dentine (Musson, 2010; Nanci, 2012). Acellular afibrillar cementum is found at the cementoenamel junction (CEJ) and consists of a mineralised matrix deficient in collagenous fibres and embedded cells. Acellular extrinsic fibre cementum is the primary cementum involved in tooth attachment and consists of dense collagenous fibres (type I collagen), perpendicularly implanted into the dentine matrix. Cellular intrinsic cementum

plays a reparative role and contains cementocytes embedded in the mineralised matrix and collagenous fibrils (Saygin *et al.*, 2000; Grzesik & Narayanan, 2002; Musson, 2010).

2.1.5   Eruption of Teeth

As mentioned previously, humans have two sets of teeth: the primary (deciduous) and the permanent. Deciduous teeth comprise of five teeth within each quadrant (two incisors, one canine, and two molars). While, the permanent teeth contain eight teeth within each quadrant (two incisors, one canine, two premolars, and three molars) (Cunningham *et al.*, 2016).

Deciduous dentition typically starts to erupt around the age of six months and are fully erupted at approximately 24 months. The permanent teeth gradually replace the deciduous teeth starting from the age of 6 years old and are fully erupted by around 25 years (Al Qahtani *et al.*, 2010; Cunningham *et al.*, 2016). The root development of both deciduous and permanent teeth continues up to three years after eruption (Lunt & Law, 1974; Berkovitz & Moxham, 2009; Al Qahtani *et al.*, 2010; Becker, 2012; Cunningham *et al.*, 2016). Moreover, evidence from archaeological sites have suggested that eruption and completion times are earlier in females, compared to males, this was found in a population in Lower Saxony, as well as other sites (Wedl *et al.*, 2004; Hillson, 2014).

2.1.6   Dental Anatomy

Dental anatomy, including tooth morphology is an essential factor in identifying teeth for both clinicians and dental students, whilst understanding the shape, size, cusp and fissures of teeth is a detrimental skill (Berkovitz & Moxham, 2009). The anatomy of each tooth depends on their relative position within the dental arch as well as its shape and function (Brand & Isselhard, 2014; Cunningham *et al.*, 2016). Permanent teeth divide into anterior and posterior teeth. Anterior teeth include the central and lateral incisors and

the cuspids; these are responsible for cutting. Posterior teeth as a group, are the bicuspids and molars, which are accountable for mastication (Brand & Isselhard, 2014; Al-Khayyat, 2018).

2.1.6.1 Anterior Teeth

Anterior teeth are located in the frontal part of the jaw and form a curving arch from one cuspid distal to the distal of the cuspid on the opposite side (Brand & Isselhard, 2014). They are characterised by having a single root and incisal edges or single-cusped crowns ending in narrow edges. The thin edges are designed for incising (bite off) relatively large amounts of food in eating (Al-Khayyat, 2018).

Incisor crowns are flat and blade-like, with a rectangular or square outline, and come in two variants: central and lateral. Maxillary incisors are broader relative to their height, and have more 'bumps' on their lingual surface, compared to mandibular incisors which have very little lingual topography. Maxillary incisor roots are typically more circular in comparison to the mandibular roots, where the latter are mesiodistally compressed (White & Folkens, 2005; Al-Khayyat, 2018).

Canine crowns, on the other hand, are conical and tusk-like, with a diamond-shaped occlusal dentine patch. Maxillary canines are typically broader relative to their height, whereas the mandibular canine is narrow. Canine roots are more extended and more substantial relative to crown height compared to incisor roots (White & Folkens, 2005; Al-Khayyat, 2018).

2.1.6.2 Posterior Teeth

Posterior teeth are located bilaterally at the back of the dental arch. They differ from anterior teeth in that they have more than one root and classed as either premolars

or molars. Posterior teeth have multiple cusps forming large occlusal surfaces designed to crush and grind food into small parts (Brand & Isselhard, 2014; Al-Khayyat, 2018).

Premolars (bicuspids) are positioned between the canines and molars combining the properties of both; therefore, classified as transient teeth. They are eight in total with two in each quadrant. They mostly have two cusps and one root; however, the maxillary first premolars typically have two roots. Additionally, the number of roots may vary between populations (White & Folkens, 2005; Brand & Isselhard, 2014; Al-Khayyat, 2018).

Molars, on the other hand, are the most posterior teeth with a flatter and large occlusal surface. The occlusal outline of maxillary molars is rhomboid in shape, while the mandibular molars have a rectangular shape depending on the number of cusps. Molars have four or more cusps and are larger and more square-shaped, mandibular first molars having five functional cusps. Molars are all multi-rooted (maxillary teeth have three roots, and the mandibular teeth having two). Third molars (wisdom teeth) are similar to second molars but are mostly irregular in shape, size, and the number of roots (White & Folkens, 2005; Brand & Isselhard, 2014; Al-Khayyat, 2018).

2.1.7   Mechanical Properties

The mechanical properties of teeth vary from the outside to the inside. Teeth's unique mechanical features enable them to carry out specific functions (Kishen *et al.*, 2000; Nanci, 2012). However, to date, no material has been found to match human teeth as regards to biological and mechanical properties. Human teeth have a more complex structure, better mechanical properties, and better biocompatibility than all dental restorative materials (Zhang *et al.*, 2014). Understanding the mechanical properties of natural teeth is the basis of dental materials research and can provide a reference for evaluating the mechanical properties of new dental materials (Cohen *et al.*, 2010; Zhang

et al., 2014). Structure and composition of teeth's mineralised tissues outlined previously, determine their mechanical properties.

2.1.7.1   Hardness

Hardness is the property that enables resistance from deformation, penetration, indentation, and scratching. It is, therefore, an essential property for teeth to have, as hardness increases, the ability to resist wear increases. Nanoindentation is cited as the most widely used technique in measuring the hardness of enamel and dentine (Cuy *et al.*, 2002). This technique collects measurements in the nano-scale range using a Berkovich indenter or a spherical indenter via atomic force microscopy and can measure both hardness and elastic modulus ($\bar{E}$). The conical Vicker's hardness (H_V) tester and Knoop hardness indenter can only measure hardness (Zhang *et al.*, 2014). Each method offers a different load range, indentation depth, and is calculated using different formulas (Table 2.1).

Table 2.1: Comparison of commonly used hardness indentation techniques. Advantages and disadvantages were adapted from Zhang *et al.* (2014).

Hardness Test	Shape of Indenter	Measuring Method	Advantages and Disadvantages
Vicker's hardness	Diamond square, pyramid formed by an opposite edge of 136˚.	Measure the diagonal length of indentation.	When load changes, the geometry of indentation remains similar; but on different scales, the indenter geometry cannot be compared
Knoop hardness	Diamond square, pyramid formed by two unequal opposite angles (α = 175.5˚ and β = 130˚).	Measure the long diagonal length of indentation.	The sensitivity of measuring the variation of the microstructure is higher than H_V.
Berkovich hardness	Triangular pyramid forming an angle of 65.3˚ between centreline and conical surface.	The real-time depth and load measurement of indentation.	It can be real-time depth and load measurement of indentation; simultaneously measured hardness and elastic modulus; on microscopic scales.

Many studies in the area of enamel hardness, have suggested that the hardness decreases from the cusp cervically (Craig & Peyton, 1958; Craig *et al.*, 1961; Meredith *et al.*, 1996; Cuy *et al.*, 2002). With an increase in hardness reported when travelling from the DEJ peripherally (Willems *et al.*, 1993; Cuy *et al.*, 2002). Cuy *et al.* (2002) demonstrated that hardness was higher along the enamel surface in the lingual enamel compared to the buccal enamel, and higher along the DEJ in the buccal enamel compared to the lingual enamel.

Mahoney *et al.* (2000); Cuy *et al.* (2002); Mahoney *et al.* (2004); Jeng *et al.* (2011) carried out hardness measurements on human enamel. Each study used varying loads but received similar hardness values of 4.87-6.00 GPa, from the enamel surface, and values of 3.66-4.52 GPa closer to the DEJ. He *et al.* (2013) used Knoop hardness and found no

significant difference between the outer (3.52 GPa) and inner (3.51 GPa) sections of enamel. Whereas in Habelitz *et al.* (2001), H_V indentation carried out, produced values of 3.9 and 4.3 GPa travelling from the occlusal to the DEJ, results in Park *et al.* (2008) and Roy & Basu (2008) also confirmed these values. Collys *et al.* (1992) indicated that a load of 50 gf for materials because lower or higher loads influence the indentation size. The authors noted that two aspects for this load influence were; an altered sample surface during the polish process producing a coating more significant than the most extensive depth reached for the indenter; and with lower loads, there is a difficulty in reading the indentation marks. However, Gutiérrez-Salazar & Reyes-Gasga (2003) noted no surface coating following sample preparation. They did, however, note some fractures with loads of 50 gf and found the indentations from loads smaller than 10 gf were difficult to measure.

Studies on the mechanical properties of dentine have focused on the microstructures, and found that factors that influence the mechanical strength include the location, density, and direction of dentinal tubules; the orientation of the collagen fibres; and the average thickness of the mineral phase (Cohen *et al.*, 2010; Zhang *et al.*, 2014).

Wang & Weiner (1998) found that the microhardness of dentine close to the DEJ is low but increases rapidly to a peak and then subsequently decreases slowly towards the pulp cavity. However, in Angker *et al.* (2005), they found that a similar trend in enamel was present in dentine. Values changed from the DEJ (0.91 GPa) to the middle of dentine (0.85 GPa), and nearest the pulp wall (0.52 GPa), Balooch *et al.* (2004) and Cohen *et al.* (2010) also confirmed this. Using atomic force microscopy, Cohen *et al.* (2010), concluded that the decreasing trend corresponds to a decrease in mineral content.

Typically, within the literature, hardness values were carried out using Berkovich nanoindentation, due to dentine's 'softer' nature (Mahoney *et al.*, 2000; Angker *et al.*,

2005; Ziskind *et al.*, 2011). However, Balooch *et al.* (2004) and Cohen *et al.* (2010) used H$_V$ indentation and obtained similar results.

2.1.7.2   Compressive Strength

Compressive strength is linked to hardness and elasticity and is defined as the material's capacity to withstand loads before permanent deformation occurs. High compressive strength is an ideal property to have in teeth, especially during mastication. In Chun *et al.* (2014), human enamel and dentine blocks from premolars, had their compressive strengths measured. The maximum stresses recorded of enamel and dentine were 0.62 and 1.93 GPa respectively. The authors concluded that the difference was due to the differences in composition and microstructures, with dentine being a more isotropic material. Blocks of the DEJ were also cut, to see the combined strength of enamel and dentine together, with the maximum stress of 1.26 GPa reported. Compressive strength has an opposite correlation to hardness. Increasing hardness increases the brittleness of materials (Figure 2.2), this was seen in the harder enamel having a lower compressive strength compared to the softer/ductile dentine (Cuy *et al.*, 2002; Zhang *et al.*, 2014).
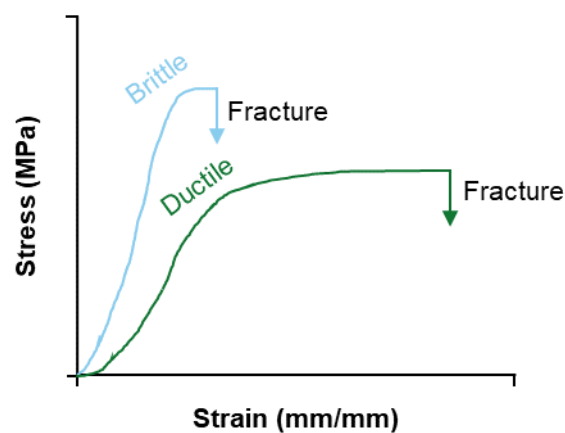
Figure 2.2: Example stress-strain curve demonstrating brittle and ductile materials.

2.1.7.3 Elastic Modulus

$\bar{E}$ or Young's modulus is the measure of a material's ability to withstand changes in shape when subjected to compression or lengthwise tension. Compression testing and nanoindentation are used in testing $\bar{E}$. Many studies have shown a linked correlation between hardness and $\bar{E}$ and have suggested $\bar{E}$, and hardness of human enamel decreases from the cusp cervically (Craig & Peyton, 1958; Craig *et al.*, 1961; Meredith *et al.*, 1996; Cuy *et al.*, 2002). Reports have also shown that an increase in elasticity is present when travelling from the DEJ peripherally (Willems *et al.*, 1993; Cuy *et al.*, 2002). Several studies have suggested that $\bar{E}$ and hardness of human enamel and dentine correlate with its degree of mineralisation (Staines *et al.*, 1981; Kodaka *et al.*, 1992; Cuy *et al.*, 2002).

2.1.7.4 Fracture Toughness

Fracture toughness (K_C) of a material, is a substance's ability to resist fractures (Quinn, 2007). Hassan *et al.* (1981) investigated the use of microindentation techniques to estimate the K_C of human enamel. By measuring the cracks that propagated from the indentation, a formula was applied to calculate toughness values. They found evidence of a pattern of increasing K_C from the incisal (0.72 MPa m$^{0.5}$ ± 0.1) to the cervical (1.09 MPa m$^{0.5}$ ± 0.1) edge in incisors. The investigators also established a statistical difference in molar, canine and incisor enamel, suggesting molar enamel was more brittle than the others. Alternatively, Yan *et al.* (2009) measured the K_C of human dentine using a three-point flexure test on third molars. The initial study was to characterise the fractography of the cracks formed, and therefore, were cutting specimens parallel and non-parallel to the dentine tubules. The data recorded noted a statistical difference between parallel (2.2 MPa m$^{0.5}$ ± 0.2) and non-parallel (2.4 MPa m$^{0.5}$ ± 0.2) dentine specimens. Quinn (2007) stated that the H_V indentation crack length has numerous drawbacks, with no universally accepted equation existing. Therefore, the values obtained are approximations not exact,

compared to K_C values used in nanoindentation studies. Furthermore, Quinn (2007) suggested that previous literature using the H_V indentation crack length should be referred to as fracture resistance (K_{ifr}) rather than K_C, due to equation variations.

2.1.7.5 Anisotropy

The term anisotropy is applied to materials whose properties are directionally dependent. Unlike materials of an isotropic nature that have material properties identical in all directions, anisotropic material's properties such as $\bar{E}$, change with direction along the object (Lees & Rollins Jnr, 1972). From the studies previously mentioned in Section 2.1.7, enamel can be defined as an anisotropic material, as its mechanical properties vary according the direction and orientation of its crystals (see Section 2.1.1). Figure 2.3 demonstrates this fact, by showing the differences in stress and strain dependent on the plane (Zaytsev & Panfilov, 2015).
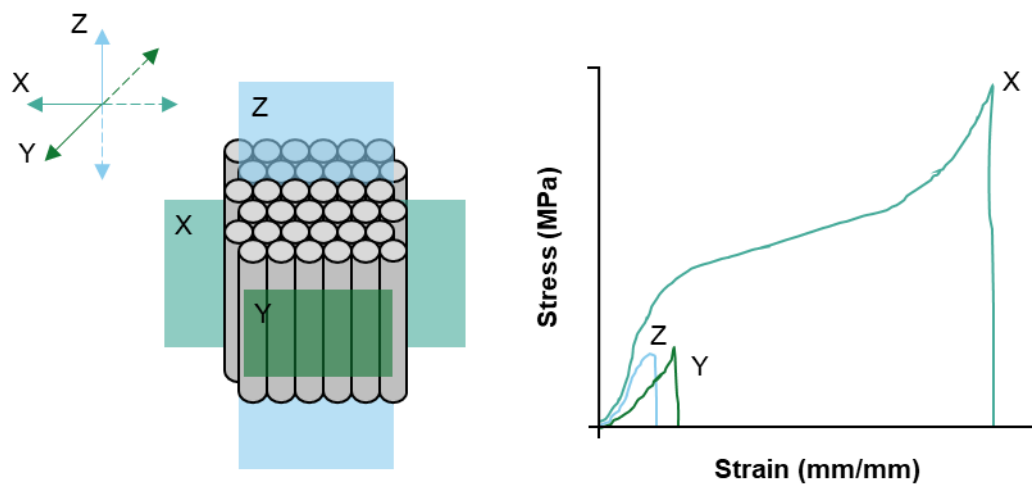
Figure 2.3: Stress-strain curves for the different orientation of prisms within enamel. Image adapted from Zaytsev & Panfilov (2015).

Spears *et al.* (1993) using finite element analysis summarised that the prismatic structure of enamel is the cause for it to behave as an anisotropic material, stiffer along the direction of these prisms than perpendicular to the prisms. In comparison, however,

Spears *et al.* (1993) defined dentine as an isotropic material, despite tubules being present in dentine, the authors argued that the less organised nature of these tubules had little overall effect on its mechanical properties. However, the authors had obtained the mechanical properties of dentine from a previous study, making no comment on where the measurements had been carried out and assuming the same $\bar{E}$ values in all directions (10 GPa). In contrast, later studies carried out by Lertichirakarn *et al.* (2001) disagreed with these findings, with the authors finding that the lowest tensile forces were present when parallel to the tubule orientation and greatest perpendicular to the tubules. Similar studies found similar results, as previously discussed in Section 2.1.7 (Cuy *et al.*, 2002; Yan *et al.*, 2009; Chun *et al.*, 2014).

2.2 Dental Education and Methods of Teaching

Dental education within the United Kingdom is continuously being updated, with the introduction of new and novel ways of teaching. The General Dental Council (GDC) states that the primary purpose is to educate students to become 'independent practitioners' as well as 'safe beginners', who can improve the overall oral healthcare in the UK (Cowpe *et al.*, 2010; Manogue *et al.*, 2011; GDC, 2020). However, the definition of dental students has also evolved over the years to include not only undergraduate dental students, but also students studying dental therapy, dental hygiene, and dental nursing (McHanwell, 2015; Bakr *et al.*, 2017; Lone, 2018). As part of their studies, students perform oral examinations, restorations, and minor surgical procedures on patients early on in their degree (Brennan & Spencer, 2005; Obrez *et al.*, 2011). Therefore, a good understanding of anatomy is essential in these early years of training to ensure safe clinical practice (Olowo-Ofayoku & Moxham, 2014; Rafai *et al.*, 2016). Anatomy modules taught are dependent upon the universities; however, the Association for Dental Education in Europe (ADEE) endorses an early dental curriculum that includes modules

on; gross anatomy, dental anatomy, histology, oral embryology, and neuroanatomy. (Guttman, 2003; McHanwell *et al.*, 2007; Gould *et al.*, 2014; ADEE, 2016; Bakr *et al.*, 2017).

The need for a universally, fully integrated dental curriculum has been widely recommended (Field & Jeffcoat, 1995; Postma & White, 2017). It has been suggested that this universal curriculum should teach the core primary science subjects with clinical skills and problem-based learning (PBL) (Crawford *et al.*, 2007; Nadershahi *et al.*, 2013; Kassebaum *et al.*, 2014). The integration of pre-clinical skills in the dental curriculum has been well-received with undergraduates (Postma & White, 2017). Moreover, in Macluskey *et al.* (2012), the authors reported that 78% of students agreed that they had received an 'adequate' level of anatomy teaching in the initial years of their degree, which they believed provided the necessary knowledge for the clinical placements.

2.2.1   Gross Anatomy

Within the first two years of their dental degree, students typically study gross anatomy with an emphasis on head and neck anatomy as well as the anatomy of the thorax and upper limb (Guttman, 2003; Snelling *et al.*, 2003; McHanwell, 2015; Lone, 2018). Gross anatomy is typically taught alongside surface anatomy and imaging, to help the students better understand the face, neck, temporomandibular joint (TMJ), and the oral cavity (Kondrashova *et al.*, 2016; Lone, 2018). Therefore the ADEE (2016) recommended that anatomy teaching should be taught alongside physiology and pathology whenever possible. Smith *et al.* (2016) suggested that dental students should learn from a focused dental curriculum, as opposed to a general medical-based curriculum on anatomy. Because of this, the anatomical topics addressed would have more significant clinical relevance, that would benefit the dental students (Manogue *et al.*, 2011; Amin *et al.*, 2017; Lone, 2018).

Some dental schools integrate patients examinations early on in undergraduate training, meaning an excellent knowledge of anatomy and clinical applications early on would be beneficial to both students and more importantly, their patients (Guttman, 2003). Rafai *et al.* (2016) reported that students had better knowledge, understanding, and learning experience when anatomy was taught alongside its clinical significance.

2.2.2 Dental Anatomy

Along with gross anatomy, dental anatomy and morphology (also taught in operative dentistry) modules are taught in the first and second years of undergraduate dentistry (Kilistoff *et al.*, 2013; Lone, 2018). As well as dental science students, tooth morphology is essential to dental therapy students, dental technicians, and dental nurses. These students need to identify teeth and develop their abilities to recognise damaged or lost tooth morphology within the laboratory setting and in their clinical work (Abu Eid *et al.*, 2013; Bakr *et al.*, 2017). The primary objectives of these lessons are to provide the necessary knowledge on topics including dental terminology, dental anatomy, and dental development, providing the information essential for the clinical years (Lone, 2018). Dental students study the morphological features of teeth to ensure correct identification. Understanding of the typical anatomical and morphological characteristics of teeth also provide the identification and diagnosis of any dental pathologies and how to correct for them (Obrez *et al.*, 2011; Bakr *et al.*, 2017).

Typical teaching methods for tooth morphology include; studying extracted or artificial teeth with clinical photographs, drawing teeth, tooth carving and wax-ups (simulated tooth repair with wax) (Obrez *et al.*, 2011; Lone, 2018). These activities help to develop the psychomotor skills that will be implemented and utilised in the clinical setting (Abu Eid *et al.*, 2013; Lam *et al.*, 2015). In the latter years of their training, students are taught root anatomy, which is an essential element for performing endodontic

procedures and surgical extractions (Ng *et al.*, 2008; Obrez *et al.*, 2011). Visualisation and understanding of the 3D features are critical in tooth morphology (Wallen *et al.*, 1997; Obrez *et al.*, 2011; Cantín *et al.*, 2015).

2.2.3   Neuroanatomy

Dental students typically learn neuroanatomy alongside gross anatomy, however with the emphasis on topics including the cranial cavity, neuronal pathways, the function of cranial nerves, pain pathways and coordinated movement of the jaw (Gould *et al.*, 2014; Lone, 2018). Neuroanatomy modules help to reinforce better the knowledge of the anatomy and physiology of mastication, swallowing, speech, and taste, and how these could differ in patients with diseases or conditions (Guttman, 2003; McHanwell, 2015; Lone, 2018).

Gould *et al.* (2014) investigated neuroanatomy modules taught in dental school in the United States; the authors found that the neuroanatomy modules were integrated into anatomy and physiology modules. Burk *et al.* (2013) and Moxham *et al.* (2015) reported a lack of dental backgrounds in teaching staff, in particular, neuroanatomy specific to dentistry. The anatomy of the cranial nerves, their clinical examination and related pathologies are essential for dental students (Klueber, 2003; Moxham, 2012; Burk *et al.*, 2013). The lack of dental backgrounds in the teaching staff meant clinical relevance was not enforced, and as discussed, is seen to be a crucial factor in dental undergraduate teaching (Manogue *et al.*, 2011). Moxham *et al.* (2015) also established, like other taught modules, there is no consensus on the core syllabus for neuroanatomy; therefore, the authors devised and presented their syllabus as a basis for a national curriculum.

2.2.4 Traditional Methods of Teaching

Traditional methods of teaching dental anatomy can come in many different forms such as; lectures, dissections, anatomical models, extracted and artificial teeth, and carving teeth (wax-ups) (Moxham *et al.*, 2014). A brief comparison of the traditional methods of teaching can be found in Table 2.2.

Table 2.2: Comparison of traditional methods of teaching. Table adapted from Sclater (2010).

Method	Active or Passive	Advantages	Disadvantages
Didactic Lectures	Passive	Efficient way of conveying to a large audience.	One-way speaker communication, difficult to maintain audience's attention.
Imaging	Passive	Helps to develop contextualisation for anatomical structures, can be easily paired with computer-aided learning (CAL) or technology enhanced learning (TEL).	Requires teacher, images can be repetitive (unless based on case studies).
Dissections/ Prosections	Active/Passive	Realistic simulation, helps to develop manual dexterity and psychomotor skills.	Time-consuming, technically demanding
Anatomical Models	Active	Helps to develop contextualisation for anatomical structures.	Synthetic apparatus lacks realism, models can be expensive.
Extracted Teeth	Active	Realistic simulation, helps to develop manual dexterity and psychomotor skills, allows for repeated practice before exposure to patients.	Low availability, risk of cross-infection, not all teeth are the same.

		Available in large quantities, helps to develop manual dexterity and psychomotor skills, allows for repeated practice before exposure to patients.	
Artificial Teeth	Active		Synthetic apparatus lacks realism.
Carving Teeth	Active	Helps to develop manual dexterity and psychomotor skills, allows for repeated practice before exposure to patients.	Time-consuming, technically demanding.
Problem-Based Learning	Active	Promotes independent active learning, information can be better retained.	Resource intensive, dependent on facilitator's skills.

2.2.4.1 *Lectures*

Didactic lectures are one of the traditionally used methods in delivering teaching; however, they depend on preparing slides to provide information to students (Johnson *et al.*, 2012; Schonwetter *et al.*, 2016; Shigli *et al.*, 2016). Bacro *et al.* (2013) assessed the students' preference for learning styles; the authors investigated this by recording lectures that were subsequently uploaded online, with student access being monitored. The results showed that more than half the students were not accessing the lectures. However, results showed that students who identified themselves as auditory learners found that after multiple viewings of lectures their grades had increased.

Park & Howel (2015) investigated an e-learning approach to teaching dental anatomy for second-year undergraduates at Harvard School of Dental Medicine. The online course material was provided to students before their lectures; after lectures, students would then attend small-group peer teaching and team discussions with members

of staff. The authors concluded that this alternative method promoted active student learning. However, the study did not gather data on students' examination scores and with students raising concerns about the validity of the information provided by their peers.

2.2.4.2   Imaging

Imaging such as radiology is one of the traditional methods teaching process during the clinical years of dental degrees. Although the topic is introduced early on in the dental degree, students utilise radiology with clinical relevance when in a clinical setting (McHanwell, 2015). Radiology is seen as an essential and vital diagnostic aid which is routinely used in dental practice, and it is typically taught in combination with anatomy. It offers students the ability to apply basic anatomical knowledge, interpret 2D images, and attain 3D visualisation and spatial understanding (Baghdady *et al.*, 2014).

Vuchkova *et al.* (2012) introduced a computer-oriented dental radiology teaching tool and evaluated it against the conventional teaching method of a textbook. Results indicated that 75% of second-year dental students preferred to use the digital tool over the textbook. However, only 50% of fifth-year students shared the same views. The authors concluded that second-year students preferred digital teaching aid as they had not yet studied the topic. Compared with the fifth-year students who had already studied from a textbook and favoured this more traditional approach. Qualitative data did show that the digital tool was interactive, and engaged the students more, enhancing the learning process (Vuchkova *et al.*, 2012; Lone, 2018; Erolin, 2019). Radiology taught simultaneously with anatomy, has shown to improve students' 3D spatial understanding (Baghdady *et al.*, 2014).

2.2.4.3 Dissections

Dissection-based teaching typically involves either dissection or prosection. The former consists of the examination of cadavers, carried out by undergraduates, whereas the latter uses previously dissected specimens prepared by professionals (Nnodium, 1990). Dissections and prosections are highly criticised methods for teaching head and neck anatomy to undergraduates (Topp, 2004). Snelling *et al.* (2003) stated that learning anatomy via dissections/prosections provided a better understanding, as students learn through visual stimuli, assisting in the knowledge of the subject. Anatomy taught via dissection was previously seen as the best teaching tool; however, studies have shown that dental students prefer prosection-based teaching (Aziz *et al.*, 2002; Snelling *et al.*, 2003; Olowo-Ofayoku & Moxham, 2014). The consensus from students is that dissections of the head and neck structures can be very tedious and technically demanding; therefore, prosection samples offer a simple way of learning anatomy. (Snelling *et al.*, 2003). However, dissections aim to help students develop their psychomotor skills as well to understand the anatomy better.

Redwood & Townsend (2011) investigated dental students' perceptions during a dissection course. Students' opinion of their professionalism, anatomical knowledge and emotional response were recorded, with students, being reviewed at the start, and again later at eight to ten weeks. Data analysis showed there was no significant change in perception of professionalism. However, anatomical knowledge and positive emotional responses of the dental students revealed a statistically significant increase during the course. The authors found that while many students enjoyed dissections, approximately 40% of the students believed that prosections could replace dissections (Redwood & Townsend, 2011).

In contrast, Snelling *et al.* (2003) demonstrated a preference for studying prosections due to the difficulty in dissecting regions of the head and neck. Interestingly, the authors noted that the difference in preference was due to the students' interest in a future surgical career. The studies, however, concluded that dissections should remain a fundamental part of the curriculum as it assists in student development (Snelling *et al.*, 2003; Redwood & Townsend, 2011).

2.2.4.4 *Anatomical Models*

Anatomical models are a standard method of teaching general anatomy. Models are easy to use and store, long-lasting, and can be used repeatedly (Sugand *et al.*, 2010; Johnson *et al.*, 2012; Lone, 2018; Erolin, 2019). This method is typically useful in studying the cranial nerves, as these can be difficult to see during prosections (Richardson-Hatcher *et al.*, 2014; Dickson & Stephens, 2015). Although anatomical models display the superficial and deep anatomical structures, the models do not offer anatomical variation, because of the manufacturing techniques used in their production (formative manufacturing, see 2.4.1). Therefore, they are not a very realistic haptic teaching technique (Sugand *et al.*, 2010; Erolin, 2019).

2.2.4.5 *Extracted Teeth*

Extracted teeth are used traditionally to study tooth morphology, identify features of the tooth, and to practise endodontic treatments (Mitov *et al.*, 2010). For many years, this technique has exclusively been used, however, with the introduction of the Human Tissues Act (2004), the way in which extracted teeth can be used has been restricted. Moreover, this method has its disadvantages such as; the possibility of cross-infection, being potentially infectious to students; the anatomical variability of extracted teeth, meaning valid assessment for students is not uniform (dos Luz *et al.*, 2015; Tchorz *et al.*, 2015). Improvement in oral health has led to a decline in tooth extractions, especially in

the older population. This reduction in tooth extractions means a decrease in obtaining healthy, extracted teeth (McCaul *et al.*, 2001; Muller *et al.*, 2007; Bernabe & Sheiham, 2014; Kassebaum *et al.*, 2014). Therefore alternatives such as artificial teeth are widely used (Obrez *et al.*, 2011).

More recently, conventional methods for teaching tooth morphology are being supplemented by innovative teaching methods through providing visualisation and 3D understanding of the morphological anatomy (Nagasawa *et al.*, 2010; Allen *et al.*, 2015; Cantín *et al.*, 2015; Salajan *et al.*, 2015; Erolin, 2019). However, students themselves prefer using extracted teeth, especially when studying the morphology (Abu Eid *et al.*, 2013).

2.2.4.6 Artificial Teeth

Commercial high-quality typodonts are an alternative method of teaching tooth morphology and endodontic procedures (Abu Eid *et al.*, 2013). Currently, these teeth have been made using opaque or transparent plastic to reproduce the characteristics of natural teeth. Artificial teeth, unlike natural teeth, do not have the risk of infection, are available in large quantities and allow for a validated assessment through their uniformity. Commercial typodonts can offer different anatomical challenges, and recent studies have investigated 3D printed artificial teeth, allowing students to repeatedly perform standardised procedures (Al-Sudani & Basudan, 2016; Reymus *et al.*, 2018; Hanafi *et al.*, 2020). By using these teeth, students can practise the same procedure until the students feel comfortable with performing a particular procedure, allowing students to practise multiple times in a safe, simulated environment (Nassri *et al.*, 2008; Tchorz *et al.*, 2015). Commercial typodont manufacturers include Acadental (USA), Frasaco (Germany), Nissin (Japan), Fabrica de Sorrisos (Brazil), KaVo Kerr (Germany), One Dental (Australia) and IDEA (USA). The models produced by these companies offer numerous

advantages and are particularly favourable in endodontic pre-clinical training (Al Shwaimi & Narayanaraopeta, 2014). ModuPRO Endo^{TM} and Real Endo-T (Acadental, Inc., USA) teeth are widespread in endodontic practise and advertised as promising models for pre-clinical endodontic training using both jaw models and artificial teeth. These models have the advantage of simulating a clinical situation, offering different anatomical, and procedural standardisation (Al-Sudani & Basudan, 2016).

To date, there is limited data on whether a model with artificial teeth is a suitable substitute for extracted tissue (Al-Sudani & Basudan, 2016). However, certain studies have investigated students' perspective on using artificial teeth for anatomy and endodontic procedures. In Al-Sudani & Basudan (2016), undergraduate students at King Saud University, Saudi Arabia, were given typodonts to perform endodontic techniques. At the end of the study, students were given a questionnaire regarding their perceptions of the difficulty of using artificial teeth compared to extracted teeth. Students were also asked to rank the perceived advantages of artificial teeth. Students stated that all procedures, except obturation, were more challenging to perform on artificial teeth compared to extracted, due to the hardness of the resin. They ranked fairness and availability as the best advantages. Similar results were also reported in Dummer (1991) and dos Luz *et al.* (2015) regarding these difficulties. Although the participants recognised the advantages of artificial teeth, they suggested that improvements in the physical characteristics, especially the hardness of the typodonts, were needed to offer a more realistic simulation (Al-Sudani & Basudan, 2016).

Moreover, Tchorz *et al.* (2015) evaluated root canal treatments performed by undergraduates on Real-T Endo artificial teeth. The results showed that the root canal treatments performed by students on artificial teeth were more acceptable with fewer errors compared to the students that performed on extracted teeth. The authors concluded that there was no effect on the technical quality of the root fillings and recommended the

use of artificial teeth. However, no reference was made regarding the students'
perceptions of the procedures carried out, nor any difficulties they faced in performing
the procedure upon an artificial tooth. Nassri *et al.* (2008) carried out a study using
professors of endodontics from different Brazilian universities. The professors were given
five artificial teeth from Fabrica de Sorrisos and asked to evaluate: internal and external
anatomy, root canal regarding their size, shape and position, resin hardness, and
visualisation of the radiographic image. The results of the survey were favourable, with
pulp space and hardness of teeth considered satisfactory, with an average grade of 8.4 for
tooth quality on a 0-10 scale. The authors concluded that the teeth had potential, but a lot
more improvements were necessary before replacing natural teeth.

Although new types of typodonts are commercially available, information
regarding the composition and mechanical properties is lacking. Loyaga-Rendon *et al.*
(2007) examined 12 brands of artificial teeth (two acrylic resins, three cross-linked acrylic
resins, and seven composite resins). The filler geometry and composition of the teeth were
examined using scanning electron microscopy (SEM) and X-ray diffraction (XRD),
respectively, with H_V indentation used to evaluate hardness. Results showed the examined
teeth were composed of two, three, or four layers of resin, and a hardness ranging from
0.17-0.47 GPa, a drastic difference compared to extracted teeth (3.9-4.3 GPa). The
authors concluded that the physical and mechanical characteristics of the evaluated
artificial teeth demonstrated unsatisfactory properties, and recommended withdrawal
from use in teaching endodontics.

Little literature is available on the current improvements made in manufacturing
artificial teeth for dental education. However, companies such as SimplyEndo (UK) and
Dental Engineering Laboratories (USA) have released Endo Reality and TrueTooth®
respectively, which they claim to be realistic and accurate to natural teeth. Both these

products have been manufactured through 3D printing, but exact materials and methods have not been revealed.

2.2.4.7   *Carving Teeth*

Carving teeth is carried out using different mediums such as; wax, chalk, or soap and is seen as useful in teaching tooth morphology (Mitov *et al.*, 2010; Obrez *et al.*, 2011). It also aids in developing manual dexterity and psychomotor skills, that are essential for building, and replacing lost tooth structure (Schroeter, 1959; Abu Eid *et al.*, 2013; Lam *et al.*, 2015). Abu Eid *et al.* (2013) conducted a study with first-year undergraduate students at the University of Aberdeen and introduced wax tooth carving practical sessions for students, along with tutorials and online resources. Results from the study found that 82% of students agreed that carving improved their psychomotor skills, and 64% of students found the sessions helpful in understanding the anatomy. However, only 55% of the students felt that the carving exercise was beneficial in developing their understanding of tooth morphology. Therefore, the authors recommended only partial carving of teeth to provide students an opportunity to develop manual dexterity but not to be time-consuming.

2.2.4.8   *Problem-Based Learning*

As previously mentioned, the recommendation from the ADEE of introducing an integrated curriculum in clinical programmes such as Dentistry allows for greater contextualisation and student engagement, promoting active learning (ADEE, 2016; Swanwick *et al.*, 2018). PBL is often defined as a way in which a problem acts as a stimulus for active student learning (Obrez *et al.*, 2011). Teaching the basic science subjects in conjunction with PBL enables students to correlate basic knowledge with clinical scenarios, allowing for better integration of knowledge and in turn leads to better results (Guttman, 2003; Obrez *et al.*, 2011; Swanwick *et al.*, 2018). Guttman (2003)

concluded that PBL allowed the student to assimilate information and provide a more in-depth understanding of the problem, a conclusion echoed by many others (Moxham, 2012; Olowo-Ofayoku & Moxham, 2014; Swanwick *et al.*, 2018).

In Obrez *et al.* (2011), the authors wanted to improve cognitive and psychomotor skills of students as well as theirunderstanding of the anatomy by introducing a revised tooth morphology module at the University of Illinois. The authors replaced the traditional didactic lectures and practicals with a more PBL-based module that involved digital materials, small group discussions and a laboratory exercise based on the clinical application of restoring teeth. The student's academic performance was evaluated and compared to the performances of students who studied via didactic lessons. The authors found no statistical difference in cognitive learning, however, they did observe a statistically significant increase in students' psychomotor skills. In comparison, McHarg & Kay (2008) introduced a similar PBL-based module focussing on clinical cases and small group discussions, with a new case being discussed at subsequent meetings. The authors noted that the students had a better knowledge of dental topics, due to their own learning assessments and the facilitator's assessment. However, it is worth noting results were not stated, with the authors surmising this increase in knowledge. In contrast, however, multiple studies have reported and analysed the benefits of PBL in teaching (Guttman, 2003; Vuchkova *et al.*, 2012; Amin *et al.*, 2017; Swanwick *et al.*, 2018).

2.2.5   Innovative Methods of Teaching

Computer-aided learning (CAL) or technology enhanced learning (TEL) has been utilised recently in undergraduate degrees and has found to be both extremely accessible and cost-effective, because of students' access to the latest electronic learning aids and gadgets (Redwood & Townsend, 2011; Yeung *et al.*, 2011; Erolin, 2019). A report carried out at the University of Birmingham discovered that laptops and smartphones were the

most favourable devices in assisting them to study and to self-test their knowledge (Khatoon *et al.*, 2014). A brief summary of the innovative methods of teaching can be found in Table 2.3.

Table 2.3: Comparison of innovative methods of teaching. Table adapted from Sclater (2010).

Method	Active or Passive	Advantages	Disadvantages
Computer-Aided Learning	Active/Passive	Helps to develop contextualisation for anatomical structures, can be easily paired with traditional methods of teaching.	Time-consuming, technically demanding, can be expensive if technology is not freely available.
3D Printing	Active	Helps to develop contextualisation for anatomical structures, novel designs can be recreated.	Time-consuming, technically demanding, can require expensive technology.
3D and Virtual Learning	Active	Helps to develop contextualisation for anatomical structures, can be easily paired with traditional methods of teaching.	Expensive, can lack realism.

2.2.5.1   Computer-Aided Learning

The use of computer-aided design (CAD) and computer-aided manufacturing (CAM) technology has been noted to effectively improve student learning (Douglas *et al.*, 2014; Lone, 2018; Erolin, 2019). Bogacki *et al.* (2004) looked into the efficacy of a CAL program about tooth morphology. The study indicated that the program was statistically equal to that of the didactic lectures given to first-year dental students at Virginia Commonwealth University. Nonetheless, the results led to the replacement of traditional didactic lectures with CAL and interactive classroom meetings. The authors

concluded that this integration was perceived to be more interactive and provided students with active control over their learning with regards to timing and pacing. Furthermore, this integration offered the teaching staff more opportunities to interact and engage with students, allowing more time to focus on the clinical relevance of dental anatomy (Bogacki *et al.*, 2004; Lone, 2018).

Garrett *et al.* (2015) experimented utilising computer software to assess student's wax-up models, to combine traditional and innovative teaching methods. Students carried out dental wax-up, that were evaluated by their peers, the staff and a software-based evaluation tool. The results suggested that computer software allowed students to confidently self-assess their practical work along with staff supervision (Garrett *et al.*, 2015; Lone, 2018).

2.2.5.2   *3D Printing*

As previously mentioned in Section 2.2.4.6, there is a demand for realistic, extensive and repetitive hands-on SBME in pre-clinical settings to prepare students for their clinical years. Typically this is executed on extracted and artificial teeth, but as previously stated in Al-Sudani & Basudan (2016), students find current artificial teeth not realistic. With 3D printing becoming more readily accessible, recent studies have tried to re-create more realistic artificial teeth. Reymus *et al.* (2018) wanted to assess the feasibility of manufacturing artificial teeth for endodontic training using stereolithography (SLA). In the study, sound extracted teeth were imaged using dental cone-beam computed tomography (CBCT) and then digitised using various software. The 3D printed replicas were given to students who were asked to evaluate the models. The questionnaires returned suggested the students favoured the availability and fairness due to the standardisation of the teeth. Still, it was also reported (71% of students) that the models were more comfortable to perform preparations on due to the hardness of the

resin. Collingwood *et al.* (2019) also imaged extracted teeth using CBCT for 3D printing; however, the authors used carious dentition to model a simulated occlusal caries for teaching and assessment. Using a multi-material inkjet 3D printer, the group printed typodonts with different materials to recreate the various structures (enamel, dentine and caries). Again, these replicas were given to students with questionnaires. The feedback from students was 'overwhelmingly positive'; however, the authors admit the 3D printed materials available were a limitation, echoing Reymus *et al.* (2018).

2.2.5.3   3D and Virtual Learning

Developments in technology have led to teaching students via a 3D interactive tooth atlas developed from computed tomography (CT) and micro-CT scanning. Advancements like this have created a 3D visualisation of the tooth structure, with layers of enamel and dentine, and the ability to remove these layers to reveal the pulp chamber (Nagasawa *et al.*, 2010; Wright & Hendricson, 2010; Cantín *et al.*, 2015; de Boer *et al.*, 2015; Salajan *et al.*, 2015; Lone, 2018).

Furthermore, studies have shown that clinical skills can be taught to the dental students using virtual 3D SBME including patient simulation, dental implant, and restoration of a 3D simulated tooth (Suvinen *et al.*, 1998; Curnier, 2010; Perry *et al.*, 2015). Similarly, Mitov *et al.* (2010) introduced 3D tooth teaching through a developed software; MorphoDent (Saarland University, Germany) to second-year students at the University of Saarland. The software utilised scans of extracted teeth in creating 3D models. Students were given access to MorphoDent, two weeks before an examination, the authors then assessed the students' perception and the effectiveness of the 3D teaching tool. Additionally, student examination compared the 3D tooth models along with extracted teeth, and results showed that while students positively received MorphoDent,

there was no statistical difference between the results of both examination methods (Mitov *et al.*, 2010).

Magne (2015) redeveloped the dental morphology module at the University of Southern California. The authors changed the module by introducing 2D-3D-4D concepts, implementing only essential practical and clinical skills. These concepts included drawing two-dimensional (2D) images of teeth, performing 3D partial and full wax-up of teeth, and the introduction of 4D utilising the histoanatomy of enamel and dentine replicated using layered acrylic mock-ups and resin restorations materials (Magne, 2015). The authors stated that the new innovative module introduced a practical and advanced learning method. Moreover, student satisfaction with the module increased, helping students in developing a clinical appreciation for dental morphology, function, and aesthetics (Magne, 2015; Lone, 2018).

In addition to previous methods, a recently developed method known as virtual reality (VR) has been introduced in dental education. VR is defined as the computer-generated simulation of a 3D image or environment in which a user can interact realistically (Curnier, 2010; Perry *et al.*, 2015). Perry *et al.* (2015) reviewed the use of VR in dentistry and found that haptic enhanced VR simulators offered a better assessment of periodontal disease, implant preparation, maxillofacial surgery, and restoration of 3D simulated teeth. The authors stated that the advantages of using VR included clinical skill development before patient exposure and the ability to practise procedures repeatedly (Perry *et al.*, 2015). Other studies have rated the advantages of VR; however, further development of VR and haptic-enhanced VR simulations would ensure more convenient access to this cost-effective teaching technique (Larnpotang *et al.*, 2013; Erolin, 2019).

2.3 X-Ray Microscopy

X-rays are classified as electromagnetic radiation with a wavelength of around 10^{-10} m, frequencies upwards of 3×10^{16} Hz, and energies ranging from 100 eV to 100 keV (Figure 2.4) (Seibert, 2004; Ahmed, 2011). X-rays play a vital role in research and are used in various techniques such as X-ray spectroscopy, XRD, CT, and microradiography. Their non-invasive nature is an ideal quality in research and medical fields, and are widely used in diagnostic radiology for dentistry and medicine (Hendee, 1995).
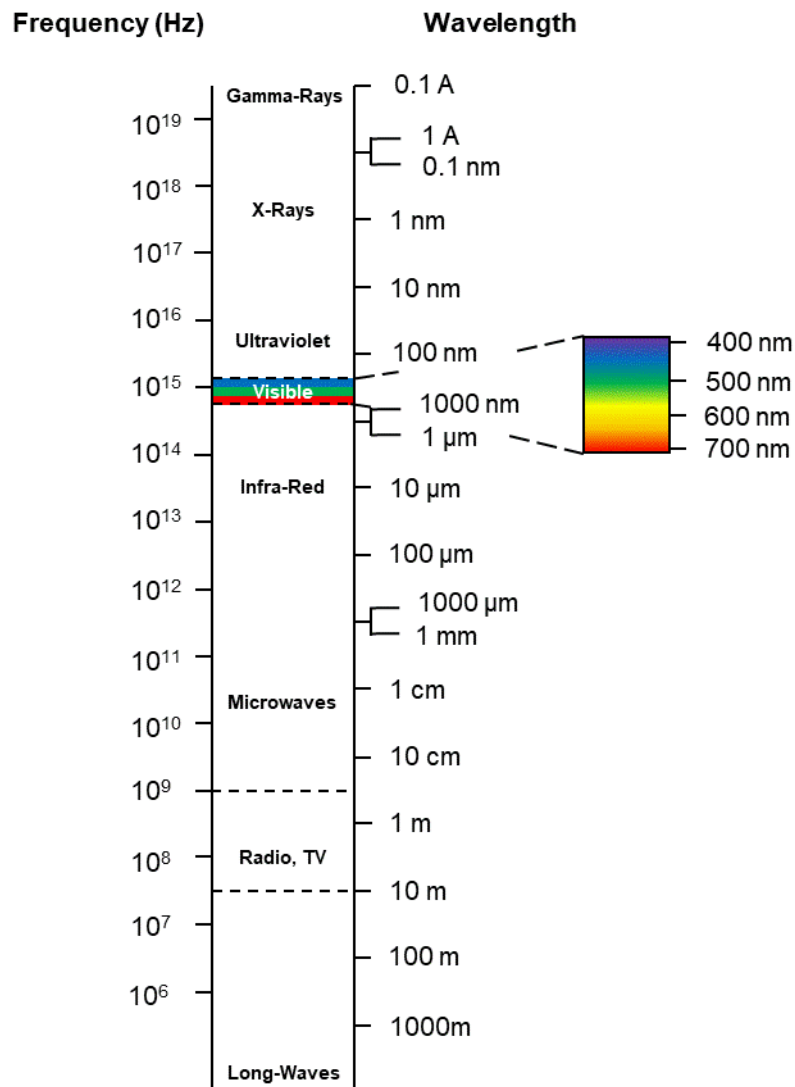
Figure 2.4: The electromagnetic spectrum. Adapted from Seibert (2004).

2.3.1   X-Ray Production

In 1895, the physicist Wilhelm Röntgen first published his findings on X-rays, while investigating cathode rays. Although X-rays had been observed prior, Röntgen was the first to study them in detail (Hendee, 1995). Performing the first medical radiography on his wife's hand (Mould, 1995), his concept remains unchanged; X-rays pass through the body, with denser materials (such as teeth and bones) absorbing more radiation, producing a softer image (Lider, 2017). X-rays are produced by bombarding a metal target with electrons. These electrons go from a negative cathode to a positive anode, producing kinetic energy which is transferred into electromagnetic energy, creating two kinds of X-rays in the process; characteristic and Bremsstrahlung radiation (Mould, 1995; Ahmed, 2011).

Characteristic radiation production comes from the transition of orbital electrons to the inner shells. It is referred to as characteristic due to radiation having precisely fixed, or discrete energies, that are dependent on the differences between the electron binding energies of a particular element. This property is used in various techniques such as X-ray spectroscopy and X-ray fluorescence spectroscopy. Radiation emittance occurs when the outer-shell electrons occupy a vacancy within the inner-shell of an atom, producing the 'characteristic' pattern to each element. If the energy gap between the shells is substantial enough, X-rays will be created (Seibert, 2004; Seibert & Boone, 2005).

Bremsstrahlung radiation, on the other hand, is produced by the deceleration of an electron when deflected by an atomic nucleus. The passing electron loses kinetic energy, converting it into a photon. Photons generated by this method are used in; CT and XMT. Bremsstrahlung has a continuous spectrum, which becomes more intense and tends to shift towards a higher frequency when the energy of the bombarding electrons increases (Pope, 1998; Seibert, 2004; Goldman, 2007). Typically, in a laboratory setting,

Bremsstrahlung radiation is produced from an X-ray tube, consisting of; an electron source (filament), a vacuum, a high positive potential to accelerate negative electrons, and an impact target (anode) (Figure 2.5) (Ahmed, 2011).
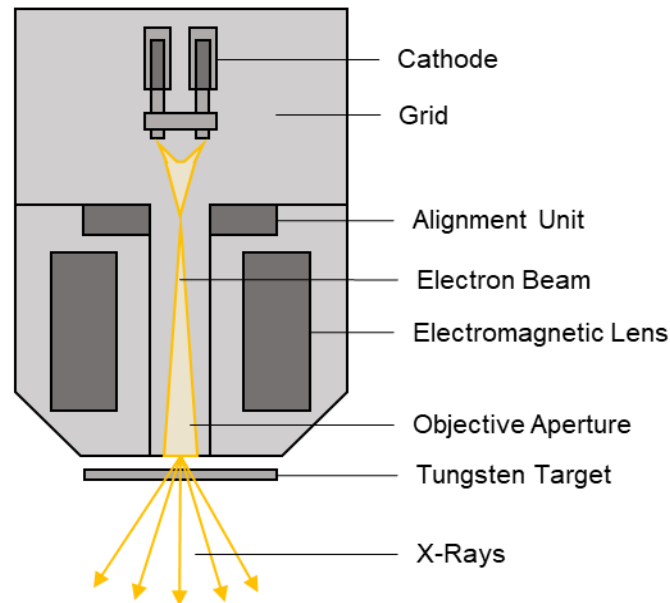
Figure 2.5: Main components of a micro-focus X-ray unit. Adapted from Ahmed (2011).

However, in modern micro-focus X-ray tubes, the number of electrons bombarding the target depends on the temperature of the filament. Micro-focus X-ray tubes can produce a micrometre-sized focal point; this is a crucial component within XMT, as X-rays with smaller focal points, can yield finer X-ray images with an increased magnification factor (Davis & Wong, 1996; Ahmed, 2011). Typically, a tungsten filament is heated (current) until electrons are released. The potential difference between the filament (cathode) and the target (anode) causes the electrons to travel from source to target. The bombarding electrons hit the target at the order of one-third of the speed of light, dependent on the voltage. The electrons pass through a hole within the anode and are directed through an electromagnetic lens by deflecting magnets, hitting the target. The target material requires a high atomic number; therefore, tungsten is an ideal material,

with an atomic number of 74 and a melting point of around 3400˚C (Cameron & Skofronick, 1978).

Outside of laboratory settings, synchrotron radiation is used. Synchrotron radiation occurs when electrons are accelerated radially due to the presence of a strong magnetic field, emitting electromagnetic radiation (Onuki & Elleaume, 2002). It is also known as 'magnetic bremsstrahlung', due to the magnetic field that keeps the electrons within a circular trajectory producing intense and parallel radiation. Because of this, monochromators can be used, creating a monochromatic X-ray beam, enabling an absolute linear attenuation coefficient (LAC) to be measured (Davis & Wong, 1996). Due to the accurate LAC measurements at high resolutions, synchrotron radiation is favourable, but the difficulty of access and expense impedes its use in extensive research (Lewis, 1997). In previous literature, synchrotron radiation has been used in texture analysis studies on dental enamel, looking at the order of crystallites, texture, and microhardness (Low, 2004; Seredin *et al.*, 2013).

2.3.2 X-Ray Interactions with Matter

The attenuation of energies used within a laboratory setting is due to two processes, absorption and scattering. The factors that can affect these include the energy of the X-rays, the density of the attenuating material, and the atomic number of the material. In absorption, the energy from the X-ray photon is transferred to the atoms of the material (Pope, 1998; Ahmed, 2011). In contrast, in scattering, the photon continues with a change of direction with or without a transfer of energy. In both instances, the photon interacts with the atoms within the material (Pope, 1998).

Photoelectric absorption occurs when a photon transfers all its energy into an inner orbital electron of the atom. The electron is ejected, and the photon is absorbed. An outer-shell electron fills the vacant space emitting a small amount of energy in the form of

characteristic radiation (Figure 2.6.B). Unlike, Rayleigh or 'simple' scattering in which the energy of the photon is not enough to dislodge the electron from its atom (the binding energy). Therefore the photon merely is deflected without transference of energy (Figure 2.6.D). Similarly, in Compton scattering, the incoming photon has more energy than the binding energy of the electron. Resulting in the photon transferring some of the energy to the electron and changing its direction (Figure 2.6.E). In pair production, however, radiation emittance only occurs in high energy photons and is demonstrated in positron emission tomography. If the photon possesses a sufficient amount of energy, this can be absorbed by the atom, producing an electron and a positron. The mass of the electron and positron must be 1.02 MeV to create the pair of particles (Figure 2.6.C).
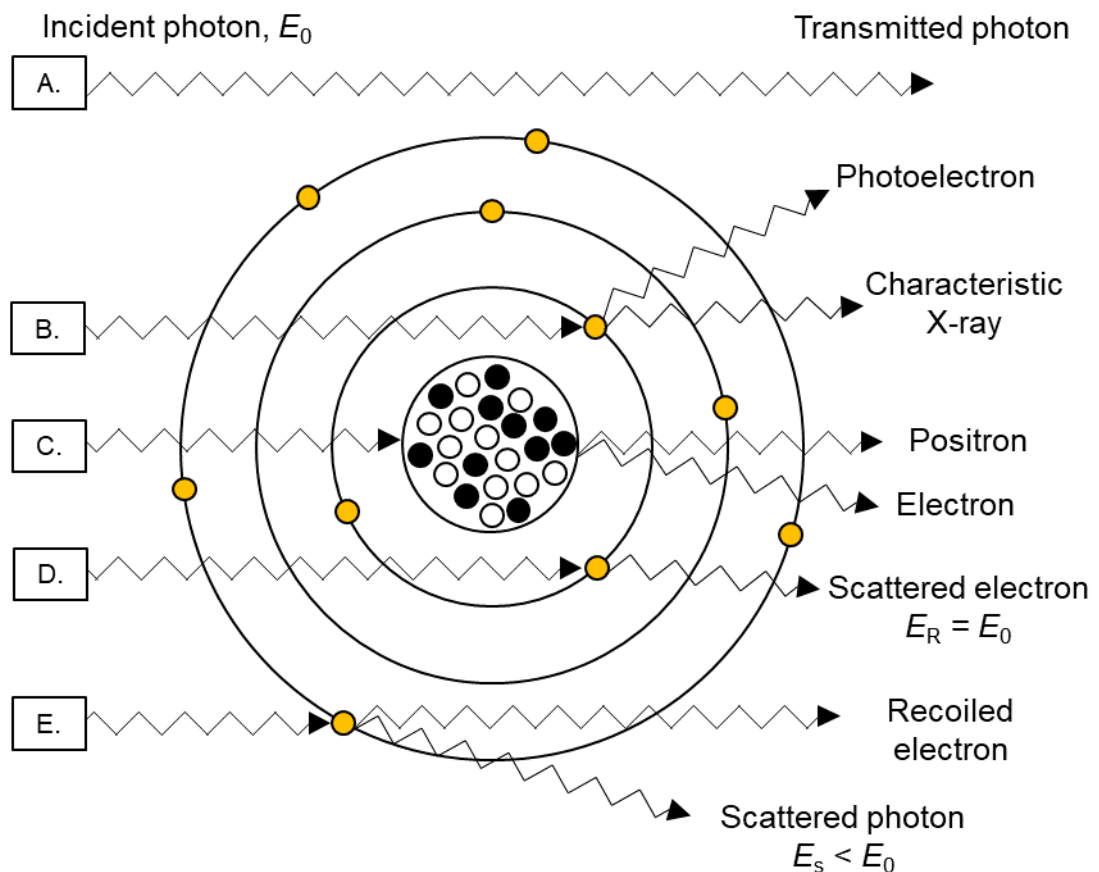
Figure 2.6: Attenuation mechanisms. A. No interaction. B. Photoelectric absorption. C. Pair production. D. Rayleigh scattering. E. Compton scattering. Adapted from Pope (1998)**.**

Photons emitted are typically described as being monochromatic X-rays. Monochromatic X-rays tend to attenuate exponentially as they pass through a material; this instance is known as Beer's or the Beer-Lambert law (Equation 2.1).

$$I = I_0 \, e^{-\mu x}$$

Where: I_0 is the initial intensity of the beam.

μ is the LAC.

x is the thickness of the medium.

The LAC describes the fraction of a beam of X-rays that is absorbed or scattered per unit thickness of the material. Mass attenuation coefficients are dependent on the absorption and scattering of the radiation and characterise how easily radiation penetrates a material—defined as μ_m which describes the attenuation per projected mass of the material penetrated (Equation 2.2).

$$\mu_m = \frac{\mu}{\rho}$$

Where: μ is the total LAC.

ρ is the density.

X-rays produced using impact sources are polychromatic, not monochromatic. As polychromatic X-ray beams pass through a sample, the distribution of X-ray energies shifts to higher energies while lower energy photons become more attenuated. The effects of polychromatic radiation results in 'dishing' artefacts in XMT images, where specimens

appear less attenuated within the centre (Davis & Elliott, 2003). A correction is required to obtain the same image as from a monochromatic beam.

2.3.3   Computed Tomography Scanning

CT was first demonstrated in 1972 by Hounsfield and Cormack. They had produced X-ray images taken around a single axis of rotation, revealing the internal structure of a specimen (Weber, 2001; Goldman, 2007; Ahmed, 2011). The first-generation CT scans consisted of a pencil beam of X-rays penetrating a sample and being received by a single detector. This coupled source-detector pair translates across the patient to produce a set of parallel projections, repeatedly at different angles (Figure 2.7.A). Second-generation CT was adapted from the translate-rotate system and used slot colimitation to generate a fan-shaped beam of radiation and multiple detectors (Figure 2.7.B). The advantage of this was the increased rate of data acquisition (Pope, 1998).
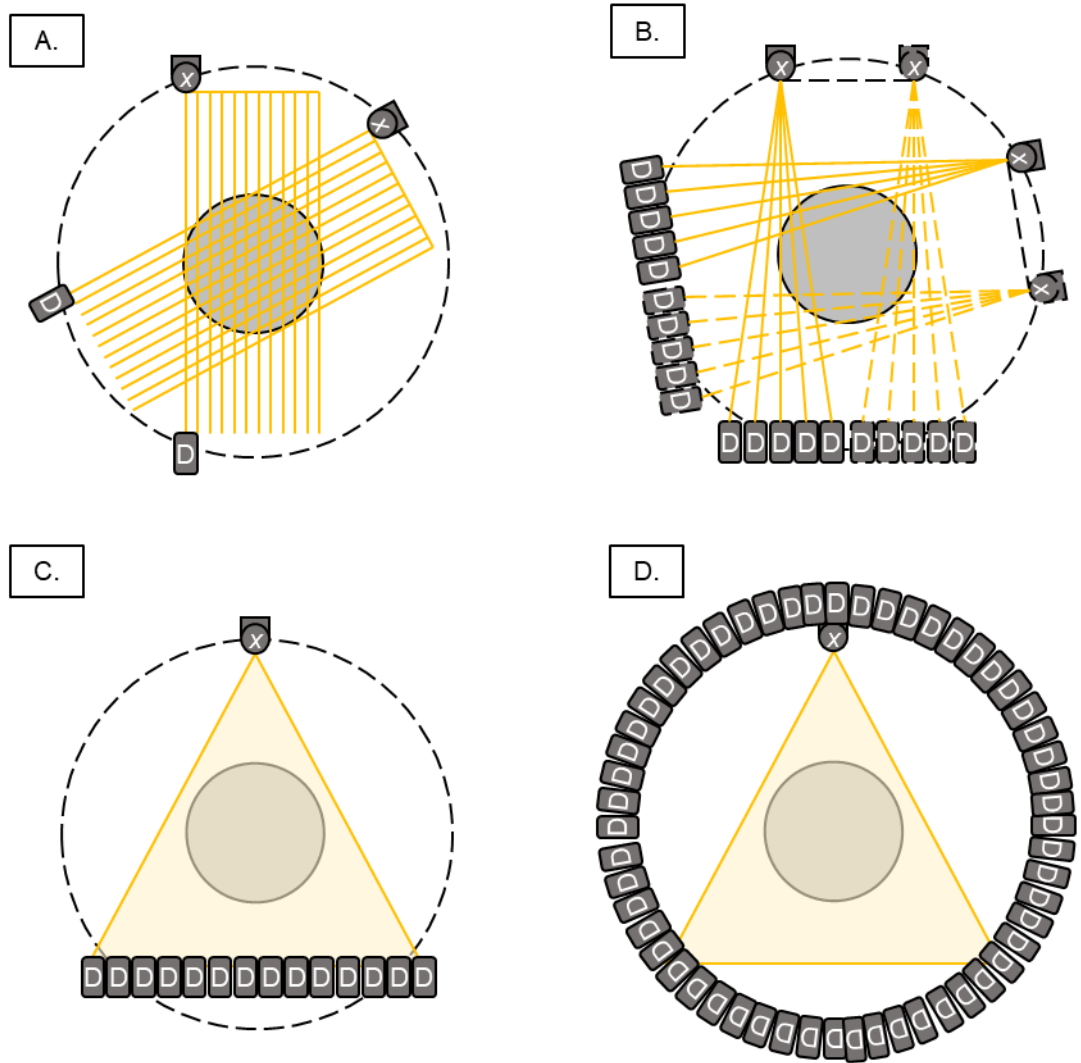
Figure 2.7: Evolution of CT scanners. Where *x = X-ray source, D = X-ray detector*. A. First-generation. B. Second generation. C. Third generation. D. Fourth generation. Adapted from Pope (1998).

Third-generation scanners saw huge progress in data acquisition and detector technology. The fan beam and detectors were wide enough to encompass an entire patient, and the tube-detectors would rotate around the patient, rather than the rotate and translate method seen in previous generations (Figure 2.7.C). This system was more efficient but was prone to ring artefacts because of the motion (Goldman, 2007). Fourth-generation scanners overcame this problem by using a stationary detector ring and a rotating X-ray source (Figure 2.7.D) (Schultz & Felix, 1980; Pope, 1998).

CBCT is a relatively new technology in clinical settings and allows 3D imaging of the patient's teeth and jaws. Third-generation scanners are the basis for CBCT technology, with the X-ray source-coupled 2D detector, rotating around the patient, exposing the patient to low-level radiation, in the form of either a round or rectangular cone-shaped X-ray beam (Sarment, 2013; Ghali *et al.*, 2018). Within a clinical setting, CBCT is an innovative way of imaging teeth, however, within research, very little literature has investigated the effectiveness of this technique, because of the nature of X-rays (Sarment, 2013). Demiriz *et al.* (2016) evaluated the accuracy of CBCT on measuring impacted supernumerary teeth. Twenty-five impacted supernumerary teeth were imaged, with each sample's tooth length and width measurements taken before extraction. After extraction, actual measurements were carried out, and results showed no statistical difference between data, concluding the technology to be very accurate. As mentioned previously, third-generation scanners were prone to ring artefacts; this has also been reported in CBCT, although advancements have been made, artefacts remain (Pauwels *et al.*, 2011; Queiroz *et al.*, 2017).

2.3.4   X-Ray Microtomography (XMT)

Elliott & Dover (1982) first developed XMT (also known as micro-CT) and is described as a miniaturised version of the medical CT scanner, both have developed alongside each other. However, XMT differs in two ways. Firstly, a reduction in scale (microns rather than millimetres). Secondly, with CT scanners, the X-ray source moves around the subject, whereas, in XMT, the X-ray source and detector remain stationary, with the specimen moving (Ahmed, 2011).

XMT is a non-destructive technique that is used to image specimens in 3D at the micron scale. In terms of scientific and clinical research, XMT has been used in multiple areas. These include; food, engineering, geology, and dentistry (Davis & Wong, 1996;

Stock, 1999; Ketcham & Carlson, 2001; van Dalen *et al.*, 2003; Dowker *et al.*, 2004; Mousavi *et al.*, 2007; Cunnigham *et al.*, 2017).

The basic set-up for XMT includes an X-ray source, an X-ray detector, and a specimen stage (Figure 2.8). In XMT a micro-focused X-ray source illuminates the region of interest (ROI), positioned accurately within the X-ray beam. During image acquisition, specimens rotate 360˚, and the absorption images are recorded by a 2D detector array at each rotational step. 2D images (or slices) based on LAC calculations from the absorption images are created using advanced computer software.
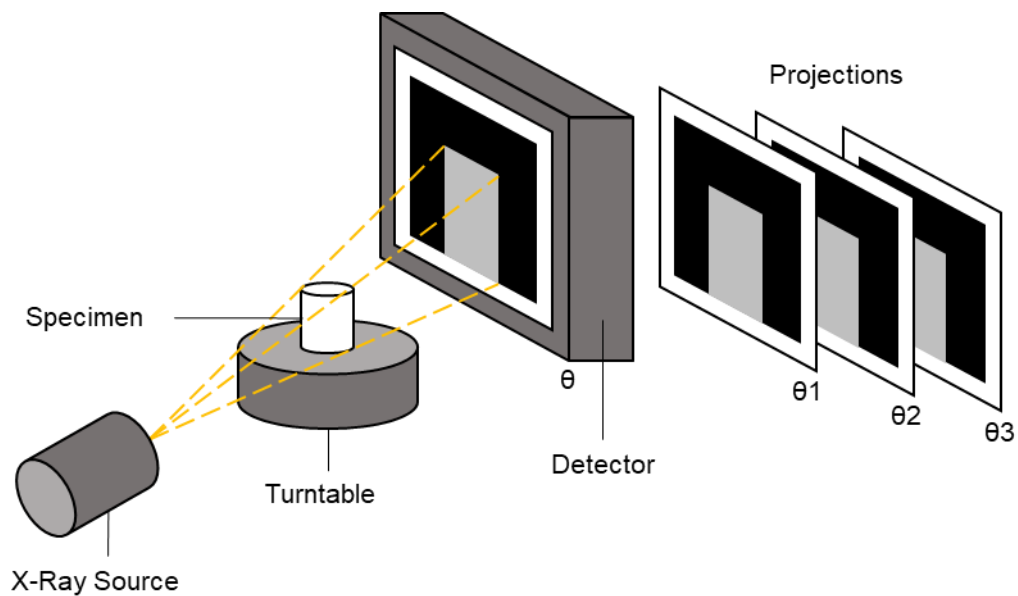
Figure 2.8: Main components of an XMT set-up. Adapted from Ahmed (2010).

Recent improvements in small X-ray tubes means it is possible to develop systems with sub-micron scale focal points, allowing for high-resolution imaging, offering significantly improved XMT results (Peyrin *et al.*, 2000). With the traditional impact X-ray source, there are disadvantages, such as beam hardening, and artefacts as previously mentioned. However, with the use of a scanner using a high dynamic range charge-coupled detector (CCD) X-ray camera, which has a time-delay integration (TDI) readout (Davis & Elliott, 2003) artefacts become reduced (outlined in detail in Section 3.1.1).

One of the significant advantages of XMT over other analytical techniques is its ability to generate a series of scans of the same specimen over a period of time. Davis *et al.* (2018) carried out *in vitro* demineralisation of a third molar. Demineralisation was recorded, visualised, and quantified giving an accurate real-time picture of the de/remineralisation process at different stages, because of the non-destructive nature of the technique (Davis & Wong, 1996; Davis *et al.*, 2013; Davis *et al.*, 2018). Other methods are mainly destructive, meaning standardised samples of HAp need to be used, as enamel mineral concentration can vary. Imaging the same specimen multiple times with XMT allows each sample to act as their own 'control' (Wong *et al.*, 1995; Ahmed, 2011).

Other advantages of XMT include its ability to produce high-resolution scans at a micron level and to measure mineral concentration quantitatively (Ahmed, 2011). These advantages allow for mineral density to be analysed, reducing the time of the experimental conditions. De/remineralisation of teeth occurs in three-dimensions, meaning 3D images produced by XMT can provide an accurate representation of this (Cochrane *et al.*, 2012). XMT studies of caries within primary teeth have shown that in dentine, a bowl-shaped lesion is formed, as opposed to cone-shaped lesions as previously seen in 2D radiographs (Wong *et al.*, 2006; Ahmed *et al.*, 2012). The XMT system used within these studies has the additional advantage of the calibration taking place during the image pre-processing. In commercial systems, mineral density is calculated post-processing using data from previous samples, which can severely reduce accuracy (Evershed *et al.*, 2012).

Farah *et al.* (2010) characterised mineral density within hypomineralised molars and incisors using XMT. Using a commercial system, 10 sound and 10 hypomineralised teeth as a comparison were scanned. Enamel blocks were used as calibration standards for beam hardening correction. Data acquisition showed in sound enamel the mineral

density increased from the CEJ to the incisal edge. In contrast, in hypomineralised teeth, the mineral density decreased from the CEJ to the occlusal region. On average, the results showed a 19% decrease in mineral density for hypomineralised teeth compared to sound. Similarly, Cherukara *et al.* (2005) and Zou *et al.* (2011) found similar data in sound enamel.

As well as research implications, XMT has looked at clinical implications. Willmott *et al.* (2007) used XMT to examine cavity preparation concerning demineralised dentine. Overpreparation of between 8.5-44.3% volume was observed; having severe clinical implications in a field where 'minimal intervention' is the objective. Additionally, Ahmed *et al.* (2012) compared the efficacy of caries removal via hand excavation and chemo-mechanical techniques through XMT scanning. The clinical implications of this study suggested that chemo-mechanical procedures were more conservative than hand excavation, preserving more layers of demineralised dentine (> 0.97 g/cm^{-3} of mineralised tissue).

2.3.5   Scanning Electron Microscopy

SEM is a technique for high-resolution scanning that uses a fine electron beam to create images, typically 1-5 nm spot size, fixated on the surface of a specimen. An electron beam travels over the sample in a series of lines and frames. The electrons bombard the sample within a minimal area, creating; elastic scattering from the specimen, losing no energy, or the sample absorbs electrons. Absorption of electrons creates secondary electrons of very low energy, together with X-rays. Electron absorption results in an emission of visible light, and electric currents within the specimen (Boyde, 1980, 2003a, 2003b).
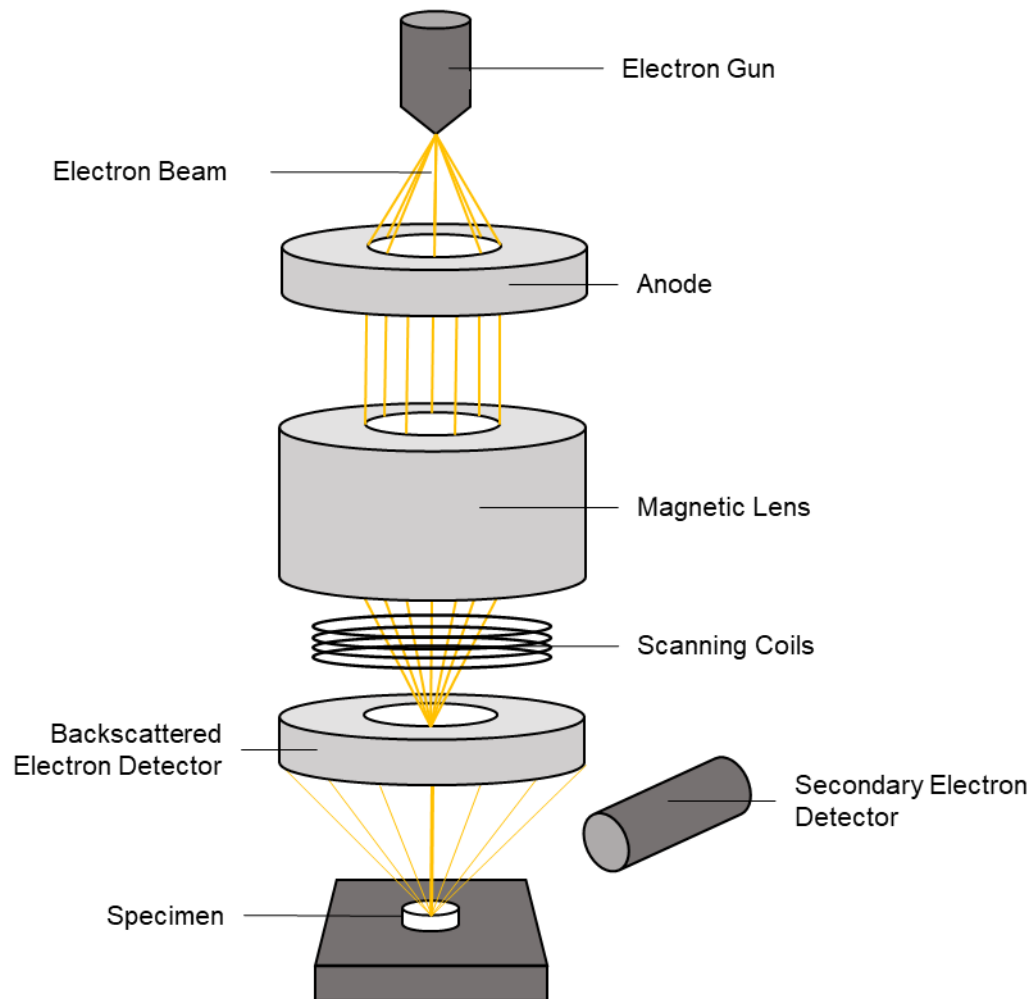
Figure 2.9: Schematic of an SEM set-up. Adapted from Ahmed (2011).

Secondary electron imaging is most commonly used for studying the topography of the surface materials. They are selectively attracted to a grid held at a low positive potential compared to the specimen. These electrons pass through the grid, coming from the sample, causing an emission of light from the scintillant. Light subsequently gets redirected down a light pipe to a photomultiplier tube, converting the photons into a voltage. The number of secondary electrons that strike the disc will determine the strength of this voltage (Figure 2.9). Thus, the secondary electrons produced will create a voltage signal of a particular strength (Boyde, 1980, 2003a, 2003b).

Although secondary electron imaging is a way of mapping the topography of the specimen's surface, the electrons are unable to penetrate the surface, so another detector

is used. Back-scattered electrons (BSE) are beam electrons that are reflected from the sample by scattering. BSE is useful in analytical SEM along with characteristic X-rays. BSE images provide information about the distribution of different elements within a sample because the intensity of the BSE signal is related to the atomic number of the specimen (Boyde, 1980, 2003a, 2003b).

Gavrila *et al.* (2016) investigated the surface topography and the remineralisation rate from various commercial products on carious teeth. SEM images showed a difference in surface topography, in particular, the remineralisation of dentine tubules. BSE microscopy was used in the study, as it can assess microscopic differences in tissue mineralisation (Reid & Boyde, 1987; Howell & Boyde, 2002). However, in Gavrila *et al.* (2016), scanning took place in between remineralisation cycles at set intervals, not in real-time.

Wang & Weiner (1998) used BSE to study the level of mineralisation of human enamel and dentine. Moreover, Boyde (1998) confirmed the existence of cross striations in the tooth structure using the same technique, while Mahoney *et al.* (2004) used BSE to compare the mineral density between sound and hypomineralised human enamel. The authors reported a reduction in mineral density by approximately 5% in comparison to sound enamel.

2.4   Manufacturing Technologies and Applications

Within the world of engineering, the most critical consideration when designing parts for production is the method of manufacturing. A design can be produced via a range of manufacturing techniques with each having their associated strengths and weaknesses (Thomas & Claypole, 2016; Redwood *et al.*, 2017). Most manufacturing techniques can be categorised into three groups; formative, subtractive, and additive manufacturing (Figure 2.10).
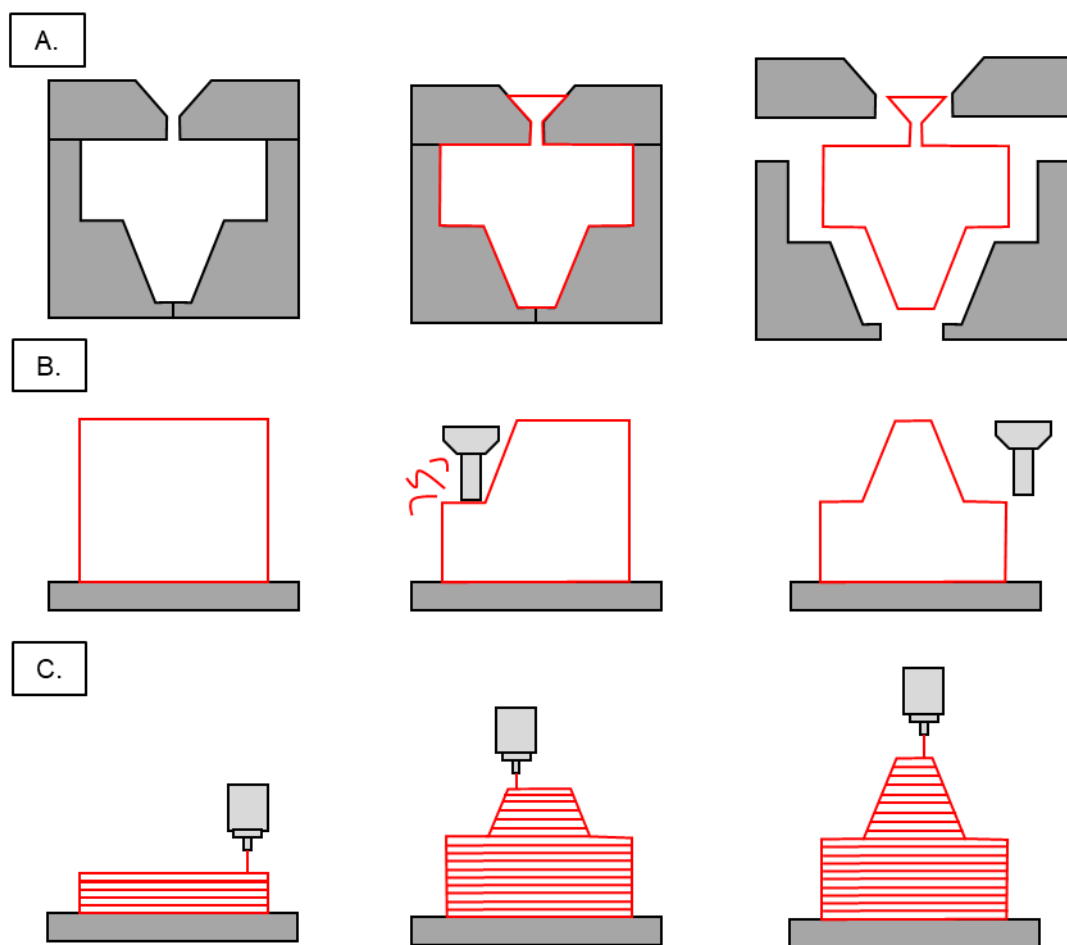
Figure 2.10: Schematic comparison of different manufacturing techniques. A. Formative. B. Subtractive. C. Additive manufacturing. Adapted from Redwood *et al.* (2017).

2.4.1　Formative Manufacturing

Formative manufacturing typically forms the material into the desired shape through heat and pressure (Figure 2.10.A). The material can be melted down and extruded into a mould (injection moulding/die-casting), melted and then poured into a mould (casting) or pressed or pulled into the desired shape (stamping/vacuum forming/forging). These techniques produce parts from an extensive range, making it only cost-effective for mass production. The main limitation of this manufacturing method is the need to build a tool (mould or die) to form the part. Tooling is often expensive and complicated to produce, increasing times and delaying manufacturing of a piece. This substantial upfront investment is why formative production is only cost-effective at high volumes (Redwood *et al.*, 2017).

2.4.2　Subtractive Manufacturing

Subtractive manufacturing starts with a block of solid material and utilises cutting tools to remove (machine) material to achieve a final shape (Figure 2.10.B). Computer numerical control (CNC) milling, turning (lathe) and machine operations like drilling and cutting are all examples of subtractive techniques. This type of manufacturing can produce highly accurate parts with an excellent surface finish in which almost every material can be machined in some way. For the majority of designs, subtractive manufacturing is the most cost-effective method of production. However, many factors limit this technique. Most designs require CAM to plot tool paths and efficient material removal, and this adds time and cost to the overall process. Tool access must also be considered when designing parts, as the cutting tool must be able to reach all surfaces to remove material. Subtractive manufacturing is also generally considered a wasteful process due to the large amounts of material that are often removed to produce the final part geometry (Redwood *et al.*, 2017).

2.4.3   Additive Manufacturing

Additive manufacturing (more commonly known as 3D printing) is the process of additively building up a part one layer at a time (Figure 2.10.C). There are multiple 3D printing technologies that each have their own advantages and disadvantages. One of the main benefits of 3D printing is that parts can be manufactured to almost any geometry (depending on the technology used). Moreover, this technique does not rely on expensive tooling and has little start-up costs; a critical advantage when developing prototypes and low-volume production parts.   However, one of the most significant limitations of 3D printing is the inability to produce parts with material properties comparable to subtractive or formative techniques. The majority of 3D printed parts are typically anisotropic or not fully dense. Repeatability is another limitation of 3D printing, as usually, parts will often have slight variations due to differential cooling or warping during curing (Thomas & Claypole, 2016; Redwood *et al.*, 2017).

2.4.4   3D Printing Process

There are many different printing technologies. Although each method of 3D printing produces parts differently, five steps are constant across all technologies (Atwell, 2017).

Firstly, a digital model is produced. The most common method for producing a digital model is through CAD. Reverse engineering can also be used to generate a digital model via 3D scanning (Laycock *et al.*, 2012; Doney *et al.*, 2013). Several considerations must be assessed when designing for 3D printing. Focussing on geometry limitations, support material (extra material required to support structures that overhang) and escape hole requirements (access for material to be removed) (Atwell, 2017; Redwood *et al.*, 2017).

Secondly, a CAD model must be converted into a format that a 3D printer can interpret. Typically, CAD models are converted into a stereolithography (STL) file, also referred to as Standard Triangle Language file. OBJ or 3DP are also common 3D printing file types. STL uses triangles (polygons) to describe the surfaces of an object, simplifying the complex CAD model. Once an STL file has been generated, the file is imported into a slicer program, which slices the design into layers that will be used to build up the part. The slicer program takes the STL files and converts them into G-code (or the slicer's own equivalent file format). G-code is a numerical control programming language used in CAM to control automated machines like CNC machines and 3D printers. The slicer program also can define the 3D printer build parameters by specifying support location, layer height, and part orientation. Slicer programs are often proprietary to each brand of 3D printer, although there are some universal slice programs like Netfabb (Autodesk Inc., 2017), Simplify3D (Simplify3D, 2018), Slic3r (Sound, 2016), and Cura (Ultimaker, 2017) (Thomas & Claypole, 2016).

Thirdly, the model is printed. Printing techniques are dependent upon the 3D printing technologies, and each method varies. (2.4.5 outlines in more detail the different technologies used in 3D printing).

Fourthly, the print is removed, separating the printed part from the build platform. However, in some instances, the removal of a part is a technical process involving precise extraction, while it is encased in the build material or attached to the build plate. These instances require strict removal procedures, safety equipment and controlled environments (Gunther *et al.*, 2014; Redwood *et al.*, 2017).
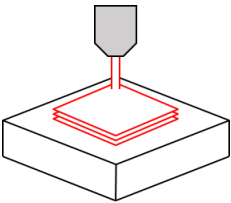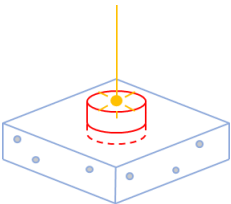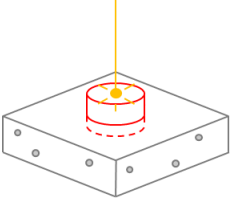
Finally, post-processing may be required to 'finish off' the part. Post-processing procedures again vary by printer technology. Some technologies require the part to cure under ultraviolet (UV) light before handling, while others allow components to be

handled right away. For technologies that utilise support, the support is also removed at the post-processing stage (Gunther *et al.*, 2014; Thomas & Claypole, 2016; Redwood *et al.*, 2017).

2.4.5   3D Printing Technologies and Materials

The International Organization for Standardization – American Society for Testing and Materials (ISO/ASTM) 52900 Standard was created in 2015 to standardise all terminology as well as classify each of the different methods and materials of 3D printing. A total of seven technology categories were established (ASTM International, 2015). Each of these and the associated process descriptions are presented in Table 2.4.

Table 2.4: Classification of 3D printing technologies. Adapted from ASTM International (2015); Zhang *et al.* (2015); Thomas & Claypole (2016); Redwood *et al.* (2017).

Process	Description	Technologies
	Material Extrusion: the material is selectively dispensed through a nozzle or orifice.	Fused filament fabrication (FFF), fused deposition modelling (FDM).
	Vat Polymerisation: a liquid photopolymer in a vat is selectively cured by light-activated polymerisation.	SLA, stereolithography bioprinting, direct light processing (DLP), laser-assisted bioprinting, biological laser printing.
	Powder Bed Fusion: thermal energies selectively fuse regions of a powder bed.	Selective laser sintering (SLS), direct metal laser sintering, selective laser melting, electron beam melting, matrix-assisted pulsed laser evaporation direct writing.
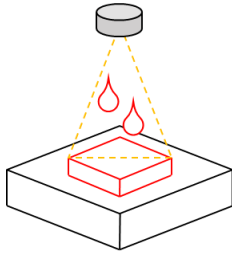
	Material Jetting: droplets of material are selectively deposited and cured on a build plate.	Material jetting, drop on demand, inkjet.
	Binder Jetting: a liquid bonding agent selectively binds regions of a powder bed.	Binder jetting, inkjet.
	Direct Energy Deposition: focused thermal energy is used to fuse materials by melting as they are being deposited.	Laser engineering net shaping, laser-based metal deposition, laser-induced forward transfer.
	Sheet Lamination: sheets of material are bonded to form a part.	Ultrasonic additive manufacturing, laminated object manufacturing.
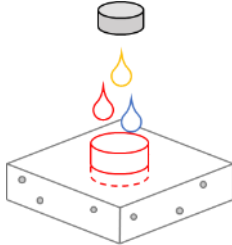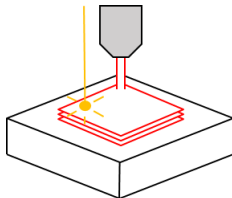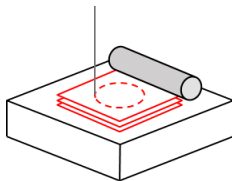
2.4.5.1   *Fused Filament Fabrication*

The most common 3D printing technology is FFF or FDM (a trademarked term by Stratasys Ltd., USA). Within this context, the raw materials may take the form of wire, rolls, laminates and pellets (Thomas & Claypole, 2016).
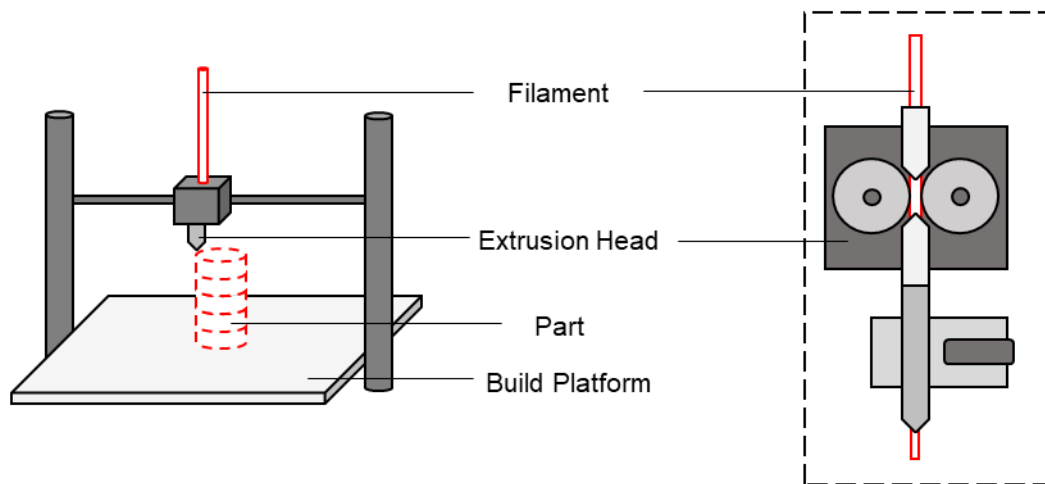
Figure 2.11: Schematic of a typical FFF printer set-up.

In FFF, the model or part is commonly produced by extruding thin (200-400 μm) threads of a polymer-based material which solidifies almost immediately to form a solid layer (Guessasma *et al.*, 2015; Thomas & Claypole, 2016). Typically, a thermoplastic is wound on a reel, which is then unwound as the material is supplied through an extrusion nozzle head. The nozzle head heats the material and turns the flow on and off via a stepper motor. In many 3D printers, the extrusion head can move in both horizontal directions, *X-axis*, and *Y-axis* while the build plate moves up and down along the *Z-axis* (Figure 2.11). This control of directions is carried out using CAM software tool, which runs a microcontroller (Thomas & Claypole, 2016).

The heated extrusion head deposits molten material onto a supportive structure, layer by layer. Various polymers are used including; acrylonitrile butadiene styrene (ABS), polycarbonate (PC), polylactic acid (PLA), high-density polyethene, PC/ABS, polyvinyl alcohol (PVA), poly-phenyl-sulfone, and high-impact polystyrene (Liu *et al.*, 2014; Mashiko *et al.*, 2014; Stone *et al.*, 2015; O'Reilly *et al.*, 2016; Thomas & Claypole, 2016; Angjellari *et al.*, 2017). In general, the polymer is in the form of a filament fabricated from pure polymers. However, recycled post-consumer plastic waste is increasingly being converted into filament (Khoo *et al.*, 2015).

FFF processes can be restricted in the variation of shapes that may be fabricated. However, using a removable support structure, any form can be manufactured. These thin supports are automatically added to the model using modelling software and can be broken away during the finishing process (Jin & Fu, 2015). Tam et al., (2013) and Tam et al., (2014), used this process when re-creating a model for a hollow aortic aneurysm—using PVA as the material for the support structure (requires dual extrusion) (Tam *et al.*, 2013). During the finishing process, water was added to the model removing any support structure, because of PVA's water solubility (Tam *et al.*, 2014).

The majority of commercially available 3D printers on the market are FFF printers because of its simplicity and easy to use interface. (Lau & Leung, 2015). Accuracy can also be high in these printers (80-50 μm); in Salmi *et al.* (2013), the accuracy of different printer techniques was evaluated using a coordinate measuring machine on printed human skull models from digital imaging and communications in medicine (DICOM) images. The models were assessed with a rating of 'original, moderate and worse', with FFF producing three models classified as 'moderate'.

The main limitation is the variety of materials available. FFF relies heavily on thermoplastic filaments, as the extrusion head is heated, the technique requires a material that changes viscosity with a change in temperature but still retains the ability to revert to a more solid state once cooled. These properties narrow the type of materials that can be used (Oropallo & Piegl, 2015). In Tan *et al.* (2015), the study looked at re-creating a soft tissue and skeletal model for injured and uninjured hands for pre-operative planning. In the review, the authors praised the accuracy and effectiveness of the skeletal models but noted the limitations in re-creating the soft tissue. Due to the lack of diversity in materials for FFF, the characteristics of the soft tissue were unable to be matched by the thermoplastics. Similarly, Fasel *et al.* (2013) and Hochman *et al.* (2014) created skull

models and temporal bone replicas (respectively), with thermoplastics and reported similar dissatisfaction.

2.4.5.1.1 Bioprinting

Bioprinting is the utilisation of 3D printing techniques (typically FFF techniques), to combine cells, growth factors, and biomaterials together, to create a biomedical part that imitates natural tissues (Zhang *et al.*, 2015). This technique of bioprinting has been used in biomedical sciences, using biocompatible polymers to create 3D constructs, most notably; prosthetics, and other implants (Dearment, 2013). When bioprinting with cells, cells are suspended within a hydrogel, which is loaded into a delivery system, and extruded to build up layers. This delivery system is typically a syringe or a capillary tube attached to a plunger. Generally, in extrusion printing, larger nozzles are used in conjunction with high extrusion pressure allowing for more viscous materials to be extruded (Walker, 2013). However with an increase in nozzle diameter, a decrease in resolution occurs, as well as requiring contact with the print substrate, this eliminates the potential for *in situ* printing (Cresswell-Boyes, 2015; Zhang *et al.*, 2015).

When printing with live cells, all the primary techniques rely on the use of bioink. Bioink is a biocompatible and printable fluid, that is used as a carrier for live cells and can come in various forms that can be developed in conjunction with or without scaffolds. However, it can be a problematic biomaterial to produce; it must provide both structures for the 3D object but also be a viable environment for cells (Schuurman *et al.*, 2016). The critical component is the hydrogel, which is typically made from agarose constituents. Some studies have proven success in encapsulating cells within spheroids and other microstructures, to create pre-assembled tissue constructs, eliminating the time needed for cells to self-organise in typical hydrogel-based bioinks (Mironow *et al.*, 2009; Cresswell-Boyes, 2015).

The limitations of bioprinting mainly surround the development of a viable bioink. Cell source is a big concern, as sourcing, a significant number of cells can be difficult. During the printing process, cells undergo extreme forces and temperatures, so the bioink must be able to provide a safe environment from these (Zadpoort & Malda, 2017). Cross-linking agents can be added to aid cells surviving the mechanical stress, but these agents need to be non-toxic to cells; otherwise, it defeats the objective. The consensus is that the current state of printing techniques need to be optimised for bioprinting to overcome specific issues, such as; spatial resolution, the viscosity of the bioink, the printing efficiency, and cell density, demonstrating the need for further research into this field (Cresswell-Boyes, 2015; Zhang *et al.*, 2015).

2.4.5.2   Stereolithography

SLA is renowned for being the original 3D printing technology. SLA uses photocuring UV/lasers (or LCDs in DLP printers) to convert liquid photopolymer resins and composites into solid layers. (Thomas & Claypole, 2016). A tank of the liquid polymer resin is exposed to controlled light, curing the exposed liquid photopolymer. The build platform then moves in small steps, revealing more liquid photopolymer to the controlled light, curing it in the process. This process repeats itself until the model has been built (Figure 2.12). Once completed, the liquid photopolymer is drained from the tank, leaving the solid model (DeSimone, 2015).
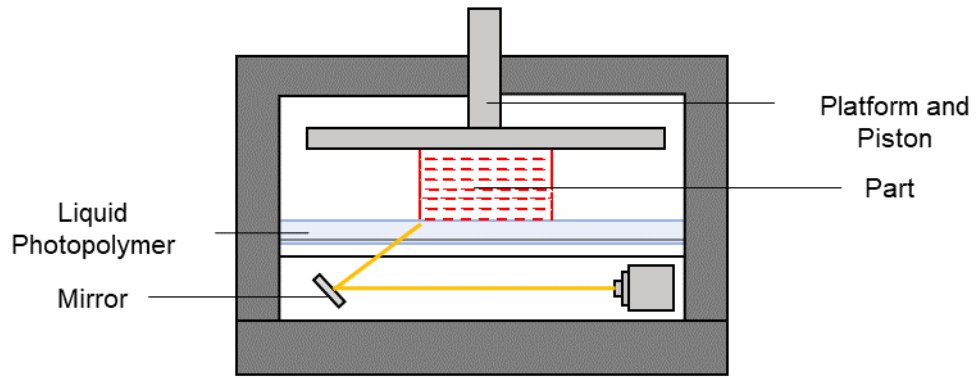
Figure 2.12: Schematic of a typical SLA printer set-up.

The laser used during the process, from a scanning laser source cures whole layers of photosensitive polymers. This process can be quite challenging to engineer and is generally at a higher cost due to the high price of resins compared to FFF filaments. However, for high-end applications, this process results in the production of parts to professional standards (DeSimone, 2015; Thomas & Claypole, 2016). These professional standards are due to the technology's high degree of accuracy, with a resolution of around 10-25 μm (Chhaya *et al.*, 2015). This technology has mainly been used to produce high-quality and high-resolution parts for biomedical applications or components with integrated moving parts (Thomas & Claypole, 2016).

Although SLA printers produce high-quality parts, the main drawback is the size of the vat and platform travel distance, which can restrict the height of the desired object. Photopolymer resin waste is also a current drawback, as the resin is an expensive material, and only the cured material is kept. The excess material is not re-used due to the possibility of excess cross-linked material that may remain in the vat, and the extensive cleaning procedure makes the process a costly manufacturing method (Gross *et al.*, 2014). With SLA, a post-fabrication step is required, using a laser to guarantee all the reactive groups of the photopolymer are polymerised, to ensure the final 3D object is strengthened. This extra step can make the process a time-consuming manufacturing technique (Sakuragi, 2014).

Maddox *et al.* (2015) used SLA printing to create 12 models of patients' kidneys for training purposes. In particular, the study was looking at recreating the 'suspicious' masses picked up in scans, to train undergraduate medical students. Both the authors and students were impressed with the high level of accuracy from the models, allowing students to get a 3D visualisation and better understanding of the masses. The high accuracy has been utilised in much of the literature, in particular to bronchial models and their intricate details. Much of the perceptions of SLA being used in recreating bronchial models has been positive (Zopf *et al.*, 2013; Bustamante *et al.*, 2014; Nakada *et al.*, 2014; Miyazaki *et al.*, 2015). The same has also been reported in heart replicas (Zopf *et al.*, 2013; Costello *et al.*, 2014a; Costello *et al.*, 2014b).

2.4.5.3 *Selective Laser Sintering*

SLS is a method in which powder-based materials are fused together to form solid models. Powdered materials including metal, nylon, alloy or ceramic, are spread in a thin layer on the build platform. The powder is then sintered to form a complex shape. When a layer has been sintered, another layer is deposited on top, and the process repeats until a final structure is completed (Figure 2.13) (Thomas & Claypole, 2016).
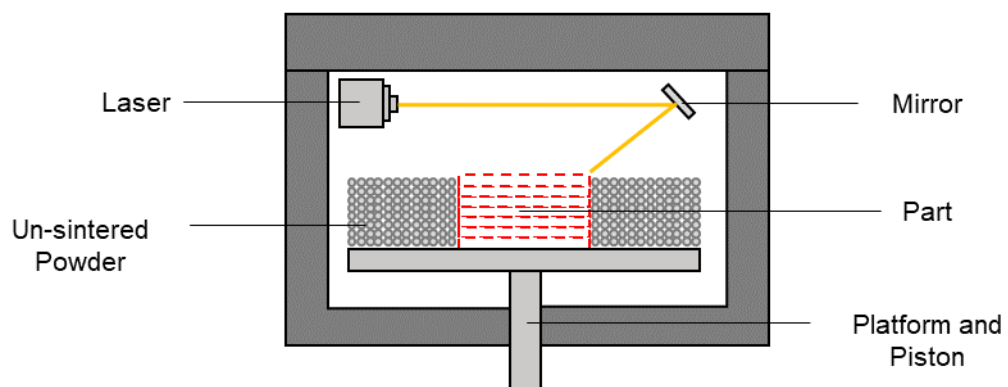
Figure 2.13: Schematic of a typical SLS printer set-up.

The SLS process can employ a technique of using joining and bonding agents instead of a laser sintering method, while some processes use a mixture of both agents and

lasers. By using different powders or particle materials, 3D components can be produced with desirable structure and aesthetic properties (Thomas & Claypole, 2016).

A commonly noted issue with SLS printing is that the printed models suffer from shrinkage or deformation due to the thermal heating from the laser and the subsequent cooling. This deformation can change the dimensions of the object, making it challenging to follow specifications when making parts to order (Gross *et al.*, 2014).

Due to the expensive nature of SLS, little literature is available on its use in medical education. However, in Waran *et al.* (2014), patient brain models were recreated from CT data, for planning surgery simulations. Spottiswoode *et al.* (2012) also created patient-specific brain models for pre-operative training in identifying tumours. Both studies reported a reasonable level of accuracy, and surgeons benefitted from the accurate anatomical models when planning surgeries. Many studies have used SLS for patient-specific models, due to the higher accuracy and types of materials that can be used (Schmauss *et al.*, 2012; Watson, 2014; Hughes *et al.*, 2017).

2.4.6   3D Printing in Dentistry

As mentioned previously (Section 2.2.5.2), 3D printing has become a subject of great interest in teaching, in particular, surgery training. However, the technology has a specific resonance within dentistry, with advances in 3D imaging and modelling techniques such as CBCT and CAD/CAM technologies becoming increasingly present in dental surgeries (Dawood *et al.*, 2015). Uses of 3D printing have included; the production of drill guides for dental implants, the production of physical models for prosthodontics, orthodontics, and surgery, the manufacture of dental, craniomaxillofacial and orthopaedic implants, and the fabrication of copings and frameworks for an implant and dental restorations (Burde *et al.*, 2015; Dawood *et al.*, 2015; David *et al.*, 2017).

In Lee *et al.* (2015), the accuracy of 3D printing replica teeth was evaluated. Fifty extracted molar teeth were scanned to generate high-resolution STL files. The files were printed using FFF and inkjet technologies. These replicas were digitally scanned, and were compared with the original through linear measurements, volumetric measurements, and mean deviation measurements. The authors reported that the FFF produced teeth were slightly smaller compared to the original, whereas the inkjet produced teeth were marginally larger compared to the original. Despite the differences, statistically, the differences were insignificant, so the authors concluded that the technologies were accurate enough for orthodontic diagnosis and treatment.

Tunchel *et al.* (2016) evaluated the use of an SLS printed titanium dental implant in a 3-year follow-up study. Eighty-two patients were given titanium implants within healed alveolar ridges and in post-extraction sockets. After 3 years of loading, it was reported that only six implants failed, giving an overall survival rate of 94.5%. The authors concluded the use of 3D printed implants was a successful clinical option for the rehabilitation of single-tooth gaps; however, further long-term studies would have to be carried out to determine the longevity of these implants. Studies like Tunchel *et al.* (2016) have led to a shift in producing restoratives from CNC methods to using 3D printing technologies (Silva *et al.*, 2011; Farré-Guasch *et al.*, 2015).

Chapter 3

General Methodologies

Chapter 3 describes the principal methodologies used in the experiments reported in this thesis. Section 3.1 outlines the system and techniques used for XMT imaging and analysis. Section 3.2 follows on from the image acquisition through XMT but explains the reconstruction procedure and visualisation of images. Section 3.3 describes the CAD/CAM process that was used throughout the different experiments, in particular, the various 3D printing methods and techniques used. Section 3.4 outlines the microscopic techniques (other than XMT) that were used, such as; SEM, white light profilometry and optical light microscopy. Section 3.5 explains the mechanical testing carried out, including, the novel automatic force cutting experiment, the set-up and procedures used to collect data on force. Section 3.6 discusses the different characterisation techniques that were carried out. Finally, Section 3.7 outlines the type of data analysis that was applied to the results obtained.

3.1   X-Ray Microtomography

The fourth-generation XMT scanner used was the 'in-house' XMT scanner at QMUL, MuCAT2 developed by Davis & Elliott (2003) with TDI (Davis *et al.*, 2010), was used in imaging specimens throughout the study (Figure 3.1). The MuCAT2 scanner was chosen as the main imaging techniques due to its ability to create high contrast 3D images, advantages and disadvantage of this system are later discussed in Chapter 5.
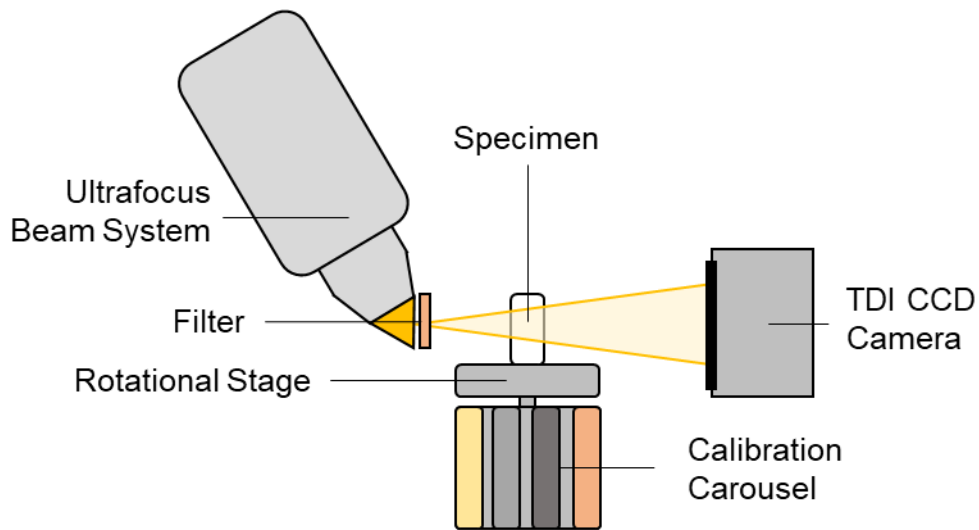
Figure 3.1: Schematic diagram of the fourth generation XMT scanner. Developed by Davis & Elliott (2003).

3.1.1   MuCAT2

MuCAT2 is the system used at QMUL which has been utilised in many hard tissues studies, as well as imaging ancient scrolls and engineering components. An enhanced XMT scanner with TDI CCD readout was used, employing an X-Tek ultrafocus beam system (Nikon Metrology Ltd., UK) of 5 μm spot size (Figure 3.2). Typically, biological materials such as extracted teeth were X-rayed at 90 keV, 180 μA, and with a 1.2 mm aluminium and 0.5 mm copper filter. In comparison, non-biological specimens were usually X-rayed at 40 keV, 405 μA, and with a 0.5 mm aluminium filter. These parameters have been previously defined in Evershed *et al.* (2012), and have proven to be effective in creating high contrast scans of these types of samples (biological and non-biological). More details of voltage and settings used for individual samples is given in Appendix A (Table A). A higher voltage increases the penetrability of X-rays, which is required for denser materials such as extracted teeth.
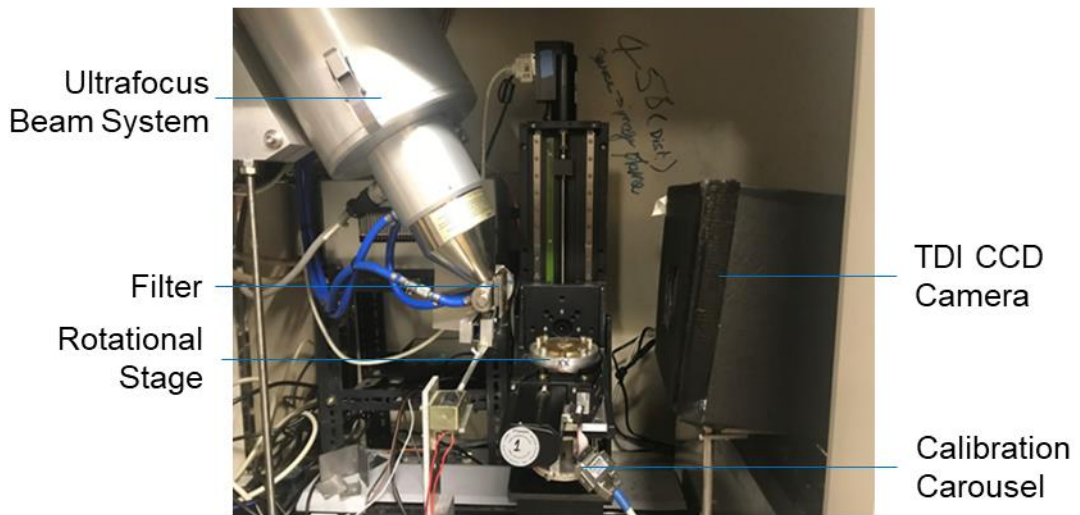
Figure 3.2: An image of the fourth generation XMT scanner. Developed by Davis & Elliott (2003).

A cooled slow-scan CCD camera (Spectral Instruments Inc., USA) was used with fibre optic 1:1 lens coupling to a 70 μm thick columnar caesium iodide scintillator (Applied Scintillation Technologies Ltd, UK). The camera has 4096 x 4096 square pixels of dimension 15 μm, which are binned at 4 x 4 to give 1024 x 1024 square binned pixels of dimension 60 μm (Figure 3.3). The geometric magnification can be varied to provide reconstructed voxel sizes between 5 and 38 μm (Ahmed, 2011; Evershed *et al.*, 2012).
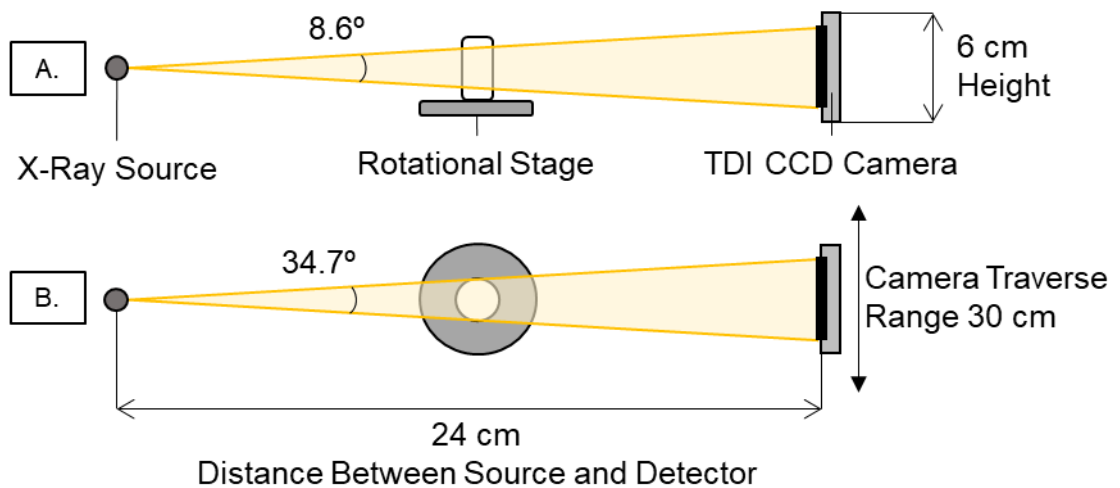
Figure 3.3: Schematic diagram of the layout of MuCAT2. A. Side view. B. Plan view of the XMT set-up adapted from Ahmed (2011).

The TDI CCD configuration eliminates the occurrence of ring artefacts by averaging the characteristics of all the detector elements in each projection. The specimens were positioned upon the rotational stage, and at each rotation, the camera moves across the X-ray beam, and simultaneously the CCD is read out (Figure 3.4). The movement of the camera and the CCD readout are timed so that the relative motion of charge along with the CCD surface matches that of the focused image, meaning the movement is effectively stationary (Figure 3.5). Each recorded pixel is derived from the accumulation of charge as it is moved along the corresponding CCD column, as the CCD is mounted at 90° to normal use, allowing for rows and columns to be swapped. This process takes place for each projection. Before the projections are taken, a dark reference image is taken, with the CCD shuttered, and then a light reference scan is taken without the specimen in the way of the X-ray beam (Ahmed, 2011; Evershed, 2013).
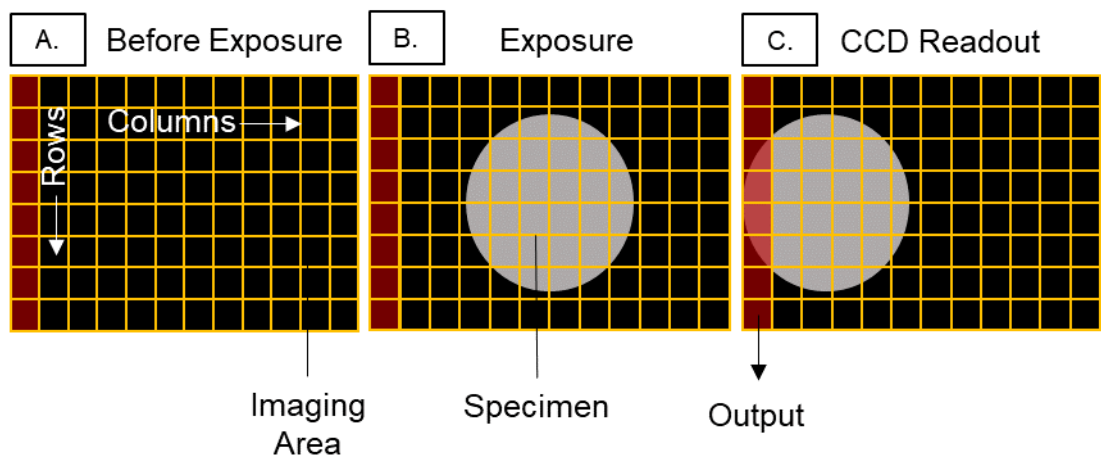
Figure 3.4: Example of a circle being imaged and how the CCD reads out the data. A. Before exposure. B. During exposure. C. CCD Readout. Adapted from Ahmed (2011).
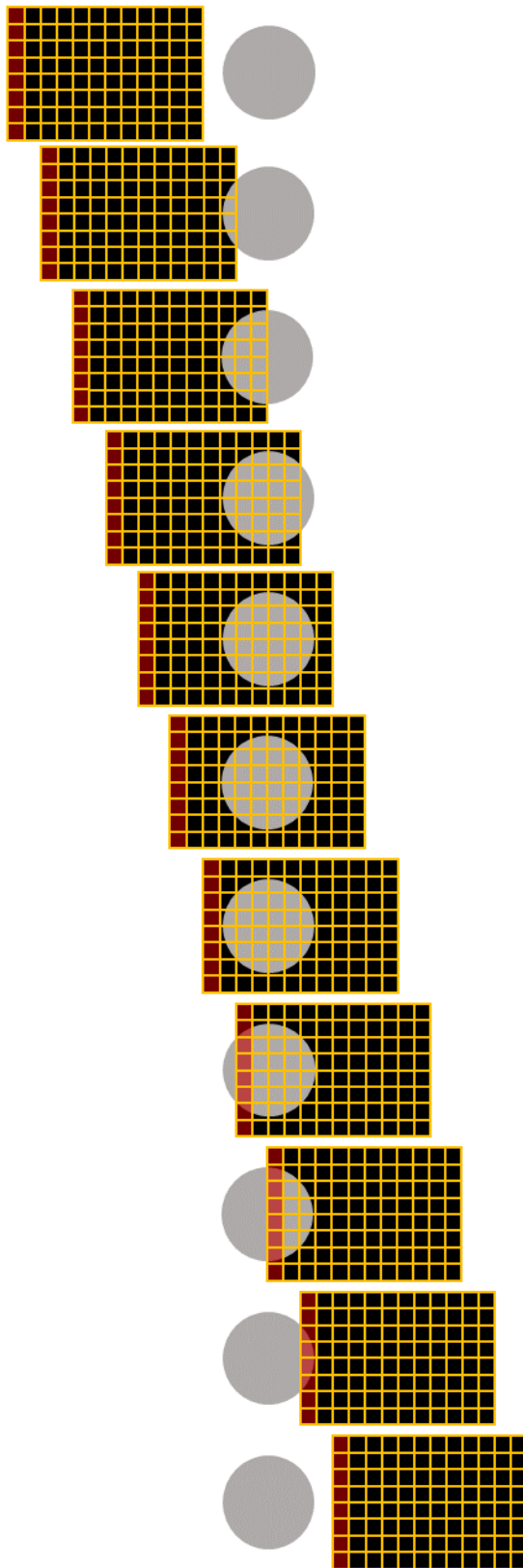
Figure 3.5: Time sequence showing TDI CCD readout of the captured image. Adapted from Ahmed (2011).

The XMT systems at QMUL has a novel design and is represented by its moving collimator. The moving collimator was designed to reduce scattered radiation and thus improve image contrast, resulting in more accurate LAC measurements. The redesigned collimator moves in synchrony with the detector, reducing the portion of the specimen that is illuminated at any point in time (Figure 3.6) (Ahmed, 2011; Evershed, 2013).
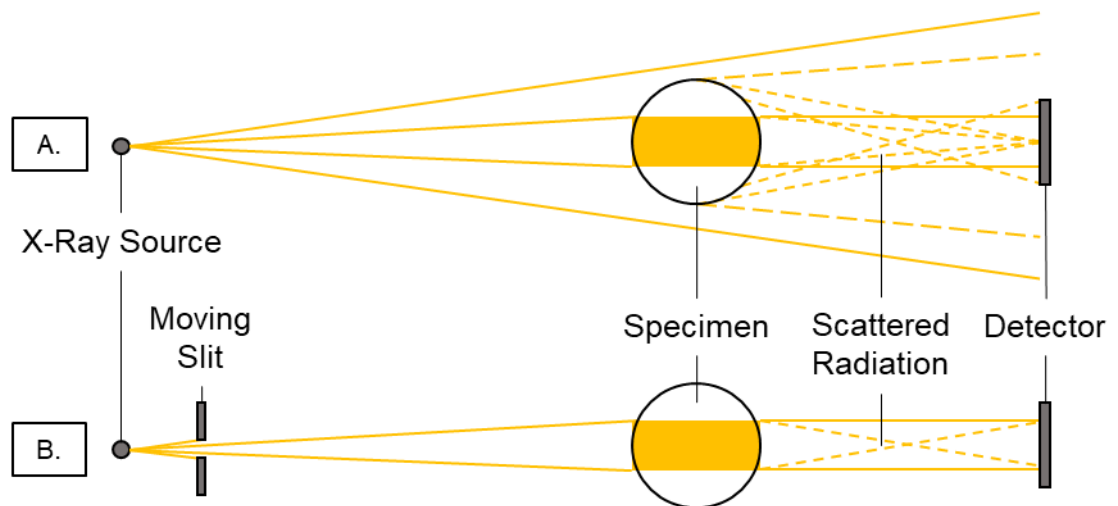
Figure 3.6: Plan view of the MuCAT2 XMT system with a moving collimator. Showing the difference between a specimen without (A.) and with moving collimator (B.), adapted from Wassif (2007).

3.1.2   Block Scanning

For higher resolution projections or larger specimens, block scanning is used. In this technique, specimens can be scanned in consecutive blocks of uniform height. The specimens were scanned to obtain 3D volumes of complete specimens at high resolution. The scan height is limited to the number of 'slices' per block, as only an ROI is covered by the area of the X-ray cone beam (Ahmed, 2011; Evershed, 2013).

A slice is defined by the resolution of the image by:

$$Number\ of\ Slices = \frac{Height}{Reconstructed\ Voxel\ Size}$$

Therefore, to build an entire stack of projections for large specimens, they require to be scanned in blocks. This is done by imaging the ROI at one full rotation, and then moving the rotational stage to bring into view the next ROI, and so on (Figure 3.7) (Ahmed, 2011; Evershed, 2013).
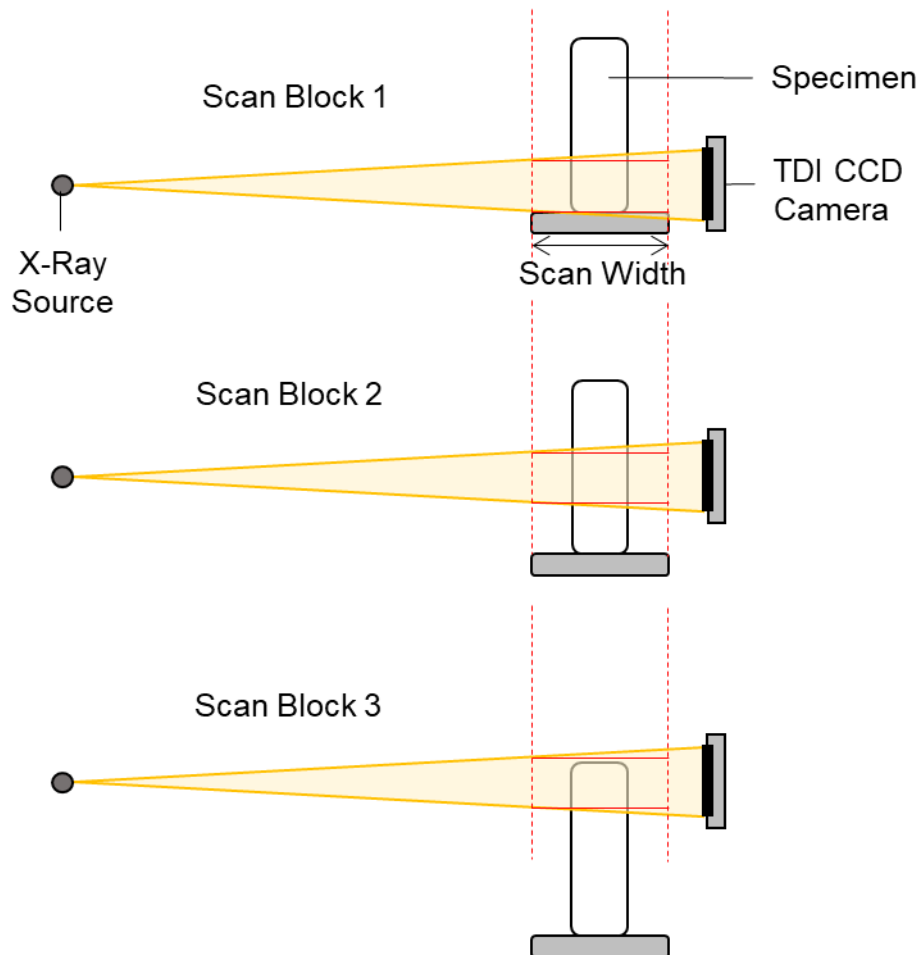
Figure 3.7: Side view showing 'block' scanning. The red lines signify the boundaries of the reconstruction region. Adapted from Ahmed (2011).

3.1.3   Calibration

As mentioned previously in Section 2.3.2, due to the nature of polychromatic radiation, correction is required for beam hardening by using an appropriate calibration material. The calibration material must be similar nature to the investigated material regarding its attenuation for any given X-ray. Aluminium is considered to be the best material in the studies of hard tissues, such as bone and teeth, as its behaviour in the absorption of X-rays is similar to that of hard tissues (Ahmed, 2011; Evershed, 2013). Its attenuation coefficient versus energy relationship is like that of HAp (Dowker *et al.*, 1997; Wong *et al.*, 2000).

Initially, the MuCAT2 system corrected for beam hardening through calibration with an aluminium step wedge (Figure 3.8.A). The wedge was elevated through the beam to produce ten projections, each with a set of attenuations corresponding to between 1 and 50 layers of aluminium. To increase the range of attenuations available, a beam hardening 'carousel' was designed and constructed, comprising of an odd number of metal sheets of known compositions (Figure 3.9) which can be illuminated individually by the cone beam (Figure 3.8.B). The samples are held vertically around the circumference of a cylindrical frame. Higher attenuations than aluminium can be achieved using titanium and copper, which, has a higher atomic number and thus a higher LAC. Once the attenuations have been collected, it is possible to correct for the specimen material, using software generalised from the modelling concept developed for the aluminium step wedge (Davis *et al.*, 2008; Evershed *et al.*, 2012).
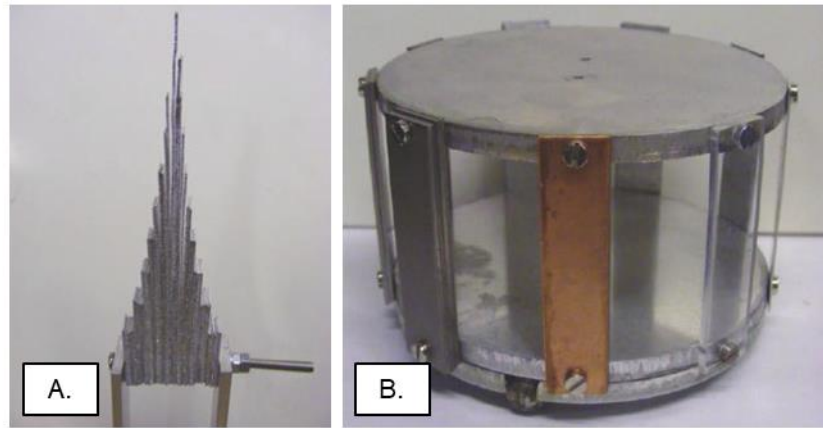
Figure 3.8: Calibration materials used in MuCAT2. A. An image of the aluminium step wedge. B. An image of the 'carousel' and its attenuation filters. Images reproduced with permission from the authors, Evershed *et al.* (2012).
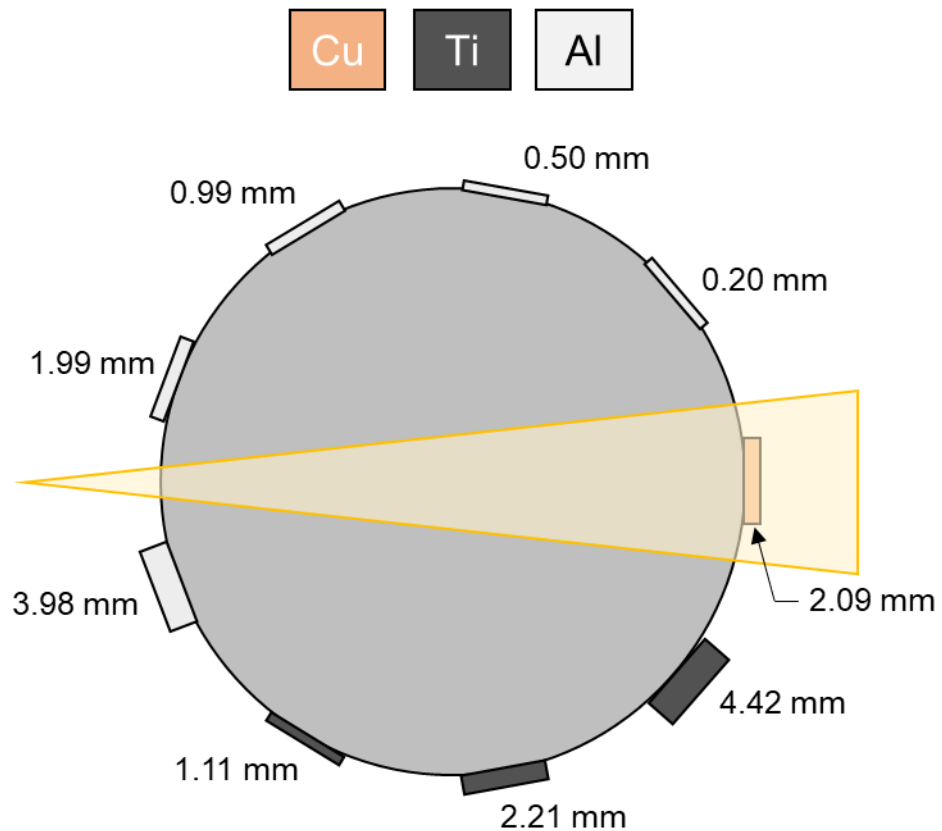
Figure 3.9: Plan view of the beam hardening 'carousel'. Showing filter types and illumination of the copper filter by the X-ray beam, adapted from Evershed *et al.* (2012).

3.2 Data Processing and Visualisation

The images obtained from MuCAT2 are created by directing X-rays through the specimen from different orientations and measuring their resulting intensity. There are some variables responsible for the collection of XMT data: the number of projections, exposure time, image resolution, the X-ray tube voltage and current. The specimen is rotated step-wise incrementally during collection, amounting to a full 360º (Davis, 1994). Each projection represents a rotational interval equal to 360º divided by the total number of views. A specialised algorithm is used to reconstruct the set of projections resulting in a 3D replica of the object (Ahmed, 2011; Evershed, 2013). To calculate the minimum number of projections needed for a sample is:

$$Number\ of\ Projections = \frac{\pi}{2}x_d$$

<div align="right">Equation 3.2</div>

Where; x_d is the width of the specimen in pixels (Kak & Slaney, 2001).

The total time for collection of each dataset is calculated using the time for each projection multiplied by the number of projections. The total time for each projection includes the flyback time and the traverse time (Ahmed, 2011; Evershed, 2013). The traverse time is expressed as:

$$Traverse\ Time = t_x\left(1 + \frac{x_d + 64}{1024}\right)$$

<div align="right">Equation 3.3</div>

Where: t_x is the exposure time (minimum of 3.3 s).

x_d is the specimen width.

64 is a constant derived by adding together 32 pixels on either side of the specimen which is used to measure the beam intensity (which may vary over time).

Therefore, by adding the constant 64 to *N*, the total distance across the field of view is encompassed, and with the constant 1024, is the width of the CCD detector in binned pixels (Figure 3.10).
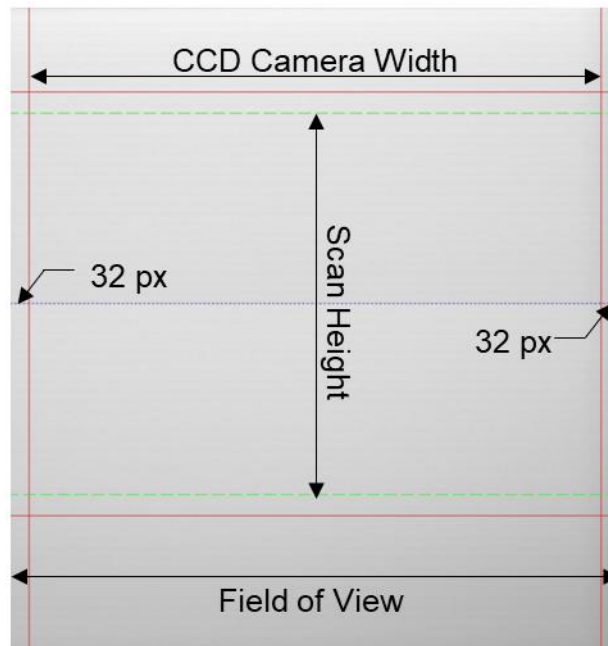
Figure 3.10: The projection window, demonstrating the field of view of the camera.

3.2.1   Pre-Processing and Linearisation

A correction applied for the polychromatic radiation, is carried out during the pre-processing stage of the data reconstruction. This stage of processing is required to ensure the data can be corrected as though monochromatic radiation was used. For hard tissue samples scanned at 90 keV, the data is adjusted so that the values are relative to 40 keV X-ray photons. Non-mineralised samples, such as polymer-based specimens these were scanned at 40 keV with the data being corrected to values relative 25 keV. During pre-processing intensity is converted to $ln\frac{I_0}{I}$ values and the polychromatic correction is

applied (Davis & Elliott, 1997; Evershed, 2013). Initially, the dark reference is deducted from the light reference and the natural log is taken.

A parabola is fitted for each CCD column and for the remaining projections the dark reference is subtracted, and the natural log of each projection is taken. It is then necessary to adjust about the mean log of the 32 pixels on either side of the projection, so a further subtraction is made from the appropriate parabola and this entire process provides corrected data (Kak & Slaney, 2001). Two files are produced here a CRA text file containing metadata (dimensional parameters) and a CON floating-point data file (Ahmed, 2011; Evershed, 2013).

3.2.2   Reconstruction

A modified Feldkamp cone-beam algorithm is used to reconstruct the corrected projections (Feldkamp *et al.*, 1984). The floating data point files are loaded into the programme, and from each projection, the centre of mass is located. The centre of rotation is calculated, remaining constant for all slices. TDI introduces a slight bias in the value of the centre of rotation; therefore, the central slice is reconstructed first. Here, the slice is reconstructed 11 times for a range of centre of rotation offsets ($\pm$ 5 pixels) with edge enhancements, producing the sharpest possible image, with the sharpness being determined from the sum of squares of the edge enhanced image. The centre of rotation is then determined by fitting a parabola to the three highest sharpness values and finding the peak of the parabola (Ahmed, 2011; Evershed, 2013).

After determining the centre of rotation, the entire volume is reconstructed to a 3D volume producing BIN files containing floating-point values corresponding to the reconstructed LAC data (stored in the form of LAC values corresponding to the X, Y, and Z coordinates of the volume). This processed data is then 'trimmed' using a program written in IDL® (Version 8.6, 2016; Harris Geospatial Solutions, Inc., USA) to reduce the

data to the minimum cuboidal volume incorporating the ROI and converted to 256 grey levels. At this point, the user selects a scale determining the ratio between the LAC and grey levels. This is done using a histogram showing the greyscale and scale factor; the peak and area under the curve of the histogram determine the ROI (Evershed, 2013).

The relationship is:

$$LAC = \frac{Greyscale}{Scale\ Factor}$$

Equation 3.4

Moreover, all the corresponding LAC values of the specimen have been previously altered and normalised to the 'calibration carousel' during the beam hardening correction. The final file produced is a TOM file which provides the data in the form of a greyscale image and can be viewed using various visualisation packages (Ahmed, 2011).

3.2.3   Visualisation and Analysis

Various types of software can be used for the analysis of reconstructed XMT data (Table 3.1); Drishti (Australia National University Vizlab, Australia), IDL®, ImageJ (National Institutes of Health, USA), and Tomview (QMUL, G.R. Davis, UK). Drishti was used mainly for manipulations of 3D images, and differentiation of various features of the dataset. IDL® and ImageJ (Version 1.52p, 2019) were used for quantitative analysis of the reconstructions such as morphometric parameters. Tomview (Version 1.11, 2003-2020) was used primarily as a reference programme to view the reconstructed data.

Table 3.1: Comparison of visualisation and analysis software used.

Software	Used For	Advantages	Disadvantages
Tomview	Visualisation of XMT datasets in *X*, *Y* and *Z* planes, exporting 3D volume.	Able to view individual slices in three planes, can be easily exported to different software.	Unable to view data in 3D.
Drishti	Visualisation of XMT datasets in 3D, exporting mesh.	Able to view data in 3D, able to segment data into different structures.	Unable to view individual slices.
ImageJ	Quantitative analysis such as size, volume and porosity.	Provides thorough quantitative analysis, allows for segmentation.	Unable to export data for modelling purposes.
IDL®	Part of the reconstruction routine, used for quantitative analysis.	Provides thorough quantitative analysis.	Manipulation of datasets must be carried out by code.

The image file after reconstruction is in the form of a 3D cuboidal volume and can be viewed using Tomview. The data is constrained by the *X*, *Y*, and *Z* planes; therefore, a Cartesian coordinate system can define any determination of particular features. The data can be viewed in three different planes: *XY*, *XZ*, and *YZ*. Using these coordinates, the location of any specific feature can be defined in 3D. The data is viewed in pixels with the size determined by the resolution used during scanning.

3.3 CAD/CAM

Figure 3.11 describes the CAD/CAM process used to convert XMT datasets (TOM) into workable 3D models suitable for either 3D printing or VR. Using Tomview, reconstructed images can be exported as a 3D volume (NC file) into Drishti (Version 2.6.3, 2016).
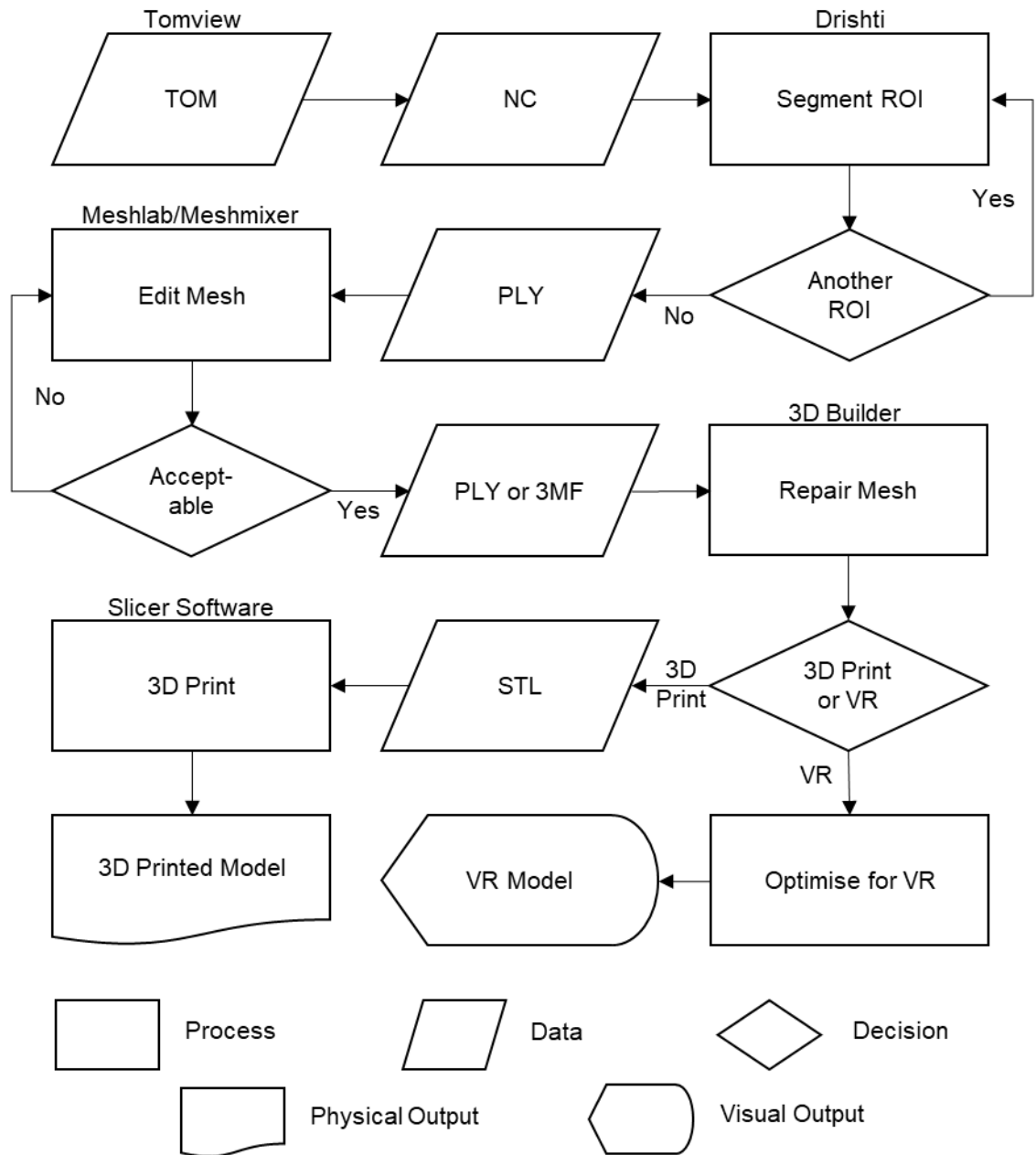
Figure 3.11: The design process used for creating files for 3D printing or VR.

Drishti is a multi-platform, open-source volume exploration and presentation tool, written for visualising tomography datasets. The segmentation (isolating or selecting) of the ROIs were carried out in Drishti by highlighting the area containing the correct LAC values (3.12 cm^{-1} for HAp [Figure 3.12]). Using a mesh generator plugin, an internal and external mesh file can be exported as a PLY file which can be used in multiple 3D modelling software, to be altered or manipulated into the desired final model.
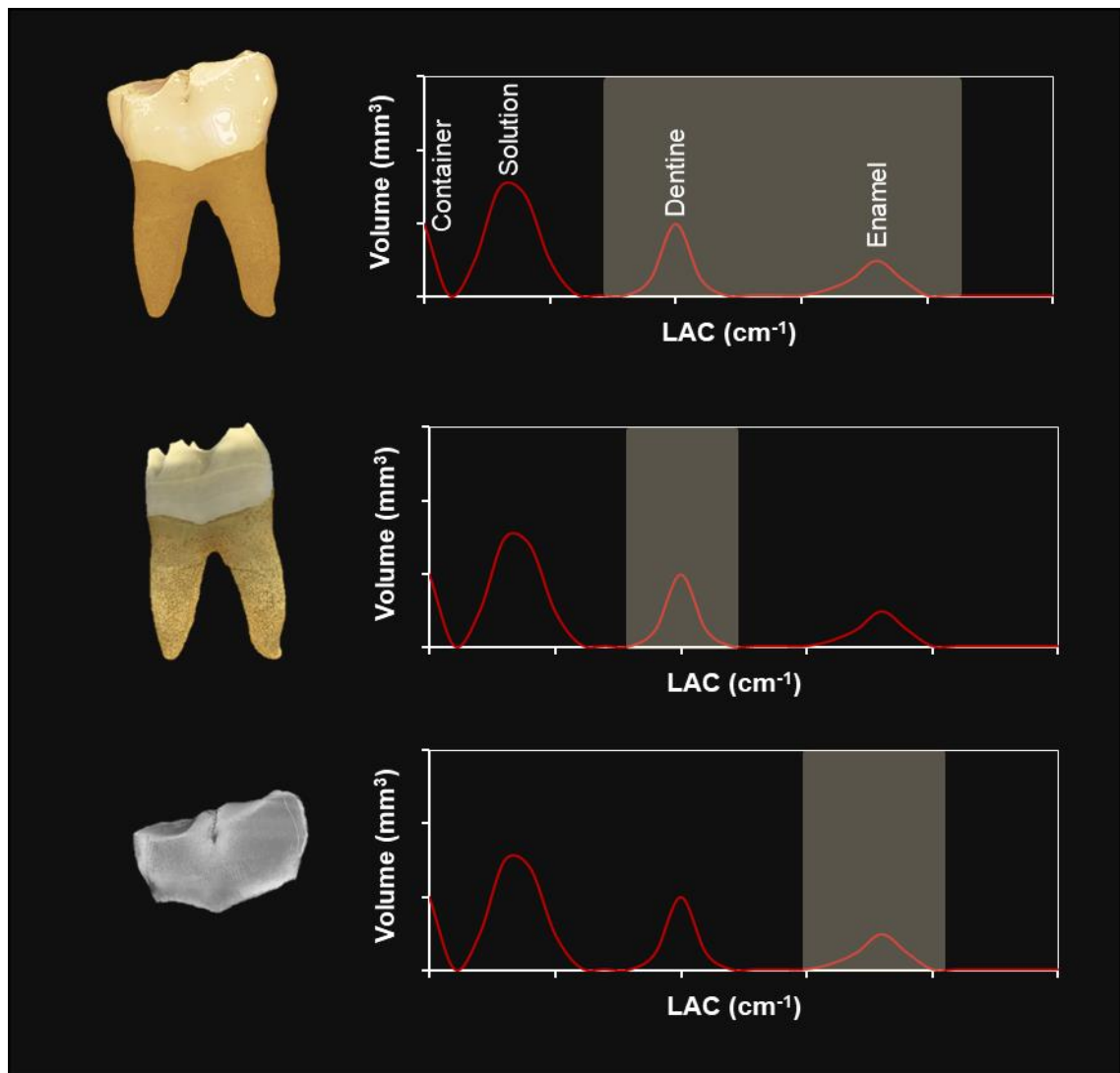
Figure 3.12: Segmentation of different ROIs of a mandibular first molar. Thresholding (segmentation), by selecting the relevant LAC values (in yellow) in Drishti allows for specific ROIs to be visualised.

Firstly, the PLY file is imported into MeshLab (Version 2016.12, 2016; ISTI-CNR, Italy) an opensource 3D mesh processing software, which was used to reduce and simplify the number of polygons present within the mesh (by running an MLX script). The script contains a series of different filters that are applied to the mesh which remove any duplicate faces, remove any duplicate vertices, remove any faces attached to non-manifold edges, and a quadric edge collapse (reduces the number of polygons by a user-defined factor). Each of these filters are applied, then reapplied (except for the quadric edge collapse) to ensure any changes made by the original application does not create more duplicate face, vertices, or non-manifold edges. The example in Figure 3.13, the

original mesh contained 6,501,509 vertices and 12,949,790 faces (Figure 3.13.A), however once the filter scripts were applied, the mesh contained 617,481 vertices and 1,234,898 faces (Figure 3.13.B). Visually only slight changes appear, but physically the PLY file size is reduced from a 3.3 GB file to a 25 MB file, once exported.
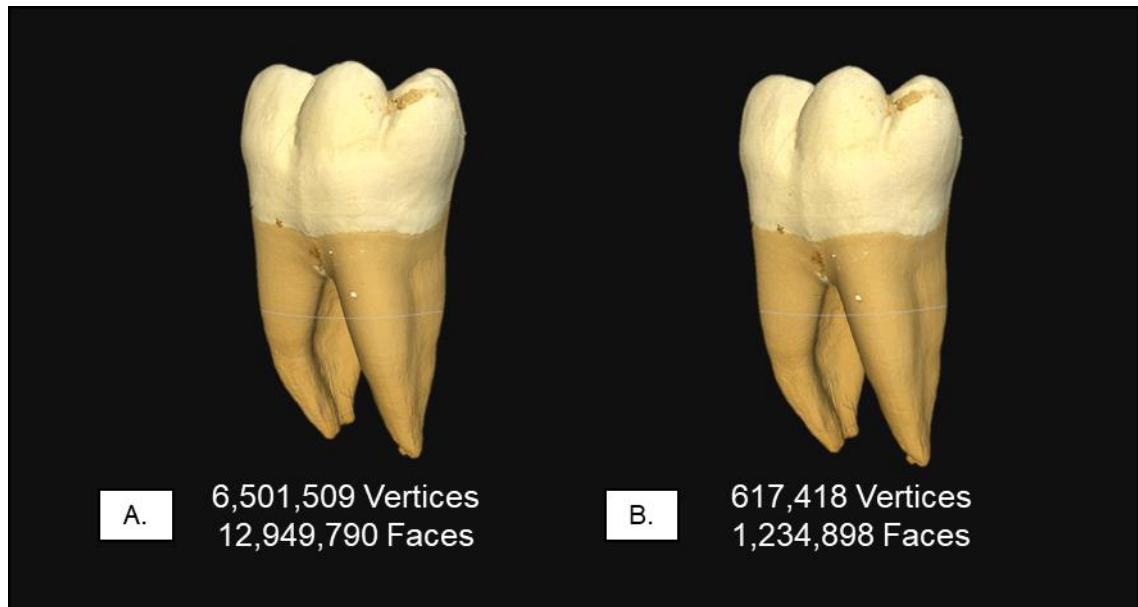
Figure 3.13: Reduction and simplification of a mandibular first molar. A. Before reduction. B. After reduction.

Autodesk Meshmixer (Version 2.2, 2016; Autodesk Inc., USA) is a modelling manipulation software, used to alter and modify the 3D mesh, removing any unwanted or excess materials or imperfections from the file (this is discussed in Section 5.4.1 in more detail).

Finally, Microsoft 3D Builder (Version 1709, 2018; Microsoft Corporation, USA) is used to repair the mesh, as, during the reduction and modification steps, errors may occur such as missing or overlapping polygons. Once repaired the file is saved as an STL file ready for 3D printing or as a PLY file for VR.

3.3.1   3D Printing

The model file was exported as an STL file format with American Standard Code for Information Interchange (ASCII) coding into different slicing programs. Cura (Version 4.3, 2019; Ultimaker, Netherlands) for FFF, Slic3r (Version 1.3.0, 2018; Sound, Italy) for the syringe-extruder, Preform (Version 3.1.1, 2019; Formlabs Inc., USA) and Anycubic Photon Slicer (Version 1.3.3, 2017; Anycubic, China). The slicing application is where parameters are set, and a 3D visualisation of each layer is provided. This information is exported into a G-code file format and fed into the 3D printer.

A total of four 3D printers were used throughout the experiments, FFF, syringe-extruder, SLA and DLP. The FFF printer used was a Wanhao Duplicator i3 (Wanhao, China), with extensive modifications in the form of a Flexion™ extruder (Diabase Engineering, USA), a Bowden extruder designed to increase the resolution of the Wanhao Duplicator i3 from 100 to 60 μm. The syringe-extruder printer was initially a FFF printer (Geeetech Prusa i3, Shenzhen Getech Technology Co. Ltd., China) with the direct drive extruder removed and replaced with a syringe driver (NE-1000, New Era Pump Systems, Inc., USA), to regulate material feed and deposition. A Formlabs Form 2 (Formlabs Inc., USA) was used for SLA printing offering a high-resolution of 25 μm, with a laser spot size of 140 μm. For the DLP printing, an Anycubic Photon (Anycubic, China) DLP printer was used to print the composite materials, offering a high-resolution of 25 μm and a UV range of 405 nm. Details of settings and materials used will be presented in the experimental chapters.

Certain prints were outsourced rather than printed 'in-house'; for these models, the company 3D Hubs (Netherlands) was used. 3D Hubs is an extensive network of manufacturing services, that specialises in 3D printing, CNC machining and injection moulding, typically, models were outsourced to 3D Hubs when SLS was required.

3.3.2   Virtual Reality

Alternatively, models were uploaded to Sketchfab (sketchfab.com, 2011; Sketchfab, France), an online database for publishing and sharing 3D, VR and augmented reality (AR) files. Sketchfab enables the viewer to move freely around or inside 3D scenes using a mouse, touch manipulation or in VR. For viewing the VR files, a Dell Visor Windows Mixed Reality headset (Dell Technologies, USA) was used.

3.4   Microscopy

3.4.1   Scanning Electron Microscopy

Samples were examined using an FEI Inspect F (Oxford Instruments, UK) SEM. Each sample was fixed to a stub with double-sided carbon adhesive tape (LabTech International Ltd., UK) and sputter-coated with gold (Emitech SC 7620, Quorum Technologies, UK), to facilitate the conduction of the electron beam. The samples were examined at 5 keV and with a working distance of 10 mm.

3.4.2   White Light Profilometry

For the analysis of the topographical surfaces, a white light profilometer (ProScan 2000, Scantron Industrial Products Ltd., UK) was used. The profilometer is a non-contact optical device that utilises either a laser or white light to measure distance. The sensor scans the surface, with the reflectance of light being recorded, determining the distance (surface roughness [Ra]) of the specimen. Measurements were collected and analysed with ProScan 2000 software (Version 2.1.1.8+, 2003; Scantron Industrial Products Ltd., UK).

3.4.3   Optical Light Microscopy

Simple optical light microscopy was carried out using an Apex Scholar microscope (Apex Microscopes, UK). All samples were mounted to a glass slide, and where appropriate a glass covering was placed on top to fix the sample. ScopeImage (Version 9.0, 2016; BP Integrated Technologies Inc., Philippines) processing software was used to correct contrast and brightness as well as capturing the image.

3.5   Mechanical Testing

This section focuses on the mechanical testing methodologies used during the project. The methods for calculating microhardness, compressive strength and $\bar{E}$ are outlined in this section.

3.5.1   Vicker's Microhardness Indentation

H_V measurements were made with a Buehler Micromet-4 (Buehler, USA) microhardness tester, with a square-based diamond indenter with a 136º angle (Figure 3.14). This tester has a microscope of high resolution and contrast magnification of ×400. Indentations were made with loads of 10, 25, 50 gf for 20 s; and never near to any edge of the sample or another indentation (at least > 150 μm). The two diagonals of the indentation left in the surface of the specimen after removal of the load are measured, and the average is calculated, along with the area of the sloping surface. The H_V is the quotient obtained by dividing the load (kgf) by the square area (mm^2) of indentation (Equation 3.5).

$$H_V = \frac{2F \sin\frac{136°}{2}}{d^2} = 1.1854 \, \frac{F}{d^2} \, (approx.)$$

<div align="right">Equation 3.5</div>

Where: F is the force used in N (1 gf = 0.001 kgf).

d is the mean value of d_1 and d_2 in mm (1 μm = 0.001 mm).

To convert H_V to MPa and GPa multiply by 9.807 and 0.009807, respectively (England, 2018).
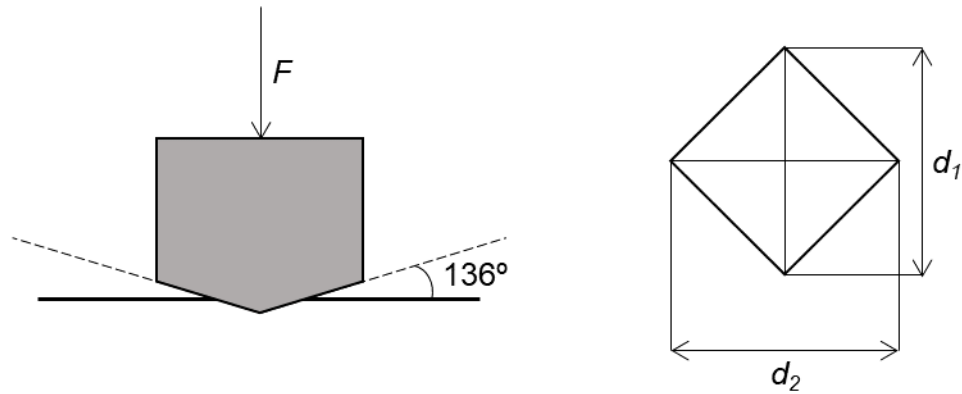
Figure 3.14: Schematic diagram of the indentation for Vicker's microhardness.

Criteria for accepting an indentation was outlined in Gutiérrez-Salazar & Reyes-Gasga (2003). The length of the axes of the square-shaped indentation was read with the micrometre scale fitted to the eyepiece of the hardness tester. The H_V values were obtained from the microhardness tester, and the mean value and standard deviations (SD) were calculated.

3.5.2 Compressive Strength and Elastic Modulus

Compressive strength and Ē were measured with an Instron 5567 (Illinois Tool Works Inc., USA) mechanical property testing machine with a 3 kN load cell. Force was

applied through a crosshead displacement at a set rate of 0.5 mm/s. Samples were measured before loading, height, width and depth for cuboidal samples, and height and diameter for cylindrical samples using a digital micrometre (± 0.01 mm; Mitutoyo Ltd., UK).

Compressive strength and Ē were calculated using the mechanical property testing machine's software; Instron Bluehill 3 (Version 3.72, 2015; Illinois Tool Works Inc., USA). Compressive strength was calculated using the formula:

$$Compressive\ Strength\ =\ \frac{F}{A}$$

Equation 3.6

Where: F is the force or load at the point of failure.

A is the surface area of the specimen in contract with the crosshead.

Ē was calculated by performing a linear regression on the stress-strain curve (Figure 3.15). The software automatically scans the curve from the first recorded stress signal (B) to the point of failure (C), applying linear regression to the curve (A). The gradient of the modulus line (A) is calculated to give the Ē.
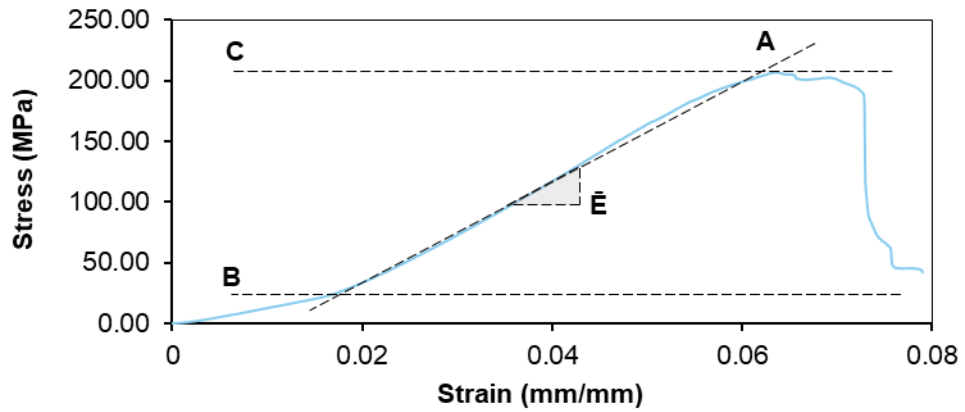
Figure 3.15: Example stress-strain curve calculating elastic modulus. A. Modulus line. B. First recorded moment of stress. C. The point of failure. Specimen of an extracted human enamel sample.

3.5.3 Automatic Stage Force Testing

Cutting forces were measured through a novel technique developed for this project. Samples were embedded in acrylic (Kemdent Simplex Rapid, Associated Dental Products Ltd., UK) blocks encompassing a 3D printed mould. Once set, the samples were mounted to a 3-axis load cell (Model 3A60A, Interface Force Measurements Ltd., UK). A high-speed dental handpiece (TE-95 BC Alegra Dental Air Rotor Handpiece, The W&H Group, Austria) was mounted to a vertical stage (LMS-180 Precision Linear Stage, Physik Instrumente GmBH, Germany), which in turn was attached to a horizontal stage (Figure 3.16). Both stages were controlled using an A-81x PIglide Motion Controller (Physik Instrumente Ltd., Germany) running PIMikroMove (Version 2.10, 2015; Physik Instrumente GmBH, Germany). The handpiece was connected and powered by a portable turbine unit (GXJ Lab, China) and kept at a constant speed of 40000 rpm. The rate in which the dental handpiece cut into the sample was held at a set rate of 0.1 mm/s and was consistently 1 mm deep (from the highest point of the surface), with the forces being measured in real-time. Load data was recorded via a 4-channel signal amplifier (ME-Meβsysteme GmbH, Germany) connected to a computer running GSVmulti (Version

1.40, 2018; ME-Meβsysteme GmbH, Germany) which records real-time load data into a dynamic graph.
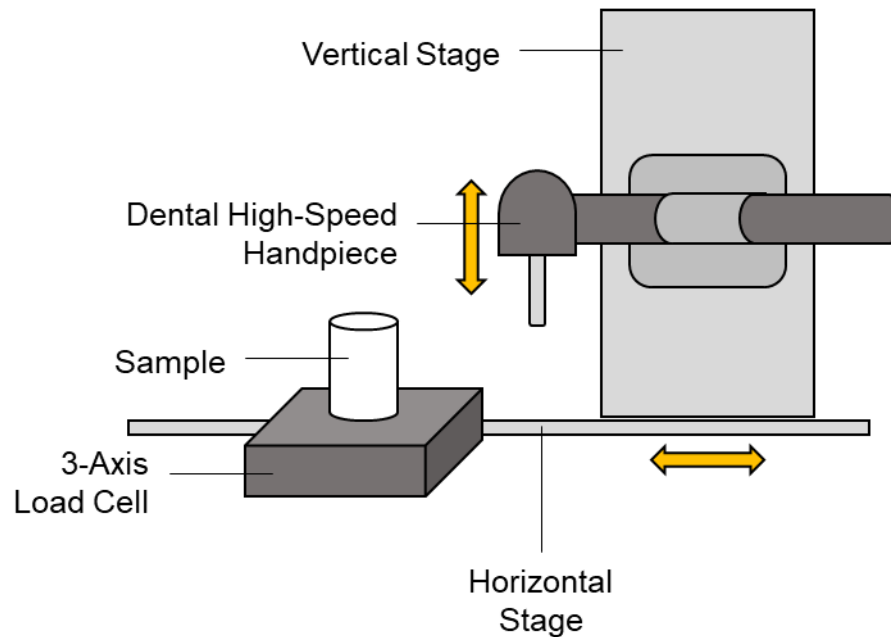
Figure 3.16: Schematic of the automatic load force cutting.

For analysis of the data, the 5–95th percentile range is taken, excluding the initial touch cut and the exit cut (Figure 3.17). This data is dependent on the geometry of the tooth as well as type, so to ensure the comparison between teeth, this data is omitted from the analysis. The remaining 5–95th percentile range is averaged to give the average force required to cut. The first cut of a sample was also omitted due to the forces being dependent on the geometry of the occlusal surface (Figure 3.18); therefore measurements were only taken after the first 1 mm deep cut.
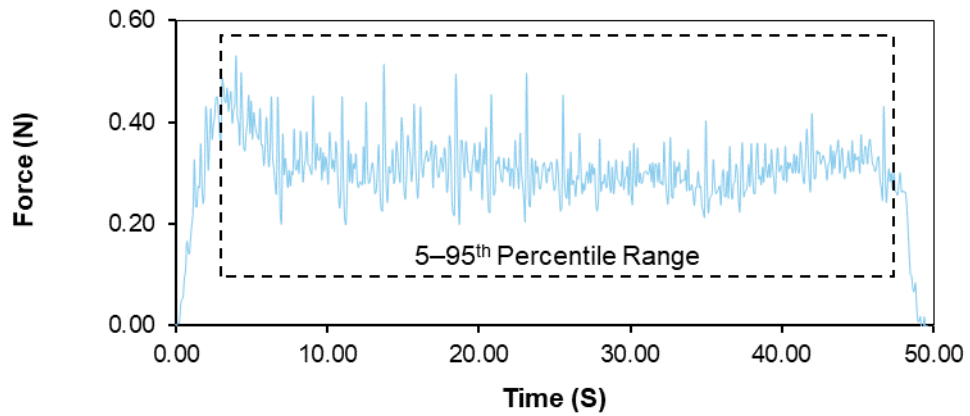
Figure 3.17: Example force data from cutting an extracted mandibular first molar. The data selected is 5-95th percentile range.
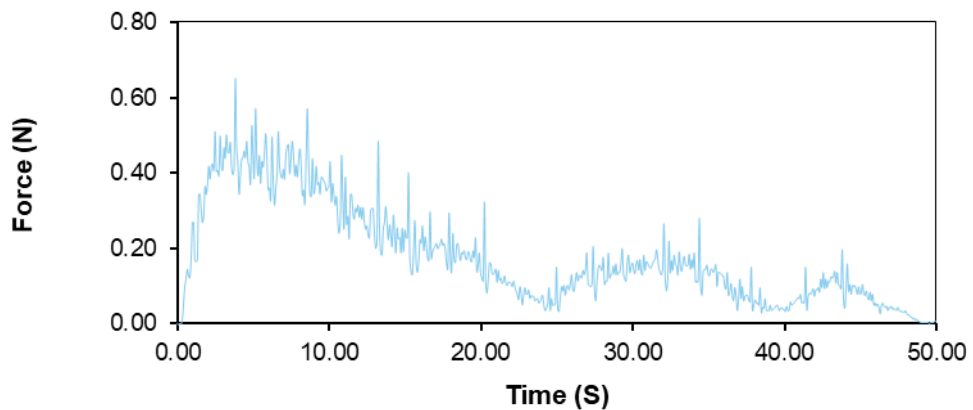
Figure 3.18: Example first cut force data of an extracted mandibular first molar.

3.6 Characterisation

Characterisation of different samples was carried out using either fourier-transform infrared spectroscopy-attenuated total reflectance (FTIR-ATR) or XRD, to try and identify them and to prove their presence in certain mixtures.

3.6.1 Powdered Sample Preparation

For characterisation techniques, powders gathered from the constituents of samples were collected by using a straight fissure diamond bur (Dentsply Sirona) and a high-speed dental handpiece with water irrigation. Cuts were made into the specimens, with the water and particles being collected. The solution was vacuum filtered using 5-

13 μm filter paper (VWR International, Germany), the paper was then left to dry in an incubator for 24 h at 37.5°C. This was found to be a sufficient time and temperature to ensure all samples were dry. Subsequently, the powder was then collected from the filter paper.

3.6.2   Fourier-Transform Infrared Spectroscopy-Attenuated Total Reflectance

FTIR is a technique used for measuring the vibrations of active groups within the molecular structure of a material (Doyle, 1992). The material's molecules can absorb the energy from the infrared beams, leading to either stretching or vibration, with the remaining energy from the incident beam is detected and plotted against the radiation wavelength. This leads to the detection and the categorisation of the vibrational and the stretched bands that absorbed the radiation energy (Siesler & Holland-Moritz, 1980). ATR is a special accessory unit which can be used with FTIR spectrometers, enabling direct measurements on the surfaces of solid-state samples by pressing the sample towards and ATR crystal. This avoids the need to prepare small concentrations of the sample, which occurs in normal transmittance mode (Jelle *et al.*, 2012).

Approximately 10-20 mg of the collected powder from the various samples were examined using a Perkin-Elmer Frontier MIR/FIR spectrometer with an ATR unit (Perkin-Elmer Inc., USA). The powder was pressed against the crystal of the ATR unit, and the absorbance spectra were collected in the range of 500-1800 cm^{-1} at a resolution of 4 cm^{-1}. FTIR-ATR spectra were analysed using Spectrum^{TM} 10 (Version 10.4.3, 2019; Perkin-Elmer Inc., USA) a software that compares FTIR-ATR spectra with an online library of known spectra. It is worth noting, that identification and interpretation of the spectra was not completely carried out using the Spectrum^{TM} 10 software, but in

conjunction with supporting literature, this is explained more in depth where FTIR-ATR was carried out.

3.6.3 X-Ray Diffraction

XRD is a non-destructive technique used to study the structure of amorphous materials and to determine the crystalline phase, and the orientation of the crystals of solid materials (Fultz & Howe, 2012). Powder collected (1-5 mg) from each sample were run in an XPertPro X-ray diffractometer (Panalytical, Netherlands) using Ni-filtered Cu-Kα radiation at 40 keV and 40 mA, with a scan range 2θ of 5-70º and a step size of 0.334º. XRD spectra produced were analysed using Match! (Version 3.8.3.151, 2019; Crystal Impact GbR, Germany) software designed for the phase identification from XRD data, comparing spectra collected with a database of known spectra from various compositions. As mentioned previously in Section 3.6.2, similarly to Spectrum^{TM} 10, Match! was used in conjunction with supporting literature when carrying out identification and interpretation of spectra.

3.7 Data Analysis

All data analysis was carried out using Microsoft Excel (Version 1909, 2019; Microsoft, USA) using a data analysis plugin. The data were subjected to one-way ANOVA test and, where relevant, a Tukey post hoc test to calculate the significance of the results, with statistical significance measured as $P < 0.05$.

Chapter 4

Differences Between Natural and Artificial Teeth

This chapter looks to compare extracted human teeth to commercially available artificial teeth that are currently used by dental students in the UK for training. The focus of the chapter will be to investigate the mechanical properties as well as the aesthetics and structures of both groups, as well as examining the different forces required to cut both extracted and artificial teeth.

4.1 Introduction

As previously mentioned in Section 2.2, the primary purpose of dental education is to educate students to be competent dentists who can improve the oral healthcare in the UK (Cowpe *et al.*, 2010; Manogue *et al.*, 2011). Students must carry out multiple procedures until mastered before they are allowed to treat their first patients; therefore, SBME is a crucial factor in undergraduate dental degrees. A mixture of extracted and artificial teeth is typically used within the curriculum in the UK; however, there are advantages and disadvantages to both methods (see Section 2.2.4.5)

Al-Sudani & Basudan (2016) established that students favoured extracted teeth over typodonts. However, the authors reported that students appreciate the advantages of using artificial over natural but feel the lack of realism in typodonts makes performing procedures on these more difficult. To date, however, there has been no literature on the tactile response of artificial teeth, to confirm students' claims that it is more challenging to practise on typodonts.

In Elias *et al.* (2003), a method was designed and implemented to measure the forces imposed on teeth when cutting with a high-speed handpiece using a tungsten carbide bur. However, the authors of the study were evaluating the force clinicians applied when using variable torque and recorded the forces in only one direction. Overall, the study found that the average force exhibited from 31 clinicians was 1.31 N, with the KaVo averaging at 1.44 N and the Midwest at 1.20 N, the authors concluded that these results were based on the operators and the magnitude of the handpieces.

Therefore, the aim of this chapter's study was to understand the subjective opinion of students that typodonts are more challenging to cut compared to extracted teeth and to study if this could be confirmed by investigating the differing mechanical properties, as well as to establish a novel method in which cutting forces imposed by a handpiece (and operator) can be measured in multiple directions.

4.2   Materials and Methods

For this study extracted human non-carious mandibular first molars were selected from a human tissue bank; with ethical approval obtained from Queen Mary Research Ethics Committee (QMREC2008/57). Commercially available first molars were chosen from a variety of artificial teeth available from six different manufacturers; Acadental (USA), Frasaco (Germany), IDEA (USA), Fabrica de Sorrisos (Brazil), One Dental (Australia) and Nissin (Japan) (Figure 4.1).

Figure 4.1: Images of the extracted and artificial teeth. A. Extracted mandibular and maxillary first molars. B. Artificial first molars; Top (Left to Right) – Acadental, Frasaco, IDEA. Bottom (Left to Right) – Fabrica, One Dental, Nissin.

4.2.1   X-Ray Microtomography

The specimens were scanned using the MuCAT2 scanner, as outlined in Section 3.1. The natural teeth were scanned at 30 μm voxel size (resolution) at 90 keV, 180 μA whereas, the plastic teeth were scanned at 40 keV, 405 μA, more information is provided in Appendix A (Table A).

4.2.2   Microhardness

Extracted and artificial teeth were sectioned vertically in the buccolingual direction (2.00 mm thickness) using a diamond wheel cutter, Accutom-5 (Struer GmbH, Germany). Sections were polished using silicon carbide papers from n^0 800 to 4000, in a progressive way, with water then with 0.05 μm polishing alumina in a low-speed metallurgic polisher Kent 4 (Kemet International Ltd., UK). The samples were then cleaned ultrasonically with distilled water for three periods each of 5 min.

The microhardness of extracted and artificial teeth was investigated using a Buehler Micromet-4 as outlined in Section 3.5.1. Location of the indentations was divided into three areas within each section: cervical, middle, and incisal third. These areas were

further divided into three further areas, creating nine lines in which the indentations would be made. No more than 10 indentations were carried out on the same line (with spacing dependent on tooth size), meaning a maximum number of indentations made on each tooth was ≈ 90 (Figure 4.2). The H_V measurements were converted to MPa or GPa (where appropriate) as seen in Equation 3.5.
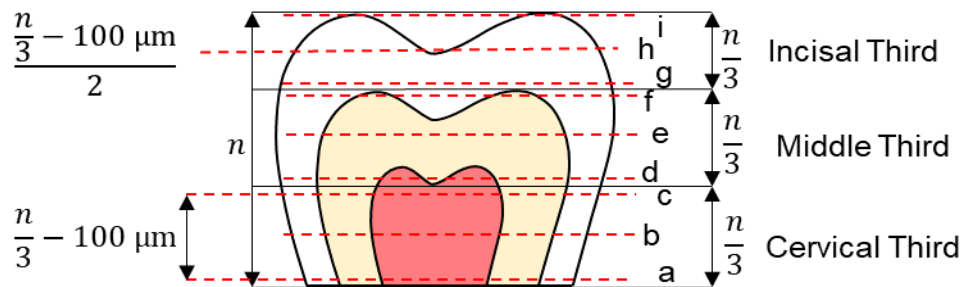
Figure 4.2: Location of the indentation made on the tooth's surface. Molars were divided into third, then divided into thirds again, determining where indentations would be made.

4.2.3   Compressive Strength and Elastic Modulus

Specimens were cut into 3.0 x 1.5 x 1.5 mm cuboidal samples from the 2 mm slices cut in Section 4.2.2 (Figure 4.3). The protocol for location and dimensions of the blocks was similar to that followed in Chun *et al.* (2014). Compressive strength and Ē measurements were taken on the Instron 5567 property testing machine, as outlined in Section 3.5.2.
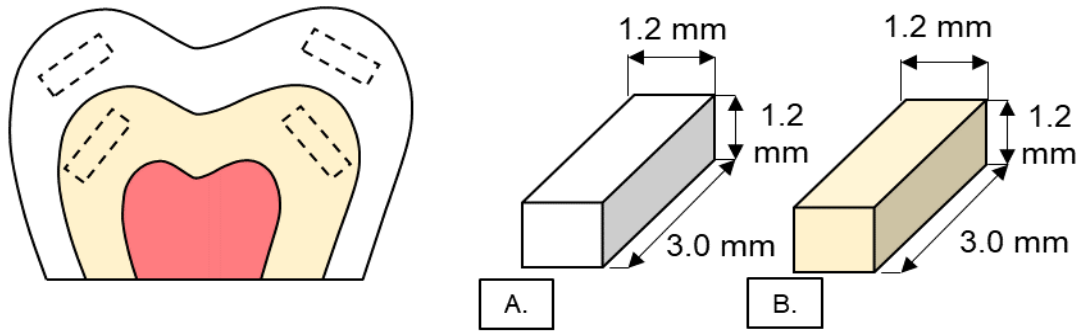
Figure 4.3: Specimen preparation and location of compressive strength samples. A. Enamel blocks. B. Dentine blocks.

4.2.4 Fracture Resistance

Specimens were prepared as per the method for microhardness testing (Section 4.2.2). The indentation process remains the same, except for a load of 500 gf was used to cause a fracture. The indentations and subsequent cracks were measured optically using a confocal video-rate laser scanning microscope (Model 1LM21 Lasertec Corp., Japan), with a Nikon 40/0.95NA dry objective. Images were analysed using ANALYSIS image analysis software (Version 1.3, 1994; SIS GMbH, Germany) to measure volume and area for each indentation, and length of the subsequent cracks produced.

$$K_{ifr} = 0.016 \left(\frac{\bar{E}}{H_V} \right)^{0.5} \left(\frac{P}{c^{1.5}} \right)$$

Equation 4.1

Where: $\bar{E}$ is the elastic modulus (GPa).

H_V is the hardness (GPa).

P is the indentation load (N).

c is the crack length (m) (Quinn, 2007).

4.2.5   Force Cutting

Force measurements were carried out as described in Section 3.5.3. In this experiment, both high-speed and low-speed handpieces were tested along with diamond burs and tungsten-carbide burs to establish any differences between the methods used, as well as the difference between extracted and artificial. The low-speed handpiece used was a Synea WA-56 A Dental Air Rotor Handpiece (The W&H Group, Austria). For the high-speed handpiece, cylindrical diamond burs (111-012M, Dentsply Sirona, USA) and tungsten carbide burs (WildCat 557, Unodent Ltd., UK) were used, for the low-speed handpiece, again, a cylindrical diamond bur (111-112M, Dentsply Sirona, USA) and a surgical tungsten carbide bur (No. 702, Dentsply Sirona, USA). Each sample was cut six times (thrice in enamel and dentine), each cut was 1.00 mm deep starting from the occlusal surface to the next cut.

A second experiment was conducted with 10 clinicians and 10 non-clinicians who were asked to prepare a Class I cavity of 2.00 mm depth (Black, 1904) on extracted and artificial (Frasaco) teeth. Non-clinicians were asked to conduct the experiment, despite having no prior clinical experience to ensure there was no bias when cutting either teeth, this is explained in more detail in Section 4.4.3. Extracted and artificial mandibular first molars were set in acrylic blocks mounted to a 3-axis load cell. A high-speed dental handpiece was used, with an option of two different diamonds burs: straight fissure (Dentsply Sirona), and inverted cone (No. 012, Dentsply Sirona, USA), to be chosen at the participants' discretion. The participants were set no time limit and were asked to try and refrain from touching the load cell itself, as this would interfere with the data recording. Plastic sheeting was utilised, as well as a 'drainage' system to ensure the load cell did not get wet, causing interference. The cavity preparation itself was recorded via an Olympus Tough TG-5 Camera (Olympus Corp., Japan) with an LED light attachment

at 1920 x 1080 px, to help match the data to which stage of cavity preparation was taking place. Both data and video were synchronised at the beginning and end of preparation.

4.2.6   Fourier Transfer Infrared Spectroscopy

FTIR-ATR was used to differentiate between the different polymers used to create the artificial teeth. A background measurement was conducted before the actual measurements to avoid any artefacts from the instrument. Approximately 10-20 mg of powder from each artificial tooth (as outlined in Section 3.6.1) was examined using a Perkin-Elmer Frontier MIR/FIR spectrometer, as described in Section 3.6.2.

4.2.7   X-Ray Diffraction

XRD was also used to differentiate between the different polymers, as well as any matrices used in the production of the artificial teeth, to identify any crystalline structures. The powder was collected as outlined in Section 3.6.1, XRD was carried out as described in Section 3.6.3.

4.2.8   Scanning Electron Microscopy

The cut surface (from the burs) and the powder collected from extracted and artificial teeth were examined using SEM, as outlined in Section 3.4.1.

4.2.9   White Light Profilometry

For the analysis of the topographical surface changes after cutting, a white light profilometer (see Section 3.4.2) After force cutting, specimens were mounted to a stage attached to the profilometer; the scanning area was outlined to form a 4 x 10 mm area (Figure 4.4) to include the volume removed from the cutting, the step size for the scan was set to 20 μm, with an average number of scans set to 4. From the scan, three

measurements were evaluated to measure the Ra of the cut using the ProScan 2000 software.
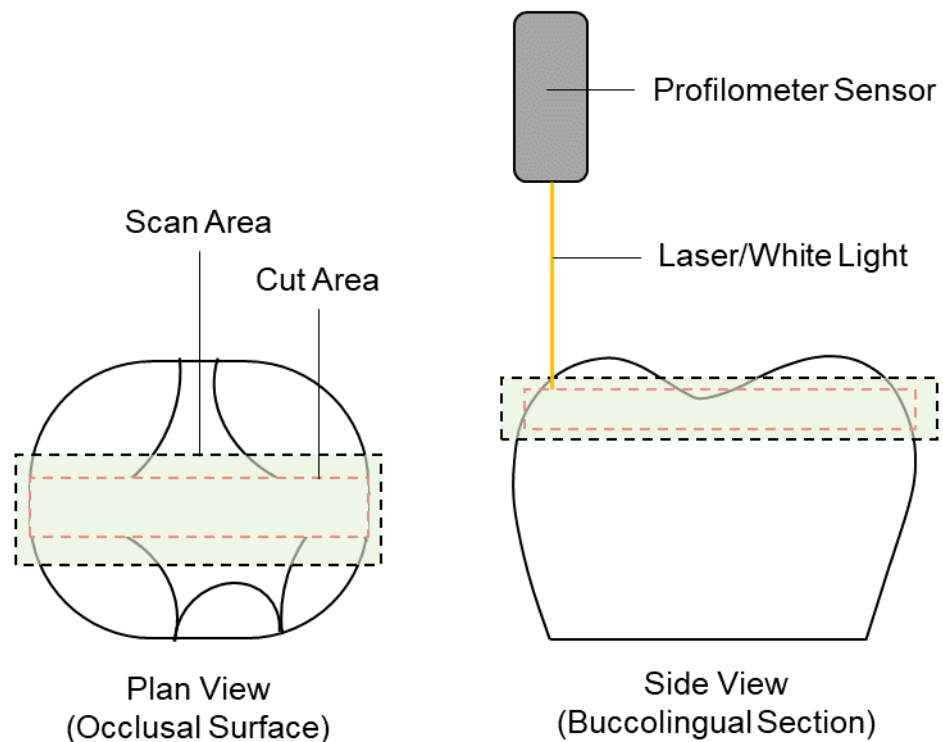
Figure 4.4: Location of the profilometer area scan on tooth samples.

4.2.10 Optical Light Microscopy

Simple optical light microscopy was carried out to image the burs before and after cutting extracted and artificial samples, to reveal any traces of material left behind on the bur. Optical light microscopy was carried out as outlined in Section 3.4.3.

4.3 Results

Reconstructed XMT datasets were visualised in Tomview which was used to view 2D slices. The datasets demonstrate the different external and internal geometries as well as different materials between extracted and artificial specimens (Figure 4.5-Figure 4.11). As outlined in Section 3.1.3, all mineralised samples (extracted teeth) were calibrated and set to the same level of brightness and degree of contrast. Non-mineralised samples

119

(artificial teeth) were calibrated differently, as lower energy was used to scan the specimens; however, all non-mineralised samples were set to the same level of brightness and degree of contrast.

Differences and comparisons between the extracted and artificial teeth can be seen in internal and external geometry (anatomy) and degrees of mineralisation (presented as changes in greyscale), this is discussed further in Section 4.4.1. All artificial teeth, except Frasaco, show different use of materials to highlight different anatomical structures (enamel and dentine). The reconstructed images also show that the artificial teeth contain highly mineralised particles within the polymers, these are later identified using FTIR-ATR and XRD.
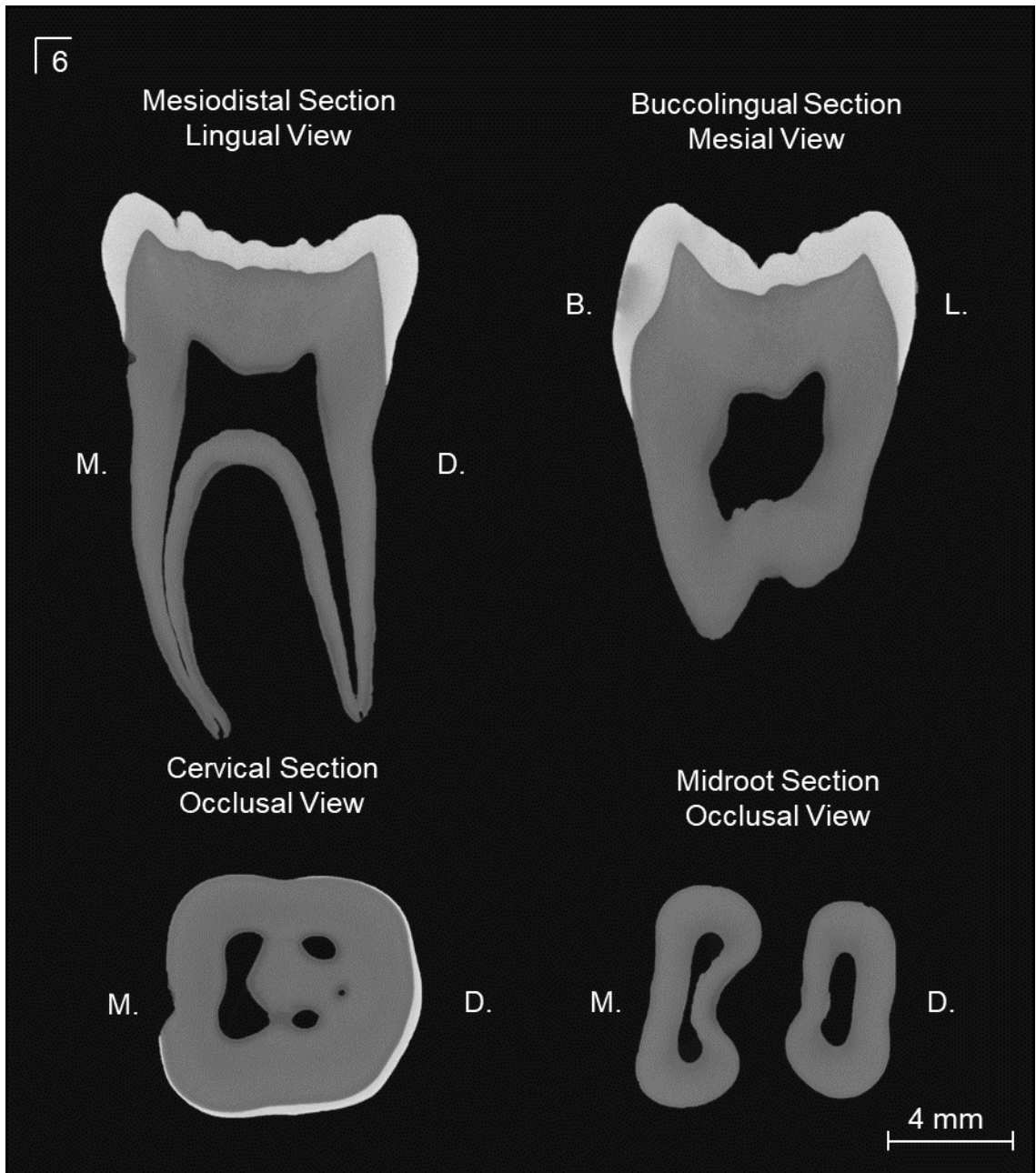
Figure 4.5: XMT image of an extracted mandibular first molar. Multiple views, showing different sections and structure of the tooth. M. Mesial side. D. Distal side. B. Buccal side. L. Lingual side.
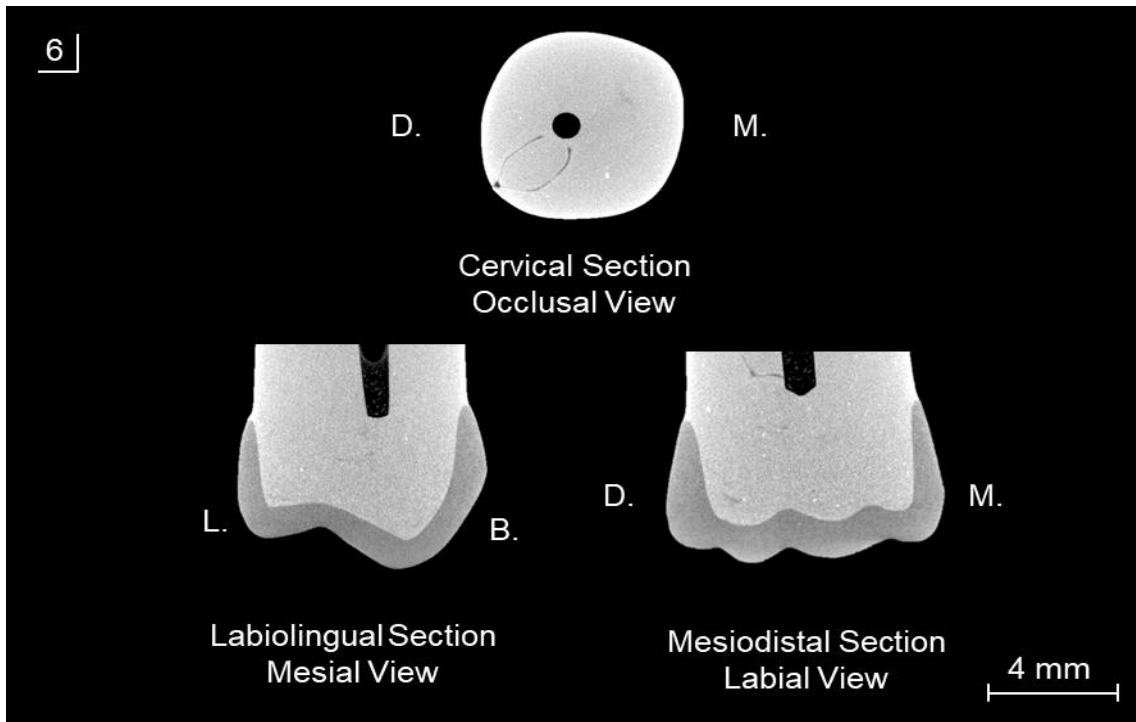
Figure 4.6: XMT image of an artificial maxillary first molar (Acadental). Multiple views, showing different sections and structure of the tooth. M. Mesial side. D. Distal side. B. Buccal side. L. Lingual side.
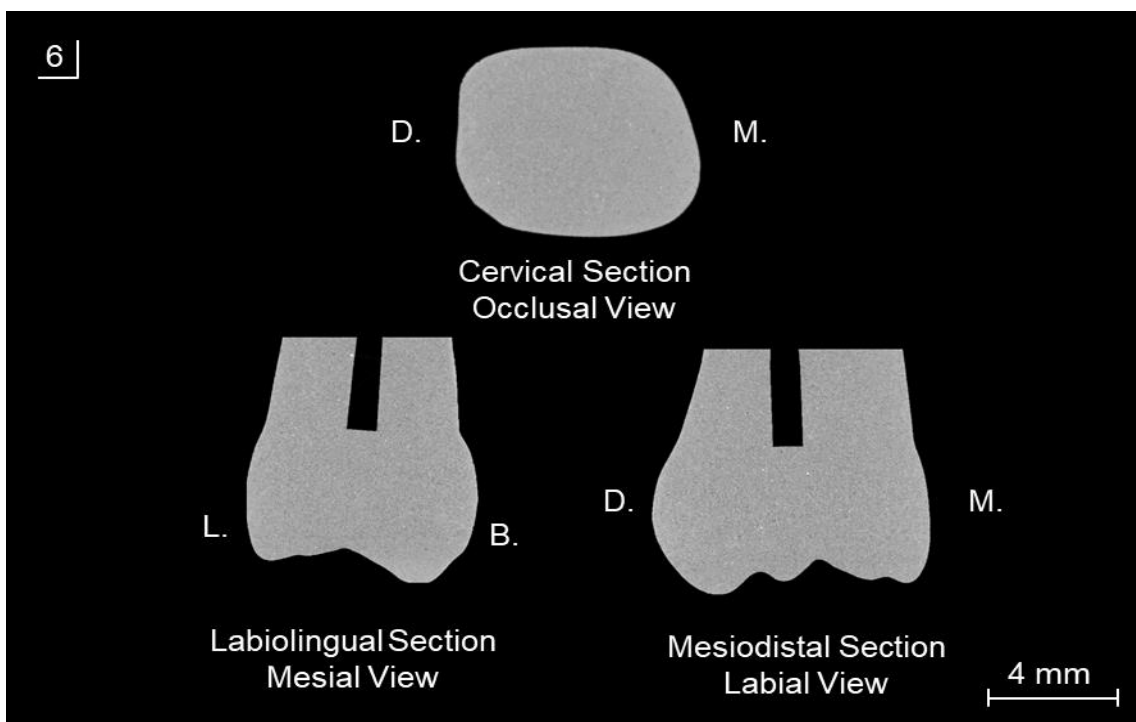
Figure 4.7: XMT image of an artificial maxillary first molar (Frasaco). Multiple views, showing different sections and structure of the tooth. M. Mesial side. D. Distal side. B. Buccal side. L. Lingual side.
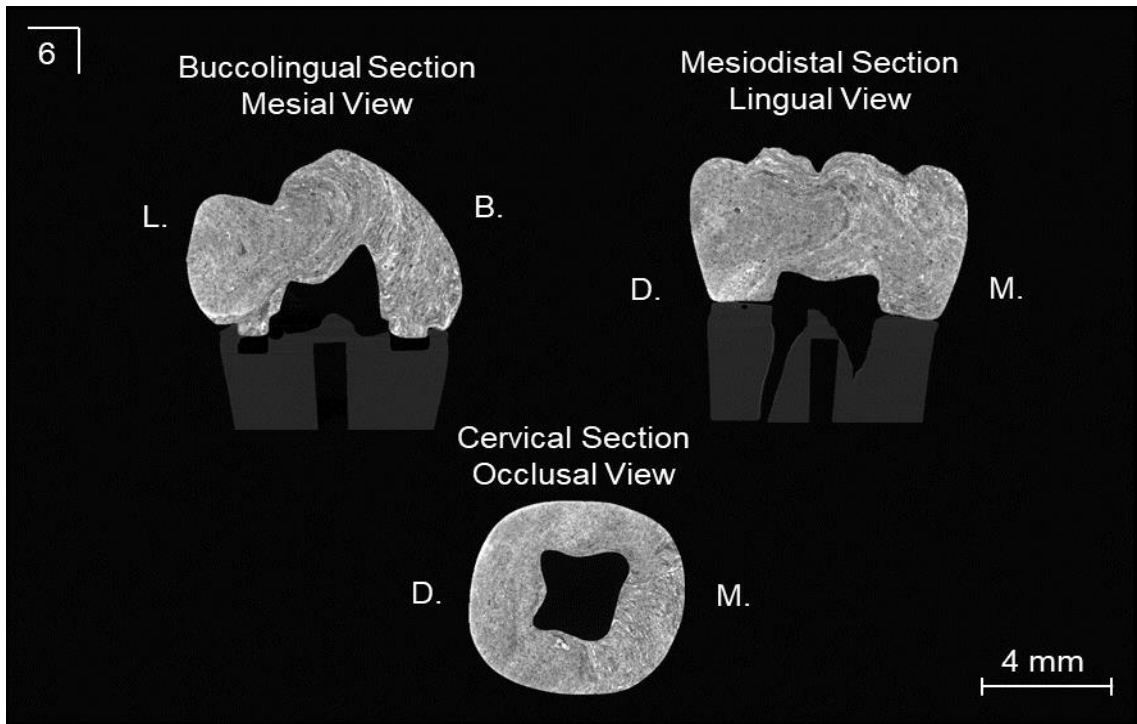
Figure 4.8: XMT image of an artificial mandibular first molar (IDEA). Multiple views, showing different sections and structure of the tooth. M. Mesial side. D. Distal side. B. Buccal side. L. Lingual side.
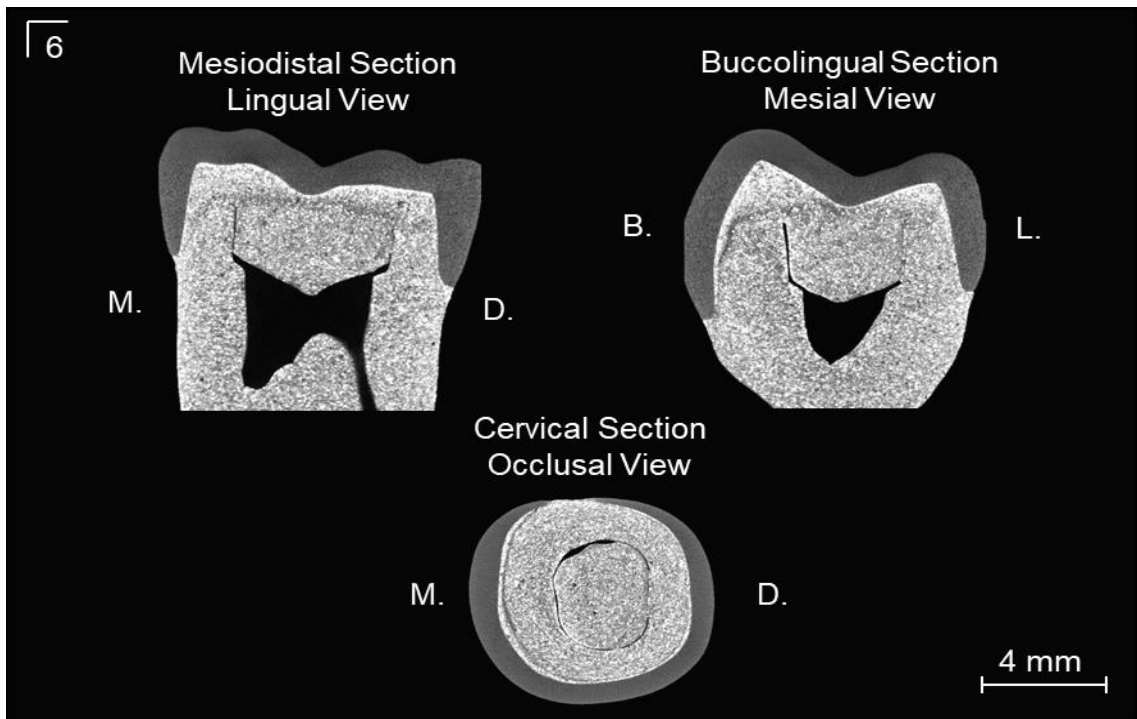
Figure 4.9: XMT image of an artificial mandibular first molar (Fabrica de Sorrisos). Multiple views, showing different sections and structure of the tooth. M. Mesial side. D. Distal side. B. Buccal side. L. Lingual side.
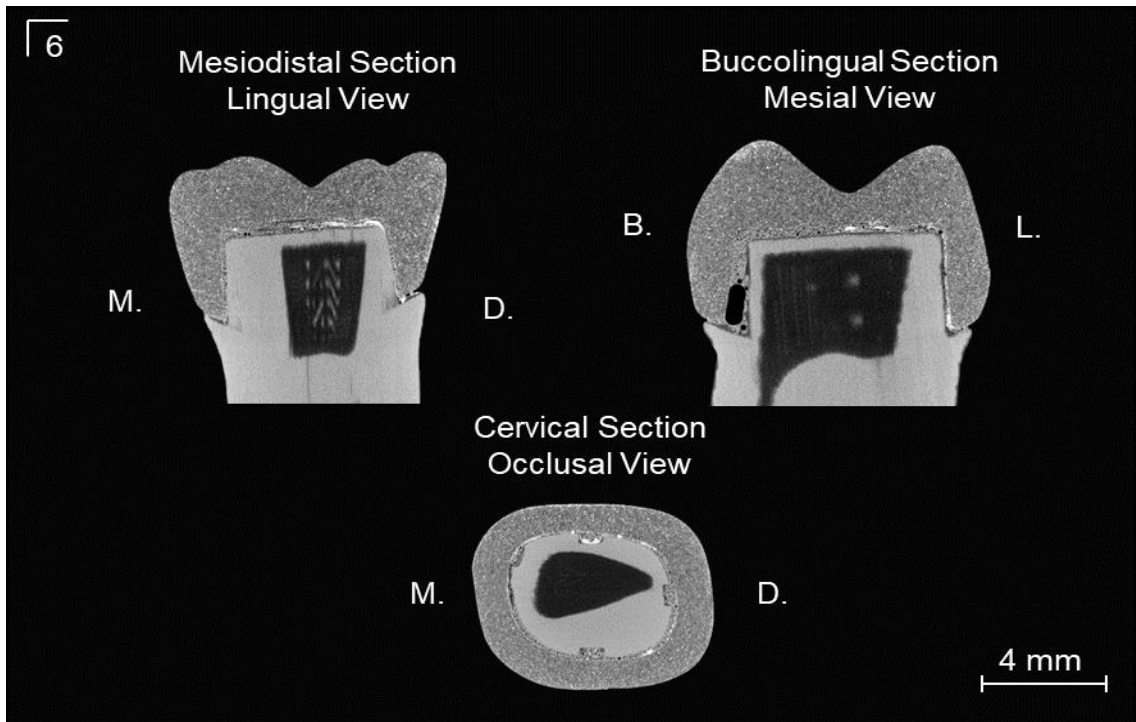
Figure 4.10: XMT image of an artificial mandibular first molar (One Dental). Multiple views, showing different sections and structure of the tooth. M. Mesial side. D. Distal side. B. Buccal side. L. Lingual side.
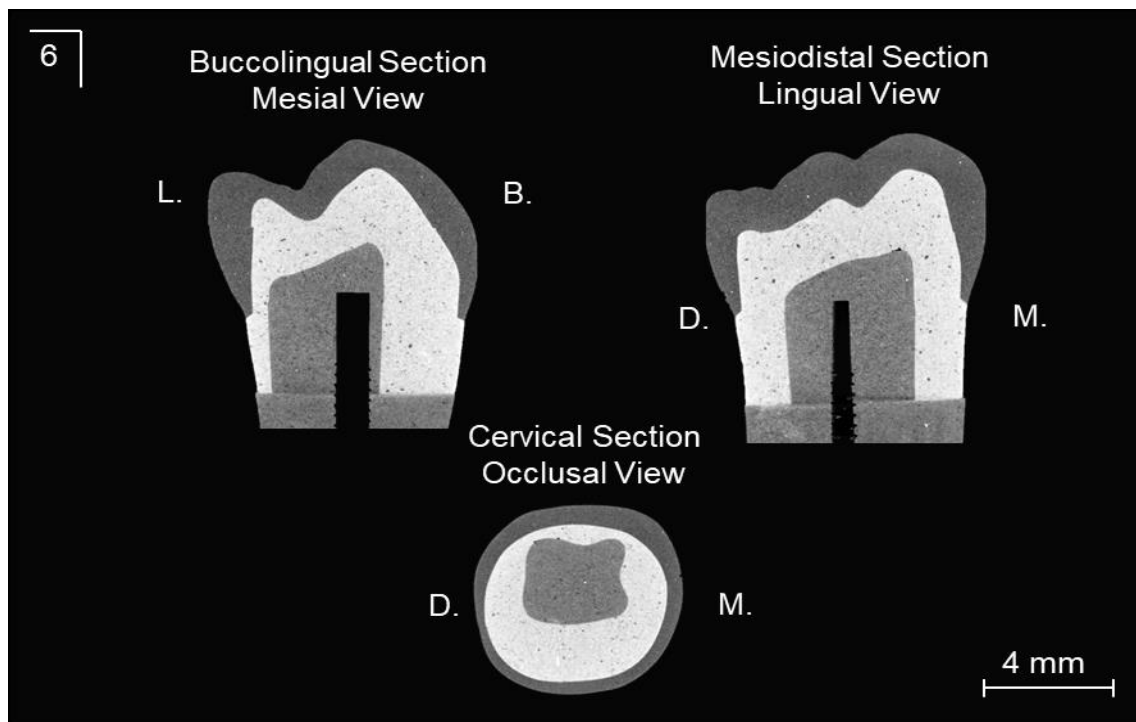
Figure 4.11: XMT image of an artificial mandibular first molar (Nissin). Multiple views, showing different sections and structure of the tooth. M. Mesial side. D. Distal side. B. Buccal side. L. Lingual side.

Figure 4.12 shows the mean hardness values and SD of all specimens. Extracted teeth samples recorded hardness values of 3078.97 MPa (± 43.52) and 938.12 MPa (± 13.90) for enamel and dentine respectively. Whereas for artificial samples the hardness values ranged from 511.07 MPa (± 5.88) to 903.65 MPa (± 5.39) for enamel and 412.87 MPa (± 6.67) to 876.62 MPa (± 3.92) for dentine. Statistical analysis showed no significant difference between all dentine samples, or between all artificial teeth ($P > 0.05$), suggesting their relative hardness is similar. There was a significant difference between extracted enamel and all artificial enamel samples ($P < 0.05$), highlighting the difference between extracted mineralised enamel compared to artificial less mineralised enamel.
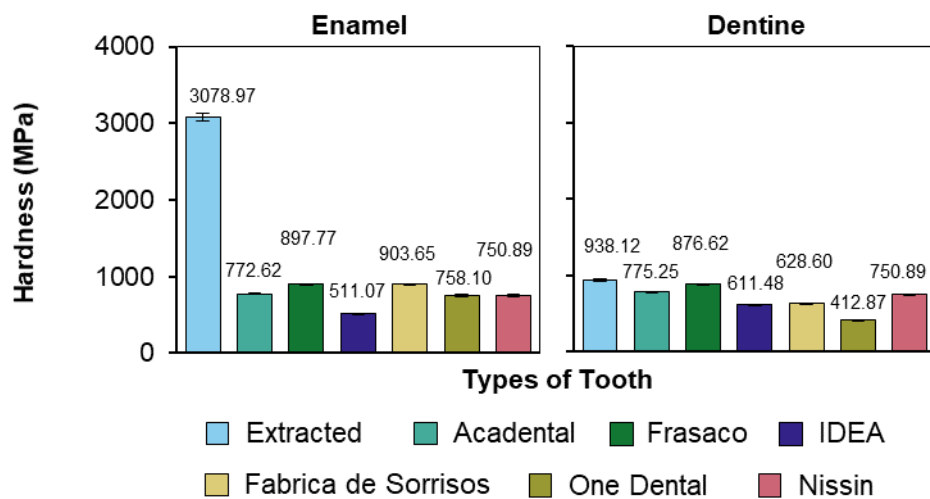
Figure 4.12: Mean hardness values for extracted and artificial teeth. Error bars presented as SD of the sample, $n = 8$.

The maximum force (N) and maximum displacement (mm) of each specimen were obtained from the mechanical property testing machine. Maximum stress (MPa), maximum strain (mm/mm) and modulus of elasticity (Ē, GPa) were calculated as seen in Section 3.5.2. Figure 4.13 shows a typical stress-strain curve of enamel samples from each different specimen, with Figure 4.14 showing the mean compressive strength for each specimen.

From the stress-strain curve (Figure 4.13), it can be concluded that the Acadental, Frasaco, IDEA, Fabrica and Nissin enamel are more ductile materials compared the extracted and One Dental enamel. This is evident by the point of fracture early on in the strain, suggesting extracted enamel (0.056 mm/mm) and One Dental (0.08 mm/mm) are more brittle materials.
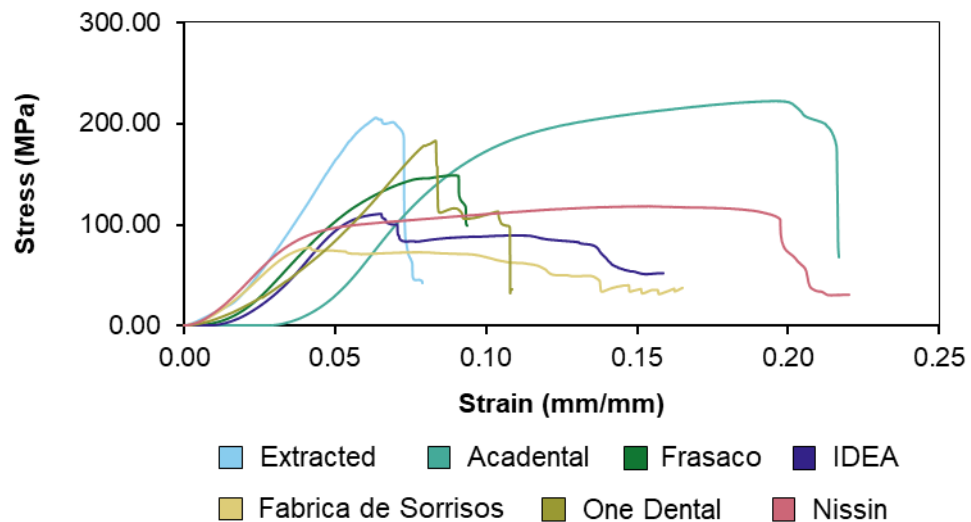
Figure 4.13: Stress-strain curve of enamel samples of extracted and artificial teeth.

Figure 4.14 is the mean compressive strength for extracted and artificial samples, which were calculated using the Instron 5567 property testing machine. The compressive strength for enamel samples ranged from 2014.33 MPa (± 96.0) for extracted and 561.90 MPa (± 110.0) to 2007.76 MPa (± 59.0) for artificial, with Fabrica de Sorrisos having the lowest compressive strength and Acadental having the highest. The dentine samples' values were 1987.25 MPa (± 52.0) for extracted and 2104.75 MPa (± 94.0) to 3501.79 MPa (± 76.0), with Acadental having the lowest compressive strength and One Dental having the highest. Overall, statistical analysis for the extracted samples showed a significant difference between extracted enamel and artificial enamel from Frasaco, IDEA, Fabrica de Sorrisos, and Nissin, suggesting the materials from Acadental and One Dental had similar values to extracted teeth. For the dentine samples, there was a

significant difference between extracted and the artificial samples from IDEA, Fabrica de Sorrisos, One Dental, and Nissin, again suggesting the materials from Acadental and Frasaco had similar values.
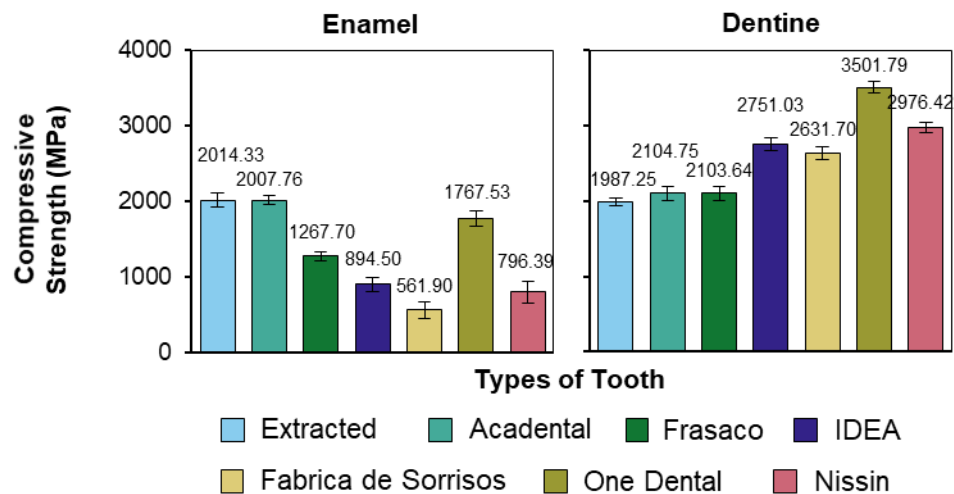
Figure 4.14: Mean compressive strength values for extracted and artificial teeth. Error bars presented as SD of the sample, $n = 8$.

Figure 4.15 shows the mean values and SD of the Ē value for each material. Extracted teeth samples recorded an Ē of 8293.56 ($\pm$ 112.57) MPa and 2166.51 ($\pm$ 54.55) MPa for enamel and dentine respectively. Whereas for artificial samples the Ē ranged from 1793.09 ($\pm$ 22.47) to 3897.80 ($\pm$ 31.98) MPa for enamel and 2527.98 ($\pm$ 42.47) to 3312.04 ($\pm$ 41.93) MPa for dentine. Statistical analysis showed no significant difference between all dentine samples, or between all artificial teeth. There was a significant difference between extracted enamel and all artificial enamel samples, as seen before in the mean hardness values (Figure 4.12).
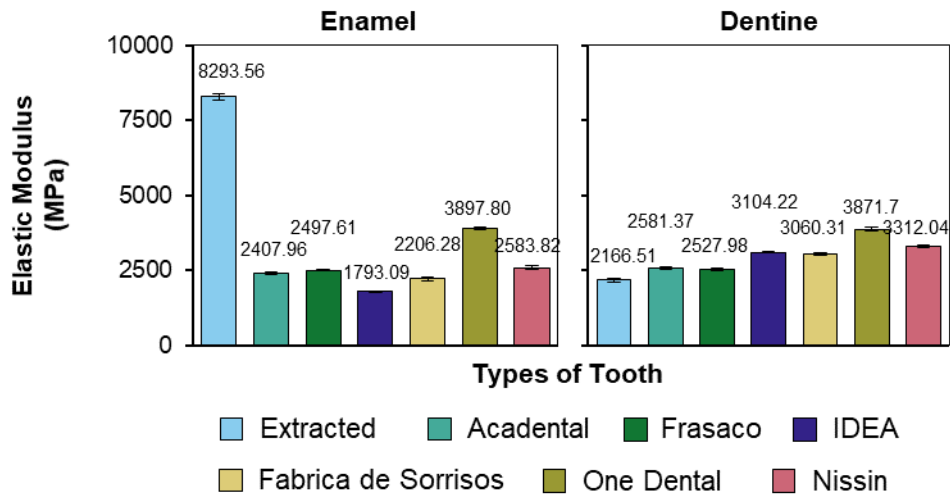
Figure 4.15: Mean Ē values for extracted and artificial teeth. Error bars presented as SD of the sample, $n = 8$.

Figure 4.16 shows an example of an indentation made on extracted dentine with evident cracking along the sharp corners, with a 3D volume analysis with measurements of the indentation, all obtained from the confocal laser scanning microscope. Figure 4.17 shows the mean K_{ifr} values and SD for all materials and specimens. Extracted teeth samples recorded a K_{ifr} of 1.16 MPa m$^{0.5}$ ($\pm$ 0.36) and 1.91 MPa m$^{0.5}$ ($\pm$ 0.18) for enamel and dentine, respectively. Whereas, for artificial samples, the K_{ifr} ranged from 2.72 MPa m$^{0.5}$ ($\pm$ 0.07) to 3.46 MPa m$^{0.5}$ ($\pm$ 0.10) for enamel and 3.54 MPa m$^{0.5}$ ($\pm$ 0.06) to 4.20 MPa m$^{0.5}$ ($\pm$ 0.13) for dentine. Statistical analysis showed a significant difference between extracted enamel and all other specimens, as well as extracted dentine compared with all artificial specimens. Between the artificial enamel and artificial dentine, there was a significant difference, as well as between all artificial enamel itself, demonstrating extracted enamel and dentine have a lower K_{ifr} compared to the artificial samples. There was no statistical difference between all artificial dentine, suggesting the materials are of similar values.
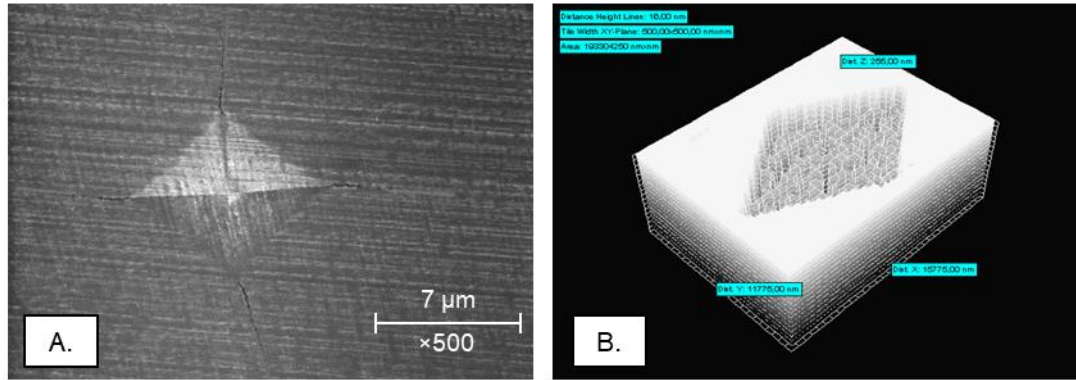
Figure 4.16: Indentation cracks on an extracted enamel surface. A. Microscope image of the cracks appearing on the sharp corners of the indentation. B. ANALYSIS image of the indentation, including dimensions of the indentation.
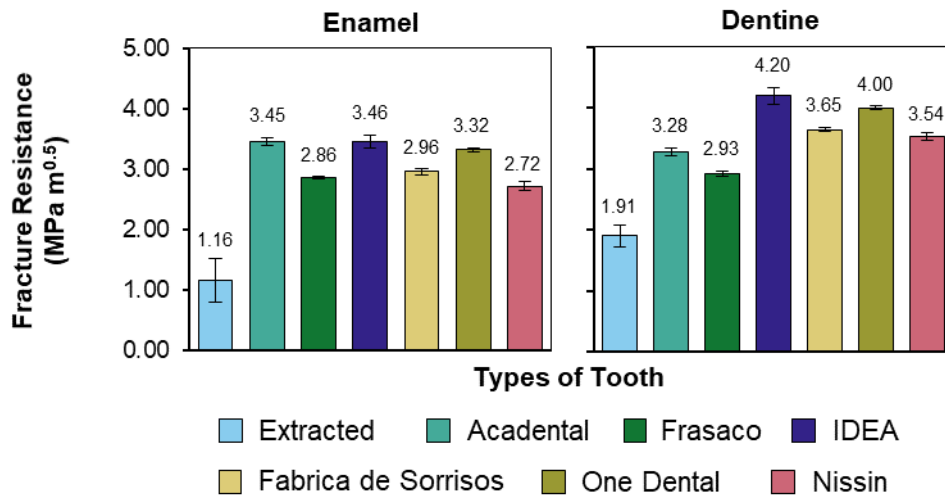
Figure 4.17: Mean K_{ifr} values for extracted and artificial samples. Error bars presented as SD of the sample, $n = 8$.

Figure 4.18 shows the forces required to cut extracted and artificial enamel and dentine using different techniques such as type of bur and speed. Figure 4.18.A shows the mean force required to cut extracted and artificial teeth using a high-speed handpiece and a diamond bur. Extracted enamel and dentine required forces of 0.31 N ($\pm$ 0.12) and 0.49 N ($\pm$ 0.15) respectively, whereas artificial enamel and dentine required 0.64 N ($\pm$ 0.08) to 1.13 N ($\pm$ 0.12) for enamel, and 0.64 N ($\pm$ 0.20) to 1.85 N ($\pm$ 0.07) for dentine. Of the artificial teeth, Frasaco and One Dental required the minimum and maximum force to cut, respectively. Statistical analysis showed there was a significant difference between

extracted samples to commercially available products. This could be said for both enamel and dentine, within the artificial teeth One Dental enamel and dentine were significantly different compared to the other commercial products.

Figure 4.18.B is the mean force required to cut extracted and artificial samples using a high-speed handpiece with a tungsten carbide bur. Results from this experiment match the same trend seen in the high-speed diamond bur experiment (Figure 4.18.A), with One Dental requiring the most force to cut compared to extracted and the artificial teeth from Frasaco. Enamel samples ranged from 0.29 N ($\pm$ 0.11) for extracted and 0.67 N ($\pm$ 0.11) to 1.20 N ($\pm$ 0.10) for the artificial products, the dentine samples required forces of 0.50 N ($\pm$ 0.14) for extracted and for artificial; 0.68 N ($\pm$ 0.10) to 1.69 N ($\pm$ 0.10). Statistical analysis showed significant differences between extracted samples to commercially available products; this could be said for both enamel and dentine; within the artificial teeth, One Dental enamel and dentine were significantly different compared to the other commercial products. Between the use of diamond and tungsten carbide bur, there was no significant difference at high-speed.

Figure 4.18.C shows the mean force required to cut samples using a low-speed diamond bur, the result of this experiment is a similar trend to what was seen in Figure 4.18.A, with results seen here four times larger. Extracted enamel and dentine required forces of 1.56 N ($\pm$ 0.05) and 1.84 N ($\pm$ 0.03) respectively, whereas artificial enamel and dentine required 3.18 N ($\pm$ 0.15) to 4.01 N ($\pm$ 0.12) for enamel and 3.17 N ($\pm$ 0.13) to 4.27 N ($\pm$ 0.05) for dentine. Of the artificial enamel, Fabrica de Sorrisos and One Dental required the minimum and maximum force to cut, respectively, for the artificial dentine, Frasaco and One Dental required the minimum and maximum force to cut, respectively. Statistical analysis showed there was a significant difference between extracted samples to commercially available products, and this could be said for both enamel and dentine,

within the artificial teeth One Dental enamel and dentine were significantly different compared to the other commercial products.

Figure 4.18.D is the mean force required to cut extracted and artificial samples using a low-speed tungsten carbide bur, again results followed similar trends to previous force experiments, with One Dental overall, requiring the most force to cut. Enamel samples ranged from 1.76 N ($\pm$ 0.07) for extracted and 3.19 N ($\pm$ 0.11) to 4.03 N ($\pm$ 0.02) for the artificial products, the dentine samples required forces of 1.97 N ($\pm$ 0.15) for extracted and 3.19 N ($\pm$ 0.15) to 4.33 N ($\pm$ 0.10) for artificial samples. Statistical analysis showed the same significant difference as seen in previous force experiments; however, no significant difference was observed between low-speed diamond bur and low-speed tungsten carbide bur. A significant difference was highlighted between high-speed and low-speed handpieces, and this was true for all samples and types of bur.
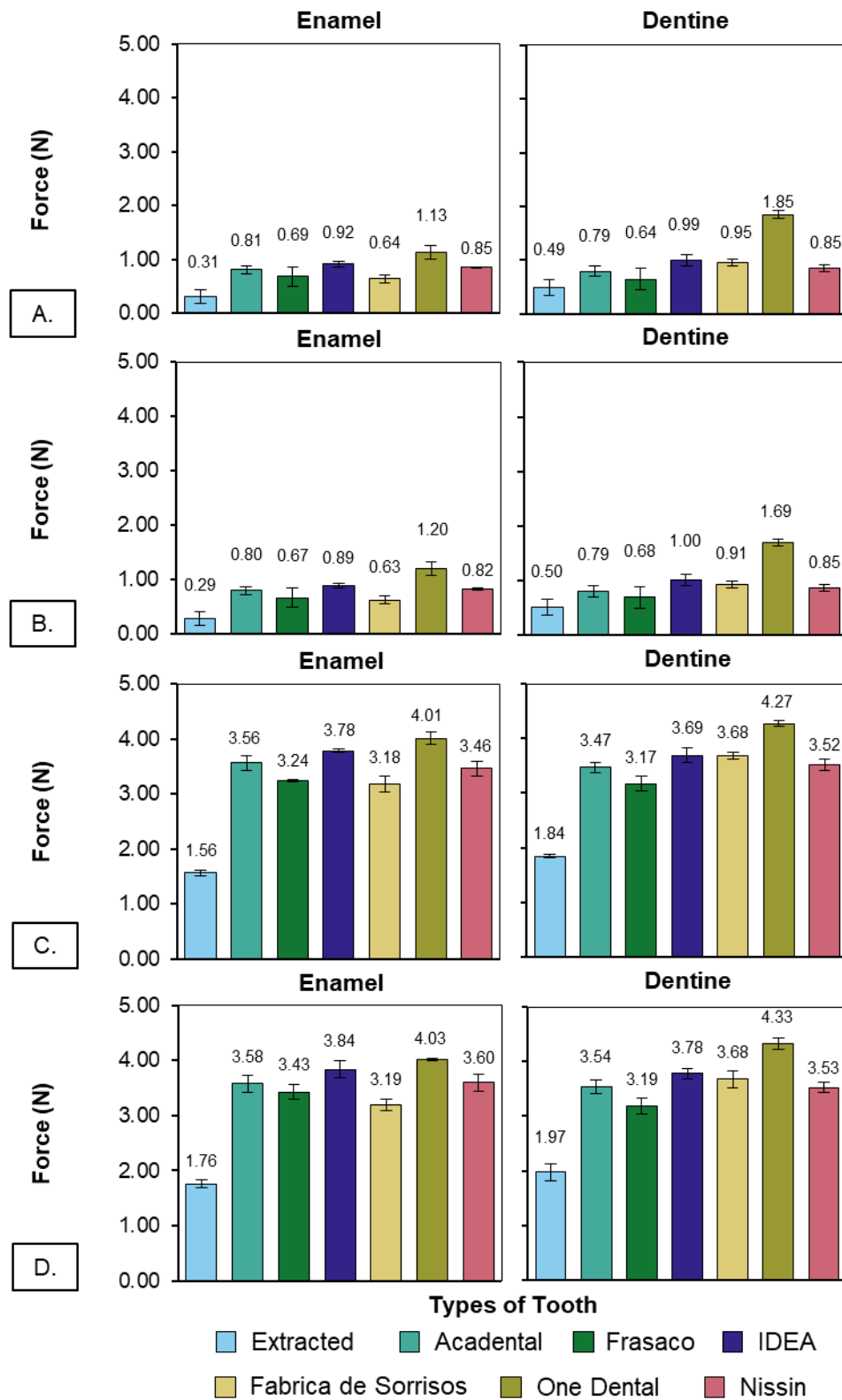
Figure 4.18: Mean force to cut samples at different speeds and burs. A. High-speed diamond bur. B. High-speed tungsten carbide bur. C. Low-speed diamond bur. D. Low-speed tungsten carbide bur. Error bars presented as SD of the sample, $n = 8$.

Results from the clinician and non-clinician cutting force experiment (Figure 4.19) showed a similar trend seen in the automatic stage set-up, in that more force was required to cut artificial teeth compared to extracted teeth, in all directions. In the buccolingual direction, for extracted teeth a range of 1.04 N ($\pm$ 0.19) to 1.35 ($\pm$ 0.28) for clinicians and non-clinicians respectively, and the artificial teeth, a range of 1.35 N ($\pm$ 0.18) to 2.28 N ($\pm$ 1.04) for non-clinician and clinician respectively. Analysis of the data showed no significant difference between the clinician and non-clinicians when cutting extracted teeth in all directions; however, there was a significant difference between cutting artificial teeth from the clinicians and non-clinicians. There was also a significant difference between extracted and artificial teeth for both clinicians and non-clinicians.
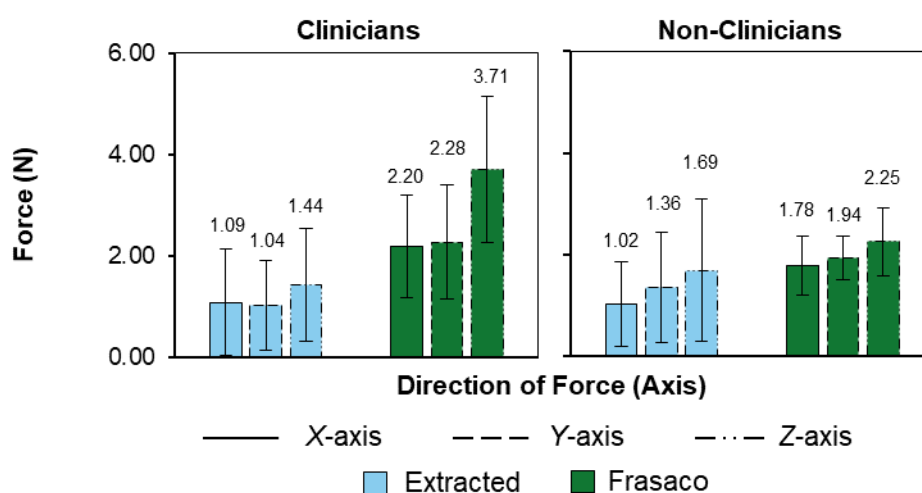
Figure 4.19: Mean force used by clinicians and non-clinicians to cut samples. Extracted mandibular molars and artificial mandibular molars from Frasaco were used as comparisons. Directions of cut were defined as; mesiodistal (X), buccolingual (Y), and occlusal (Z). Error bars presented as SD of the sample, $n = 8$.

FTIR-ATR spectra (Figure 4.20) for the commercially available artificial teeth, showed that there were two main polymers used in the manufacturing of the teeth, poly(methyl methacrylate) (PMMA) and poly(glycidyl methacrylate) (PGMA). These polymers were initially identified using Spectrum[TM] 10 (see Section 3.6.2) and later confirmed using reference literature from Elliott (1969) and Siesler & Holland-Moritz

(1980). From the spectra, it can be seen that Acadental, Frasaco, and One Dental use PMMA as the base material within the teeth, however, it was not possible to identify the crosslinking agents used confidently. PMMA can be identified as the base material from the sharp peak at 804 cm^{-1}, the broad peak at 965 cm^{-1}, and the two peaks at 1307 and 1431 cm^{-1} (Elliott, 1969; Siesler & Holland-Moritz, 1980) and it can be seen from the two spectra that both enamel and dentine for these three companies is made from the same material. PGMA was identified as the base material for IDEA, Fabrica de Sorrisos, and Nissin from the broad peak at 1014 cm^{-1}, and a sharp peak at 1706 cm^{-1} (Elliott, 1969; Siesler & Holland-Moritz, 1980) again from the two spectra it can be seen that the same material was used for both enamel and dentine, however, for the dentine, more peaks were detected, possibly due to the crosslinking agent used in the manufacturing process. The main purpose of using FTIR-ATR was to identify the 'pure' or base material used in the manufacturing of these artificial teeth.
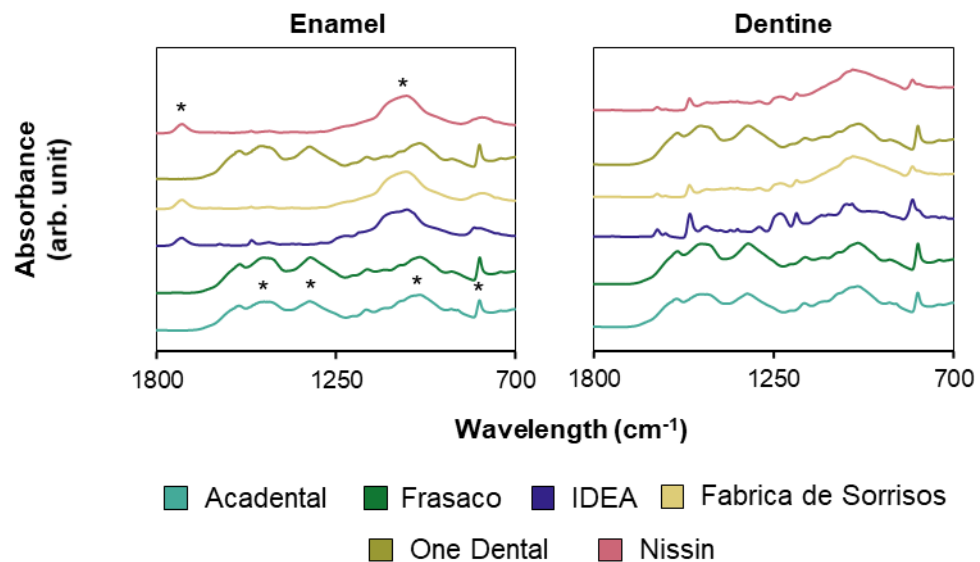
Figure 4.20: FTIR-ATR spectra for commercial artificial samples. (* denotes key identifiable peaks; PMMA 804, 965, 1307 and 1431 cm^{-1} [represented on the Acadental enamel spectra], PGMA 1014 and 1706 cm^{-1} [represented on the Nissin enamel spectra]).

Figure 4.21 shows the XRD spectra for the commercially available artificial teeth, highlighting any crystalline structure within the materials. Within both materials used to

create the enamel and dentine for IDEA and Fabrica de Sorrisos, no crystalline structures were detected, suggesting the teeth were solely polymers with no filler materials. The same was seen in the enamel material for Nissin. Match! (see Section 3.6.3), identified the peaks within the materials as vermiculite (23.2, 29.9, 36.2, 39.5, 43.4, 47.7, 48.7°) in the dentine for Nissin, a common additive in plaster materials and fertilisers (Rosario *et al.*, 2010), carbonated HAp (CHAp [22.7, 26.0, 26.9, 28.9, 31.8, 32.9, 43.0° (Ivanova *et al.*, 2001)]) within the enamel and dentine materials for One Dental, and various silicates and carbonates (15.4, 22.3, 29.5, 36.1, 39.5°), such as calcite (Kontoyannis & Vagenas, 2000) for the enamel and dentine materials of Acadental and Frasaco.
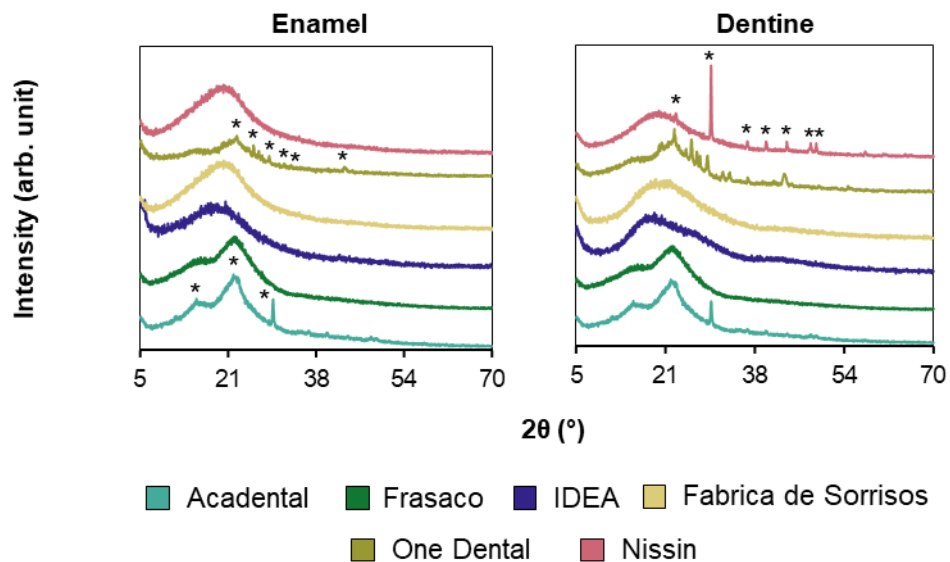
Figure 4.21: XRD spectra for commercial artificial samples.

SEM images (Figure 4.22) highlight the difference in particle sizes and morphology, the particles were defined as spherical particles with flat forms, as outlined by Maroof *et al.* (2020).
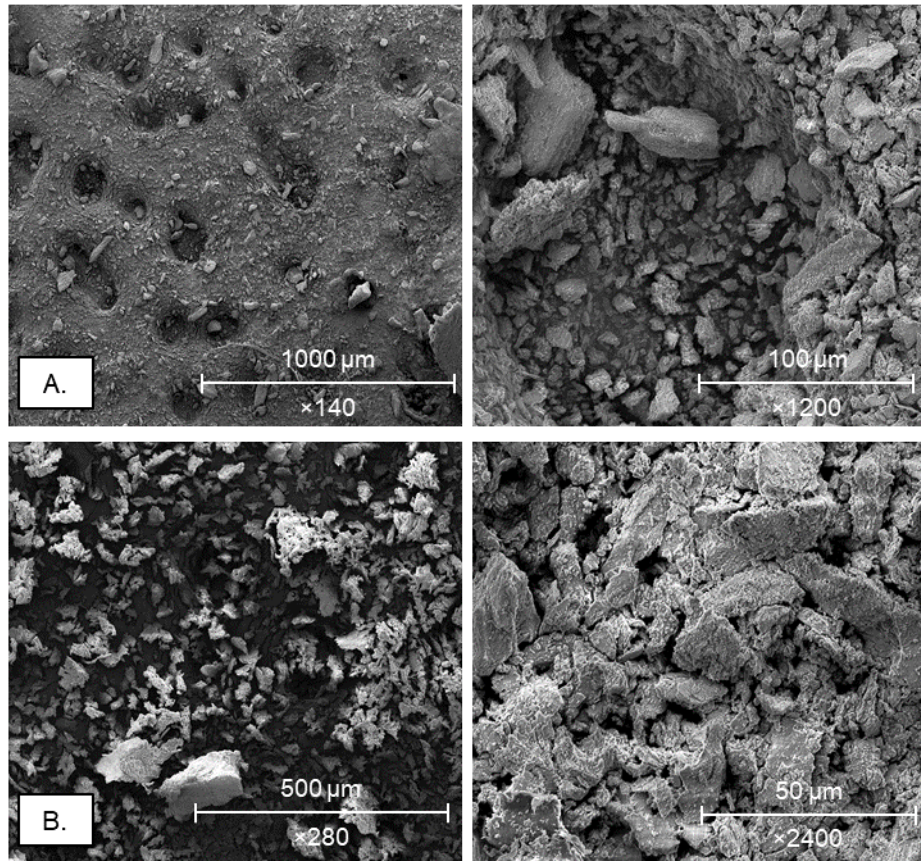
Figure 4.22: SEM of particles of extracted and artificial samples after cutting. A. Extracted tooth cut using a diamond bur. B. An artificial tooth (Frasaco) cut using a diamond bur.

Figure 4.23 shows the mean Ra values for extracted and artificial samples after being cut using either a high-speed diamond or tungsten carbide bur. Samples cut using a diamond bur ranged from 88.27 μm (± 4.18) for extracted and 33.30 μm (± 0.33) to 298.30 μm (± 0.51) for the artificial products, the samples cut with a tungsten carbide bur had Ra values of 31.80 μm (± 0.16) for extracted and 17.74 μm (± 1.64) to 201.76 μm (± 2.73) for artificial samples. Statistical analysis showed a significant difference between the Ra values of specimens cut with diamond and tungsten carbide burs; there was also a significant difference between extracted and artificial samples using the same bur.
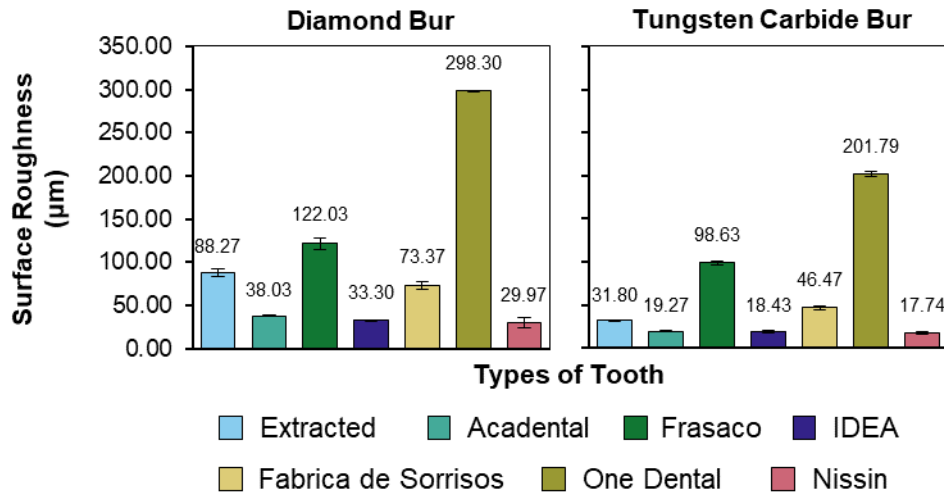
Figure 4.23: Mean Ra values for extracted and artificial samples after bur cutting. Error bars presented as SD of the sample, *n* = 8.

Light microscopy was carried out on burs before and after cutting extracted and artificial samples to ascertain if particles were attaching to the burs' surface (Figure 4.24). It was established that little particles remained attached to the burs' surface after cutting (with irrigation) extracted and artificial samples. These particles were identified as being from the teeth rather than the bur due to their colour, these are highlighted with arrows in Figure 4.24.
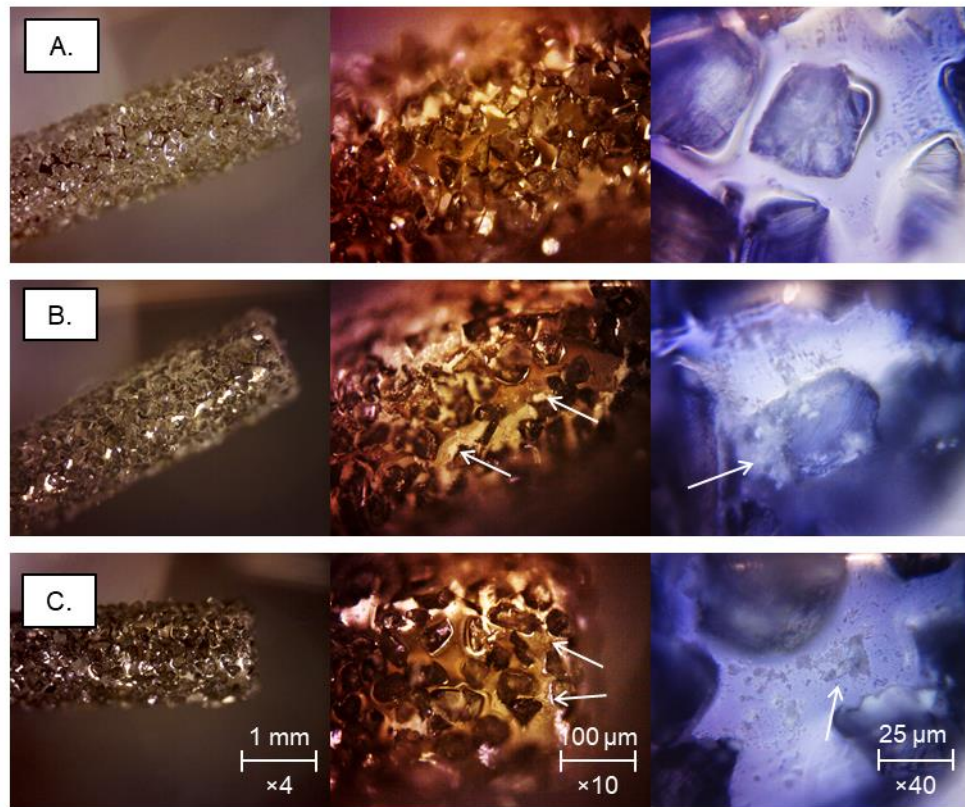
Figure 4.24: Light microscopy of a diamond bur under different magnifications. A. Control diamond bur. B. Diamond bur after cutting an extracted tooth. C. Diamond bur after cutting an artificial tooth (Acadental). Evidence of residual material is highlighted with arrows. Images in each row were taken at the same scale and magnification as the image at the bottom of the corresponding column (C).

Figure 4.25 is a collection of SEM images of the topography of extracted and artificial teeth after cutting with either tungsten carbide or diamond bur. Cuts made on the surface of the artificial tooth lack distinct striation marks, however, evidence of 'scabbing' or 'healing' is evident in both tungsten carbide and diamond bur cuts, where the polymer material has been heated and stretched causing material to displace over the surface (Figure 4.25.A & B). Cuts made on the extracted tooth's surface appear 'cleaner' with clear evidence of striations for both types of burs; with striations appearing more prominent on the surface cut prior with a tungsten carbide bur (Figure 4.25.C).
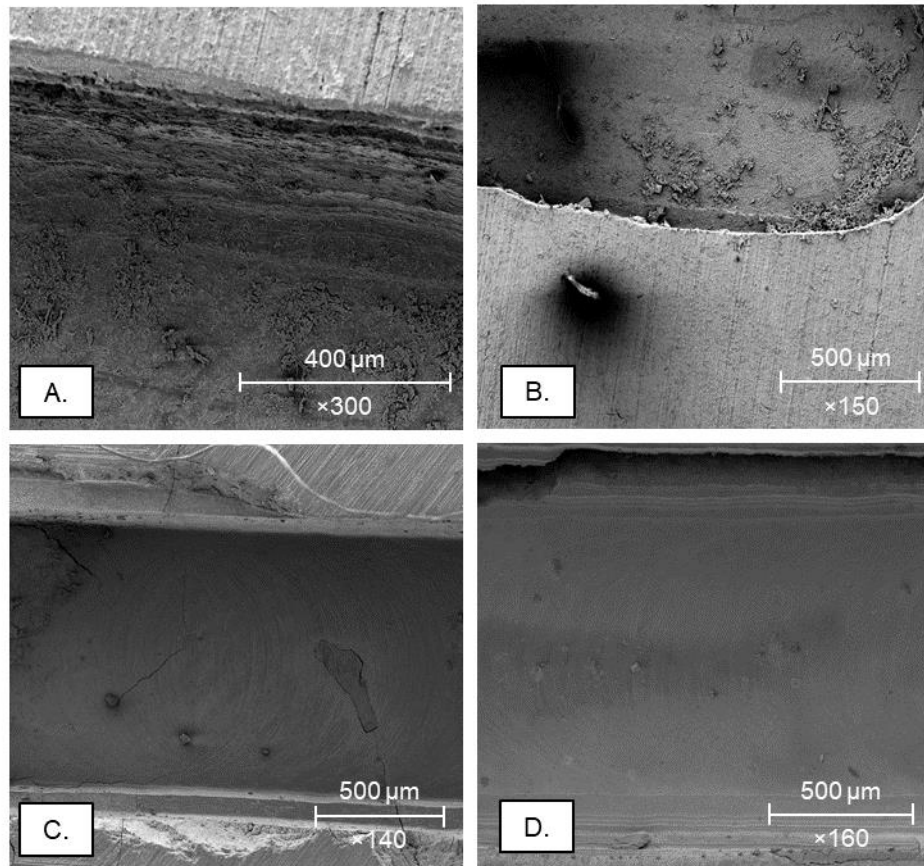
Figure 4.25: SEM images of the surface before cutting with a dental handpiece. A. Artificial tooth cut with a tungsten carbide bur. B. Artificial tooth cut with a diamond bur. C. Extracted tooth cut with a tungsten carbide bur. D. Extracted tooth cut with a diamond bur.

4.4 Discussion

4.4.1 Materials Analysis

The reconstructed XMT datasets produced high-resolution scans of both extracted and artificial teeth, highlighting the different structures and materials. This is demonstrated, with the extracted tooth (Figure 4.5), the high-contrast scan clearly defines the difference between the highly mineralised enamel and less mineralised dentine. In contrast, with the Frasaco artificial tooth (Figure 4.7), there is only one structure, with no definitive enamel or dentine layers present. However, the remaining five (Acadental, IDEA, Fabrica de Sorrisos, One Dental, and Nissin) all differentiated between enamel and dentine by using different materials; this was further demonstrated in the FTIR-ATR

spectra (Figure 4.20), with different peaks appearing. The spectra suggested that the base materials for the artificial teeth were PMMA and PGMA, but with each tooth having a different matrix, offering different mechanical properties. XRD (Figure 4.21) suggested there were mineral-based materials within the materials for the enamel and dentine used in IDEA and Fabrica de Sorrisos; this was also eluded to in the reconstructed XMT images (Figure 4.8 and Figure 4.9 respectively). However, XRD analysis showed no crystalline structure within the enamel material for Nissin teeth, although, the reconstructed XMT images suggest presences of a dense material within the enamel material (Figure 4.11). XRD did identify vermiculite within the dentine structure for Nissin, with XMT confirming the presence of mineralised particles within the polymer. For One Dental, calcium-deficient CHAp was identified within the enamel and dentine materials, XMT confirms the presence of a mineralised particle within the materials, however, more of the particulate is evident within the enamel (Figure 4.10). Calcite was identified in both Acadental and Frasaco models. Yet, the presence of a mineralised particle is seen in Acadental (Figure 4.6) through XMT, and the presence is minimal within the Frasaco models (Figure 4.7).

4.4.2   Mechanical Properties

Previous studies have tried to establish the mechanical properties of teeth, in particular, the $\bar{E}$ through various means (compression tests, nanoindentation tests, and nanohardness tests). However, as stated in Chun *et al.* (2014), a comparison of the mechanical properties of teeth is unlikely due to the non-homogeneous and anisotropic nature of both enamel and dentine. These material qualities mean that the elasticity of the material does not increase linearly with the amount of force applied (Hooke's law) (Yang *et al.*, 1998). Therefore, the results gathered in this study were not designed to define the mechanical properties of natural teeth, but to act as a comparison for commercially available artificial teeth. It is also worth noting that this study was not designed to

compare or evaluate different artificial teeth but to highlight the differences between extracted and artificial.

The results listed in Figure 4.12, demonstrate that extracted enamel and dentine have different mechanical properties. The mean hardness of enamel and dentine was 3078.97 ($\pm$ 43.52) and 938.12 MPa ($\pm$ 13.90) respectively, with enamel being three times higher than that of dentine. Hardness values for artificial teeth ranged from 511.07 ($\pm$ 5.88) to 903.65 MPa ($\pm$ 5.39) for enamel and 412.87 ($\pm$ 6.67) to 876.62 MPa ($\pm$ 3.92) for dentine, less than half compared to extracted dentine and less than a third for extracted enamel. The values measured here matched those that were obtained by Loyaga-Rendon *et al.* (2007), 0.17-0.47 GPa. It was found that the differences were due to the variations in composition and microstructure of the dental hard tissues. Enamel specimens comprise of rows of HAp embedded in a protein matrix (see Section 2.1.1). Dentine specimens comprise of mineralised connective tissues, whereas artificial teeth are made up of polymer chains, and in the instance of four of the samples with the addition of mineral-based materials.

Figure 4.15 showed the Ē of enamel and dentine obtained within this study from compression tests. From the compression tests, the Ē of extracted enamel was of 8293.56 MPa ($\pm$ 112.57) and for dentine was 2166.51 MPa ($\pm$ 54.55). Compared with previous studies that used compression testing, the Ē for enamel ranged from 1.34-95.80 GPa and for dentine 0.005-13.30 GPa (Stanford *et al.*, 1958; Craig *et al.*, 1961; Jantarat *et al.*, 2002; Chun *et al.*, 2014). The values of Ē for both enamel and dentine were within the range of previous studies, however, both values were far from the upper range (95.80 and 13.30 GPa for enamel and dentine respectively) of the values. However, as mentioned previously, comparisons of the mechanical properties of dental hard tissues based on the Ē alone are not feasible because they do not obey Hooke's law. Furthermore, from the stress and strain curves of enamel seen in Figure 4.13, extracted enamel tended to fracture

earlier than artificial enamel and therefore can be considered to be more brittle than artificial enamel. Moreover, from the hardness values measured, extracted enamel was much harder than artificial, this is typical of polymers, as they are made up of long chain-like molecules comprising of small repeating units allowing them to tangle and stretch easily, compared to crystal-like structures. From the XMT images, the degree of mineralisation was shown to be more apparent and uniform within extracted teeth (Figure 4.5) when compared to artificial teeth, that only included slight mineralisation from the mineral-based particles. This degree of mineralisation would help to determine if a material was brittle or ductile which is shown within the stress-strain curve (Figure 4.13), extracted enamel is shown to be a highly mineralised material and from the curve appeared quite brittle. One Dental from the XMT images (Figure 4.10) was also shown to be quite mineralised, and from the curve was also quite brittle, whereas the other artificial teeth showed varying degrees of mineralisation which was less than the extracted and One Dental teeth and were shown to be quite ductile materials.

The mean K_{ifr} values for extracted enamel was 1.16 MPa m$^{0.5}$ ($\pm$ 0.36), and for extracted dentine 1.91 MPa m$^{0.5}$ ($\pm$ 0.18) both these values were similar to values reported in previous studies (Hassan *et al.*, 1981; Iwamoto & Ruse, 2002; Zheng *et al.*, 2013). Compared to the artificial teeth which ranged from 2.72-3.46 MPa m$^{0.5}$ for enamel and 3.54-4.20 MPa m$^{0.5}$ for dentine, the values are doubled when compared to the extracted counterparts. These results suggest that less force is required to fracture extracted teeth than artificial teeth, explaining why undergraduate dental students find it difficult to perform procedures on artificial teeth, as it requires more force to create fractures and to remove any material, this is also evident from the stress-strain curve (Figure 4.13). However, Quinn (2007) states that the H_V crack length has numerous drawbacks, with no universally accepted equation existing; therefore, the values obtained are approximations not exact, compared to K_C values used in nanoindentation studies. Furthermore, previous

literature using the H_V crack length should be referred to as K_{ifr} rather than K_C, due to equation variations. Despite these drawbacks, the ability to measure the crack length helps to give a better understanding to fracture mechanics, in terms of actual length and how the crack propagates. Longer cracks imply the material is easy to fracture.

All the results collected in this study are typical when comparing ceramic material with polymers. Many studies have documented the properties in detail for each material, however very few have looked at comparing the mechanical properties of ceramics compared to polymers, especially concerning extracted and artificial teeth for training purposes.

4.4.3   Force Requirement

Throughout all the force experiments carried out, it was established that more force was required to cut artificial teeth compared to extracted, in the instance of the clinician and non-clinician study (Figure 4.19), the clinicians applied more than double the force to cut artificial, the same trend was seen in the non-clinicians, however, the amount of force needed to cut artificial was not double that of extracted. Compared to the values established in Elias *et al.* (2003), the values were similar to that obtained within this study.

In Amini & Miserez (2013), the authors investigated the wear and abrasion resistance of biological materials based on their "stiffness", which was the ratio of hardness (H) to Ē, using the ratio of $\frac{H^3}{\bar{E}^2}$. The authors established that as the "stiffness" of the material increased, the energy required to crack the material with a blunt contact decreased; the ratio was established in Miserez *et al.* (2007) to try and understand how unmineralised squid beak could break down mineralised objects such as shells and bone. Using the ratio established by Miserez *et al.,* the hardness and Ē values were plotted against the average force required to cut, as shown in Figure 4.26. From the plotted data,

it can be surmised that a negative correlation is seen between force and the properties ratio, as the average force required to cut decreases the ratio increases. This can be summarised that the 'stiffer' material is the less force is necessary to cut or fracture the material. This was also seen in Miserez *et al.* and in Amini & Miserez, as materials with a higher ratio were seen as brittle materials with enamel having a ratio of 7.0-9.0 MPa and dentine 0.3-1.3 MPa, these figures are very low compared to the ratios seen in this study; 0.42 and 0.18 GPa for enamel and dentine respectively. However, the hardness and $\bar{E}$ values presented in the Miserez *et al.* study were collected from previous reviews which varied on their testing protocols.
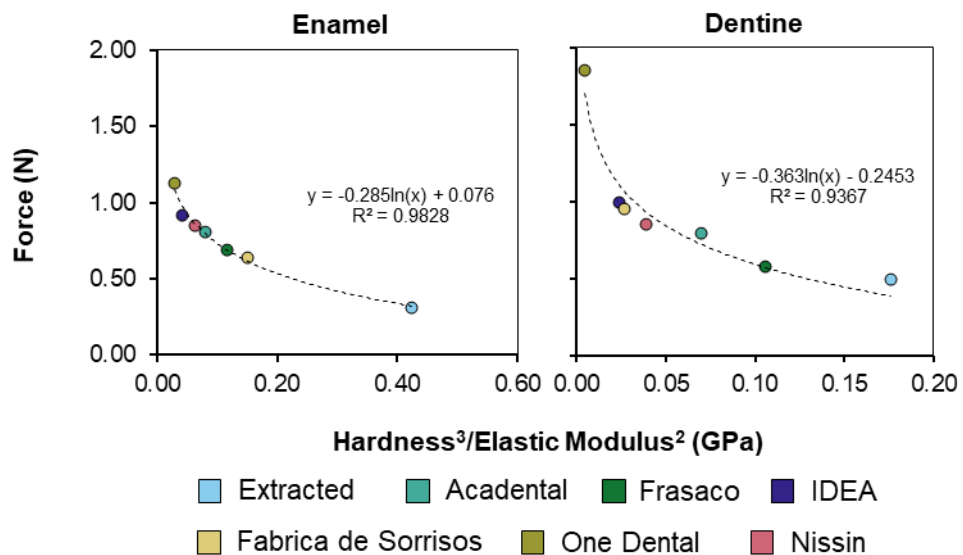
Figure 4.26: Average force needed to cut extracted and artificial teeth against $\frac{H^3}{\bar{E}^2}$. A logarithmic trendline was fitted, with the equations and R^2 values referring to the artificial teeth and extracted teeth values.

Miserez *et al.* (2007) also established that the stiffer the material (higher ratio), the less resistant the material was to abrasion, this is also seen in Figure 4.25, with the SEM images showing little abrasion contact on the artificial teeth. In contrast, clear striation was seen on the extracted teeth. However, Ra values seen in Figure 4.23 suggest Ra of extracted teeth is more or less than the values seen in artificial teeth, this difference could be due to the artificial teeth's elastic nature under varying temperatures with the

bur essentially flattening the surface of displacing and depositing material throughout the cut, explaining the vast differences in Ra values. This is commonly seen in plastic materials with highly crystalline structures, the material suffers strain hardness when enduring cold work (Bertram Broberg, 1999).

It was hypothesised that as the bur cut into artificial teeth material would attach itself onto the bur, reducing the sharp edges needed to cut the material, explaining the extra force required to cut. However, light microscopy (Figure 4.24) showed little evidence of material remaining on the bur after cutting, this is probably due to the small sizes of the material once cut and the constant irrigation with deionised water throughout the procedure.

4.5 Conclusions

In conclusion, this study has shown empirical evidence to the differences in fracture and hardness of extracted and artificial teeth. It is then hypothesised that these differences may explain why many undergraduate dental students dislike the use of artificial teeth within dental education, as from the experiments carried out, more force is required to cut plastic artificial teeth compared to extracted teeth. These results form the basis of how artificial teeth could be improved to allow a better perception of their use in dental education. However, although the mechanical properties have been established, a lot more work is required to be able to recreate the biomimicry of natural teeth.

Chapter 5

3D Printing from X-Ray Microtomography

This chapter explores the mechanism and process in which data was converted from X-ray microtomography datasets to 3D printed models through different techniques and multiple software. Information regarding data conversion has been previously published in Cresswell-Boyes *et al.* (2018a) and Cresswell-Boyes *et al.* (2018b).

5.1 Introduction

3D Printing, known initially as rapid prototyping, has been around since the late 1980s and has been used as a way to quickly produce cost-effective prototypes during the design process (O'Brien *et al.*, 2016). However, over time, rapid prototyping has evolved, creating a variety of printers and printable materials that facilitate use by any individual or business (O'Brien *et al.*, 2016; Thomas & Claypole, 2016).

As previously mentioned in Section 2.4.3, 3D printing has been used for a variety of applications; however, the use of 3D printing in SBME has increased in popularity. Although advanced visualisation in SBME has been crucial in diagnosis and communication, there is an advantage to rendering DICOM images as 3D prints. 3D models capable of offering tactile feedback and depth information on anatomic and pathologic states is an invaluable tool in both clinical and teaching settings (Mitsouras *et al.*, 2015; O'Brien *et al.*, 2016). However, typically 3D printers do not recognise DICOM images, with the printers taking individual objects defined by surfaces that enclose a region of space (STL, see Section 2.4.4). Once these objects of interest have been identified, they can be 3D printed, with the process of this being divided into three stages;

image acquisition, image post-processing, and 3D printing (Mitsouras *et al.*, 2015; Redwood *et al.*, 2017).

With image acquisition, a 3D medical model can be manufactured from any volumetric dataset, that has enough contrast to differentiate between tissues or structures, this is typically why CT and MRI images are commonly used for 3D printing. The high contrast, signal to noise ratio, and spatial resolution allow for structure differentiation. However, a common drawback of these imaging techniques is the inclusion of image noise and ring artefacts or beam hardening artefacts which may interfere with the image acquisition, requiring more input at the image post-processing stage (Rengier *et al.*, 2010; Mitsouras *et al.*, 2015).

Manipulating DICOM images for 3D printing requires a lot of accurate segmentation for the desired tissue by selecting them in ROI. Typically, ROI segmentation can be an automated process (depending on the software used); however, with the introduction of noise and artefacts from the image acquisition stage, manual input may be required to overcome these. A typical example seen in CT is the artefact seen from beam hardening, this can affect the blood pool attenuation seen in blood vessels, without manual input at this stage, an error in the model can cause nonanatomic holes or voids. However, the opposite is also true when the artefact gets mistaken as solid material filling in anatomic voids such as those seen in cancellous bone (Suzuki *et al.*, 2004; Harryson *et al.*, 2007; Mitsouras *et al.*, 2015).

After segmentation and image manipulation, most commercial software can generate an STL file of the 3D model, which is then suitable for 3D printing. At this stage the user can edit printing settings for the desired outcome, however, conversion from the ROI to STL is a balancing act in terms of the number of faces and vertices; too few will compromise the anatomical features in the model, while too many will lead to an

unnecessary roughness if the object in the initial segmented surface was smooth, most likely due to noise contours (Mitsouras *et al.*, 2015; Redwood *et al.*, 2017).

In this study, a method of collecting structural biological data and converting it into a 3D model using open-source software is presented, utilising XMT techniques to overcome specific issues regarding ring artefacts and noise from beam hardening. Demonstrating an open-source method to converting XMT to 3D prints and discussing the benefits of using SLA over FDM and SLS, when recreating anatomical structures.

5.2 Materials and Methods

For this study, a selection of healthy extracted human teeth was selected from a human tissue bank; with ethical approval obtained from Queen Mary Research Ethics Committee (QMREC2008/57).

5.2.1 X-Ray Microtomography

The specimens were scanned using the MuCAT2 scanner, as outlined in Section 3.1. The natural teeth were scanned at 15 μm voxel size (resolution) at 90 keV, 180 μA and were scanned individually using multi-block imaging (Section 3.1.2), in a specimen tube with 70% ethanol and mounting wax to keep the specimens stable throughout, scanning of each tooth typically took around 16-26 h. Non-biological samples were scanned at 40 keV, 405 μA at 30 μm voxel, usually for 1-2 h, more information is provided in Appendix A (Table A).

5.2.2 Visualisation and Modelling

Reconstruction of the XMT datasets was carried out (Section 3.2.2), with the datasets being viewed in Tomview before being exported to Drishti (Section 3.3). The selection and segmentation of the ROIs were carried out in Drishti by highlighting the

area containing the correct LAC values (Figure 3.12), before being exported into Meshlab for reducing and simplification of the mesh surface (reducing the triangle count), any manipulating or 'sculpting' was carried in Meshmixer, 3D Builder was used to repair mesh surfaces and create the final STL file (see Section 3.3).

5.2.3   Fused Filament Fabrication

As mentioned previously in Section 3.3.1, a Wanhao Duplicator i3 was used to print FFF models of tooth samples. A selection of materials have been used including; PLA (3D Prima, Sweden), flexible thermoplastic polyurethane ([TPU] FFF World, Spain), wood-PLA (RS Components, UK), and ABS (3D Prima, Sweden), the settings used for each material can be found in Table 5.1.

Table 5.1: Printer settings used for different FFF materials. Parameters based on manufacturer's recommendations as well as trial and error.

Material	Layer Height (mm)	Printing Temperature (°C)	Material Flow (%)	Print Speed (mm/s)
PLA	0.06	185-195	100	60
TPU	0.08	200-205	95	40
Wood-PLA	0.05	195-205	100	60

5.2.3.1   Slicer Programs

To check the dimensional accuracy of the slicing software, multiple software was used to print cylinders of a specific size (20.00 x 5.00 mm), made from different materials and repeated eight times (Figure 5.1). The slicer software chosen were popular open-source software, which is widely available, they included; Cura, Slic3r, Repetier-Host (Version 2.1.6, 2018; Hot-World GmbH & Co. KG, Germany), and Matter Control (Version 2.19.10, 2019; MatterHackers Inc., USA). The same printer parameters were

used on all software for the materials, and three cylinders were printed, the cylinders were then imaged using XMT techniques, and the datasets were analysed using ImageJ to compare dimensional accuracy (more details in Section 5.2.6).
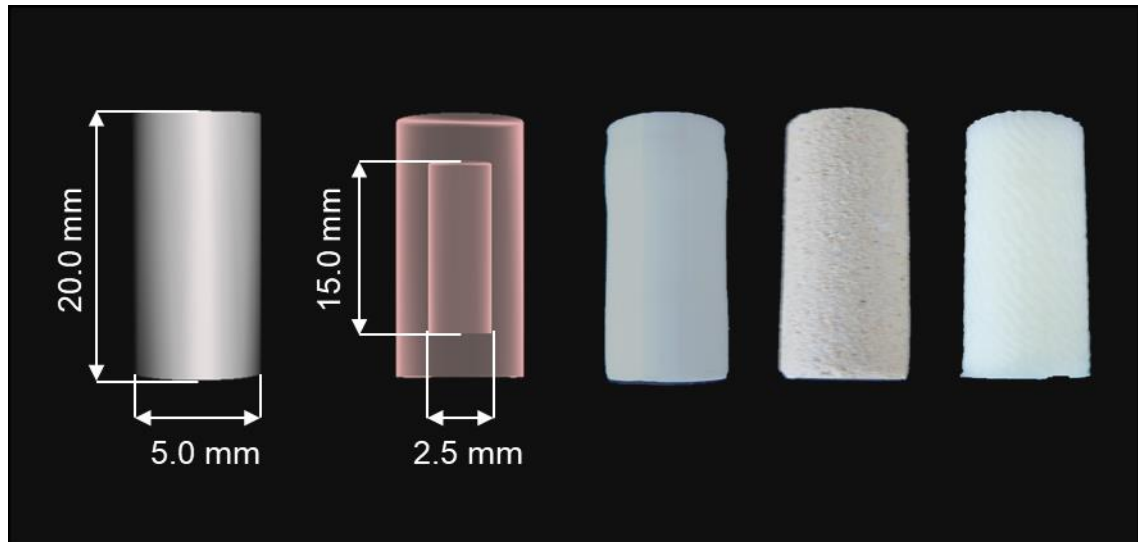
Figure 5.1: Cylinders of known sizes were designed and manufactured. *Left to Right:*3D rendering of the test print, translucent view, cylinder printed in PLA, cylinder printed in wood-PLA and cylinder printed in TPU.

5.2.3.2   *Extrusion Deposition Modelling*

As previously mentioned in Section 3.3.1, a repurposed FFF printer with a direct syringe extruder was used to print viscous material such as that of dental composite. An UV LED was attached to the nozzle of the extruder to cure the material as it was deposited onto the printer bed. Dental composites materials used included Cention N (Ivoclar Vivadent AG, Lichtenstein) and Activa[TM] BioActive-Restorative[TM] (Pulpdent Corp., USA); these materials were kept in UV reflective containers to prevent polymerisation before extrusion. Composites were extruded at a set rate of 0.25 mm/s, with a print speed of 10%, and a layer height of 1.00 mm, overall prints took 1-2 h to complete.

5.2.4 Stereolithography

As explained in Section 3.3.1, for stereolithography, two printers were used; an SLA printer, Formlabs Form 2, and a DLP printer, Anycubic Photon. The materials used for the printers were the companies' brand materials suited for the respective printers, white resin (Formlabs Inc., USA), transparent resin (Formlabs Inc., USA) and white Anycubic 405 nm Rapid Resin (Anycubic, China). Details regarding printing parameters are shown in Table 5.2.

Table 5.2: Printer settings used for different SLA and DLP materials. Parameters based on manufacturer's recommendations as well as trial and error.

Material	Layer Height (mm)	Curing Time (s)	Rest Time (s)	Printing Temperature (°C)
Formlabs White Resin	0.05	0.1-2	5	31
Formlabs Transparent Resin	0.05	0.1-2	8	31
Anycubic 405 nm Rapid Resin	0.05	11	8	26

Once printed the models were then washed in 90% ethanol for 20 min using a Formlabs Wash (Formlabs Inc., USA) to remove any uncured resin, the models were then transferred to a Formlabs Cure (Formlabs Inc., USA) where the models were subjected to further curing for 30 min at 60°C as per manufacturer's recommendation.

5.2.5 Selective Laser Sintering

As mentioned in Section 3.3.1 tooth models created using SLS techniques were outsourced to 3D Hubs, with STL files being uploaded to the website, where dimensions and materials could be selected, Nylon PA 12 (Stratasys Ltd., USA) was chosen with a layer height of 50 μm. The parameter setting of the SLS printed models was unknown.

5.2.6   Morphometric Analysis

Quantitative analysis of the reconstructed XMT images was carried out using ImageJ with the BoneJ plugin (Version 1.4.3, 2018; Wellcome Trust, UK; Doube *et al.* [2010]) in conjunction with the additive manufacturing software Autodesk Netfabb® Basic (Version 7.4, 2019; Autodesk Inc., USA) for quantifying the density and quantifying any voids within the structure. Datasets were directly exported from Tomview into ImageJ, and datasets were converted to PLY files into Netfabb®, as shown in Section 3.3.

5.2.7   White Light Profilometry

White light profilometry was used to highlight the differences in printing methodologies by measuring the topography of the occlusal surface, as previously used in Section 3.4.2. The mesiobuccal cusp was imaged throughout the specimens with a 3.00 x 3.00 mm area examined (Figure 5.2), a 3D printed bracket was created to ensure all samples were placed in the correct position before scanning.
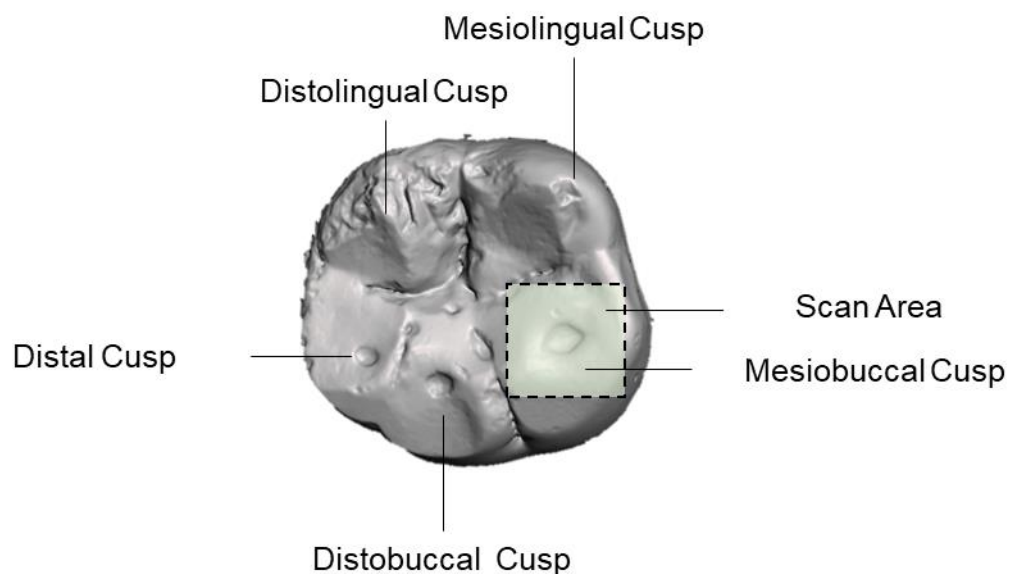
Figure 5.2: Scan area on a mandibular first molar identifying the mesiobuccal cusp.

5.3   Results

Reconstructed XMT datasets were visualised in Tomview collating all views in the *X*, *Y*, and *Z* planes. Figure 5.3-Figure 5.10 are a selection of the extracted teeth imaged, highlighting the differences in geometry and structure between the different types of teeth. As outlined in Section 3.1.3, all mineralised samples (extracted teeth) were calibrated and set to the same level of brightness and degree of contrast.

Due to the high contrast nature of the XMT system used (see Section 3.1.1), from the reconstructed XMT images (Figure 5.3-Figure 5.10), the different structures of human teeth can be easily identified and distinguished. Enamel appears whiter than dentine due to its higher mineral content, however with some of the extracted teeth different types of dentine can even be identified, in particular in Figure 5.10, evidence of secondary and tertiary dentine can be identified. Remnants of the cementum can be seen on the root in Figure 5.7. The ability to be able to clearly distinguish different structures with high contrast allows for easy segmentation, which is discussed later on in this section.
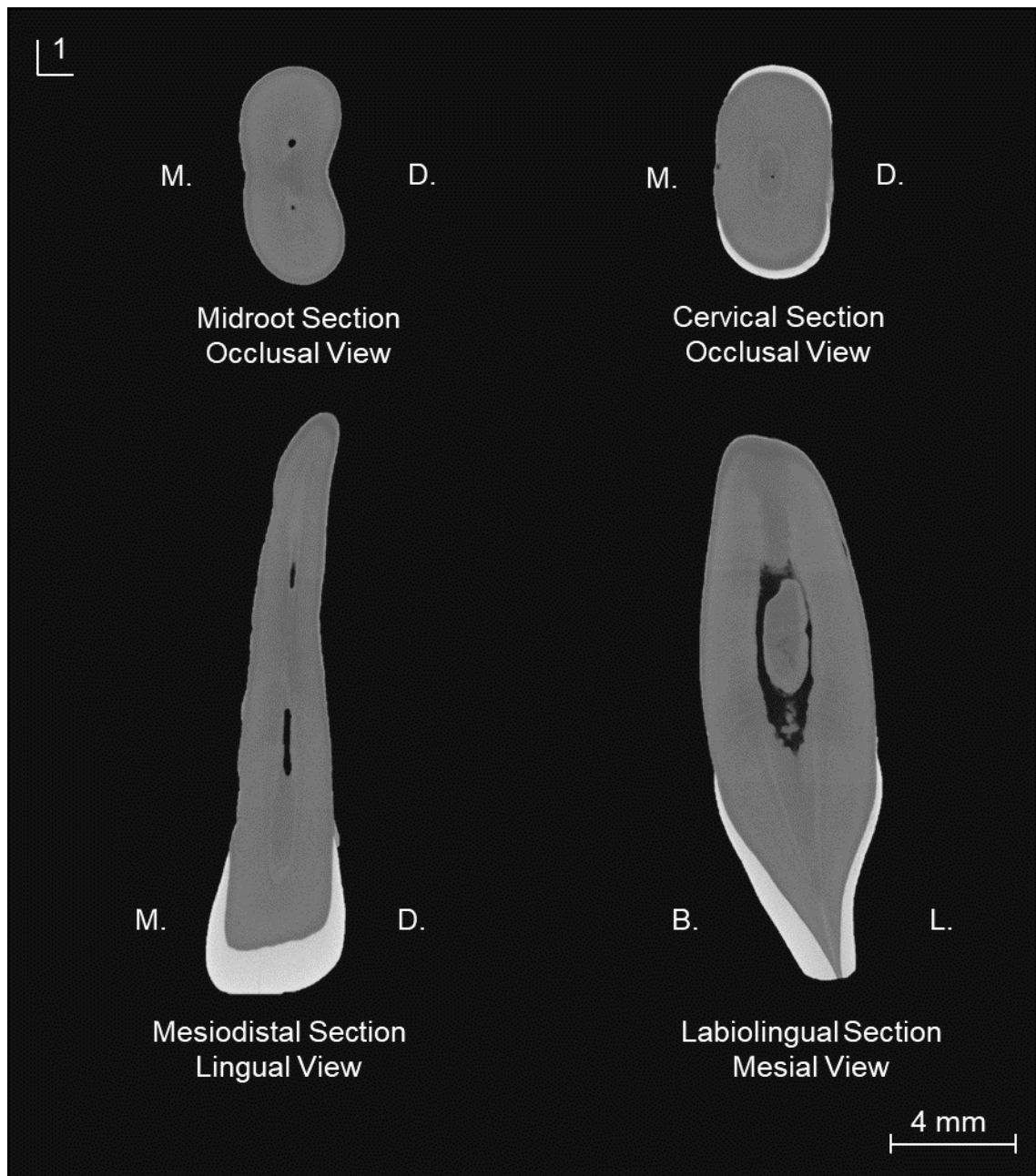
Figure 5.3: XMT image of an extracted maxillary central incisor. Multiple views, showing different sections and structure of the tooth. M. Mesial side. D. Distal side. B. Labial side[1]. L. Lingual side.

---

[1] For consistency and clarity, the anterior teeth are labelled with *B.* for buccal side to signify the labial side.

M.   D.

**Cervical Section
Occlusal View**

M.   D.

**Midroot Section
Occlusal View**

B.   L.

**Labiolingual Section
Mesial View**

M.   D.

**Mesiodistal Section
Lingual View**

4 mm
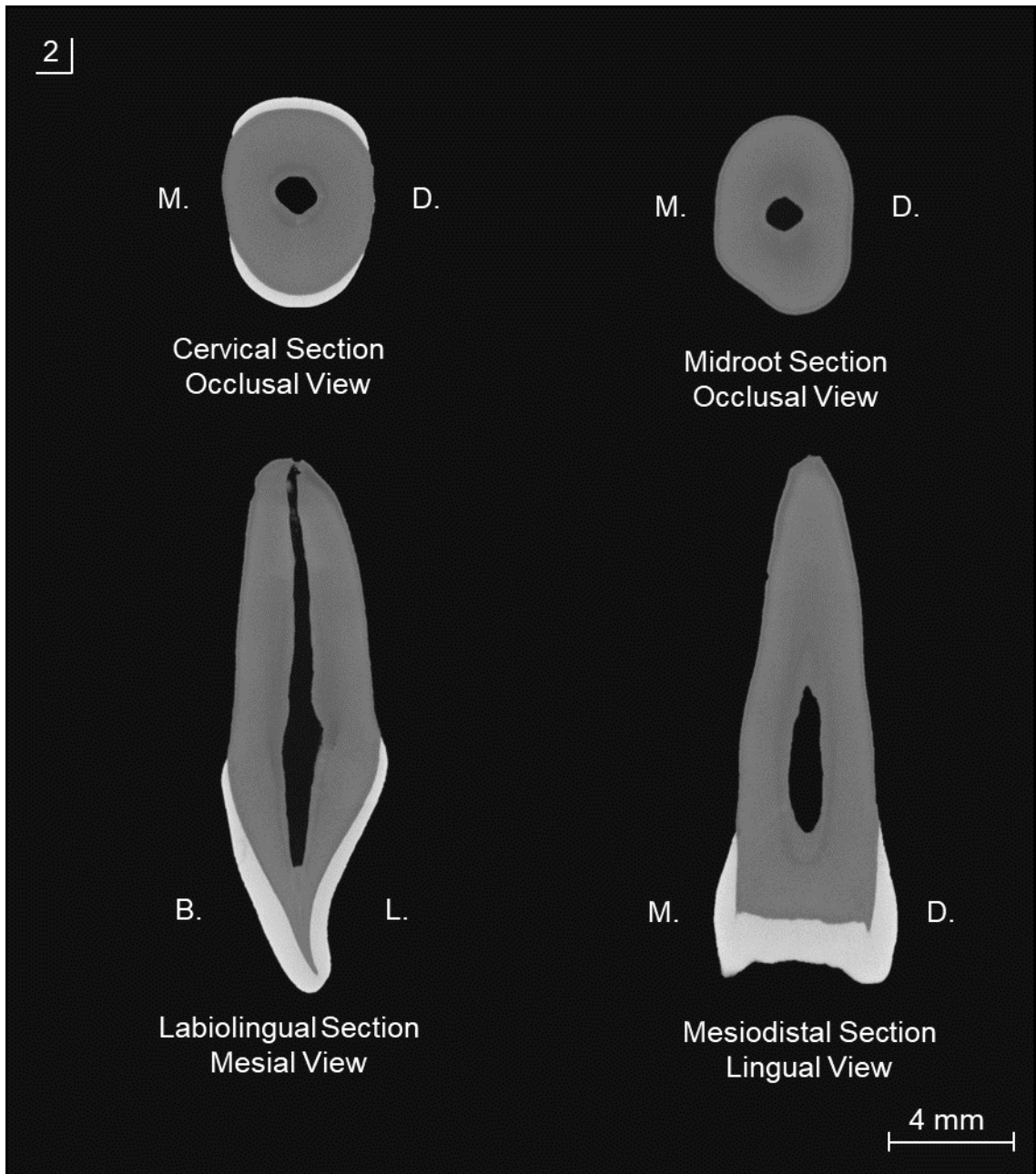
Figure 5.4: XMT image of an extracted maxillary lateral incisor. Multiple views, showing different sections and structure of the tooth. M. Mesial side. D. Distal side. B. Labial side. L. Lingual side.

155
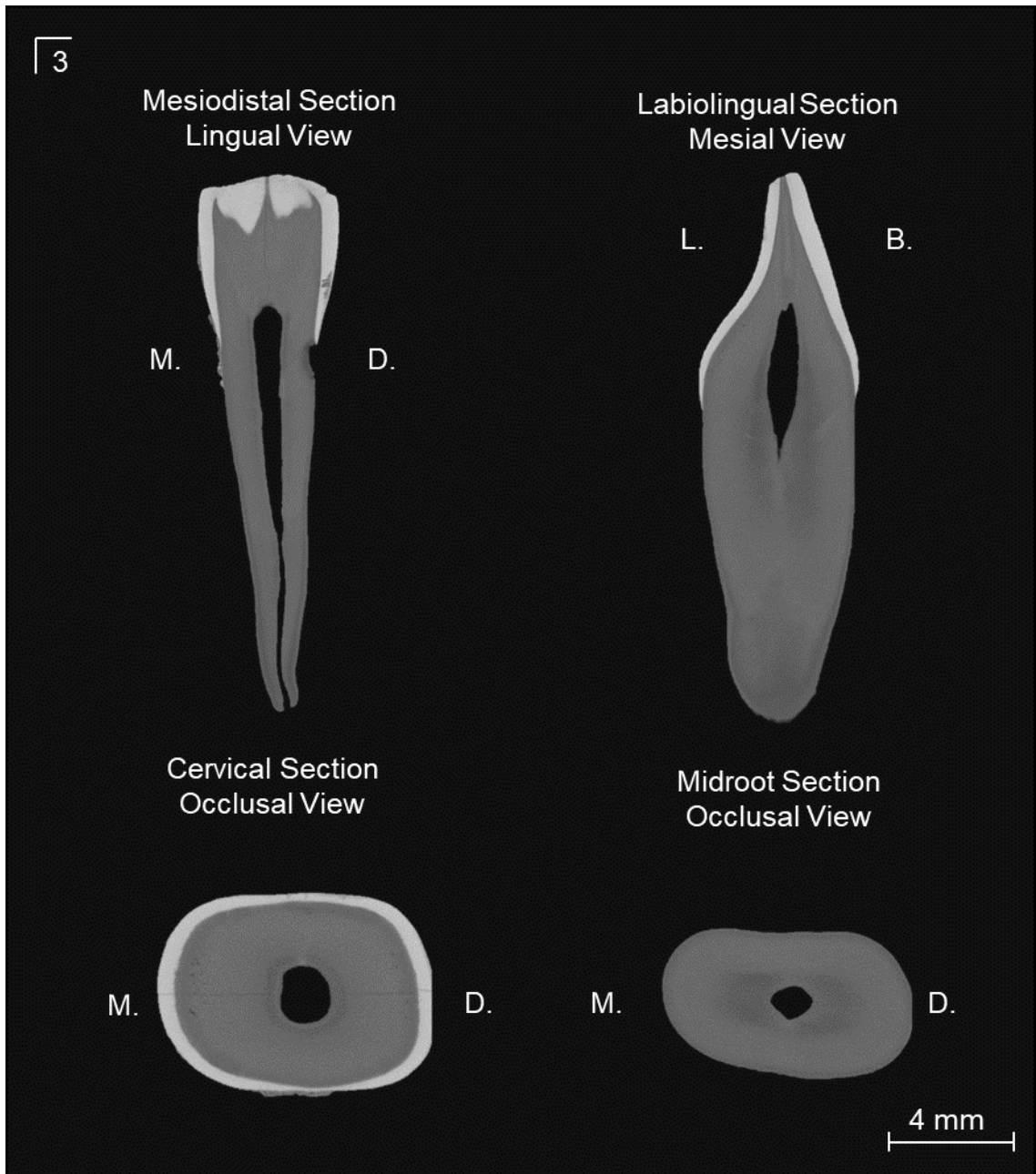
Figure 5.5: XMT image of an extracted mandibular canine. Multiple views, showing different sections and structure of the tooth. M. Mesial side. D. Distal side. B. Labial side. L. Lingual side.
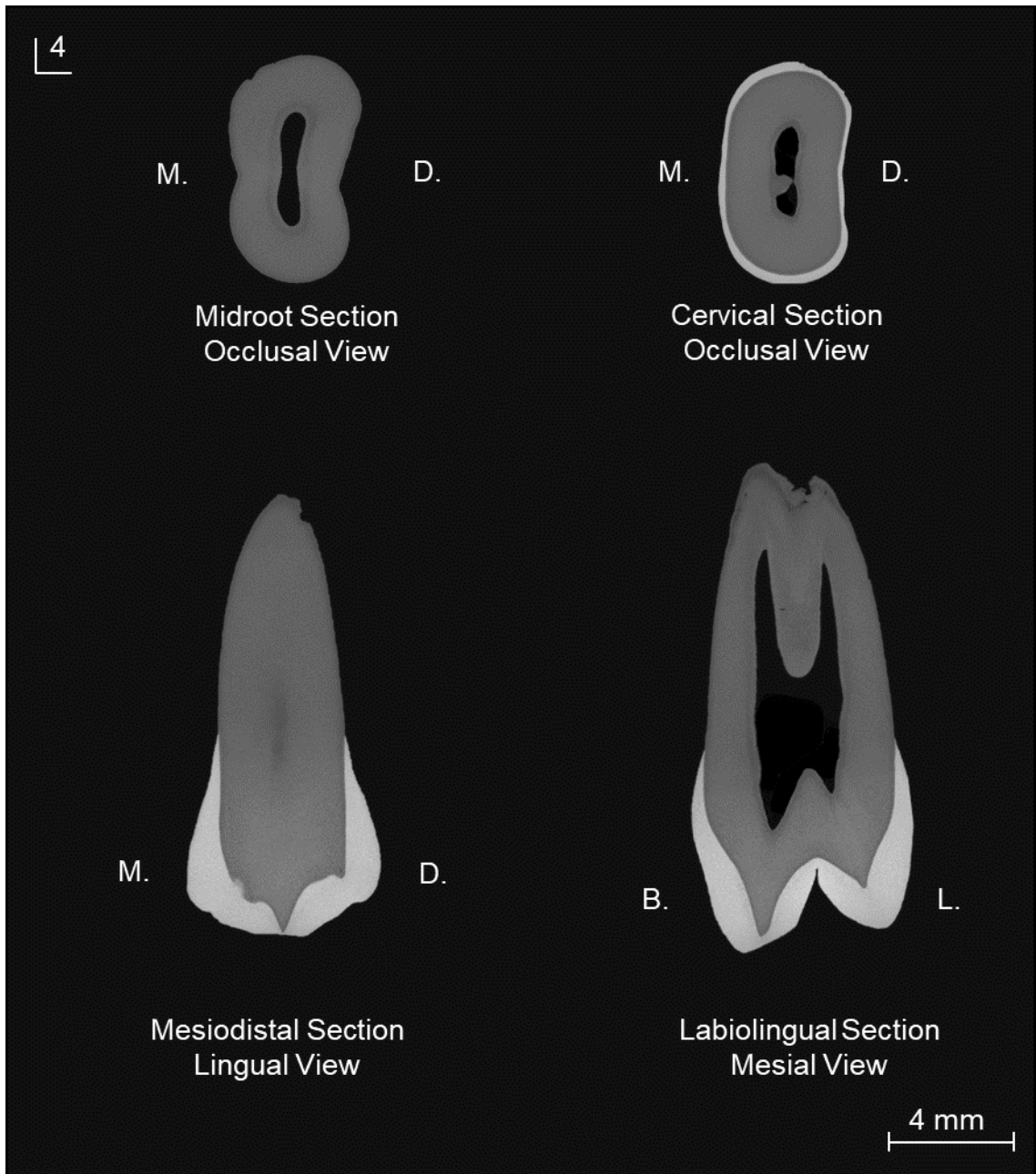
Figure 5.6: XMT image of an extracted maxillary first premolar. Multiple views, showing different sections and structure of the tooth. M. Mesial side. D. Distal side. B. Buccal side. L. Lingual side.
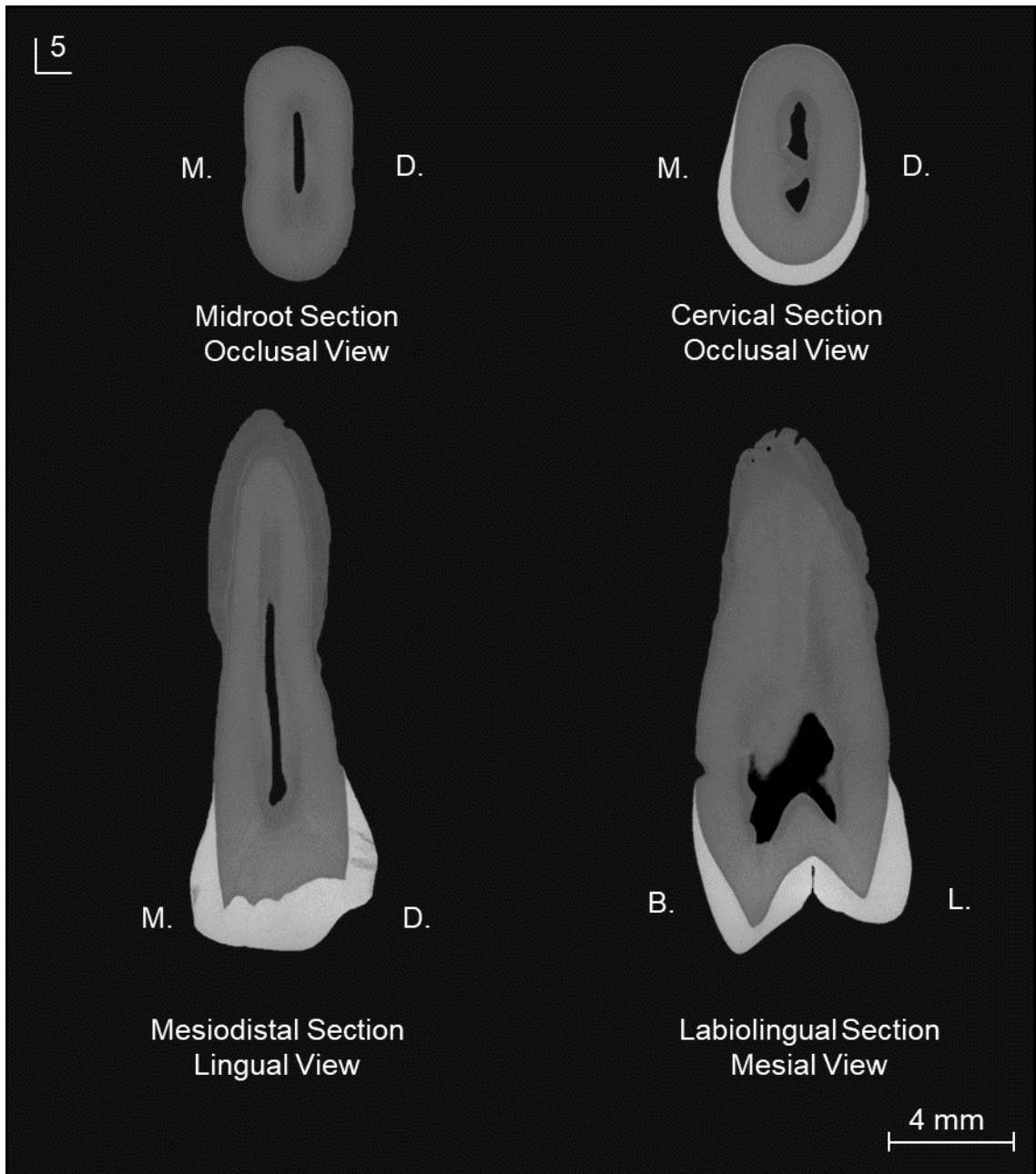
Figure 5.7: XMT image of an extracted maxillary second premolar. Multiple views, showing different sections and structure of the tooth. M. Mesial side. D. Distal side. B. Buccal side. L. Lingual side.
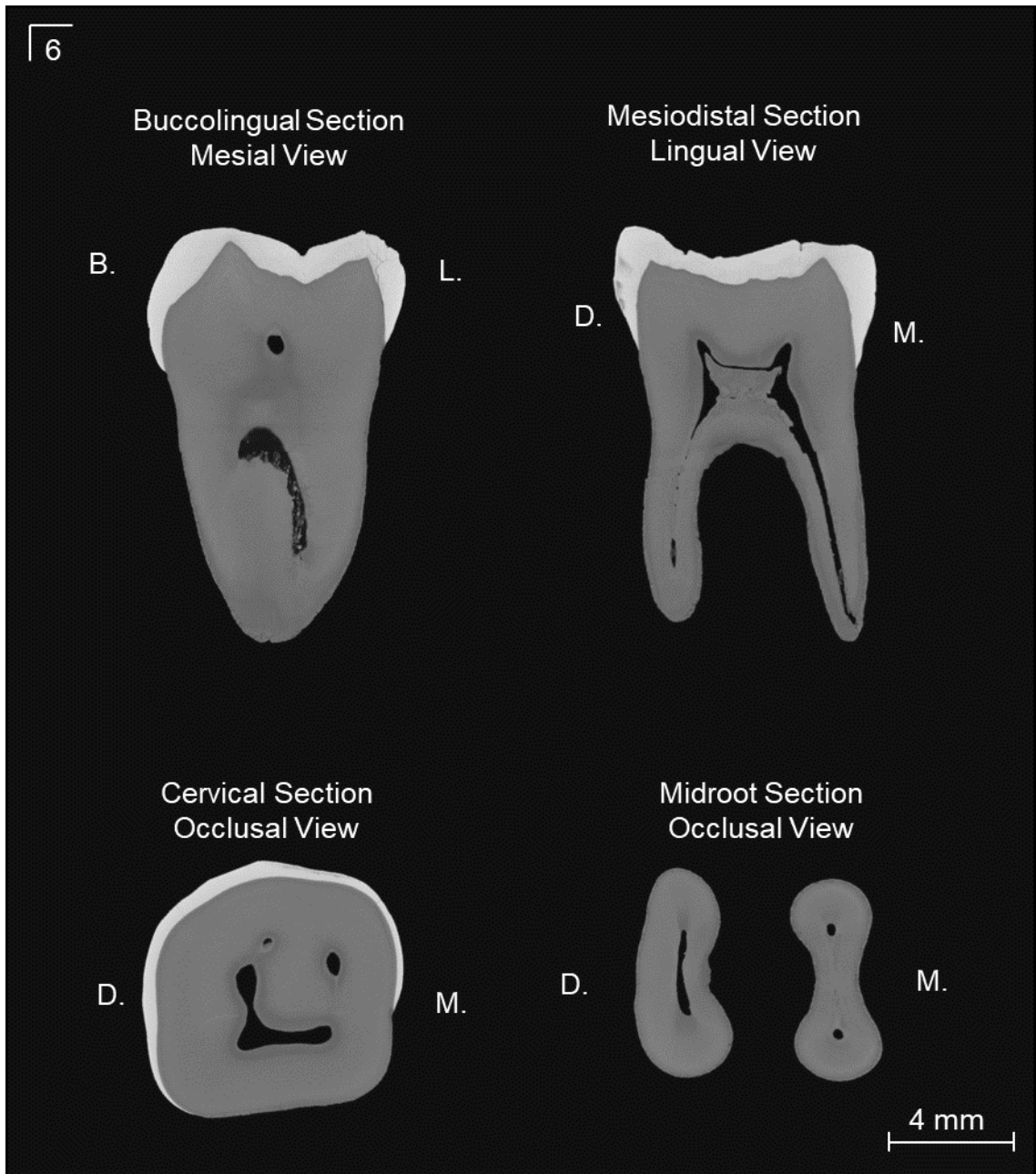
Figure 5.8: XMT image of an extracted mandibular first molar. Multiple views, showing different sections and structure of the tooth. M. Mesial side. D. Distal side. B. Buccal side. L. Lingual side.
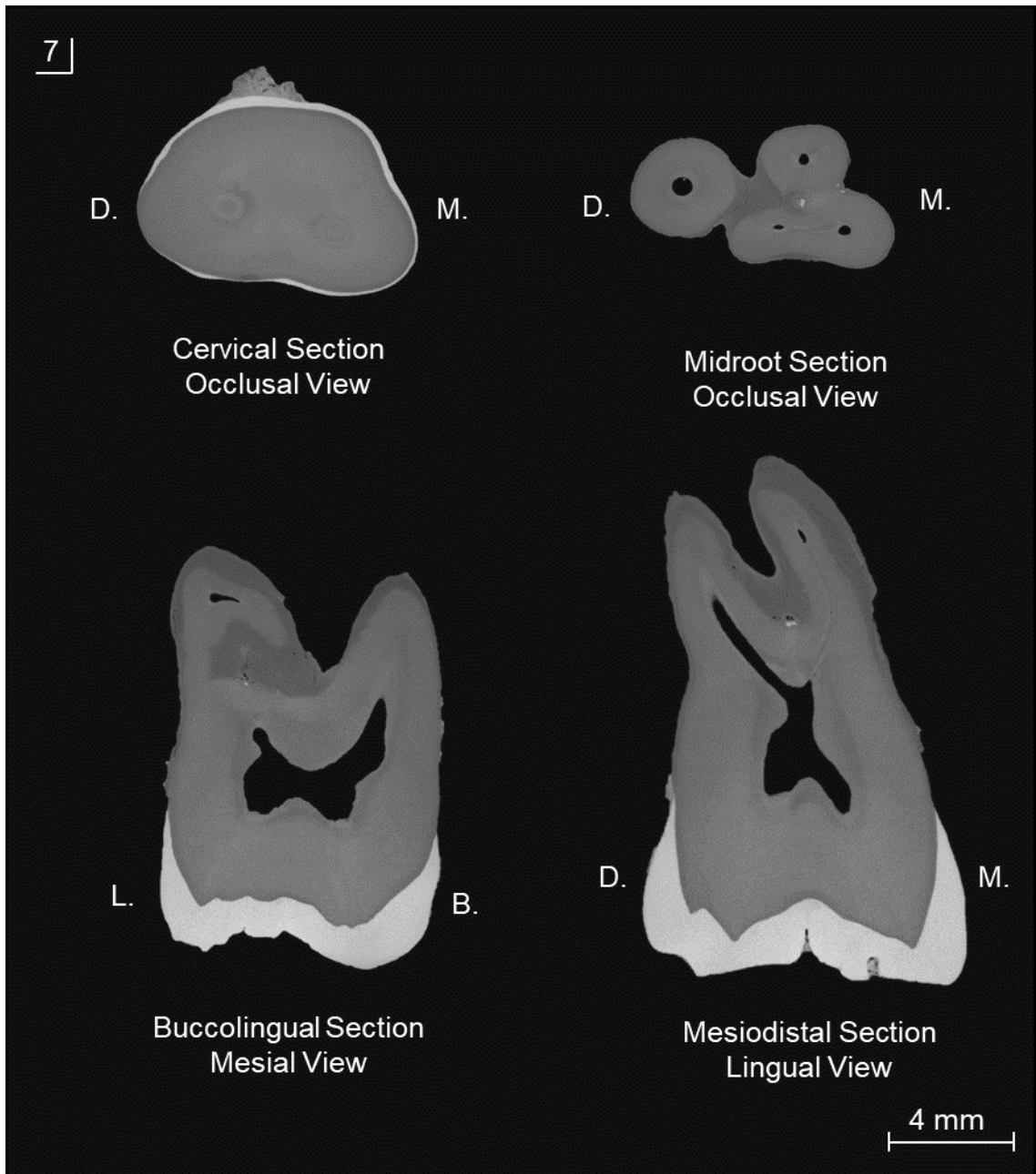
Figure 5.9: XMT image of an extracted maxillary second molar. Multiple views, showing different sections and structure of the tooth. M. Mesial side. D. Distal side. B. Buccal side. L. Lingual side.
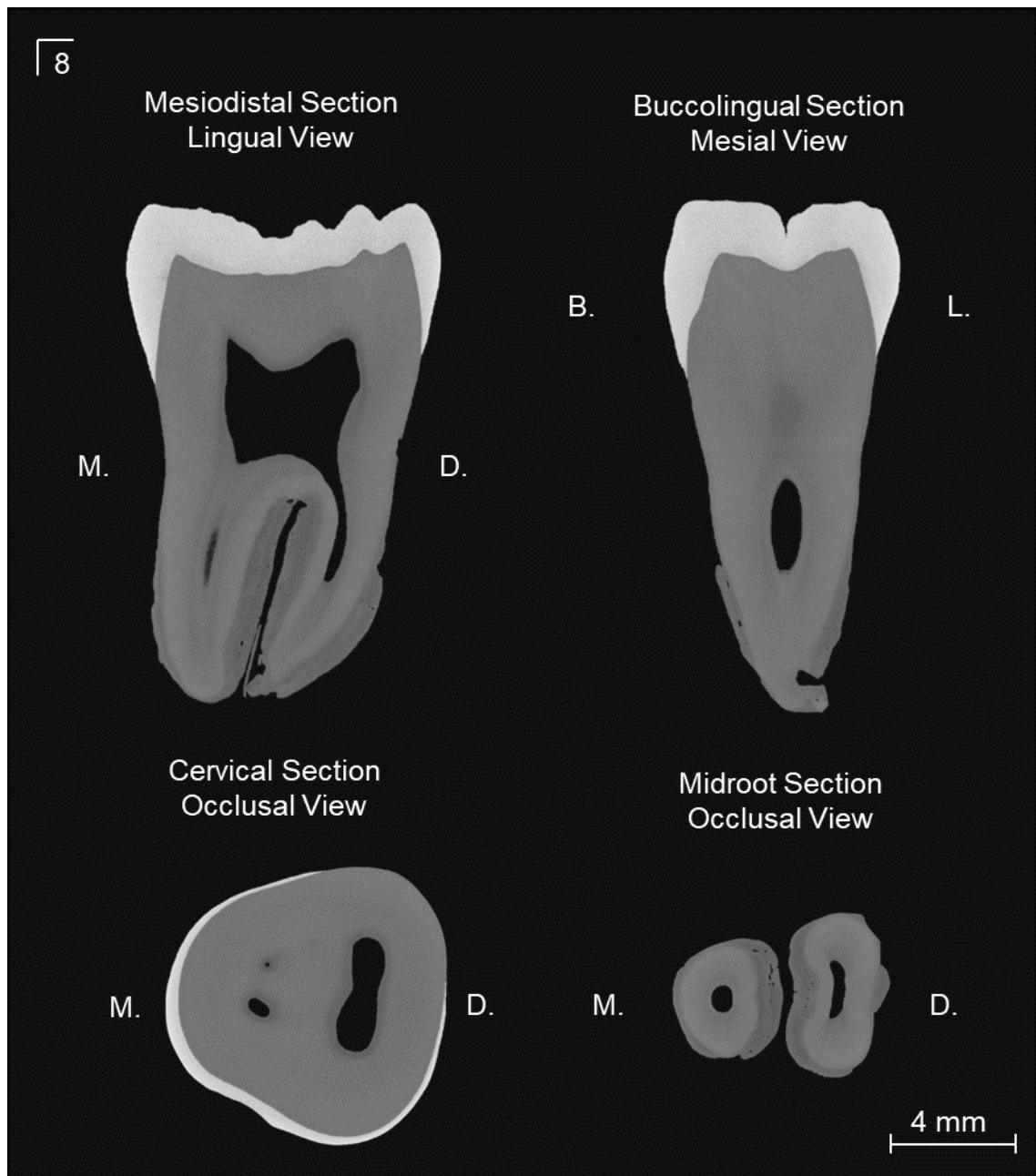
Figure 5.10: XMT image of an extracted mandibular third molar. Multiple views, showing different sections and structure of the tooth. M. Mesial side. D. Distal side. B. Buccal side. L. Lingual side.

Figure 5.11 demonstrates the rendered teeth after conversion, segmentation and thresholding carried out in Drishti. Figure 5.11.A is the rendered models for the reconstructed XMT datasets shown in Figure 5.3-Figure 5.10, highlighting the different structures shown with artificial colours; orange for dentine and white-yellow for enamel. Colour choice is user-defined; however, the assignment is dependent on the LAC values of the specimen scanned. Figure 5.11.B is the segmented structures of the reconstructed

XMT dataset shown in Figure 4.5; the segmentation of structures was carried out by altering the ROI within the histogram (Figure 3.12). The pulp chamber was rendered within Autodesk Meshmixer, by inverting the pulp cavity within the dentine structure to create a solid mesh.

Figure 5.11: 3D rendering of multiple extracted teeth, as viewed in Drishti. A. *Left to Right:* maxillary central incisor, maxillary lateral incisor, mandibular canine, maxillary first premolar, maxillary second premolar, mandibular first molar, maxillary second molar and mandibular third molar. B. *Left to Right*: Segmented enamel, dentine and pulp chamber.

Visual comparison of the 3D printed cylinders created using different slicing software revealed a lot of differences in both external and internal geometries. Figure 5.12 shows the reconstructed XMT datasets as well as 3D renderings of the outer mesh of each cylinder. From initial observations, it is clear that cylinders printed using Cura and Slic3r produced more aesthetic surfaces compared with Repetier and Matter Control, except for Matter Control cylinder printed in PLA. However, cylinders printed with Repetier and

Matter Control appear to have different finishes. From the XMT images, it appears Repetier extrudes more material as evident in the PLA cylinder as there appears to be no flat surface within the internal chamber. Both the TPU cylinders for Repetier and Matter Control have a wave striation on the external surface, suggesting again, an over extrusion of material.
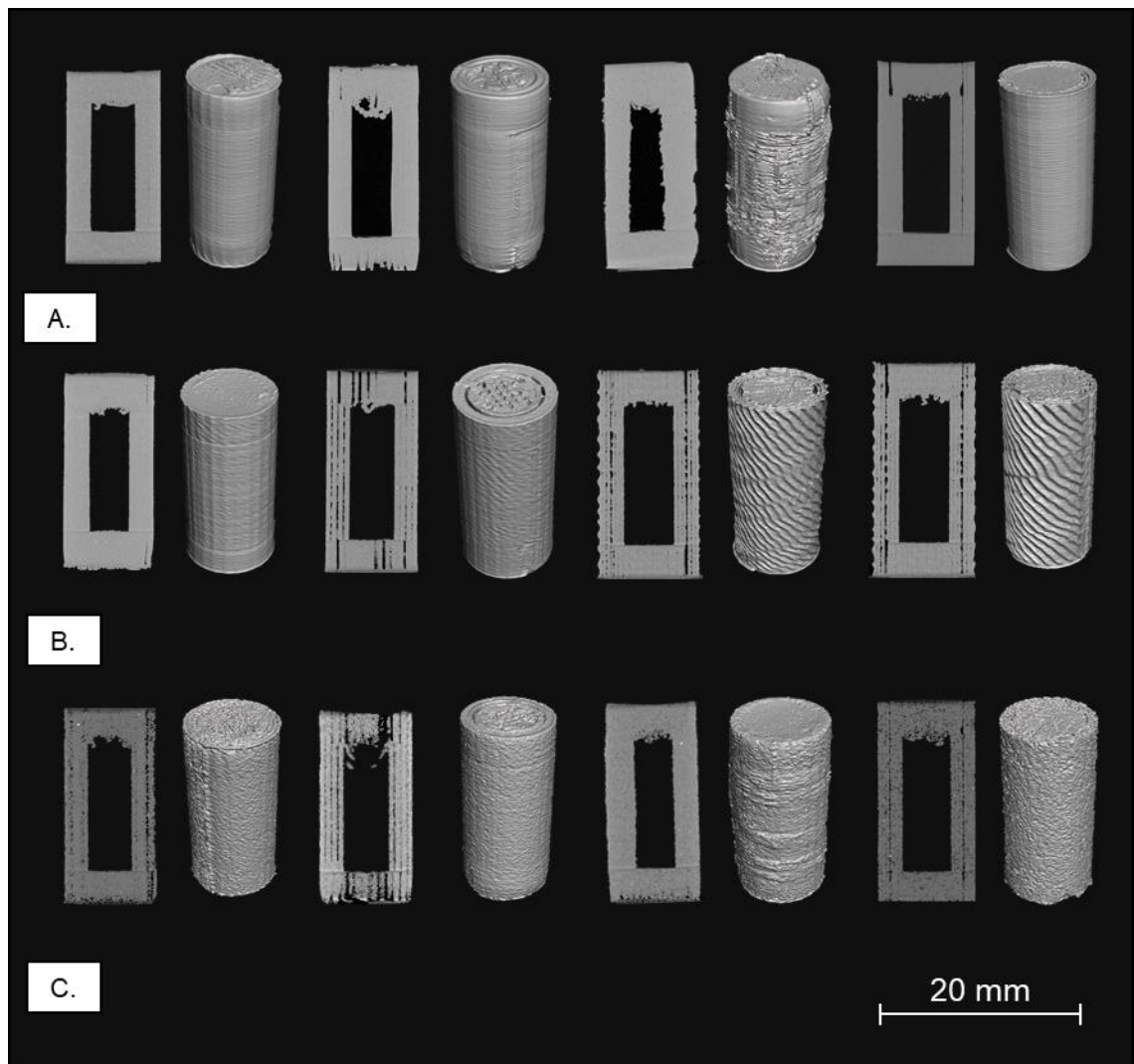
Figure 5.12: XMT image and 3D rendering of the printed test cylinders. *Left to Right*: Cura, Slic3r, Repetier and Matter Control. A. Cylinders printed in PLA. B. Cylinders printed in TPU. C. Cylinders printed in wood-PLA.

Table 5.3 is the morphometric analysis that was carried out on the reconstructed XMT images of the printed cylinders using ImageJ, and measurements were taken and then compared to the projected height, circumference and volume. The expected height

of the test cylinder was 20.00 mm; eight of the printed cylinders came within 3.0% of this, with the closest being the TPU cylinder printed using Matter Control with a height of 20.22 mm, which was 1.10% ($\pm$ 0.22) larger than the projected. The most significant difference from the projected was the wood-PLA print using Slic3r at 20.94 mm, a 4.70% ($\pm$ 0.03) increase. Overall, in terms of recreating the correct height, the material TPU was the most accurate, with Matter Control being most accurate slicing software, wood-PLA and Repetier were deemed to be less accurate due to the larger deviance from the projected height. Statistical analysis also suggests this, as Repetier was the most significantly different compared with the other slicing software, wood-PLA was also significantly different compared to the other materials.

When comparing the circumference of the cylinders, the projected circumference was 31.42 mm, similar to the height, none of the printed cylinders came within 3.0% of this. The closest was the wood-PLA using Slic3r and TPU using Matter Control at 33.18 mm, a 5.60% ($\pm$ 0.22) increase, the largest was PLA using Repetier at 37.89 mm, a 20.59% ($\pm$ 0.18) increase, this was evident from the XMT images (Figure 5.12). Overall, Cura was the most consistent and accurate in terms of recreating the circumference with all materials being produced at 33.68 mm a 7.19% increase, again the least accurate overall was Repetier. The statistical analysis supported this by revealing that cylinders produced using Repetier were the most significantly different. In contrast, there was no significant difference between the cylinders produced with Cura, suggesting Cura to be the most consistent.

Table 5.3: Morphometric differences between the printed test cylinders. Variations in height, circumference and volume were compared with the projected height, circumference and volume; 20.00 mm, 31.42 mm and 1.31 cm^3 respectively. $n = 8$.

Slicer Software	Material	Difference in Height (%)	Difference in Circumference (%)	Difference in Volume (%)
Cura	PLA	2.45 ($\pm$ 0.16)	7.19 ($\pm$ 0.15)	-12.21 ($\pm$ 0.13)
	TPU	1.40 ($\pm$ 0.05)	7.19 ($\pm$ 0.06)	-3.82 ($\pm$ 0.04)
	Wood-PLA	1.85 ($\pm$ 0.13)	7.19 ($\pm$ 0.11)	-9.92 ($\pm$ 0.10)
Slic3r	PLA	2.90 ($\pm$ 0.08)	7.19 ($\pm$ 0.10)	6.11 ($\pm$ 0.10)
	TPU	2.15 ($\pm$ 0.07)	8.59 ($\pm$ 0.08)	-5.34 ($\pm$ 0.08)
	Wood-PLA	4.70 ($\pm$ 0.03)	5.60 ($\pm$ 0.05)	2.47 ($\pm$ 0.03)
Repetier	PLA	4.25 ($\pm$ 0.24)	20.59 ($\pm$ 0.18)	18.32 ($\pm$ 0.24)
	TPU	3.55 ($\pm$ 0.18)	16.71 ($\pm$ 0.12)	13.74 ($\pm$ 0.09)
	Wood-PLA	4.10 ($\pm$ 0.14)	13.08 ($\pm$ 0.14)	10.69 ($\pm$ 0.10)
Matter Control	PLA	2.15 ($\pm$ 0.07)	8.59 ($\pm$ 0.06)	-5.34 ($\pm$ 0.08)
	TPU	1.10 ($\pm$ 0.22)	5.60 ($\pm$ 0.22)	-16.79 ($\pm$ 0.18)
	Wood-PLA	1.25 ($\pm$ 0.16)	7.13 ($\pm$ 0.15)	-12.21 ($\pm$ 0.09)

Table 5.3 also compares the differences in volume when compared to the projected (1.31 cm^3), wood-PLA produced by Slic3r had the closest volume at 1.34 cm^3 which was 2.47% ($\pm$ 0.03), Repetier with a PLA cylinder produced the furthest removed volume at 1.55 cm^3 an 18.32% ($\pm$ 0.24) increase. Moreover, this is also evident in the XMT images (Figure 5.12). Statistical analysis showed that Repetier, Matter Control and Cura were significantly different compared to the projected volume, whereas Slic3r produced cylinders were not, highlighting the accuracy Slic3r had in recreating the volume.

Figure 5.13 is the reconstructed XMT images of a mandibular first molar (Figure 5.8) printed using FFF, SLA and SLS methodologies and PLA, Anycubic 405 nm Rapid

Resin and Nylon PA 12 respectively. 3D renderings (Autodesk Meshmixer) of the printed

molars allow for a better examination of the external geometry of the different printing

techniques. In contrast, the XMT provides the analysis of the internal geometry.
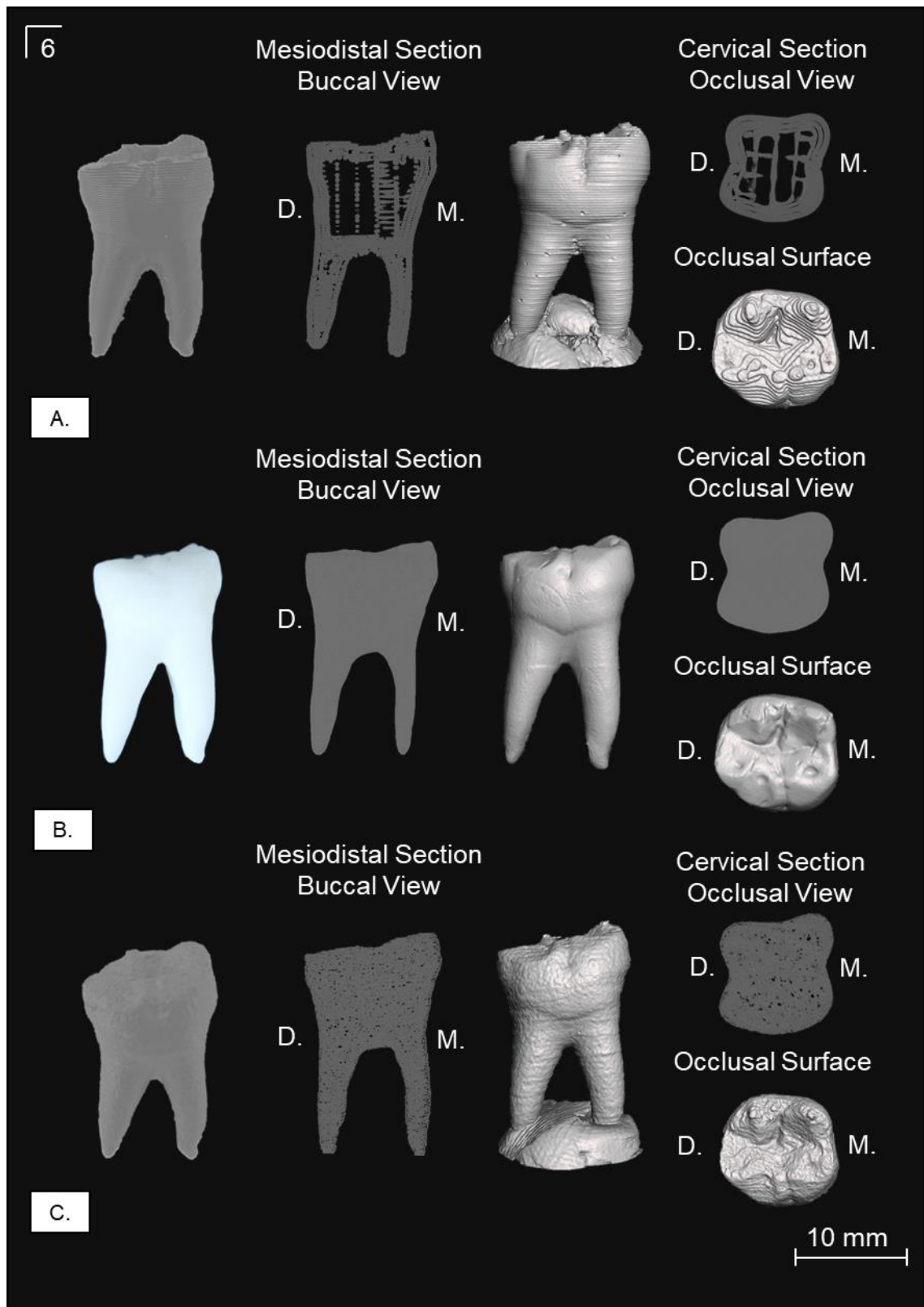
Figure 5.13: Mandibular first molar printed using FFF, SLA and SLS techniques. *Left to Right*: printed tooth, XMT of the printed tooth (buccal view), 3D rendering of the printed tooth (buccal view), XMT of the printed tooth (occlusal view) and 3D rendering of the printed tooth (occlusal view). A. FFF. B. SLA. C. SLS.

White light profilometry was carried out on an extracted molar (Figure 5.8) and the printed molars (Figure 5.13), trying to identify and analyse the topography of the occlusal surface and whether the different 3D printing technologies could replicate the topography of the extracted tooth. Figure 5.14 is a selection of heat maps produced on the mesiobuccal cusp with a 3.00 x 3.00 mm scan area, and the maps show the depth of the exposed dentine (where the enamel has eroded).
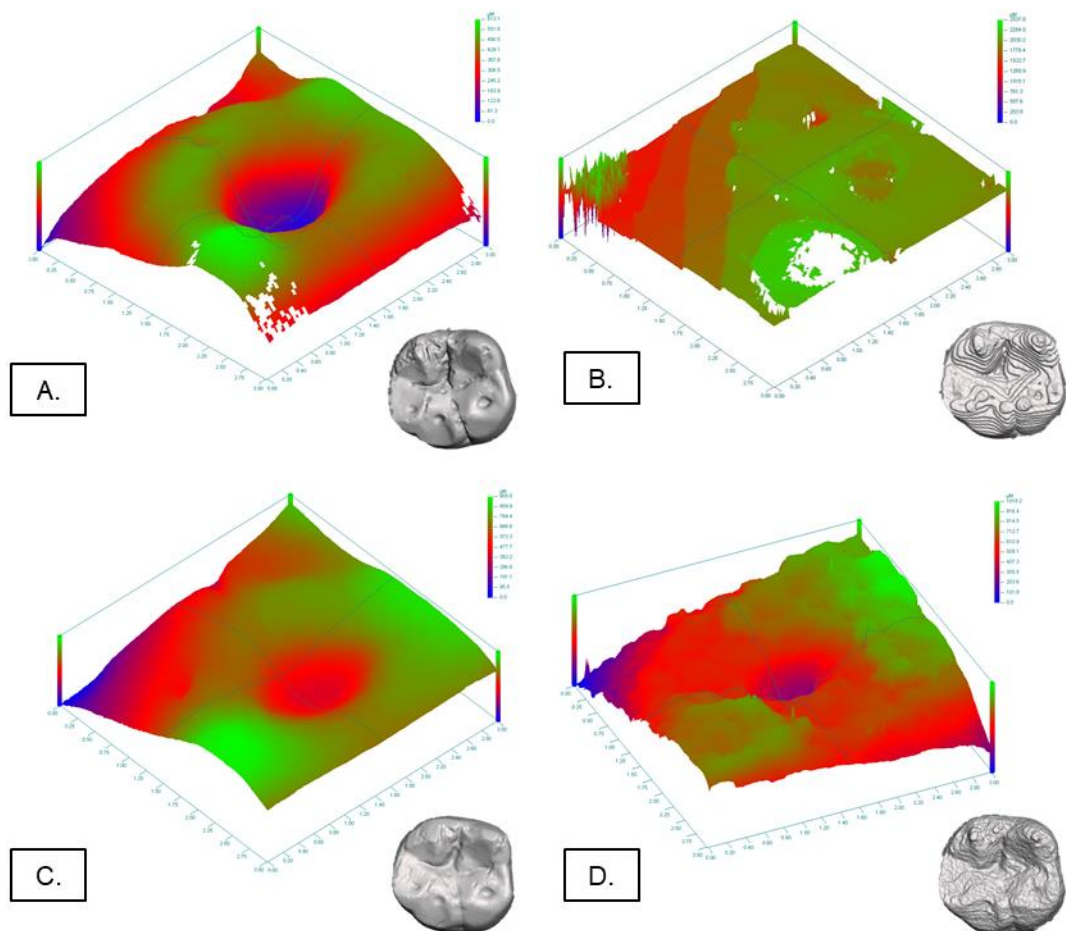
Figure 5.14: Heat map of the topography of the mesiobuccal cusp of printed teeth. A. Extracted. B. FFF. C. SLA. D. SLS.

To compare the heat maps, a line plot was generated (Figure 5.15) because, although the specimens were mounted and scanned in the same position each time, differences in geometries between printing technologies meant areas differed slightly between samples. Therefore, a line plot was taken from the middle of the mesiobuccal

cusp where the dentine was exposed for each specimen, highlighting the step sizes seen in the fabrication of the FFF molar and the uneven surface of the SLS molar. From the line plot, it can be seen that on the extracted molar the lowest depth recorded was 61.30 μm and a peak height of 551.80 μm, none of the printed molars matched the lowest depth, with the SLS molar being the closest at 122.60 μm. The position and length of the exposed dentine also differ between molars, extracted molar exposure begins at 0.40 mm and ends at 3.00 mm, whereas for FFF's exposure starts at 1.40 mm and ends at 2.00 mm, SLA's exposure at 0.80 mm to 2.60 mm, and SLS's exposure at 0.80 mm to 2.60 mm.
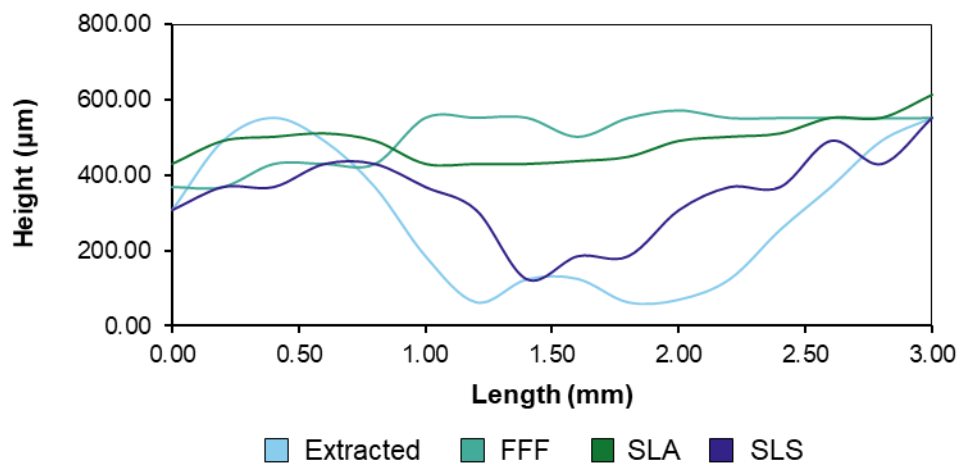
Figure 5.15: Line plot of the topography of the mesiobuccal cusp of printed teeth.

Figure 5.16 is the reconstructed XMT images, and 3D renderings of a mandibular first molar (Figure 4.5) printed using FFF, SLA and SLS methodologies and PLA, Anycubic 405 nm Rapid Resin and Nylon PA 12 respectively. These were printed to establish the presences of a pulp cavity; this is evident in the PLA model. However, the root canals are not well defined, in the SLA model there is a distinct lack of a cavity, except for a few voids in the canals, the SLS model has evidence of a cavity; moreover, this is filled with unsintered material and blocked root canals.

Figure 5.16: Mandibular first molar printed using FFF, SLA and SLS techniques. *Left to Right*: printed tooth, XMT of the printed tooth (buccal view), 3D rendering of the printed tooth (buccal view), XMT of the printed tooth (occlusal view) and 3D rendering of the printed tooth (occlusal view). A. FFF. B. SLA. C. SLS.

Table 5.4 shows the morphometric analysis carried out on the printed mandibular molars, looking in particular at differences in height and volumes compared to the extracted molar (Figure 4.5). The height of the extracted tooth was 21.65 mm, the FFF molar was the only printed tooth with the smallest height at 20.30 mm, a 6.21% ($\pm$ 2.34) decrease, SLA and SLS printed molars came out at 24.64 mm, a 13.83% ($\pm$ 0.67) increase and 24.82 mm, a 14.66% ($\pm$ 0.97) increase, respectively. Statistical analysis showed that SLA and SLS were significantly different, as they did not closely match the extracted tooth's height, whereas the FFF molar was not significantly different.

Volume differences between the printed and the extracted molars showed that none of the printed molars within 3.0% of the volume of the extracted tooth (1.21 cm^3), with FFF measuring 1.06 cm^3 a decrease of 12.40% ($\pm$ 4.78), SLA measuring 1.42 cm^3 an increase of 17.36% ($\pm$ 1.56) and SLS measuring 1.09 cm^3 a decrease of 9.92% ($\pm$ 4.14). SLA reported the only increase in volume, and from the XMT images (Figure 5.16) it is due to the filled pulp cavity, it also worth noting that in the case of the SLS print, the unsintered material was not taken into account and was not measured in the volume. Statistical analysis showed all the prints were statistically different from the extracted tooth, as all the prints' volumes were far from the originals.

Table 5.4: Morphometric differences between the printed teeth. Differences in height and volume were compared with the extracted tooth height and volume; 21.56 mm and 1.21 mm^3, respectively. *n* = 8.

3D Printing Technology	Difference in Height (%)	Differences in Volume (%)
FFF	-6.21 ($\pm$ 2.34)	-12.40 ($\pm$ 4.78)
SLA	13.83 ($\pm$ 0.67)	17.36 ($\pm$ 1.58)
SLS	14.66 ($\pm$ 0.97)	-9.92 ($\pm$ 4.14)

Results from the extrusion deposition modelling methodology produced one model using the Activa™ (Figure 5.17), the Cention N failed to form a solid shape after extrusion. The Activa™ maintained shape; however, the material took a long time to set, with the XMT showing different degrees of curing within the structure (as evident by the difference in greyscale), and evidence of step sizes on the external geometry. The roots of the model were lost due to movement before the model had fully set.
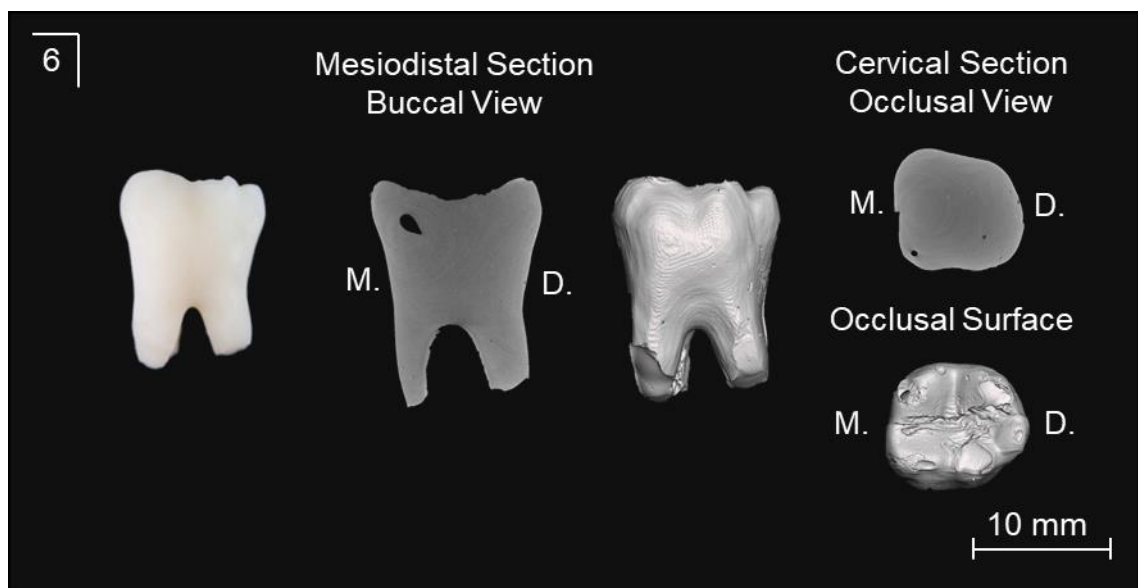
Figure 5.17: Mandibular first molar printed using extrusion deposition modelling. *Left to Right*: printed tooth, XMT of the printed tooth (buccal view), 3D rendering of the printed tooth (buccal view), XMT of the printed tooth (occlusal view) and 3D rendering of the printed tooth (occlusal view).

Figure 5.18 is a selection of multi-material prints that utilise the segmentation function (Section 5.2.2), by isolating individual structures and printing them separately. Figure 5.18.A shows a detachable model created using FFF techniques, with enamel printed in PLA, and the dentine and pulp printed in TPU, the pulp cavity was printed slightly smaller to allow fitting into the dentine model. Figure 5.18.B shows a detachable model created using SLA techniques with a Formlabs Form 2, using opaque white resin for the enamel, and transparent resin for the dentine. Due to the Form 2's advanced spot

size and resolution compared to the Anycubic, the pulp cavity was printed freely without any difficulties, allowing for a coloured hydrogel (see Appendix A) to be injected inside.
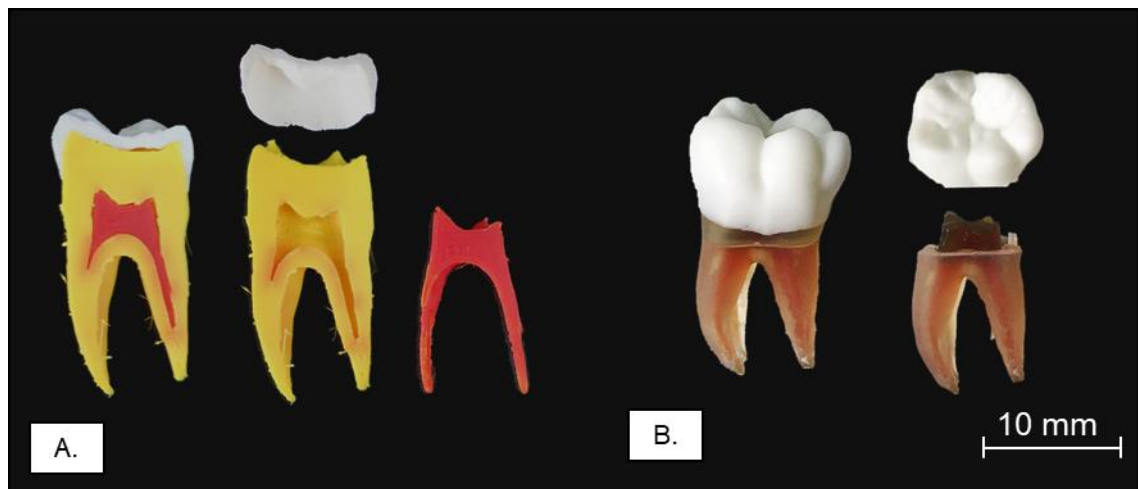
Figure 5.18: Multi-material prints of a mandibular first molar. A. FFF printed molar. B. SLA printed molar, with hydrogel pulp.

5.4 Discussion

5.4.1 CAD

The utilisation of the MuCAT2 scanner and its specific design (Section 3.1.1), meant the elimination of beam hardening and ring artefacts, creating 'clean' datasets suitable for segmentation and conversion. As previously stated in Section 3.3, multiple software was used in the design and manipulation of the reconstructed XMT datasets to give the desired outcome. Initially, files were exported from Tomview to Drishti (NC file), where the segmentation and thresholding of particular structures took place, allowing for individual meshes to be created for enamel and dentine, a useful tool when wanting to visualise (Figure 5.11.B), manipulate or print individual structures (Figure 5.18). The generation of the mesh was carried out via a plugin within the Drishti software, allowing for detailed parameter settings; however, mesh generation does not consider 3D volume, only external geometry.

Although these files are typically high-quality with similar resolution to that of the XMT scanner, problems do arise. A noted issue is a stepping artefact which occurs on a plane where slice stepping is exaggerated (Figure 5.19.A); however, this is easily overcome by either generating the mesh in the low-resolution mode in Drishti or by simplifying the mesh in Autodesk Meshmixer. Another issue that can occur during the reconstruction process is the misalignment of blocks during multi-block scanning (Section 3.1.2), this leads to a disjointed connection between the top and bottom of blocks of where the samples were scanned (Figure 5.19.B). Again, this is easily rectified by either simplifying the mesh or by redoing the reconstruction process and removing some overlapping slices. When scanning non-mineralised specimens, a common issue is that excess materials with similar voxel intensity values are captured within the mesh generation. An example in Figure 5.13, with both the FFF and SLS molars, have similar intensities to the mounting wax, meaning the wax appeared in the 3D rendering images, however, this issue is easily remedied in Autodesk Meshmixer, by removing any polygons that are not attached to the main mesh, or by using the sculpting tool, to smooth out affected surfaces.
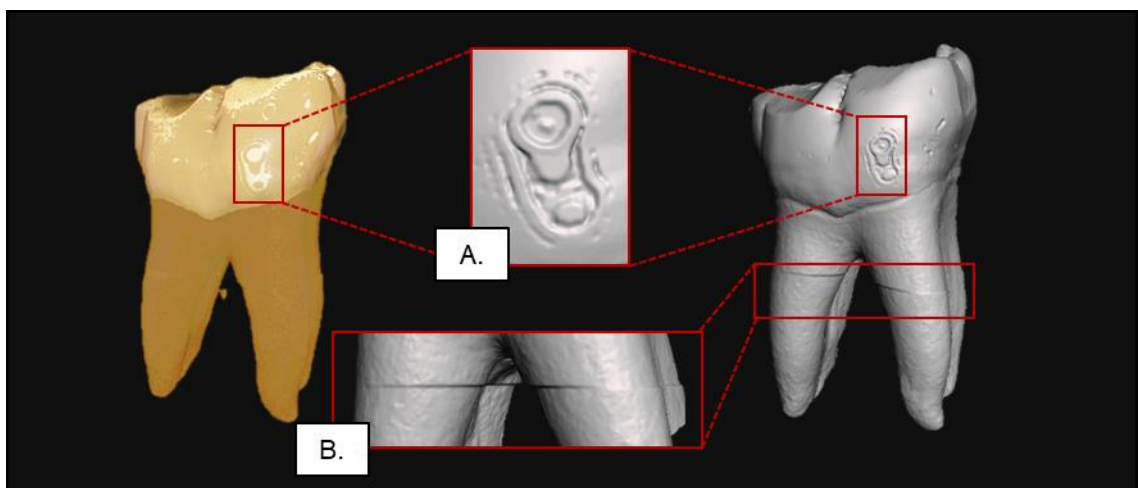
Figure 5.19: Evidence of artefacts within the mesh generation process. A. Exaggerated stepping size. B. Misalignment between blocks.

MeshLab was used to reduce and simplify the number of polygons present within the mesh (Figure 3.13). This process is effective in reducing the file size of a mesh and removing any duplicate edges or faces. This is an important step, especially when using the file in modelling and VR software, as the model runs smoother with higher frames per second (FPS) when the file size is smaller. Dependent on computer specifications, the process of simplification can take around 5-10 min.

Autodesk Meshmixer allows for the modification and manipulation of meshes and can be utilised to change the geometry to give the desired shape. This is a useful technique in creating clean models, removing any unwanted or excess material. It can also be useful in replacing missing material; if the material was lost during extraction, Autodesk Meshmixer can be used to create material and fill in a void. A useful tool present in Autodesk Meshmixer is the ability to smooth a mesh's geometry. This technique slightly increases the number of polygons present in the mesh in specific locations (as not to undo the reduction carried out in Meshlab), to give a more 'rounder' appearance (Figure 5.20). This process is useful when creating models for 3D printing, as it removes intricate detailing, giving the printer a more basic outline. The disadvantage however of this method is a vast of loss of resolution in the model; however, this is not a concern if the printer resolution is not high, or if the design being replicated does not contain any intricate details.
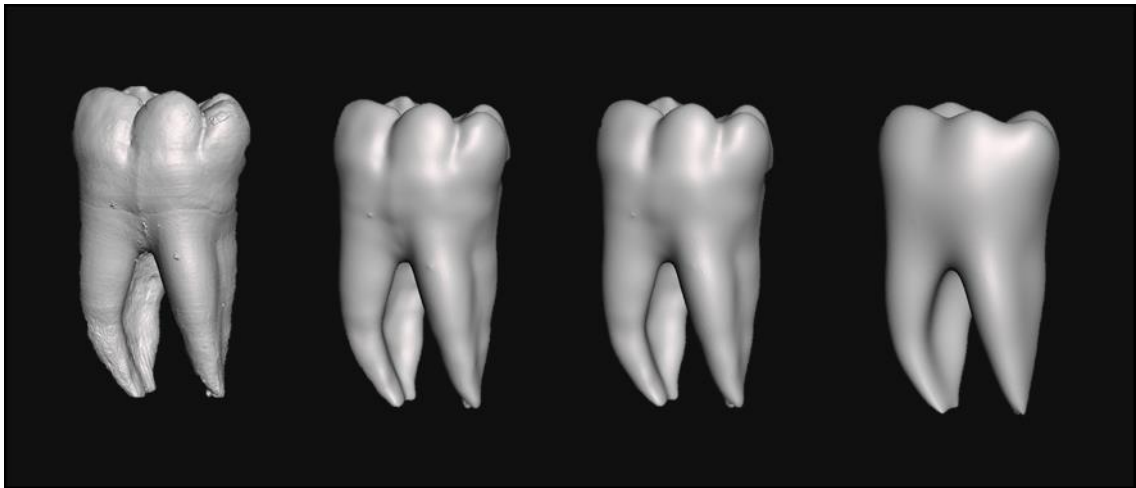
Figure 5.20: Smoothing of the mesh of a mandibular first molar. *Left to Right*: before smoothing, smoothing at 25%, smoothing at 50% and smoothing at 100%.

3D Builder was only used once meshes had been manipulated in Meshmixer when material was added, or geometry was moved or altered to give a different desired outcome (changing the direction of the pulp canal). 3D Builder analyses the mesh and detects any voids or overlapping polygons and repairs the mesh by filling in voids or deleting overlapping polygons. Generally, no visual changes occur, as the errors are typically too small to see, and repairing priority is to maintain shape.

5.4.2 CAM

Many studies have looked at the accuracy of 3D printed models, establishing differences in materials and technologies used (Salmi *et al.*, 2013; Bortolotto *et al.*, 2015). However, there is a distinct lack of literature regarding the type of slicing software used, especially when using FFF methodologies. It has been established that FFF produces the least accurate models, due to its manufacturing process of depositing material with such large step sizes, due to its low resolution. However, from this study, it can be concluded that the type of slicing software may also influence the accuracy outcome of the 3D printed models. In this study, four open-source software were evaluated, to see if the choice of slicing software affected the accuracy of prints at all, it is also worth noting (as mentioned before in Section 3.3.1) that only FFF slicing software was chosen to compare,

due to SLA and SLS software, at the moment are not currently open-source, and only company-specific software can be used with these types of printers.

From the XMT images (Figure 5.12), it was evident that the external geometry of the printed cylinders manufactured using Repetier, did not match that of the designed cylinder, morphometric analysis (Table 5.3) also proved this, as the main differences in height, circumference and volume came from the Repetier-produced cylinders. The PLA Repetier-printed cylinder shows evidence of over extrusion, where more material was deposited than necessary, the same can be said for the wood-PLA Repetier-printed cylinder. Striation patterns on the surface of the TPU cylinders printed with Repetier and Matter Control suggested an excess of infill, and due to the elastic nature of the material, voids appear within the internal geometry as the material is forced onto the external surface. Overall, on average Matter Control accurately matched the height with a 1.5% increase, and circumference with a 7.11% increase, Slic3r closely matched the volume with a 1.11% increase overall. However, in terms of finish and the least amount of post-processing, Cura and Slic3r appear to have matched shape more closely, compared to Repetier and Matter Control. From these results, there seems to be a trade-off between accuracy and aesthetics.

The differences in 3D printing methodology between FFF, SLA and SLS has been well documented. Salmi *et al.* (2013) assessed the accuracy, and described FFF as producing 'moderate' models and SLA and SLS as creating 'original' models, on a scale of 'original, moderate and worse'. Thomas & Claypole (2016) and Redwood *et al.* (2017) ordered the accuracy in technologies from FFF, SLA to SLS, with SLS being the most accurate, and best suited for manufacturing industrial parts, due to each technology's limitations on the resolution. However, it is estimated that on average, discrepancies between segmented anatomy and 3D printed models are typically of the order of an imaging voxel size, < 1.0 mm and < 3.0% with these errors usually classed as clinically

negligible (Ibrahim *et al.*, 2009; Taft *et al.*, 2011). Yet, in this study, the margin of error was seen to be considerably higher than that of 3.0%, with relative differences in the height of 6.21%, 13.83% and 14.66% for FFF, SLA and SLS respectively (Table 5.4), the differences in error, however, could be due to the small voxel size and the small nature of the 3D printed teeth and its intricate structure, whereas, in previous studies, the accuracy has been measured on larger samples such as that of skulls, and subsequently scanned at lower resolution (Fasel *et al.*, 2013; Huotilainen *et al.*, 2014). Huotilainen *et al.* (2014) summarised that a model of the same design could vary drastically depending on the DICOM to STL conversion as well as the technical parameters used.

Moreover, as well as the difference in height, the topography also changed drastically depending on technology, giving each model a different finish. Figure 5.14 and Figure 5.15 showed clear evidence of step size with the FFF models, whereas the topography was smoother and more rounded with the SLA models. Although the SLS more closely matched the accuracy of the mesiobuccal cusp, there was a clear rougher surface present. Again, suggesting a trade-off between efficiency and aesthetics.

In terms of internal geometry, there was no significant difference between the technologies, but a considerable difference between the extracted molar and the 3D printer molars (Table 5.4). Both FFF and SLS had the presence of a pulp cavity within the models, with no cavity present in the SLA models; however, both FFF and SLS models had no root canals, and in particular, for the SLS model meant the material was trapped inside. This may explain as to why there was no cavity within the SLA model, as the root canals may be too small (below the resolution of the printer), to allow the appropriate evacuation of the excess material. This was apparent, with the model seen in Figure 5.18.B, this model was printed using the Form 2, a printer with a higher resolution and spot size, compared to the Anycubic printer (as mentioned in Section 3.3.1) which printed models in Figure 5.13 and Figure 5.16, meaning a pulp cavity was present. Due

to the absence of a pulp cavity, the SLS model measured a higher relative difference in volume at 17.36%, whereas, although the FFF and the SLS models contained pulp cavities, the models contained voids throughout the structure meaning relative differences in volumes were -12.40% and -9.92% respectively. Despite the inaccuracy within the model produced in Figure 5.17, the varying degrees of cured material within the model could offer a possible way of replicating different degrees of mineralisation as seen in dentine, with primary, secondary and tertiary dentine as seen in Figure 5.10. However, greater control over the curing rate of resin would be required (as the material could cure over time) as well as a greater resolution; this could be achieved by using SLA and DLP techniques; however, the composite is too viscous to be used in these techniques (viscosity of materials is discussed in more depth in Section 7.4.1). The lack of pulp and canal system would make this unsuitable for endodontic training but could still be used as a prosthodontic teaching aid, although out of the scope of this study, could, however, form the basis of future work.

5.5   Conclusions

In conclusion, this study has shown an effective open-source method of converting XMT datasets into 3D models, which in turn could be used for 3D printing or visualisation (VR). In terms of the accuracy of 3D printing technology, three factors contribute to this; how DICOM images are converted to STL, the choice of slicing software as well as parameters used and the choice of methodology (FFF, SLA or SLS). The results here help to create an understanding and raise awareness in the decisions made when 3D printing from scanned specimens.

Chapter 6

Approaches to Printing Novel Materials

This chapter investigates the different methods in which novel 3D printing materials are manufactured and processed as well as exploring the possibility of developing materials to create mimetic artificial teeth. With the focus on FFF, SLA and SLS technologies, considering the different materials used in these methodologies and comparing the forces required to cut each one (as shown in Section 3.5.3).

6.1 Introduction

With an increased demand for product complexity and multi-functionality, many new materials have been investigated for 3D printing. Such materials include nanomaterials, functional materials, biomaterials and smart materials (Zhang *et al.*, 2015; Lee *et al.*, 2017). However, there is limited literature on the recent development of novel materials and applications in 3D printing (Lee *et al.*, 2017).

As discussed in Section 2.4.5, there are seven different 3D printing technologies as defined by the ISO/ASTM 52900 Standard; these were categorised based on the method of layer fabrication (Chua *et al.*, 1998; ASTM International, 2015; Lee *et al.*, 2017). With this understanding, 3D printing can be considered as a relationship between the material mass (m) and energy (W), which results in a single layer with a total power variation:

$$\delta(mW) = m\delta W + W\delta m$$

Equation 6.1

Where: *m* is the raw material mass.

W is the energy (Lee *et al.*, 2017).

Equation 6.1 represents two terms in which 3D printing technologies are categorised; the first term shows a 3D printing process in which a constant mass is bonded selectively by variable energy (δW) controlled by the material mass. Material extrusion and material jetting are examples of this process (Lee *et al.*, 2017). The second term represents a process where layer formation controls a variable mass (δm) acted on by fixed energy; this categorises powder bed fusion, binder jetting, sheet lamination and vat photopolymerisation. When both terms exist, the process is direct energy deposition, in which both energy and material mass are variable when fabricating a single layer (Lee *et al.*, 2017; Redwood *et al.*, 2017).

Material extrusion, as mentioned in Section 2.4.5.1, is the process of pushing material through a nozzle. At the same time, constant pressure is applied, the extruded material deposits at a continuous speed and solidifies once the material has been ejected. The following material must bind with previous material so that a solid part can form and remain in the structure throughout the printing process (Thomas & Claypole, 2016; Lee *et al.*, 2017; Redwood *et al.*, 2017).

Typically, materials for material extrusion printing are thermoplastic, due to the requirement of the plastic needed to be heated past its glass transition state, to be pushed through a nozzle (Thomas & Claypole, 2016). However, base thermoplastic has limited properties and mechanical strength; therefore, many commercial materials have been developed as a mixture of thermoplastic and filler material such as wood-PLA (used in

Chapter 5), a 30% mixture of wood pulp and PLA, conductive filament, a combination of metal particles such as copper and tin with PLA, and carbon fibre filament, a PET-based material with 20% carbon fibres (Zhang *et al.*, 2015; Redwood *et al.*, 2017). Moreover, recent studies have looked at manufacturing biocompatible materials, Senatov *et al.* (2016) and Corcione *et al.* (2017) both developed HAp-PLA composite materials for 3D printing for use in tissue engineering and creating porous scaffold suitable for bone grafts. Both studies found an increase in mechanical properties via compressive strength without a negative effect on the rheological performance.

Vat photopolymerisation is the process in which photocurable resins are exposed to a laser or UV light and go through a chemical reaction to become solid. The chemical reaction is called photopolymerisation and involves many chemical compounds such as photoinitiators, additives and reactive monomer/oligomers (Figure 6.1) (Eng *et al.*, 2017b; Lee *et al.*, 2017). Typically, photopolymers used in commercial systems are curable in the UV range (405 nm) and involves linking small monomers into chain-like polymers. A catalyst (i.e. photoinitiator) is usually required for the reaction to take place at a reasonable rate. The polymers must be sufficiently cross-linked so that the polymerised molecules do not re-dissolve into the liquid monomers and possess enough strength to remain structurally sound, this is an important factor within the clinical setting with the use of methacrylate monomers in dental restorative materials (Ngo, 2010; Lee *et al.*, 2017; Redwood *et al.*, 2017).
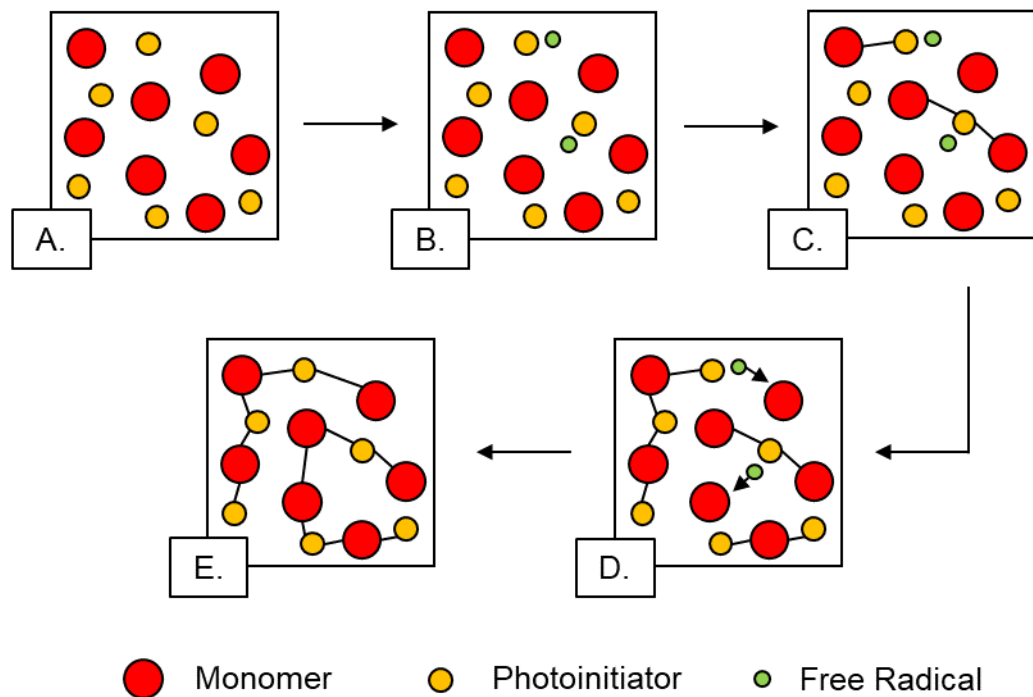
Figure 6.1: Mechanism of free radical photopolymerisation. A. Monomer and photoinitiator before exposure. B. Photoinitiator excitation and free radical generation, after exposure. C. Chain initiation. D. Chain propagation. E. Chain Termination. Adapted from Lee *et al.* (2017).

Certain studies have found that parts produced via vat photopolymerisation tend to have much lower mechanical properties compared to parts fabricated through traditional methods such as formative and subtractive manufacturing. The thermoset nature of parts printed this way typically has a high cross-link density, which results in low elongation with brittle fracture (Salmoria *et al.*, 2005; Eng *et al.*, 2017b). Therefore, an enhancement to mechanical properties has been explored, with commercial products such as ceramic resin, a photopolymer with silica particles added (Formlabs Inc., USA). Moreover, this has been a keen interest within the literature with fillers such as carbon nanotubes, graphene, clay and nanocellulose crystals have been added to photopolymer resin to enhance its mechanical properties (Salmoria *et al.*, 2005; Kumar *et al.*, 2012; Eng *et al.*, 2017a; Eng *et al.*, 2017b; Manapat *et al.*, 2017). From the literature, in general, the addition of fillers increases the stiffness of printed parts, as the $\bar{E}$ increases by $\approx 60\%$ (Eng *et al.*, 2017b). However, it has been noted that as elongation decreases with the addition

of filler and the tensile strength remain relatively similar, this results in a printed part with lower mechanical properties. This is most likely due to the random orientation of the fillers within the 3D printed part, reinforcing the part isotropically over the planes perpendicular to the build direction (Eng *et al.*, 2017a; Eng *et al.*, 2017b).

Powder bed fusion utilises a thermal source such as a laser is used to induce partial or full fusion between powder particles, followed by a roller or blade coater to add and smooth another powder layer. The binding mechanisms of powder bed fusion process are mainly sintering and melting. The main difference is that sintering is considered as a partial melting process while melting is believed to be a full melting process. In solid-state sintering, the particles fuse at the surface only resulting in inherent porosity, whereas, in liquid-state melting, all particles fully melt and fuse that gives a fully dense part with almost zero porosity (Lee *et al.*, 2017; Redwood *et al.*, 2017).

Typically, SLS is used to print powders of metal, nylon or ceramic materials, with the benefit of producing a multi-material printed part (Thomas & Claypole, 2016). By alternating layers with different materials, composite parts can be created producing novel materials. Commercial products include glass-filled PA, carbon fibre-filled PA and aluminium-filled PA (Goh *et al.*, 2018). Within the literature, there is a consensus that although adding reinforcements leads to enhanced tensile modulus, however, some issues of the weak interface due to poor adhesion and voids are observed (Goodridge *et al.*, 2011; Salazar *et al.*, 2014; Arai *et al.*, 2017). Arai *et al.* (2017) investigated the poor adhesions and voids and concluded that there was poor dispersion of the fibres in the powder feedstock, leading to a higher internal porosity. It was suggested that by increasing the laser intensity it would improve surface adhesion with the fibres; however, this led to a degradation in the mechanical properties.

This study aims to experiment with novel composite materials using different 3D printing technologies to identify the most suitable technology as well as starting material.

6.2 Materials and Methods

6.2.1 FFF Printing

As shown in Section 3.3.1, all FFF printing was carried out using a Wanhao Duplicator i3 and Cura as the slicing software.

6.2.1.1 HAp-Polymer Filament

HAp-polymer filament was manufactured similar to that seen in Senatov *et al.* (2016) and Corcione *et al.* (2017), using a solvent method outlined in Russias *et al.* (2006).

Two HAp-polymer filaments were created using PLA and ABS pellets (OmniDynamics Ltd., UK), with varying loadings of HAp (5, 10, 15%). Polymer pellets were dissolved in 100 ml of 1.0 mol methylene chloride (Merck, Germany) at room temperature while being continuously mixed using a magnetic stirrer; complete dissolution took around 2 h. Synthetic HAp powder (Capital® 98.8% purity, Plasma Biotal Ltd., UK) was added to the dissolved polymer and continuously mixed for 2 h to create a homogeneous slurry. The 'slurry' was then subsequently cast into multiple cylindrical acrylic moulds (10.00 x 100.00 mm) and dried within a vacuum oven for 48 h at 37°C, to remove all traces of the solvent used. The dried composite cylinders were then cut into smaller pieces (≈ 5.00 x 5.00 x 5.00 mm), using a diamond wheel cutter (Accutom-5) and fed through a filament extruder (Noztek Pro Filament Extruder, NoztekLtd., UK) set at a temperature of 170°C and 190°C for PLA and ABS respectively. In total, 2.00 m (ø 1.75 mm) of filament was created for each composition and stored in a container with silica gel, to ensure no moisture uptake.

Cylinders (10.00 x 5.00 mm) were printed using the settings shown in Table 5.1, with the composites made from ABS printed at a higher temperature 210-220°C, compared with the PLA. Eight of each material were printed for further mechanical testing.

6.2.1.2 Chalk-Polymer Filament

The commercially available composite material was used as a comparison to the filament developments using the filament extruder, LayBrick sandstone filament (Lay-Filaments by Kai-Parthy, Germany) was chosen. Despite being called sandstone filament, the material comprises of chalk and PLA, with 'sandstone' describing the aesthetics and finish of the material. The filament was printed using the same settings as previous PLA filaments, creating cylinders of the same specifications as shown in Section 6.2.1.1.

6.2.1.3 Dental Composite

As previously mentioned in Section 5.4.2, the dental composite was too viscous to be printed using traditional means of SLA or DLP; therefore, FFF methods were used. Using the same set-up and settings used in Section 3.3.1 and 5.2.3.2, cylinders were printed using Activa[TM] BioActive-Restorative[TM] to the same dimensions. Throughout the experiment, the uncured composite was kept in UV reflective containers to prevent polymerisation before extrusion. Activa[TM] is a composite resin containing a fluoro-alumino-silicate ionomer glass (Tiskaya *et al.*, 2019).

6.2.2 SLA Printing

As shown in Section 3.3.1, SLA and DLP printing were carried out using a Form 2 or an Anycubic Photon, utilising their slicing software (Preform and Anycubic Photon Slicer).

6.2.2.1 HAp-Polymer Resin

HAp powder was added to a photopolymer resin (Anycubic 405 nm Rapid Resin, Anycubic, China), the resin itself a mixture of acrylate oligomer (17%), acrylate monomer (40%), methacrylate monomer (40%) and a photoinitiator (3%). The powder was added to the resin at different weight percentages (5, 10, 15%), the composition was then mechanically mixed for 24 h at 31°C to allow for complete dispersion. The mixture was placed within an opaque container to ensure no curing took place before printing and stored in shaking incubator at 31°C, to ensure no sedimentation of the filler material.

The composite material was deposited inside the Anycubic Photon; it was noted that previous curing times (Table 5.2) were not enough to cure the layers. Therefore, curing time was increased to 30 s. Again, cylinders of set sizes were printed, with a layer height of 0.05 mm, taking around 2 h to print, the cylinders were then washed in 90% ethanol and cured for a further 30 min (as outlined in Section 5.2.4).

6.2.2.2 Ceramic Resin

Similar to the FFF materials, SLA includes a range of composite materials, therefore, to act as a comparison to the developed composite, Formlabs Ceramic Resin (Formlabs Inc., USA) was chosen and printed using the Form 2 printer. Cylinders of set sizes were printed using settings similar to Formlabs White Resin (Table 5.2), and the same post-curing procedure was carried out (Section 5.2.4).

6.2.2.3 Dental Resin

Formlabs offer dental-based materials as part of their commercial composites for SLA printings; these materials were developed for the use of surgical guides, castable wax and dental models. Formlabs Surgical Resin (Formlabs Inc., USA) was chosen as this material is designed to be drilled and cut with dental handpieces; therefore, may offer

haptic feedback similar to that of real teeth. This material was printed using the same settings as Formlabs Transparent Resin (Table 5.2) with the same post-curing procedure (Section 5.2.4).

6.2.3 SLS Printing

As previously mentioned in Section 3.3.1, printed cylinders were outsourced via 3D Hubs, and printed using PA filled with glass particles (PA-GF, Materialise NV, Belgium). Although most of the parameters of the SLS printed models were unknown, a layer height of 0.05 mm was selected.

6.2.4 X-Ray Diffraction

XRD was used on the developed materials only, to ensure the presence of HAp, and that it was not lost during the printing process. XRD was carried out as outlined in Section 3.6.3.

6.2.5 Microhardness

Cylinders from all materials (commercial and developed) were cut into 2.00 mm thick discs using a diamond wheel cutter (Accutom-5) and polished using silicon carbide paper and metallurgic polisher (Kent 4, as outlined in Section 3.5.1). Microhardness measurements were carried out using a Buehler Micromet-4 (Section 3.5.1), with eight indentations made on each sample in different locations, the H_V measurements were converted to MPa or GPa (where appropriate) as seen in Equation 3.5.

6.2.6 Elastic Modulus

$\bar{E}$ was measured using the compressive method (Section 3.5.2) on the different composite cylinders utilising an Instron 5567 property testing machine.

6.2.7   Force Cutting

Using the same protocol and set-up as shown in Section 3.5.3, cylinders were mounted to the 3-axis load cell, and each sample was cut eight times using a cylindrical diamond bur (111-012M) with a high-speed handpiece (TE-95 BC Alegra), each cut was 1.00 mm deep and at a set rate of 0.1 mm/s.

6.2.8   Optical Light Microscopy

After cutting using the automatic stage set-up, the burs used to cut the samples were examined under light microscopy using an Apex Scholar microscope, as outlined in Section 3.4.3.

6.3   Results

XRD was carried out to confirm the presence of HAp in the developed composites, and from the HAp reference (Figure 6.2), HAp is identified by sharp diffraction peaks at 26, 31.8, 32.2 and 32.9°. The polymer spectra showed no crystalline structure, meaning the polymer is amorphous, making it easier to identify the presence of HAp; this was more apparent as the wt. % increased, the HAp-related peaks became sharper.
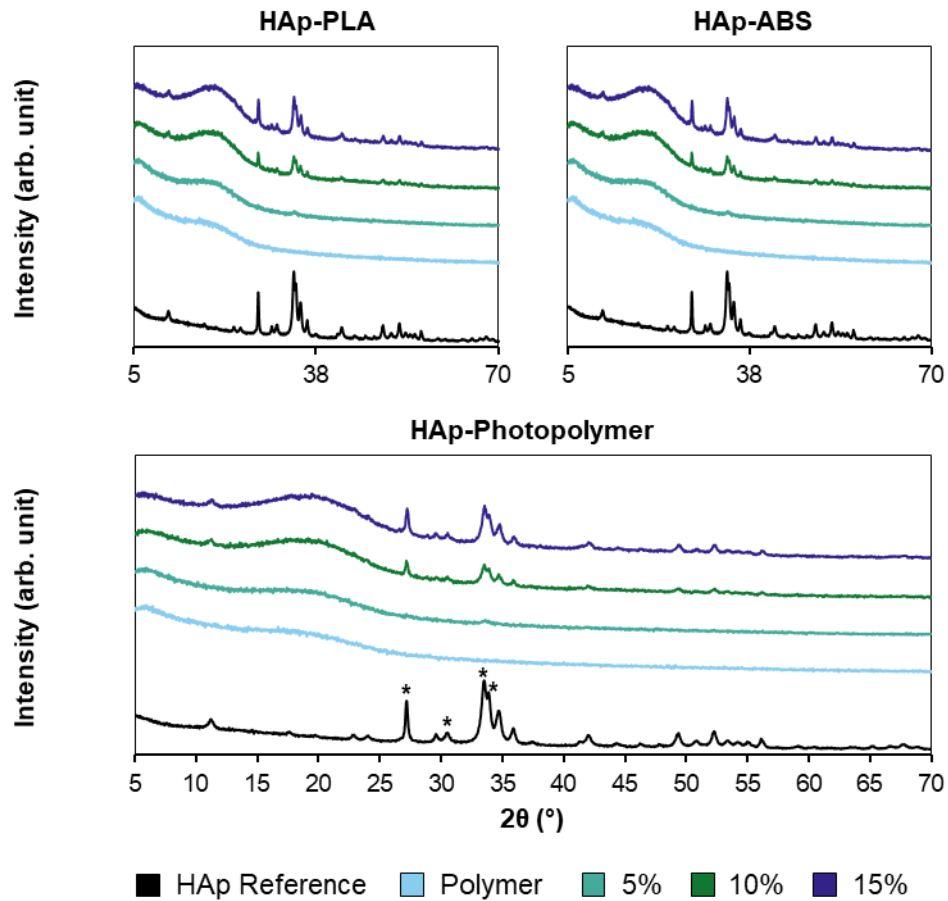
Figure 6.2: XRD spectra for the developed composite materials. (* denotes the identifiable HAp peaks seen on the HAp-Photopolymer spectra [26, 31.8, 32.2 and 32.9°]).

Figure 6.3 shows the mean hardness values and SD for all composite materials, with the highest recorded hardness from Activa[TM], 1578.14 MPa ($\pm$ 21.47) and the photopolymer recording the lowest at 79.89 MPa ($\pm$ 10.84). In terms of the developed composite materials, 15 wt. % photopolymer was the hardest material at 397.40 MPa ($\pm$ 61.58), with the photopolymer with no added filler the least hard material. A trend can be seen in the developed composite materials, at wt. % increases, the mean hardness also increases. Statistical analysis confirms significant differences in the materials' hardness. The hardness of the HAp-PLA increases by 76.27%, from 0 to 15 wt. %, HAp-ABS and HAp-photopolymer see a 26.27% and 397.43% increase, respectively. For the commercial materials, Activa[TM] was the hardest material (1578.14 MPa $\pm$ 21.47), with the LayBrick Sandstone 187.36 MPa ($\pm$ 15.14) recording the lowest hardness value. All

the commercial materials had statistically different hardness values. Compared to the developed materials, the commercial materials were not significantly different except for the Activa[TM], as this was significantly harder compared to the 15 wt. % HAp-photopolymer.
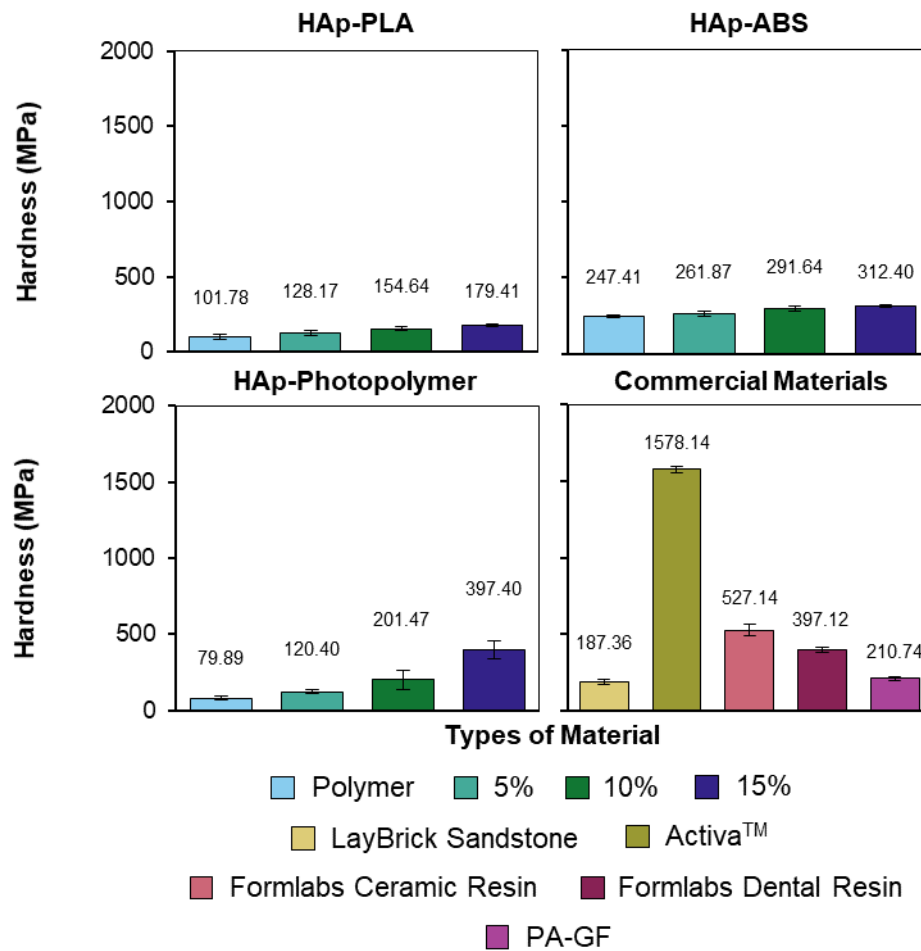
Figure 6.3: Mean hardness values for the composite materials. Error bars presented as SD of the sample, $n = 8$.

Ē (Figure 6.4) was measured for all developed and commercial composites, with Activa[TM] recording the highest Ē 6214.21 MPa ($\pm$ 184.47), and the photopolymer measuring the lowest, 862.47 MPa ($\pm$ 18.07). Similar to the results seen from the hardness measurements (Figure 6.3), in the developed composites, as wt. % increases, Ē also increases, with an increase from 0 to 15 wt. %, a rise of 26.76%, 26.61% and 108.97% for HAp-PLA, HAp-ABS and HAp-photopolymer respectively. For the commercially

available materials, Formlabs Dental Resin had the highest $\bar{E}$, with LayBrick Sandstone recording the smallest $\bar{E}$, 2069.84 MPa ($\pm$ 124.05). Statistical analysis showed an increase in wt. % as significantly different; however, the materials were not statistically different from each other, for the exception of Formlabs Dental Resin.
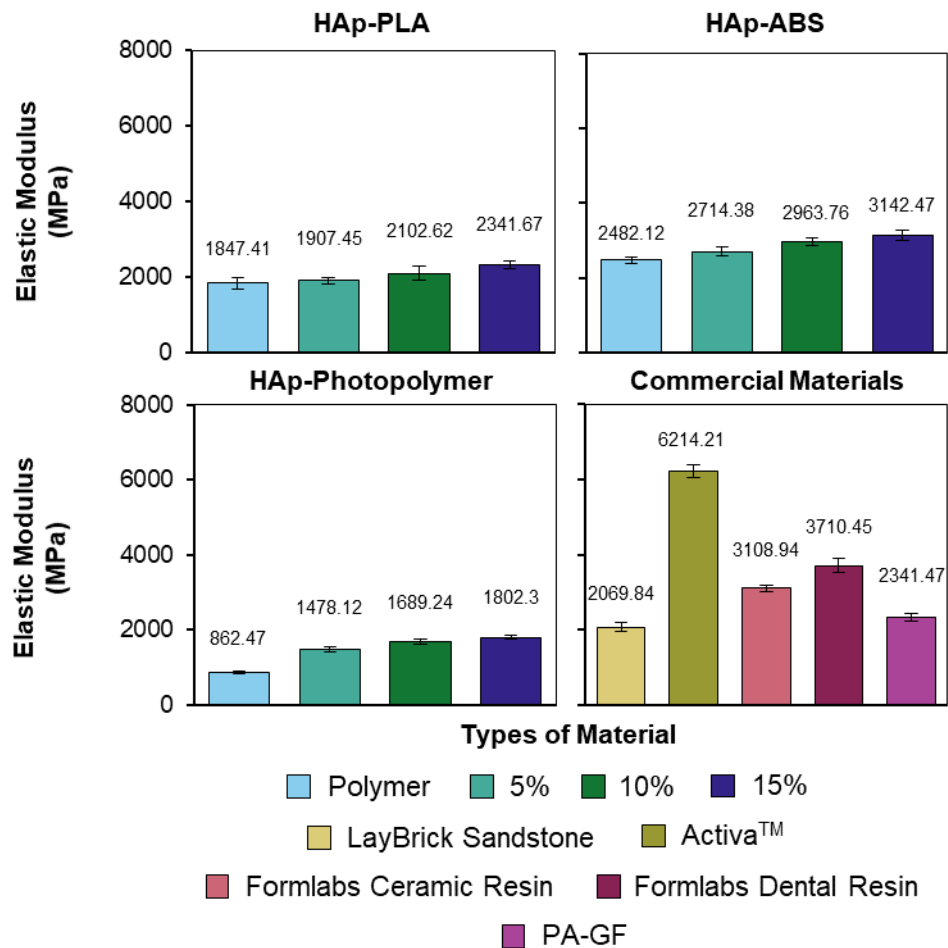
Figure 6.4: Mean elastic modulus for the composite materials. Error bars presented as SD of the sample, $n = 8$.

Results from the force cutting for the FFF printed materials (Figure 6.5), both developed and commercial were inconclusive; this was due to the material binding to the diamond bur used, preventing the bur from cutting further material. This prevention eventually led to the snapping of the bur; this typically occurred approximately 0.2-0.4 mm into the material, meaning not enough force data were recorded for analysis. However, for the dental composite, the Activa™ was not binding to the material. Still,

the bur failed to cut the material, with, again the bur snapping upon contact with the cylinder. Nevertheless, the SLA and SLS printed cylinders were successfully subjected to the force cutting, with the photopolymer measuring the largest required force, 1.13 N ($\pm$ 0.03), with PA-GF requiring the lowest, 0.21 N ($\pm$ 0.09). A trend was seen in the developed composites, as wt. % increased, the mean required force to cut, decreased, from the photopolymer to the 15 wt. % HAp-photopolymer a 53.98% decrease was recorded. Statistical analysis showed the composite materials were not statistically different when compared to each other, except the photopolymer and the PA-GF, which were the highest and lowest recorded forces respectively, the remaining materials had statistically similar forces.
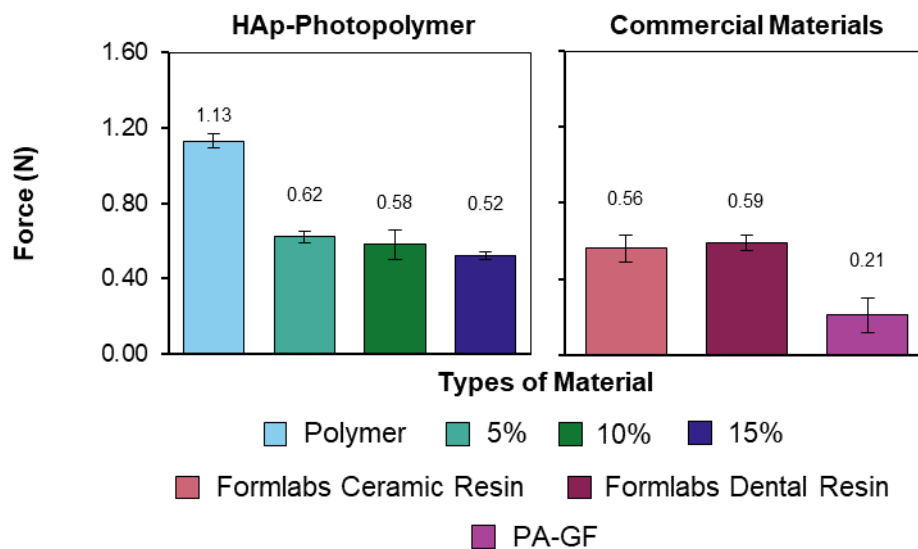
Figure 6.5: Mean force to cut photopolymer composites. Error bars presented as SD of the sample, $n = 8$.

Similar to what was seen in Figure 4.24, light microscopy was conducted on the burs before and after cutting the composite materials, to determine if particulates were left after cutting (Figure 6.6 and Figure 6.7). As mentioned previously, the composite materials printed using FFF techniques produced inconclusive force data, this was due to the material wrapping around the diamond bur, as seen in Figure 6.6.A. Figure 6.6.B shows the diamond bur after cutting the 15 wt. % HAp-photopolymer, and shows little

residual material attached to the surface after cutting, this was the same for all the wt. %

photopolymers.
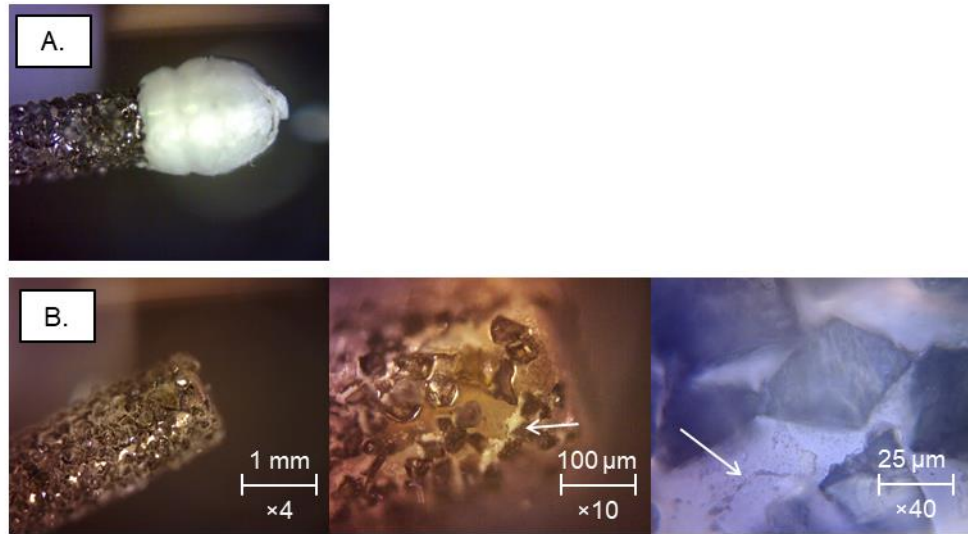
Figure 6.6: Light microscopy of a diamond bur under different magnifications. A. Diamond bur after cutting HAp-PLA filament. B. Diamond bur after cutting the 15 wt. % HAp photopolymer resin. Evidence of residual material is highlighted with arrows. Images in each row were taken at the same scale and magnification as the image at the bottom of the corresponding column (B).

Figure 6.7 is the light microscopy of the diamond burs after cutting the commercial composite material, excluding the LayBrick Sandstone, as the bur had a similar appearance of the HAp-PLA filament (Figure 6.6.A). From the images, it was established that all the composite materials appeared to leave residual material on the bur after cutting, with the PA-GF (Figure 6.7.C) leaving the most residual material.
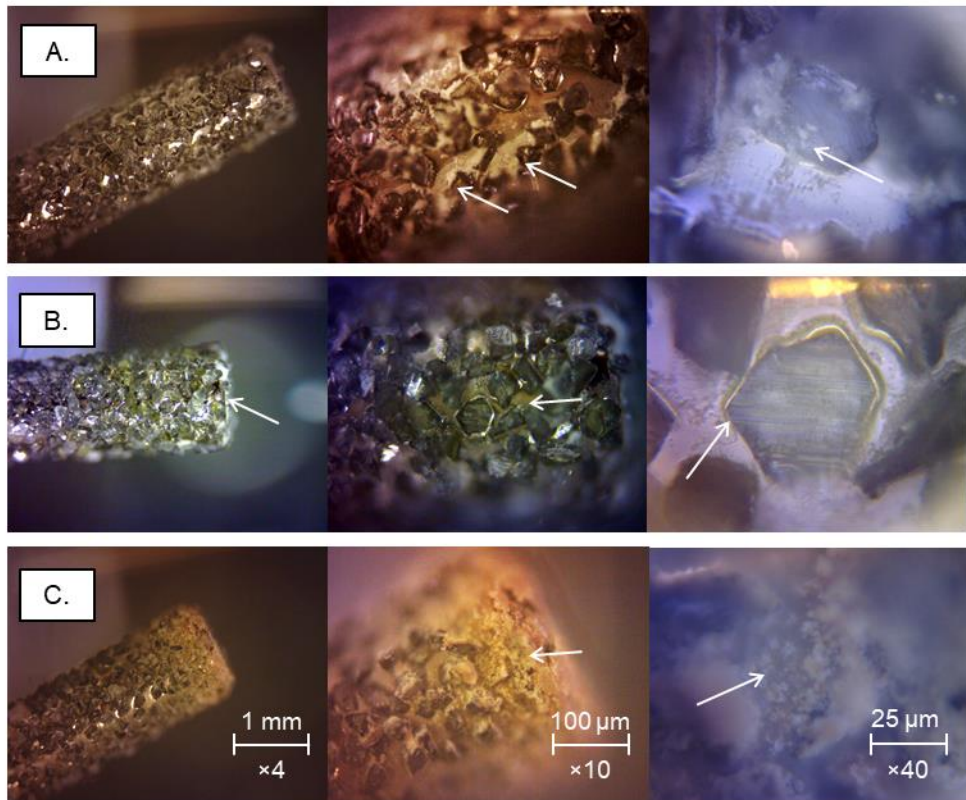
Figure 6.7: Light microscopy of a diamond bur under different magnifications. A. Diamond bur after cutting the Formlabs Ceramic Resin. B. Diamond bur after cutting the Formlabs Dental Resin. C. Diamond but after cutting the PA-GF. Evidence of residual material is highlighted with arrows. Images in each row were taken at the same scale and magnification as the image at the bottom of the corresponding column (C).

6.4   Discussion

6.4.1   Fused Filament Fabrication

As established in Section 5.3, the composite materials were printed using Cura, due to its higher dimensional accuracy compared to other slicing software; the cylinders were printed to an accuracy of ± 0.05 mm for all materials.

Overall, it was established that ABS, had the higher hardness and Ē measurements suggesting the material is harder and less elastic compared to PLA and the LayBrick Sandstone. These findings were similar to that of the specifications of the materials provided by the manufacturer as well as established in previous literature, 80-120 MPa

and 220-280 MPa for hardness, and Ē being 1800-2200 MPa and 1800-2800 MPa for PLA and ABS respectively (Thomas & Claypole, 2016; Redwood *et al.*, 2017). For the Laybrick Sandstone, its hardness was comparable to the hardness of the 15 wt. % HAp-PLA and the Ē of the 10 wt. % HAp-PLA. In both developed materials, an increase in wt. % meant an increase in both hardness and Ē. This trend seen is explained as more particulates were added, the amount of polymer is decreased, simply making the material more brittle due to the composition of the composite becoming dominated by the increasing volume fraction of particulates. In terms of mechanical properties, the addition of more particulates increases hardness substantially and Ē slightly. This was a similar trend seen in Russias *et al.* (2006), as the wt. % of the particulate increased, Ē also increased, with a maximum of 95 wt. % achieving an Ē of ≈ 10.00 GPa. However, these composites were produced using a hot compression method. In both Corcione *et al.* (2017) and Corcione *et al.* (2018), a filament extrusion technique was used to create filament for 3D printing, a similar method to which was used in this study, and were able to produce composites with a 50 wt. % loading. However, in this study, it was noted that after loading of around 20 wt. %, residual HAp was found in the filament extruder, suggesting the composite was not precisely 20 wt. %, this was most likely due HAp having a much higher melting temperature (1670°C) compared to PLA (130-180°C), therefore as the PLA pellets were heated past 180°C, the HAp particulates were free to move out of the polymer. These findings were not obvious for the smaller wt. % (5, 10, 15) and was not mentioned in the Corcione *et al*. studies, therefore it was decided that for this experiment 15 wt. % would be the maximum loading.

Despite inaccuracies in dimensions (as seen in Section 5.3), Activa^{TM} was chosen as a comparison within this study as the manufacturers claim the material to have similar mechanical properties as real teeth. However, from this study, it was shown that the hardness and Ē were 1578.14 MPa (± 21.47) and 6214.21 MPa (± 184.47) respectively

when comparing to the values obtained in Section 4.3 (Figure 4.12 and Figure 4.15), it can be seen that the values fall short of that for extracted enamel, with values of 3078.97 MPa (± 43.52) for hardness and 8293.56 MPa (± 112.57) for Ē, highlighting a statistical difference. However, as mentioned previously (Section 4.4.2), a comparison of mechanical properties of teeth is unlikely due to the differences in compositions, however, the anisotropy of both materials maybe similar due to the non-homogeneous nature of them. Although within the literature there is a broad range of values for hardness and Ē of enamel. Although the values did not match that of the values obtained during the previous experiment (Section 4.3), they do match the range seen within the literature and the range as specified from the manufacturer. It is also worth noting that the samples prepared in this study, and Chapter 4 were of different shape and dimensions, meaning comparison is difficult.

As mentioned previously, the force cutting results for the FFF printed cylinder were inconclusive, due to the polymer wrapping around the bur and preventing further material from being removed, as evident in Figure 6.6.A. This occurrence is most likely due to the thermoplastic nature of PLA and ABS, as these materials can be heated and cooled several times, changing the geometry of the material but without change to their chemistry or mechanical properties. The interaction between the bur and the material generates heat, despite irrigation; the temperature must have reached the point where the polymer becomes slightly liquid, with the material then cooling onto the bur rather than being removed. This occurrence is commonly found when cutting 3D printed parts made of PLA and ABS, with the material 'budding' at the contact point with the sharp object, with many manufacturers recommend sanding or polishing to remove this excess material (Redwood *et al.*, 2017). Due to this property of FFF materials being thermoplastic, it can be concluded that these materials would not be suitable for creating SBME models that can be used as cutting models. The snapping of the bur also occurred when testing the

cylinders made from Activa™, despite the material designed to match the mechanical properties of real teeth and clinicians being able to use burs to reshape most dental composites; the snapping was most likely due to the rate at which the diamond bur was driven into the material as well as the amount of material. Clinicians typically use dental handpieces to remove small amounts of material (0.1-1 mm) rather than the bulk of the material, to help reshape the composite not to affect the dentition. It has been noted when clinicians try to remove more material; burs tend to snap if not done slowly and in stages.

6.4.2   Stereolithography

During the printing process, it was observed that as the particulate wt. % increased, so a longer curing time was required. This could be possibly explained by the increased presence of HAp reflecting the UV light, therefore requiring a longer curing process, to allow layers to adhere to each other. Absorbance and reflection studies of the composite material would prove or disprove this, as well as indicating on the optimal curing time. It was also observed that after printing, bigger particles were left within the vat of polymer, suggesting there is a size limitation to the particulates that are incorporated into the printed model, this size limitation could be determined by the layer height set by the user, in this instance layer height was 50 μm, meaning only particles < 50 μm would be uptaken within the layers; light microscopy and particle size analysis could be used to determine if this is the case.

The SLA models produced were the least and hardest materials printed, the Anycubic photopolymer and the Formlabs Ceramic Resin. This trend was also noted with the $\bar{E}$, as the Anycubic photopolymer and Formlabs Dental Resin recorded the lowest and highest $\bar{E}$, respectively. As shown with the FFF developed material, a conclusion can be drawn that the addition of particulates increases both hardness and $\bar{E}$, as shown in both

developed and commercial materials. This is most evident within the developed materials, with the increasing HAp wt. %.

All samples were subjected to the force cutting experiment; however, the SLA models were the only specimens to be measured successfully, and it was found that with increasing the wt. %, the force required to cut decreased. As the force recorded was 1.13 N (± 0.03), 0.62 N (± 0.04), 0.58 N (± 0.03) and 0.52 N (± 0.08) for the 0, 5, 10 and 15 wt. % respectively, compared to the extracted teeth (Section 4.3), enamel was 0.31 N (± 0.12) and dentine 0.49 N (± 0.15), the 15 wt. % composite was not statistically different from the extracted dentine. The addition of particulates meant that the composite materials required less force to cut than the commercially available teeth, with the lowest being 0.64 N (± 0.08) and 0.64 N (± 0.20) for Fabrica de Sorrisos enamel and Frasaco dentine, respectively. The commercial materials, Formlabs Ceramic Resin and Formlabs Dental Resin required 0.56 N (± 0.07) and 0.59 N (± 0.04) respectively, with similar forces of 10-15 wt. % HAp-photopolymer.

In Section 4.4.3 it was established that cutting force was related to the ratio of $\frac{H^3}{\bar{E}^2}$ as devised by Miserez et $al.$ (2007), suggesting the higher the ratio (stiffer the material), the less resistant the material is to abrasion, meaning less force is required to remove material. Figure 6.8 is the average force required to cut plotted against the $\frac{H^3}{\bar{E}^2}$ ratio, from the plotted data, it can be surmised that a negative correlation is seen between force and the properties ratio, as the average force required to cut decreases the ratio increases. This can be summarised that the 'stiffer' material is the less force is required to cut or fracture the material; this was also seen in Section 4.4.3. However, it is clear from the data, that none of the materials matches the ratio of for extracted dentine; it is worth noting that that the geometry of the composite materials did not match that of an extracted tooth, for a more accurate representation, the geometry of the materials would have to be similar. In

Figure 6.8, it can be seen that the polymer does not fit the trend; it is suggested that due to the lack of additional mineral-based material, the polymer does not behave the same way as shown with the 5, 10 and 15 wt. %.
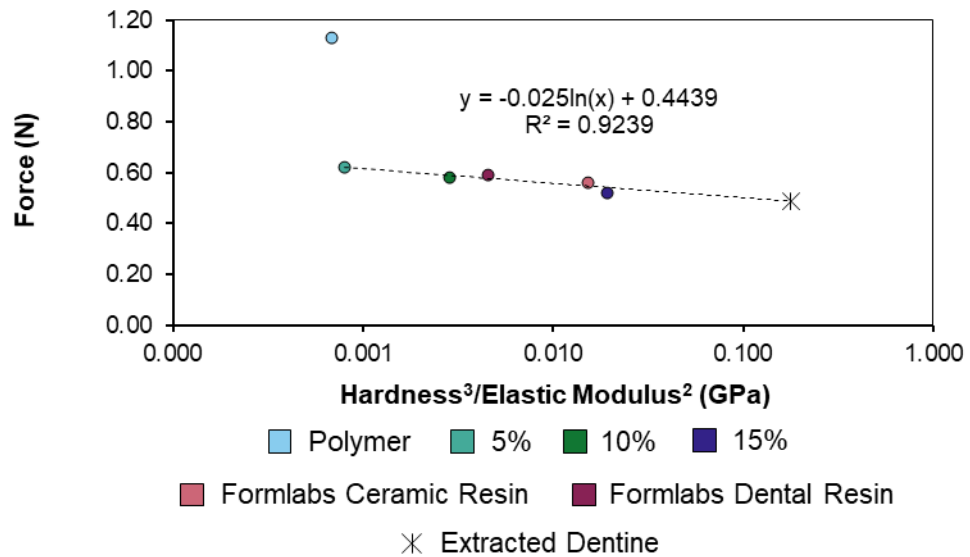
Figure 6.8: Average force required to cut extracted and artificial teeth against $\frac{H^3}{\bar{E}^2}$. The *X*-axis was set to a logarithmic scale to present the data points clearly. A logarithmic trendline was fitted, with the equations and R^2 values referring to all materials.

6.4.3   Selective Laser Sintering

As the PA-GF printed cylinders were outsourced, the parameters used to print are unknown, however, from the technical specifications of the material, we can summarise that the material was sintered at a temperature above 275°C. In this study, the hardness and $\bar{E}$ of PA-GF was 210.74 MPa ($\pm$ 12.56) and 2341.47 MPa ($\pm$ 108.22), respectively, which are within the range of the technical specifications (165-250 MPa for hardness and 2200-2800 MPa for $\bar{E}$).

From the force cutting experiment (Figure 6.5) PA-GF had the lowest force required to cut, 0.21 N ($\pm$ 0.09), it was observed during the investigation that the material appeared to be easily displaced compared with the other composite materials, producing a lot of powder despite the irrigation. Figure 6.7.C highlights a lot of residual material on

the diamond bur after cutting, suggesting despite the PA-GF being sintered; it was easy to break this bond and return to its powdered constituents. This breakdown of the structure may also explain why the PA-GF did not fit the trend seen in Figure 6.8. XMT could be used to confirm if the printed cylinders were fully sintered before cutting, or if any voids were present as seen previously in Section 5.3. These voids may explain why little force was required to cut the material, suggesting SLS as an inappropriate method to produce cuttable SBME models, similar to FFF.

6.5   Conclusions

To conclude, this study has offered a brief insight into the development and printing of novel composites, comparing composites developed in this study (and in previous literature) to commercial composites. The developed composites produced similar results as seen in previous studies, and it was shown that FFF and SLS printed composites were not suitable in producing cuttable SBME models, however, from previous sections, may be suitable to produce other types of SBME models. From the results, SLA appears to be the most applicable technology when creating cuttable SBME models, and the initial force cutting results suggest composite materials would be more suited for recreating the tactile feedback of extracted enamel and dentine.

Chapter 7

Development of Printable Dental Materials

This chapter focusses on the development of photopolymer composites that offer a mimetic experience similar to that of natural human teeth, taking the work that was carried out previously (Chapter 6) and exploring other dental materials as potential filler constituents for the photopolymer resin and exploring the mechanical properties, as well as aesthetics and force feedback.

7.1   Introduction

As previously established, teeth have outstanding mechanical properties which, as of yet, have not been replicated artificially. Aesthetically, however, artificial teeth can match the colour and the shape of natural teeth (Nassri *et al.*, 2008; Hanafi *et al.*, 2020). Therefore, the challenge remains in producing an engineered tooth that is morphologically like a natural tooth, while providing a mechanical function that can mimic the haptic response of natural teeth. The benefits of having a mimetically designed artificial tooth for dental education have been previously mentioned in 2.2.4.6.

Although there is limited literature on the composition of commercially available artificial teeth, work carried out in Chapter 4 established that these typodonts were typically polymer-based. These teeth aim to provide a simulated experience; therefore, a material with a high K_{ifr}, as well as being aesthetically comparable, is generally desirable (Clements *et al.*, 2018). PMMA resin has been used in dentistry for over 80 years due to its high availability, low costs, biocompatibility and customisable aesthetics (Bacali *et al.*, 2019). However, PMMA has been noted to crack easily due to fatigue making it difficult to work with (Cevik & Yildirim-Bicer, 2016), this was also observed in Abu Eid

et al. (2013) and Chapter 4. Although there is a lack of literature on typodonts, in the field of dentures, the addition of fillers has been investigated and found to improve the impact strength. However, preparation is difficult as the filler materials increase the viscosity of the PMMA, thus reducing its ability to flow into the desired shape (Bera *et al.*, 2011; Cevik & Yildirim-Bicer, 2016).

Development of materials that mimic the mechanical properties of the native tissue requires a better understanding of both the materials processing and composition that define resultant product performance. Therefore, multiple studies have investigated the addition of different fillers in manufacturing PMMA-based materials (i.e. dentures) (Cevik & Yildirim-Bicer, 2016; Clements *et al.*, 2018; Preis *et al.*, 2018; Bacali *et al.*, 2019), applying increasing filler content to produce a composite has improved the mechanical properties such as hardness and K_{ifr}, but the practicality of preparing these is difficult due to a higher tactile perception threshold compared to natural teeth (Cevik & Yildirim-Bicer, 2016). This higher tactile perception is observed throughout the clinic and pre-clinic, especially in undergraduate dental courses (Al-Sudani & Basudan, 2016).

Although many studies look to produce mimetic materials by recreating the hardness of natural teeth, however, as established in Chapter 4 and Chapter 6, this may not be necessary. As mentioned previously, Amini & Miserez (2013) investigated the relationship between hardness and $\bar{E}$ in explaining the wear and abrasion properties of materials, with the ratio of $\frac{H^3}{\bar{E}^2}$, helping to explain how the 'stiffer' the material was, the less force required to fracture was needed. Therefore, the emphasis on recreating a mimetic material in terms of cutting resistance would be on the relationship between hardness and $\bar{E}$ rather than those properties being separate.

The aim of this study is the continuation of the material development seen in Chapter 6, and to develop a 3D printable composite material that can mimetically match

natural teeth, when evaluated with the force feedback system designed in Section 3.5.3. With the focus of using filler materials commonly used within dental research and the clinic.

7.2 Materials and Methods

7.2.1 Filler Material

A selection of commonly used dental materials was chosen to act as filler materials. These materials were grouped into three categories: apatite, glass and ceramic. All filler materials, once prepared, were milled with a Gy-ro mill (Glen Creston, UK) separately with 100 g of material at a time for 45 s, to produce smaller particle sizes. Once milled, the 100 g of material was sieved through three different mesh size sieves (Endecotts Ltd., UK), 150, 63 and 38 μm for 45 min by using a vibratory sieve shaker (Retsch vs 1000, Retsch GmbH, Germany). Powders with a particle size of 63-150 μm and > 150 μm were collected, milled and sieved again until only 38 μm sized powder remained, the subsequent powder was then collected and sealed within a plastic bag and placed within a desiccator to prevent any water absorption.

7.2.1.1 *Hydroxyapatite*

Synthetic HAp powder (Plasma Biotal Ltd.) was used, as previously seen in Section 6.2.1.1.

7.2.1.2 *Carbonated-Hydroxyapatite*

The CHAp was produced using the same protocol as outlined in Landi *et al.* (2003). A 540 ml solution of 0.15 mol calcium nitrate tetrahydrate (Sigma-Aldrich, Merck, Germany) was prepared, with pH being maintained between 12-13 with ammonium hydroxide solution (Merck, Germany) with ≈ 10 ml of the solution being added. A second

solution of 0.09 mol ammonium hydrogen phosphate (Sigma-Aldrich, Merck, Germany) and 0.06 mol sodium hydrogen carbonate (Sigma-Aldrich, Merck, Germany) was prepared to 480 ml, with pH again, being maintained between 12-13 with ammonium hydroxide solution. The second solution was then brought to a volume of 960 ml with deionised water. The second solution was then added to the first solution via titration over 2 h, with the first solution being continuously mechanically stirred at 95°C, with the pH being stabilised > 11 with ammonium hydroxide solution ($\approx$ 280 ml in total). The suspension was then maintained at 90°C and stirred for a further 48 h; the precipitate was then washed with deionised water three times and filtered under vacuum with 5-13 μm filter paper. The precipitate was then dried at 80°C before being milled and sieved.

7.2.1.3   Bioactive Glass

45S5 Bioglass® was chosen as the bioactive glass (BAG) for use in this study and was prepared using the protocol outlined in Lefebvre *et al.* (2008). A composition of 46.1 mol % silica dioxide, 26.9 mol % calcium oxide, 24.3 mol % sodium oxide and 2.6 mol % phosphorus pentoxide was obtained from high purity reagents silica dioxide (Prince Minerals Ltd., UK), sodium carbonate, calcium carbonate and phosphorous pentoxide (Sigma-Aldrich, Merck, Germany). Reagents were measured ($\pm$ 0.01 g) and mixed vigorously in a sealed glass container via a powder mixer (Turbula® T2F, Glen Mills Inc., USA) for 20 min. BAG powder was produced in batches of 200 g. Each batch was poured into a clean platinum-rhodium crucible and placed within an electric furnace (EHF 17/3, Lenton Thermal Designs, UK) at 1400°C for 4 h. The melted glass was then rapidly quenched into deionised water to prevent crystallisation and dried at 80°C for 2 h.

7.2.1.4   Glass Flake

Glass flake (GF) was obtained from Glass Flake Ltd. (UK), with a batch of electrical and chemical resistant GF with an average particle size of 160 μm.

7.2.1.5 Fluormica Glass

A barium fluormica glass (FM) was produced following the procedure outlined in Rashwan *et al.* (2019). A composition of 8.0 mol % silica dioxide, 1.3 mol % aluminium oxide, 3.8 mol % magnesium oxide, 2.3 mol % magnesium fluoride and 1.6 mol % barium oxide was again obtained from high purity reagents (Sigma-Aldrich, Merck, Germany). Reagents were measured, mixed and melted at 1500°C for 1.5 h (see Section 7.2.1.3). The melted glass was stirred for 10 s within the crucible before being quenched in deionised water; the glass was then subsequently dried at 80°C for 2 h.

7.2.1.6 Ceramic

Three types of ceramic porcelain were chosen, they included Vitadur® Alpha 337N Porcelain (White), Vitadur® Alpha 348N Porcelain (White) and Vitadur® Alpha 337N Porcelain (Pink), all from Vita Zahnfabrik (H. Rauter GmbH & Co., Germany).

7.2.2   Preparation of the Composite

Once the filler materials had been milled and sieved to < 38 μm, the powders were added to the photopolymer resin at different wt. % (5, 10, 15, 20 and 25), this was carried out as outlined in Section 6.2.2.1.

7.2.3   Particle Size Analysis

Particle size analysis was used to determine the size and distribution of particles from the filler materials to ensure powders were < 38 μm after milling. The technique measures the intensity of scattered light from a suspension when exposed to a laser beam. The angle of the scattered light increases relatively as the size of the particle decreases (Beuselinck *et al.*, 1998).

Two different particle size analysers were used to plot the distribution ranging from nanometre to micrometre: Zetasizer (0.1 nm to 1 μm) and Mastersizer 2000 (0.3-1000 μm) (Malvern Instruments Ltd., UK).

7.2.4　UV-VIS

A Lambda^{TM} 365 UV-VIS spectrophotometer (Perkin-Elmer Inc., USA) was used to measure the absorbance and reflectance of UV light (405 nm) when in contact with the composite photopolymer. The spectrophotometer was first calibrated using light, and dark controls before ≈ 3 ml of composite photopolymer were added to a transparent cuvette, the sample was run once for reflectance and once for absorption before the sample was replaced with fresh resin, this procedure was carried eight times for each wt. % of the composite. Data was collected by the in-built software UV WinLab (Version 7.1. Standard, 2019: Perkin-Elmer Inc., USA).

7.2.5　Oscillating Rheometry

The curing time for each composite photopolymer was determined using an oscillating rheometer (Sabri Dental Enterprises, USA); approximately 1 ml of the material was placed on a fixed plate, before being compressed by an oscillating plate and was subjected to UV light. The amplitude of the oscillation was measured by PicoLog 6 software (Version 6.14.10, 2019; Pico Technology, UK), the time taken for the amplitude to reduce from 95% of its value to 5% was recorded as the curing time (Figure 7.1). Measurements were performed at 21.0°C (± 3.0).
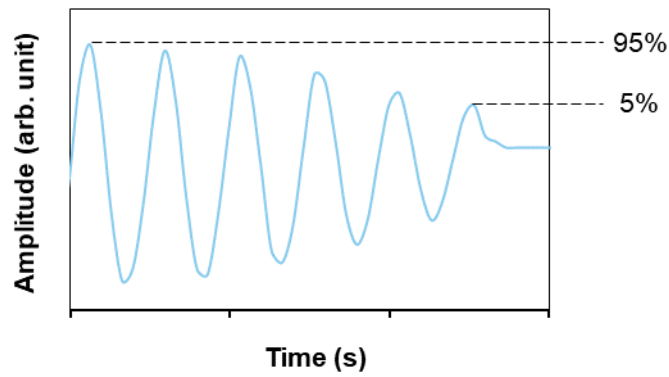
Figure 7.1: An example of an oscillating rheometer trace.

7.2.6   Zahn Cup

Relative viscosity (η) was measured using a dip viscosity cup (Zahn cup) as used in Harun *et al.* (2009). A Brookfield dip viscosity cup (Zahn type #4, Brookfield Engineering Laboratories Inc., USA) was dipped into the composite photopolymer and then lifted to around 30 cm, with the time taken for the composite to stop flowing uninterrupted (efflux) from the Zahn cup measured via a digital stopwatch. Before flow measurements were taken the density (ρ) was calculated when the cup was full (48 ml) using digital scales, this was calculated using the following equation.

$$\rho = \frac{m}{V}$$

Equation 7.1

Where: *m* is the mass of the material.

V is the volume in which the material is stored.

The viscosity is then calculated in poise (Pa·s) with the following equation;

$$\eta = \rho\big(K(t - C)\big)$$

Equation 7.2

Where: ρ is the density of the material.

K is a constant assigned to the cup number; in this instance, the constant is 14.8.

t is the efflux time.

C is a constant assigned to the cup number; in this instance, the constant is 5.

7.2.7   Direct Light Processing

The composite photopolymers were printed using the Anycubic Photon printer (see Section 3.3.1), to the shape and dimensions of a mandibular first molar (see Figure 4.5) however with a flat bottom to allow easier mounting for the force cutting. The same settings were used as shown in Table 5.2; however, the curing time was altered according to the results from the oscillating rheometer (Figure 7.6), the updated curing times are shown in Table 7.1. The time taken to cure was rounded to the nearest integer, as the Anycubic Photon allows only whole numbers when changing the curing time.

Table 7.1: Curing settings used for the developed composite photopolymers. Parameters based on the results shown in Figure 7.6.

Material	5 wt. %	10 wt. %	15 wt. %	20 wt. %	25 wt. %
HAp	13.0 s	14.0 s	14.0 s	20.0 s	20. 0 s
CHAp	14.0 s	21.0 s	26.0 s	29.0 s	31.0 s
BAG	21.0 s	22.0 s	23.0 s	27.0 s	30.0 s
GF	16.0 s	21.0 s	27.0 s	27.0 s	28.0 s
FM	17.0 s	26.0 s	28.0 s	29.0 s	33.0 s
338N	15.0 s	25.0 s	28.0 s	28.0 s	30.0 s
347N	14.0 s	20.0 s	26.0 s	29.0 s	30.0 s
352N	16.0 s	17.0 s	25.0 s	28.0 s	30.0 s

Once potential analogues for extracted enamel and dentine were identified, the materials were printed individually (enamel and dentine separately). To fix the two materials together, the dentine structure was reduced in size by 2%, using the Anycubic Photon slicer software. Uncured enamel material was placed on the inside of the enamel 'cap' and then subsequently placed on the dentine structure. The model was then cured for a further 1 min; a miniature G-clamp was used to fix the enamel 'cap' and dentine until the excess enamel material had cured.

7.2.8 X-Ray Microtomography

As per Section 3.1, the printed composites were imaged using the MuCAT2 system, with each scan taking on average 22 h to complete. Reconstructed images were then analysed for porosity using the method described in Section 5.2.6. More information on scanning parameters can be found in Appendix A (Table A).

7.2.9 Scanning Electron Microscopy

Before being mixed with the photopolymer, the filler materials were imaged using SEM techniques to support the findings from the particle analysis, images. Images were also taken of the increasing wt. %, where printed composites were fractured using liquid nitrogen to show the increasing filler material within the layers. Powder collected after force cutting was also imaged as well as a section of the mix-and-match model made from different materials. All SEM was carried as outlined in Section 3.4.1.

7.2.10 Fourier Transfer Infrared Spectroscopy

FTIR-ATR was used to confirm the presence of filler material after printing; the collection of powders and use of FTIR-ATR is shown in Section 3.6.2.

7.2.11   X-Ray Diffraction

XRD was used in conjunction with FTIR-ATR to support the findings and was carried out, as seen in Section 3.6.3.

7.2.12   Microhardness

Printed composites were cut into smaller samples (Section 6.2.5) for microhardness to be carried out. H_V was used as outlined in Section 3.5.1.

7.2.13   Elastic Modulus

$\bar{E}$ was carried out via compression testing, as outlined in Section 3.5.2.

7.2.14   Force Cutting

All printed composites were mounted to the 3-axis load cell, and force cutting measurements took place as outlined in Section 3.5.3, a high-speed handpiece with a diamond bur was used throughout. A separate experiment was carried out using 10 qualified clinicians; they were asked to prepare a Class I cavity on the multiple material models, with force being recorded, this was carried out as seen in Section 4.2.5.

7.3   Results

Once powders had been milled and sieved to below 38 μm, particle size analysis was undertaken (Figure 7.2). It was found that all the materials were < 38 μm, with average particle sizes of 18.61, 21.43, 19.76, 22.71, 18.99, 18.22, 20.58 and 22.37 μm for HAp, CHAp, BAG, GF, FM, 338N, 347N and 352N respectively. Figure 7.3 shows the SEM images taken of the materials after milling and sieving, confirming particle sizes were below 38 μm.
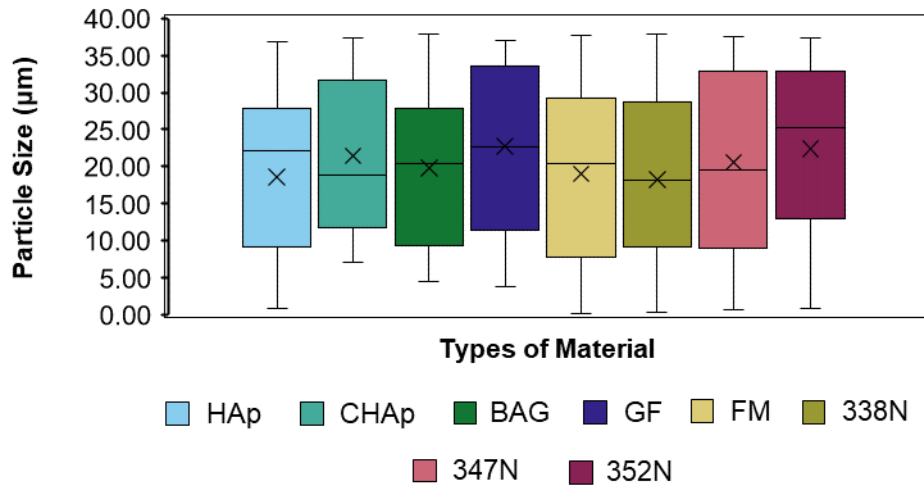
Figure 7.2: Particle size distribution of filler materials after milling and sieving.

From the SEM images (Figure 7.3) it can be seen that the materials have different shapes, the particles were classified by shape using the criteria outlined in Maroof *et al.* (2020). All materials (except for GF) were classified as spherical particles with different forms, with HAp an equant form, CHAp a low form, BAG a slab form and FM, 338N, 347N and 352N having flat forms. GF was classified as being an ellipsoid particle with a blade form.
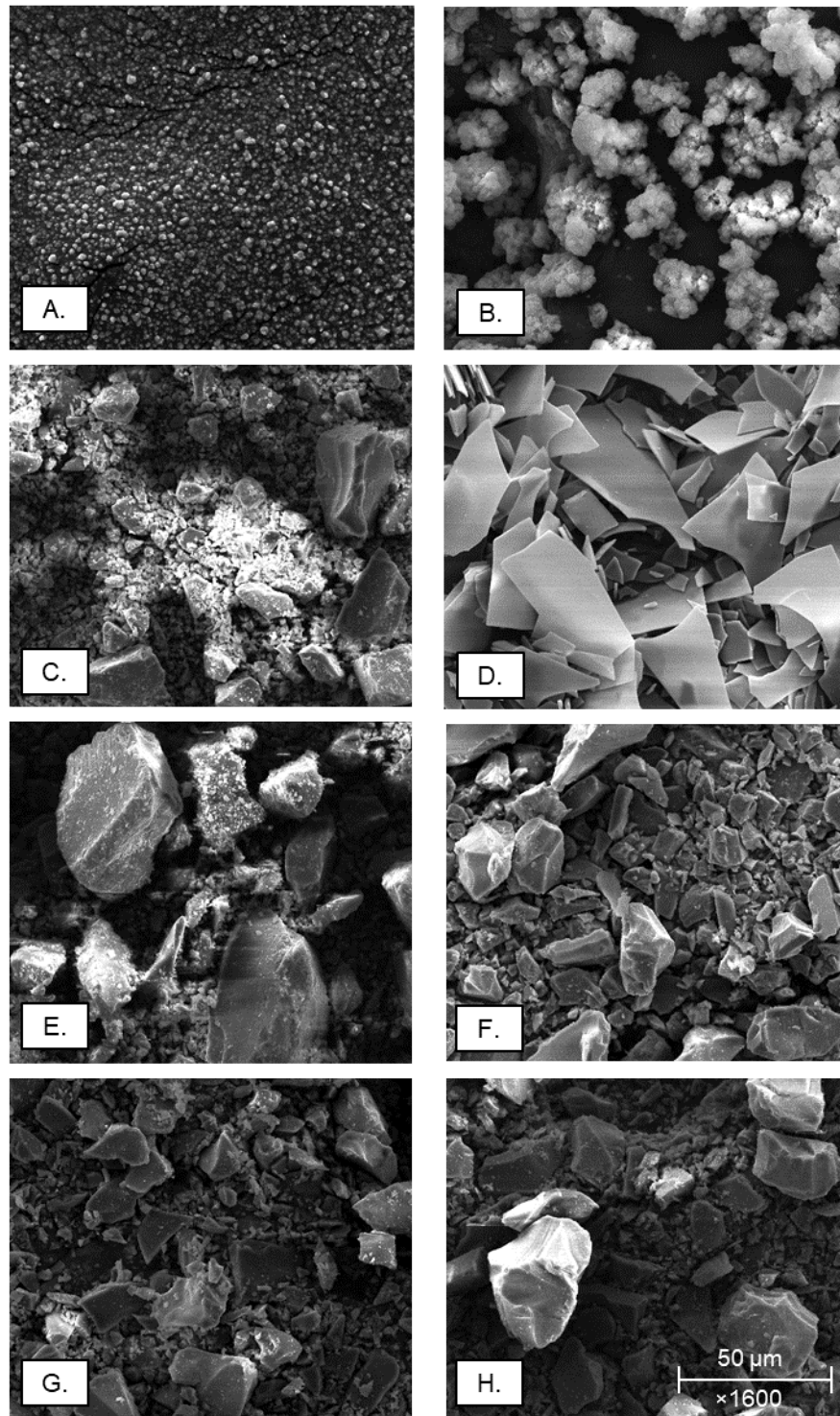
Figure 7.3: SEM images of the different filler materials after milling and sieving. A. HAp. B. CHAp. C. BAG. D. GF. E. FM. F. 337N. G. 347N. H. 352N. All images were taken at the same scale and magnification, as shown in H.

Figure 7.4 and Figure 7.5 show the absorbance and reflectance (respectively) of the composite photopolymers with different filler material and wt. %. A trend was seen as wt. % increased, absorbance decreased; the inverse was seen for reflectance, as wt. % increased, reflectance also increased. The two trends were observed throughout the different filler materials. The photopolymer without any filler material (0 wt. %) was the most absorbent of UV light at 71.99% ($\pm$ 0.02) and the least reflective of UV light at 19.33% ($\pm$ 1.02), this was statistically different when compared with all of the wt. % of composites, suggesting the addition of filler material has a significant effect on absorbance and reflectance.

Apart from the 0 wt. %, the most absorbent material was 5 wt. % CHAp, 59.22% ($\pm$ 1.04) with 25 wt. % FM being the least absorbent, 20.50% ($\pm$ 0.50). Statistical analysis showed no significant difference between the different filler materials at their respective wt. %, however, when comparing the filler materials individually, there was a significant difference between the different wt. % for most filler materials, again suggesting the increasing wt. % affects the absorbance of UV. FM had the biggest percentage change from 5 wt. % to 25 wt. % with a decrease of 55.92%, whereas HAp had the smallest difference from 5 wt. % to 25 wt. % with a reduction of 31.51%. However, when comparing HAp's extra wt. % (30 and 35), the biggest change is observed with this group with a decrease of 62.54% between 5 wt. % and 35 wt. %.

Although an inverse trend compared to absorbance was seen in the reflectance data (Figure 7.5), the most reflective material was 25 wt. % CHAp, 62.05% ($\pm$ 0.95) the least reflective material (excluding 0 wt. %) was 5 wt. % 347N, 25.74 wt. % ($\pm$ 0.60). Statistical analysis showed a similar trend as seen as in the absorbance data.
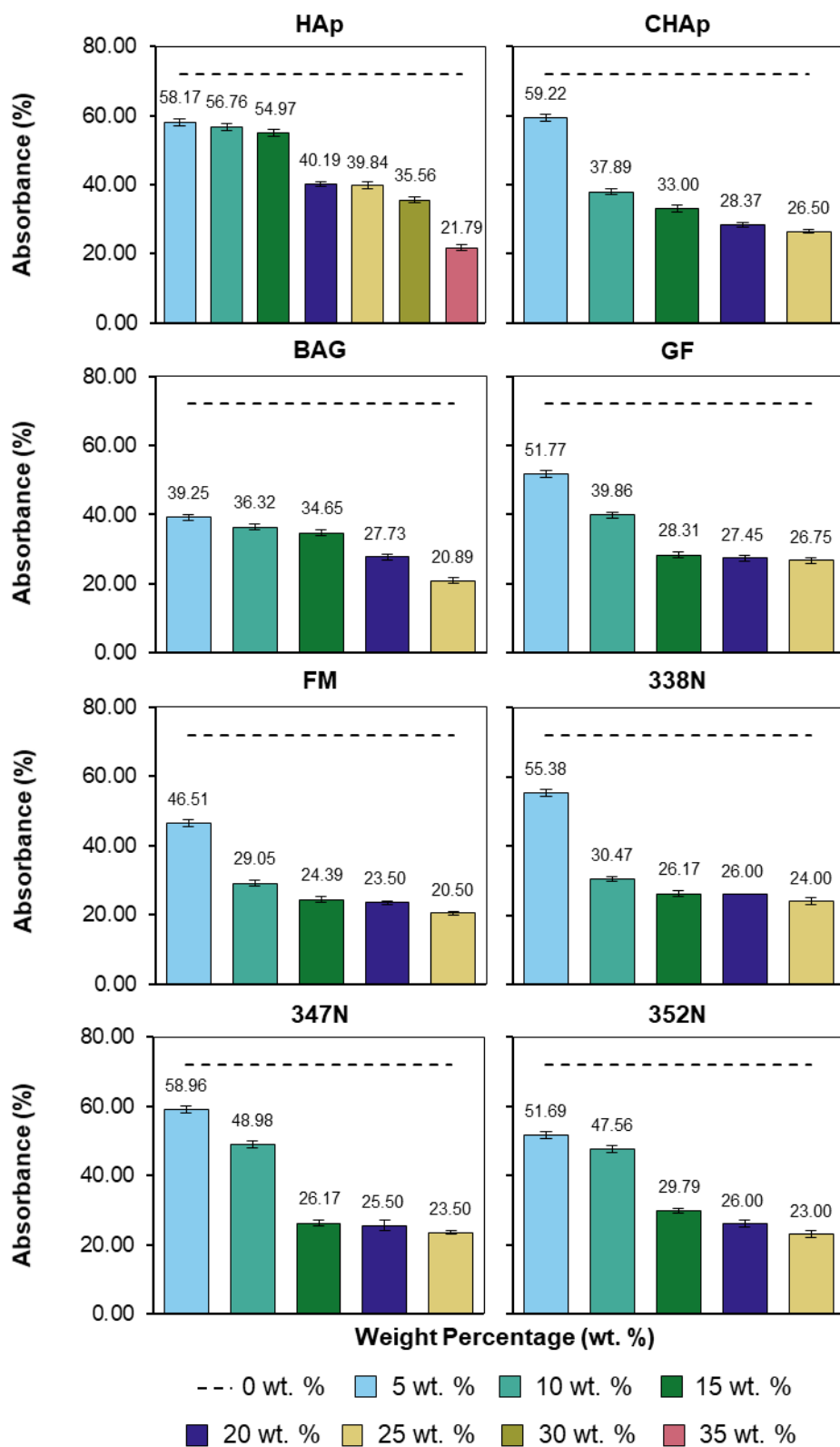
Figure 7.4: Absorbance data of the developed composite photopolymers. 0 wt. % shown in all graphs at 71.99% ($\pm$ 0.02). Error bars presented as SD of the sample, $n = 8$.
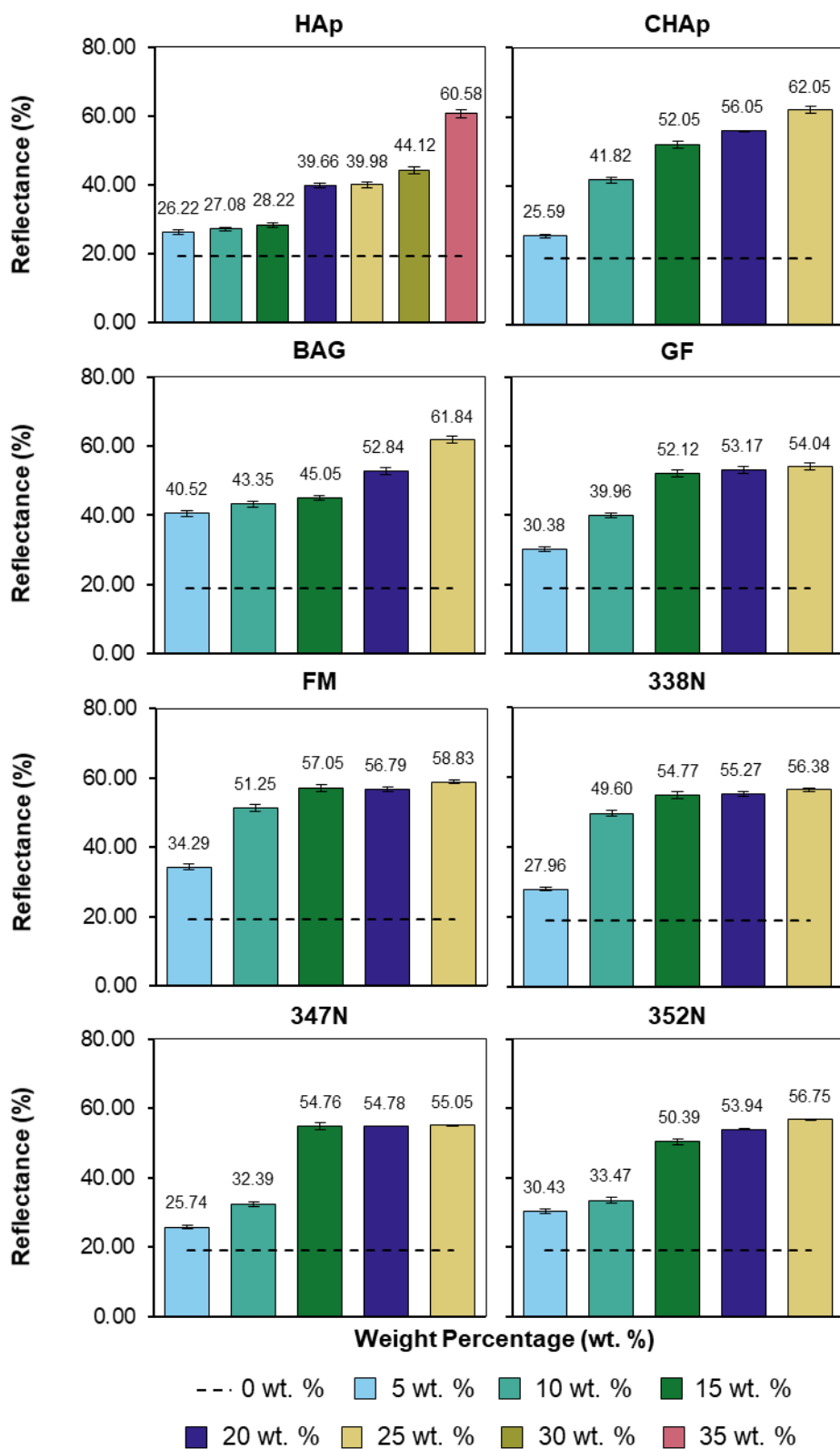
Figure 7.5: Reflectance data of the developed composite photopolymers. 0 wt. % shown in all graphs at 19.13% (± 1.02). Error bars presented as SD of the sample, $n = 8$.

Similar to the reflectance data (Figure 7.5), a trend was shown in Figure 7.6, as wt. % increases the time taken to set (cure) also increases. The 0 wt. % took 8.75 s ($\pm$ 0.81) to set, however, once filler material was added (5 wt. %) there was a significant statistical difference between 0 wt. % and all 5 wt. % of different materials.

Excluding 0 wt. %, the material set in the quickest time was 5 wt. % HAp at 13.01 s ($\pm$ 0.35) with 35 wt. % HAp taking the longest time to set at 33.82 s ($\pm$ 2.21), however, it was observed that even at this stage, the 35 wt. % HAp was not fully set, and when removed from the oscillating rheometer, the material did not hold its shape as other wt. % did, this was similarly observed with the 30 wt. % HAp. Between 5 wt. % and 25 wt. % the largest increase in setting time was seen in the CHAp composites with a 129.48% increase, BAG saw the smallest increase with a 46.08% increase.

Statistical analysis showed little difference when comparing different material composites; however, when comparing the composites individually, there was a significant difference between the increasing wt. %, suggesting that wt. % and the addition of filler materials has a significant effect on the setting time of the photopolymer composite. A trend was seen previously in the absorbance and reflectance data. Results from this experiment helped to determine the curing time for printing the composite photopolymers at different wt. % (Table 7.1).
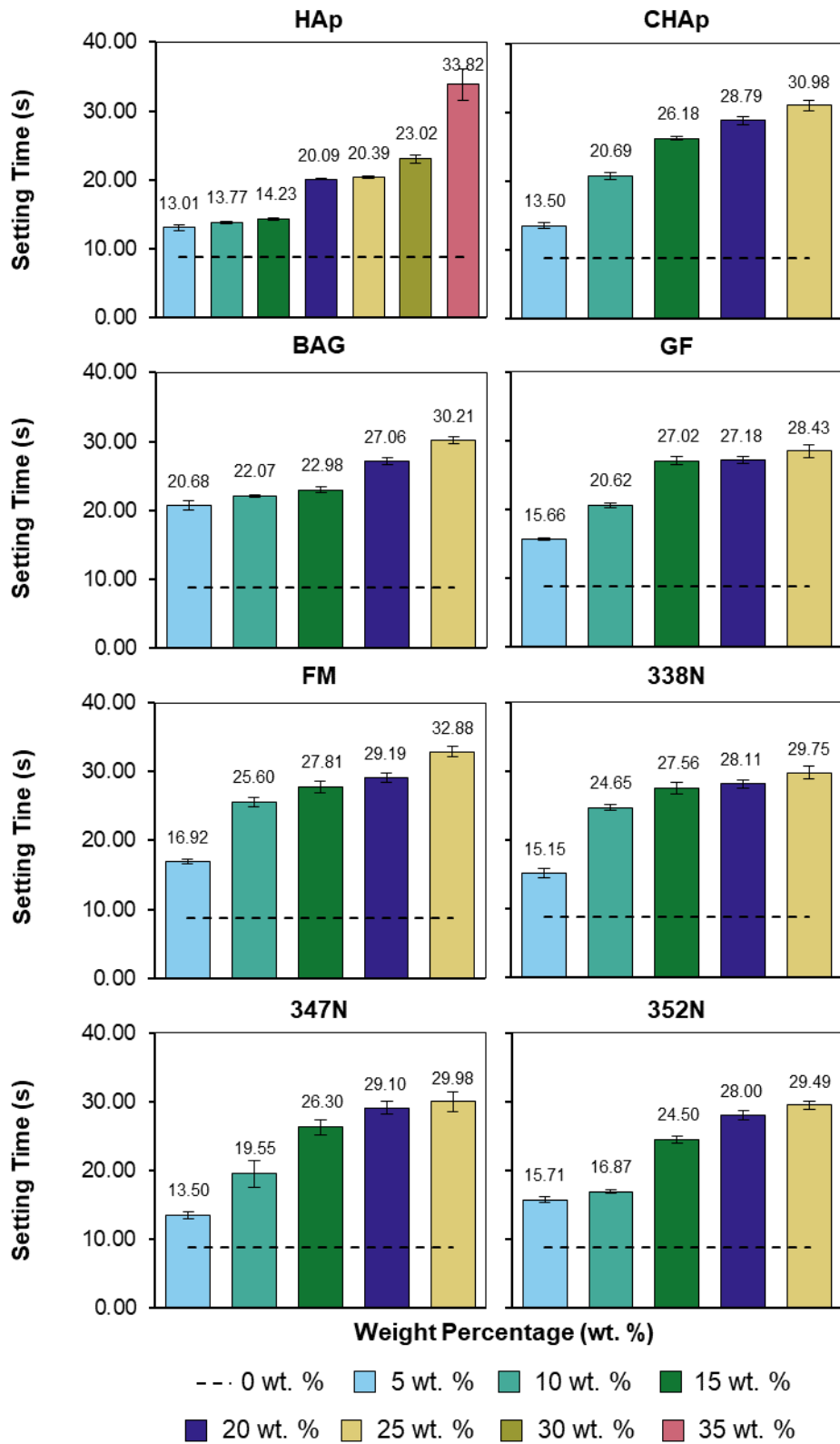
Figure 7.6: Mean setting time of the developed composite photopolymers. 0 wt. % shown in all graphs at 8.75 s (± 0.81). Error bars presented as SD of the sample, *n* = 8.

Relative viscosity was measured for all developed composite photopolymers (Figure 7.7) using a dip viscosity cup (Zahn cup). The least viscous material was the 0 wt. % at 508.14 Pa·s ($\pm$ 28.88), with the most viscous material being the 35 wt. % HAp at 803.40 Pa·s ($\pm$ 56.40). There was a significant statistical difference between the 0 wt. % and all other wt. % of different materials, suggesting the wt. % affects the viscosity of the material. A trend was noted as wt. % increased viscosity also increased; this trend has been seen previously in other measurements (reflectance and setting time).

Except for the 0 wt. %, 5 wt. % 338N recorded the lowest viscosity of the developed composite photopolymers, 539.10 Pa·s ($\pm$ 14.71), similar to the viscosity of the 5 wt. % HAp at 539.78 Pa·s ($\pm$ 22.17). As seen in the absorbance, reflectance and setting time data, there was no significant difference between the different materials; however, a significant difference was noted between the wt. % for individual materials.

The material with the most significant percentage increase was HAp, with a rise of 32.72% between the 5 wt. % and 25 wt. %, with CHAp having the lowest increase of 29.59%. Between 5 wt. % and 35 wt. % HAp, a rise of 39.25% was recorded.
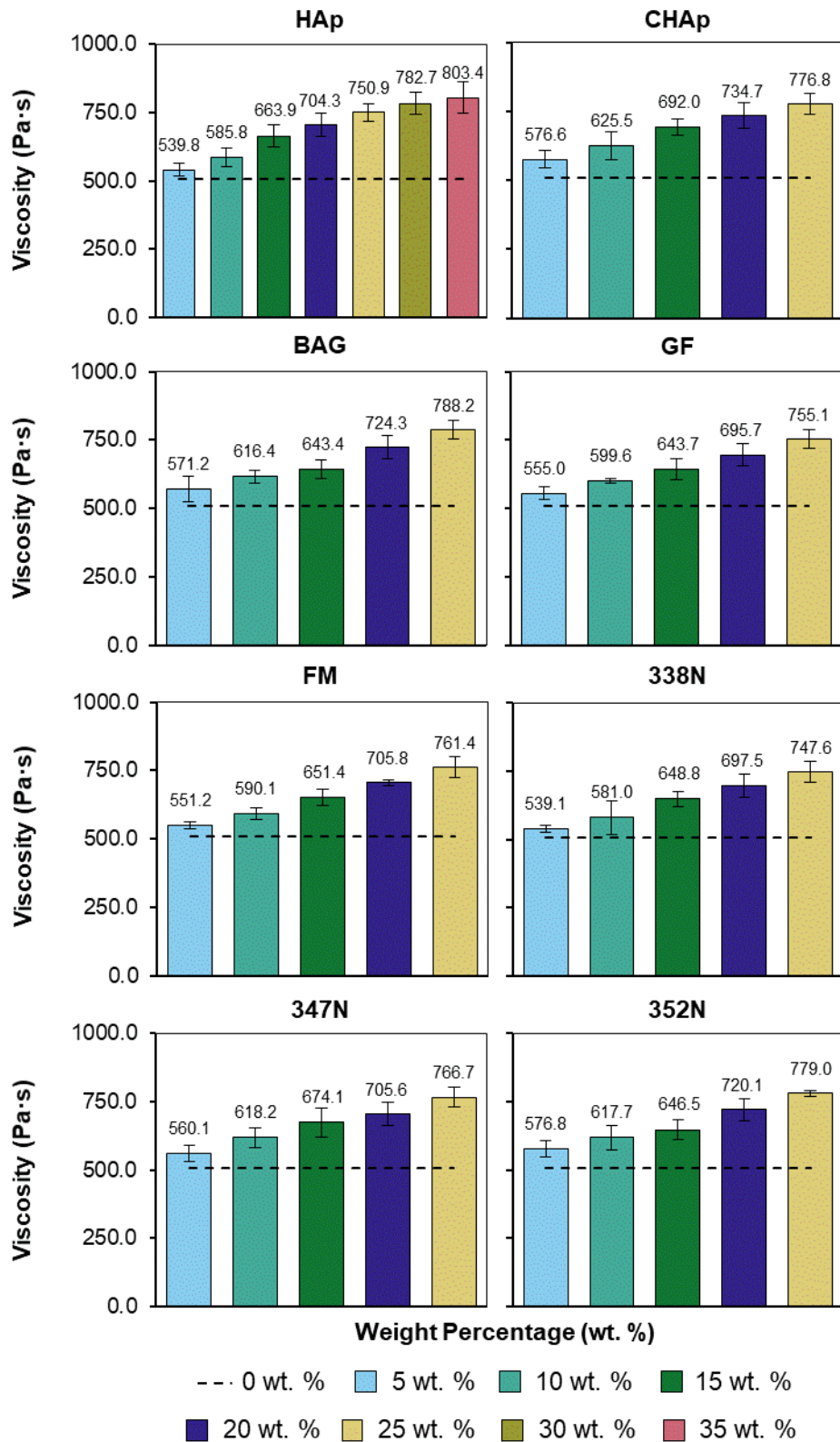
Figure 7.7: Mean viscosity of the developed composite photopolymers. 0 wt. % shown in all graphs at 508.14 Pa·s (± 28.88). Error bars presented as SD of the sample, $n = 8$.

XMT was carried out on all the 3D printed developed composite photopolymers, Figure 7.8, Figure 7.9 and Figure 7.10 show the reconstructed images, as well as 3D, rendered models of the prints. It is worth noting that for some of the 3D renderings, the distolingual cusp failed to render completely, this was due to problems during the segmentation process and was repaired by adding additional triangles and faces, as discussed previously in Section 5.4.1.

Figure 7.8 shows the apatite materials, HAp (Figure 7.8.A) and CHAp (Figure 7.8.B), revealing the distribution of particles within a 25 wt. % printed tooth. HAp appears evenly distributed amongst the tooth, whereas the CHAp distribution is less even, with less distribution towards the occlusal surface.

Figure 7.9 shows the glass materials, BAG (Figure 7.8.A), GF (Figure 7.8.B) and FM (Figure 7.8.C), with the distribution of particles appearing even throughout the three materials, however, with the FM it so noted the particles are of smaller sizes which are seen in the particle size distribution (Figure 7.2).

Figure 7.10 shows the ceramic materials, 338N (Figure 7.10.A), 347N (Figure 7.10.B) and 352N (Figure 7.10.C), again particle distribution appears even throughout the three materials; however, deposition of a large number of particles on the occlusal surface for the 338N can be seen (Figure 7.10.A) tooth.
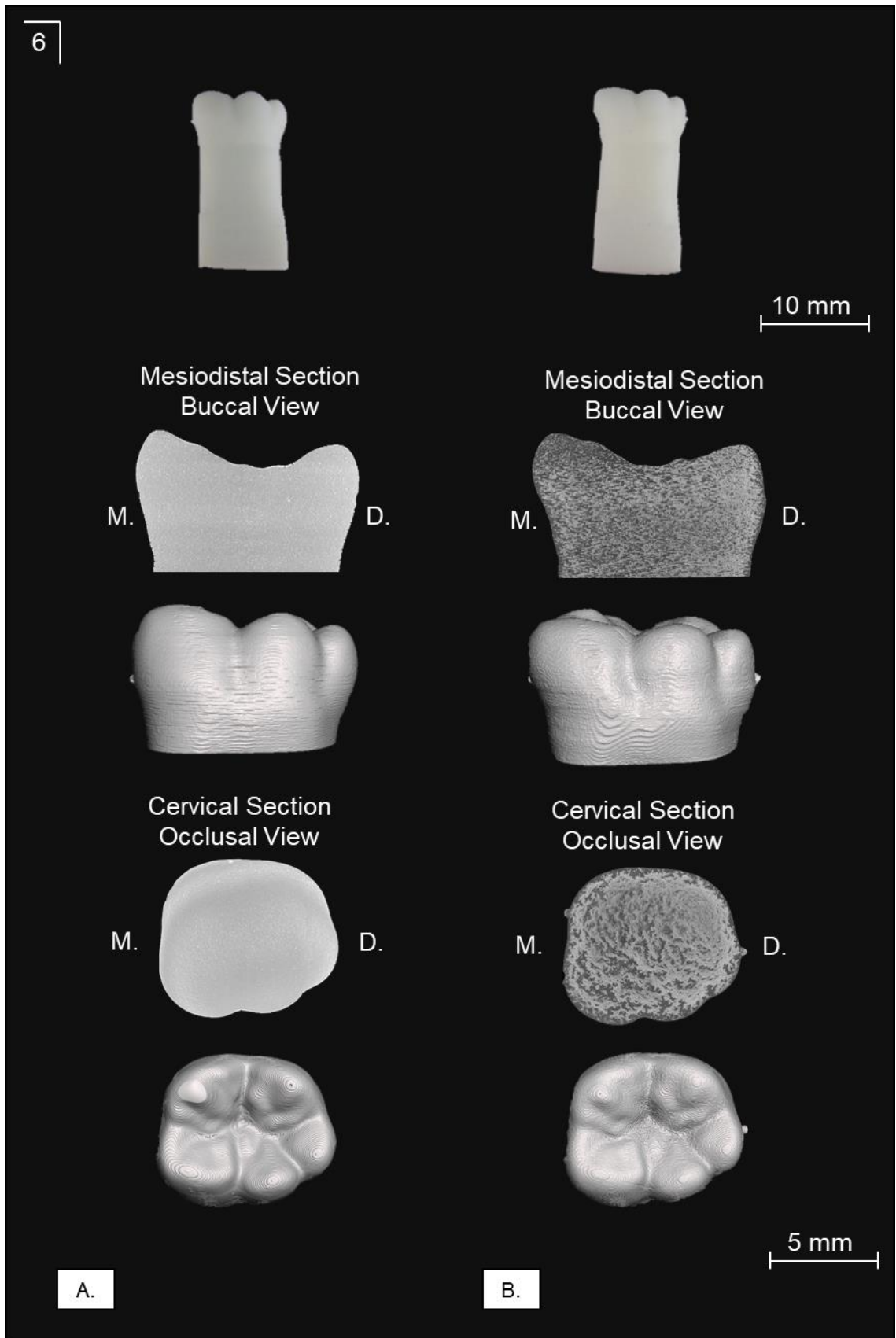
Figure 7.8: Mandibular first molar printed using developed apatite-photopolymer. A. HAp. B. CHAp.
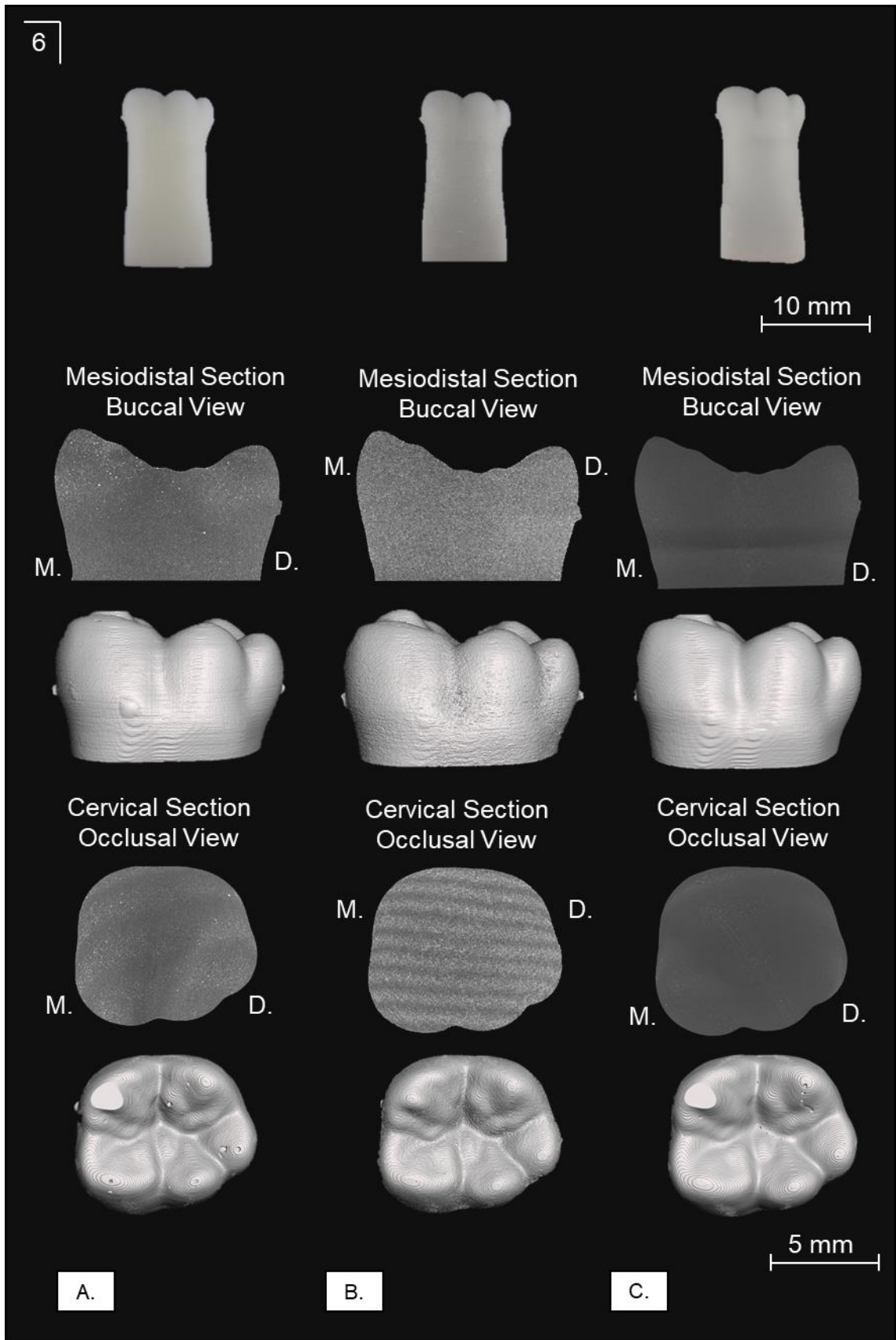
Figure 7.9: Mandibular first molar printed using developed glass-photopolymer. A. BAG. B. GF. C. FM.
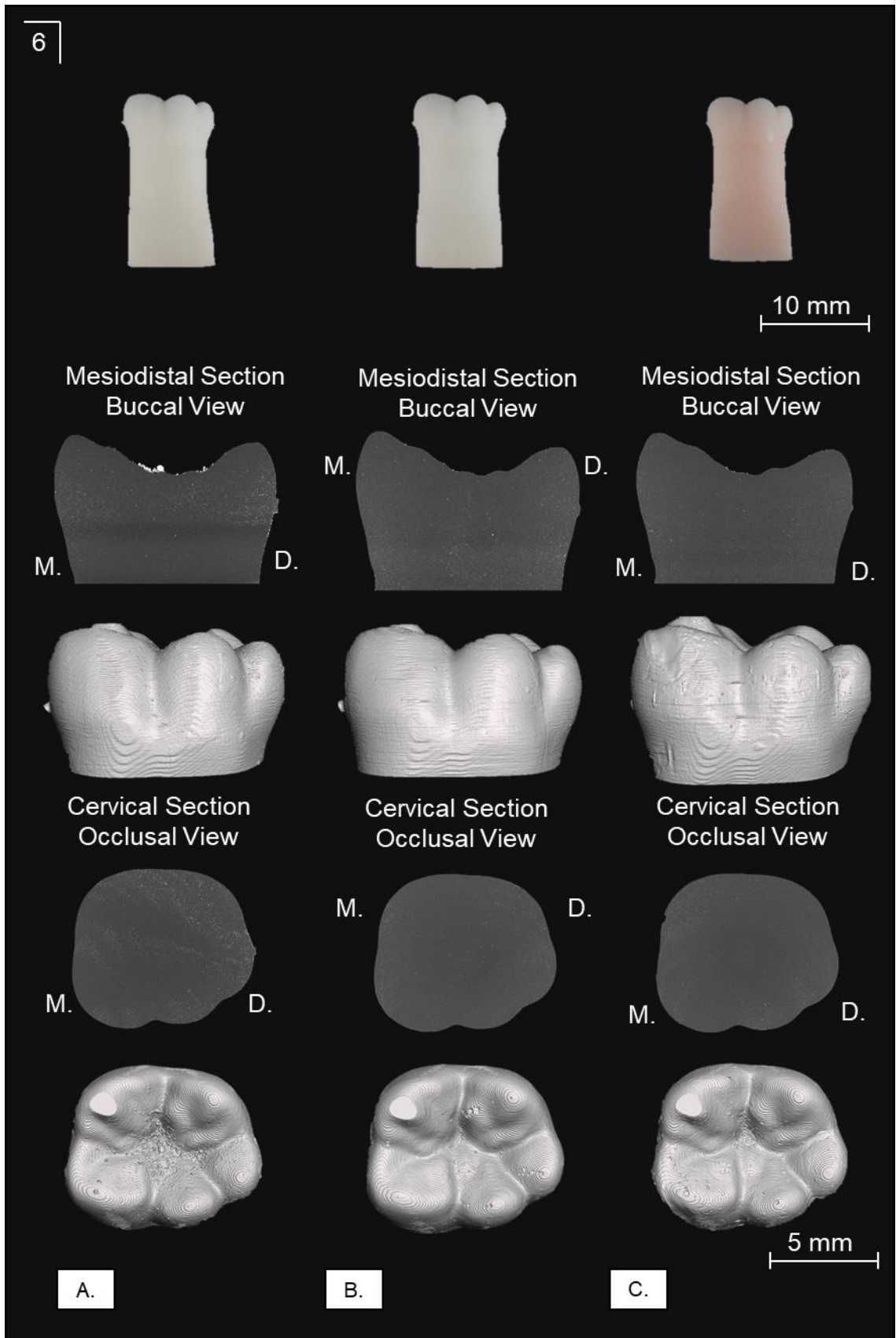
Figure 7.10: Mandibular first molar printed using developed ceramic-photopolymer. A. 338N. B. 347N. C. 352N.

From the XMT, differences in volume could be calculated using ImageJ and BoneJ plugin (Section 5.2.6) against the theoretical volume of 1.39 cm^3, the 0 wt. % printed tooth had a -0.14% ($\pm$ 0.06) difference; this was the lowest difference recorded for all developed composite photopolymers. The composite with the highest difference was the 25 wt. % CHAp at -1.24% ($\pm$ 0.03), and the lowest except for the 0 wt. % was 5 wt. % HAp at -0.56% ($\pm$ 0.07). Statistical analysis showed no significant difference between the material groups; however, when analysing the materials individually, a significant difference was shown between the wt. %. This significant difference as well as the apparent trend of increasing wt. % increases the volume difference suggests that wt. % influences the volume difference.
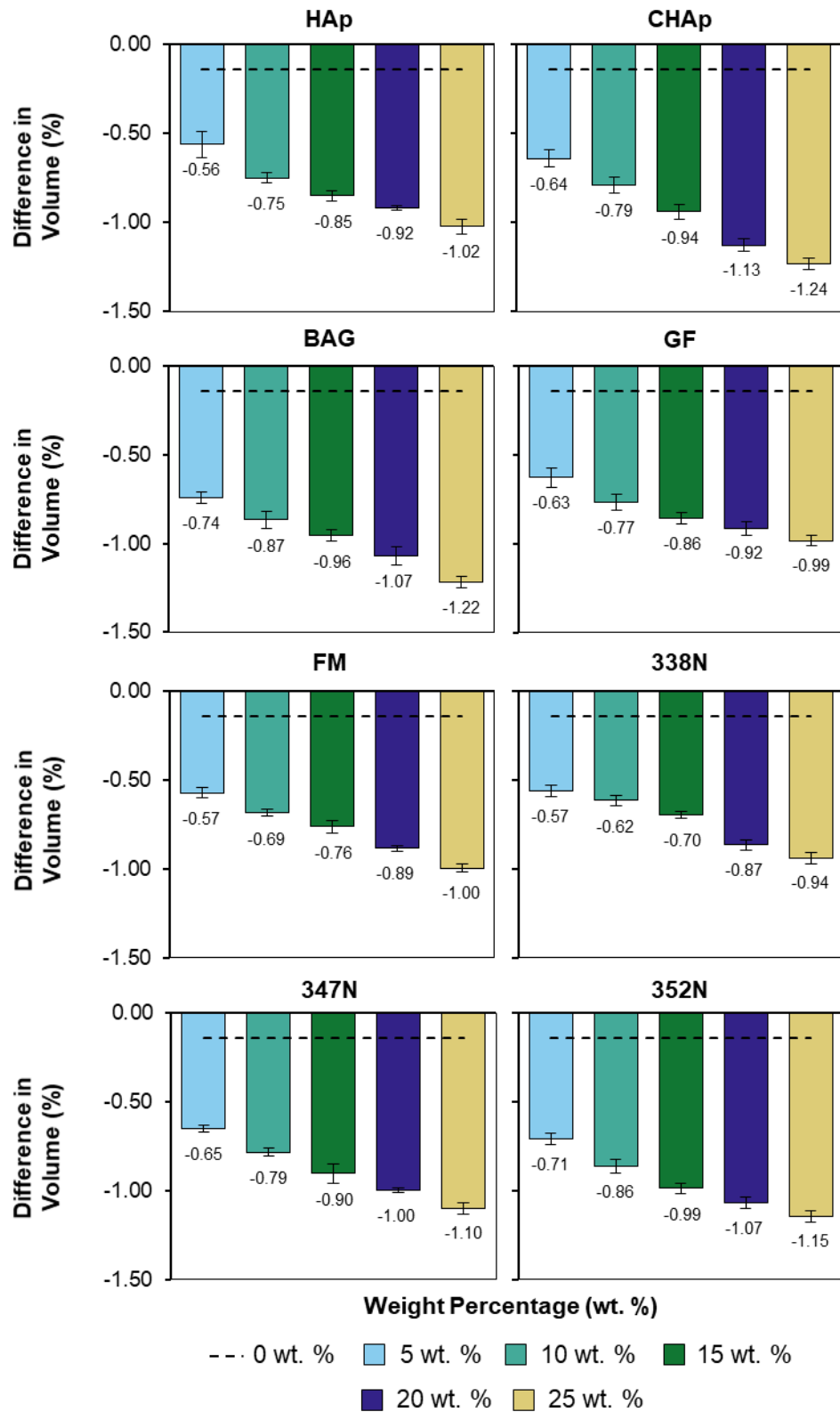
Figure 7.11: Volume difference between the developed composite photopolymers. The theoretical volume of the tooth was 1.39 cm^3, with 0 wt. % shown in all graphs at -0.14% ($\pm$ 0.06). Error bars presented as SD of the sample, $n = 8$.

Figure 7.12 shows the FTIR-ATR spectra for all developed composite photopolymers at different wt. %, this data, in conjunction with spectra obtained through XRD (Figure 7.13), should help to identify the presence of filler materials in each wt. %, as previously shown in Section 6.3.

The HAp spectra are easily identified by the defined peaks at 1015 cm^{-1} and 550-600 cm^{-1}, and this can be seen as the wt. % increases, a more defined peak at 1015 cm^{-1} emerges within the photopolymer spectra, as well as a second peak around 600 cm^{-1}. The peaks appear to become more defined as the wt. % increases. Similar to the HAp, the CHAp spectra can also be identified by peaks at 1015 cm^{-1} and 550-600 cm^{-1} but differs from HAp with the absence of a peak at 970 cm^{-1}. The peaks are broader in CHAp than compared to HAp; however, it is noticeable as the wt. % increases a broad peak emerging at 1015 cm^{-1}, suggesting an increasing presence of CHAp.

BAG is identified by a large, broad peak at 830-1100 cm^{-1} and a sharp peak at 505 cm^{-1}, it is difficult to identify the peak at 830-1100 cm^{-1} in the increasing wt. %, however, as the wt. % does increase, the photopolymer peaks at 815-830 cm^{-1}, become less defined, suggesting the BAG peak of 830-1100 cm^{-1} is masking this. GF, similar to BAG has a broad peak at 830-1080 cm^{-1}, and as the wt. % increases the photopolymer peaks at 815-830 cm^{-1} become less defined. A broad peak also identifies FM at 830-1100 cm^{-1}, as well a sharp peak at 515 cm^{-1}, it is this sharp peak, that becomes more apparent in the photopolymer as wt. % increases.

For all the ceramic spectra, the ceramic materials are identified by the sharp peak at 1745 cm^{-1}, 1340-1375 cm^{-1} and 520 cm^{-1}, however, it is the peaks at 1340-1375 cm^{-1} that become more apparent in the photopolymer spectra at wt. % increases.
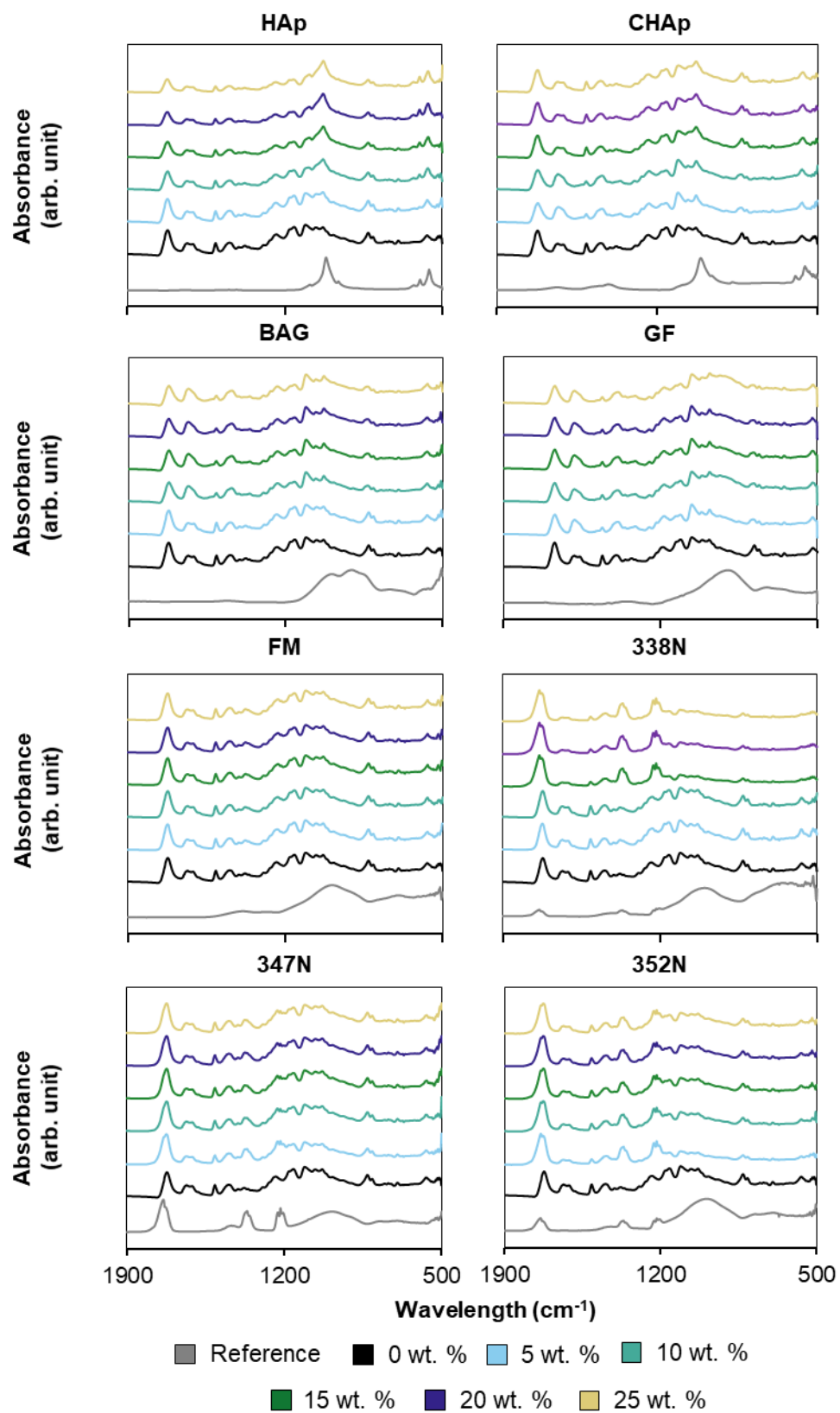
Figure 7.12: FTIR-ATR spectra for the developed composite photopolymers.

The XRD spectra (Figure 7.13) was used in conjunction with the FTIR-ATR spectra (Figure 7.12) to confirm the presence of filler materials as wt. % was increased.

As mentioned previously, HAp is easily identified from the spectra by the sharp diffraction peaks at 26, 31.8, 32.2 and 32.9°; these peaks are noticeable within the photopolymer from 10 wt. % onwards. CHAp has similar diffraction peaks as HAp, and like HAp, the distinct peaks begin to emerge from the photopolymer from 10 wt. % onwards.

For all the glass materials, there are no defined diffraction peaks within the spectra, except for a broad peak 30-35°, suggesting the glass material is amorphous. With, the photopolymer also being an amorphous material, the peaks are difficult to identify as the two materials are masked by the amorphous structure.

Similar to the glass materials, the ceramics also comprise of an amorphous structure, except for 338N, that has sharp diffraction peaks at 27, 37, 46 and 61°, these peaks are noticeable within the photopolymer from 10 wt. % onwards, similar to the HAp and CHAp composites.
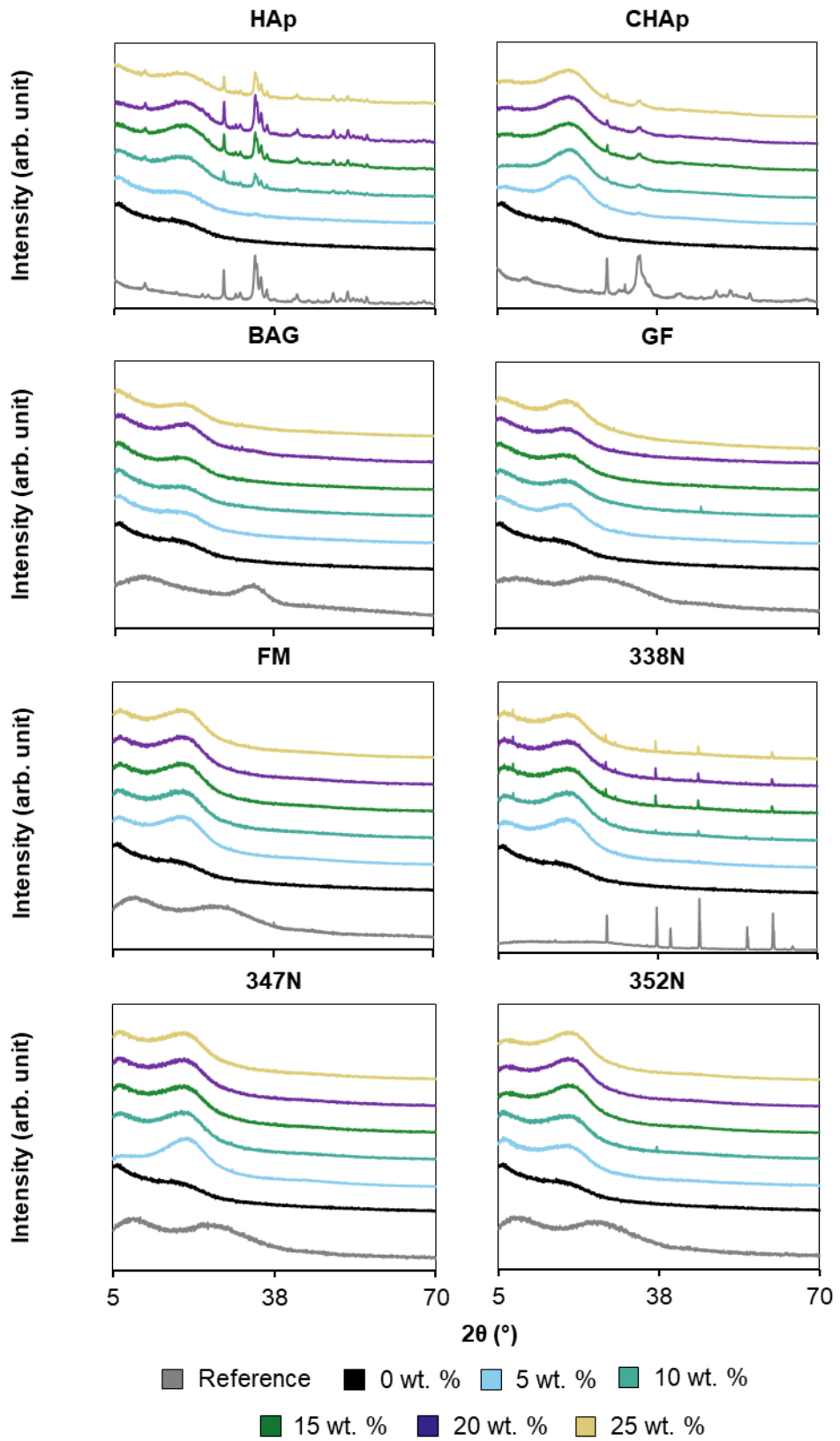
Figure 7.13: XRD spectra for the developed composite photopolymers.

As a comparison to the XMT images, SEM was utilised to identify the presence of particulates at different wt. %, Figure 7.14 shows BAG composite photopolymer at different wt. %. From the images, it can be shown that as the wt. % increases, there is a noticeable presence of spherical slab particles (as defined in Figure 7.3), with none being identified within the 0 wt. % (Figure 7.14.A). The particles appear to be present within the layers of photopolymer as established in the XMT images (Figure 7.9).
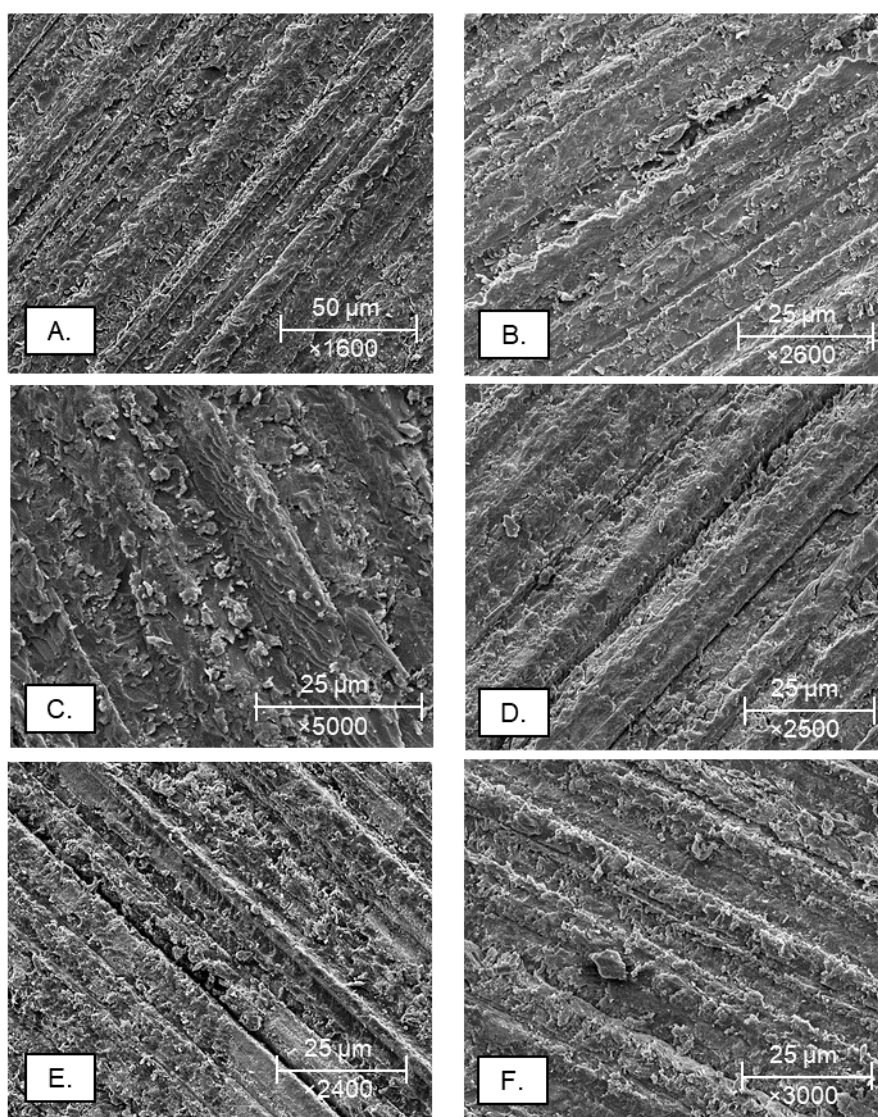
Figure 7.14: SEM images of BAG composite photopolymer at different wt. %. A. 0 wt. %. B. 5 wt. %. C. 10 wt. %. D. 15 wt. %. E. 20 wt. %. F. 25 wt. %.

Figure 7.15 shows the mean hardness and SD of all the developed composite photopolymers, with the 0 wt. % photopolymer recording a mean hardness of 182.95 MPa (± 10.84), this was the lowest mean hardness of all the photopolymers. The lowest recorded hardness of a composite photopolymer was 5 wt. % BAG with a mean hardness of 211.59 MPa (± 120.45) and highest recorded mean hardness was 25 wt. % CHAp at 2263.46 MPa (± 83.31).

A trend that was established in Section 6.3 (Figure 6.3) is observed here, as wt. % increases the mean hardness also increases. Statistical analysis shows a significant difference between all material groups as well as individual material groups, between different wt. %. This significant difference suggests that wt. % has a positive correlation on the mean hardness.

The most significant percentage increase in increasing wt. % was seen with the BAG composite photopolymers with a 460.24% increase between 5 wt. % and 25 wt. %, the composite photopolymer with the least change was FM with a 131.43% increase.
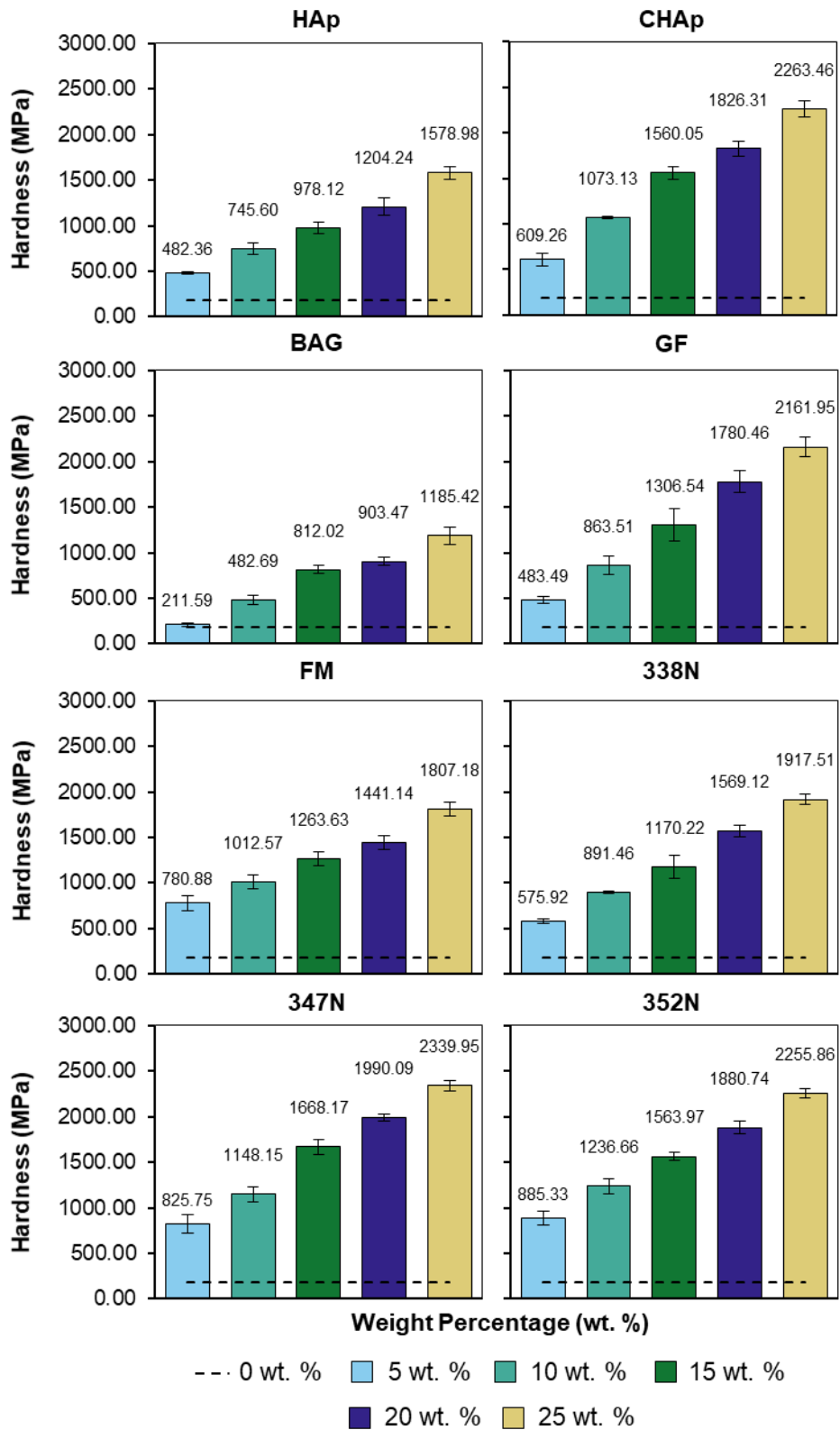
Figure 7.15: Mean hardness values of the developed composite photopolymers. 0 wt. % shown in all graphs at 182.95 MPa (± 10.84). Error bars presented as SD of the sample, $n = 8$.

Ē (Figure 7.16) was measured for all developed composite photopolymers, with the 0 wt. % recording the lowest Ē of 833.82 MPa (± 18.07). Of the composite materials, 5 wt. % CHAp had the lowest Ē with 876.84 MPa (± 23.18), with 25 wt. % 352N having the highest recorded Ē of 2137.26 MPa (± 77.14).

Statistical analysis showed that all materials were significantly different as well as the wt. % of each material, except for FM composite, it was found the different wt. % were not significantly different. A trend, however, can be seen within the other materials, as wt. % increases Ē also increases, although this trend is also in the FM composite, the increase is not significant, with an increase of only 9.46%. In contrast, the 352N had an increase of 68.29% increase between 5 wt. % and 25 wt. %.
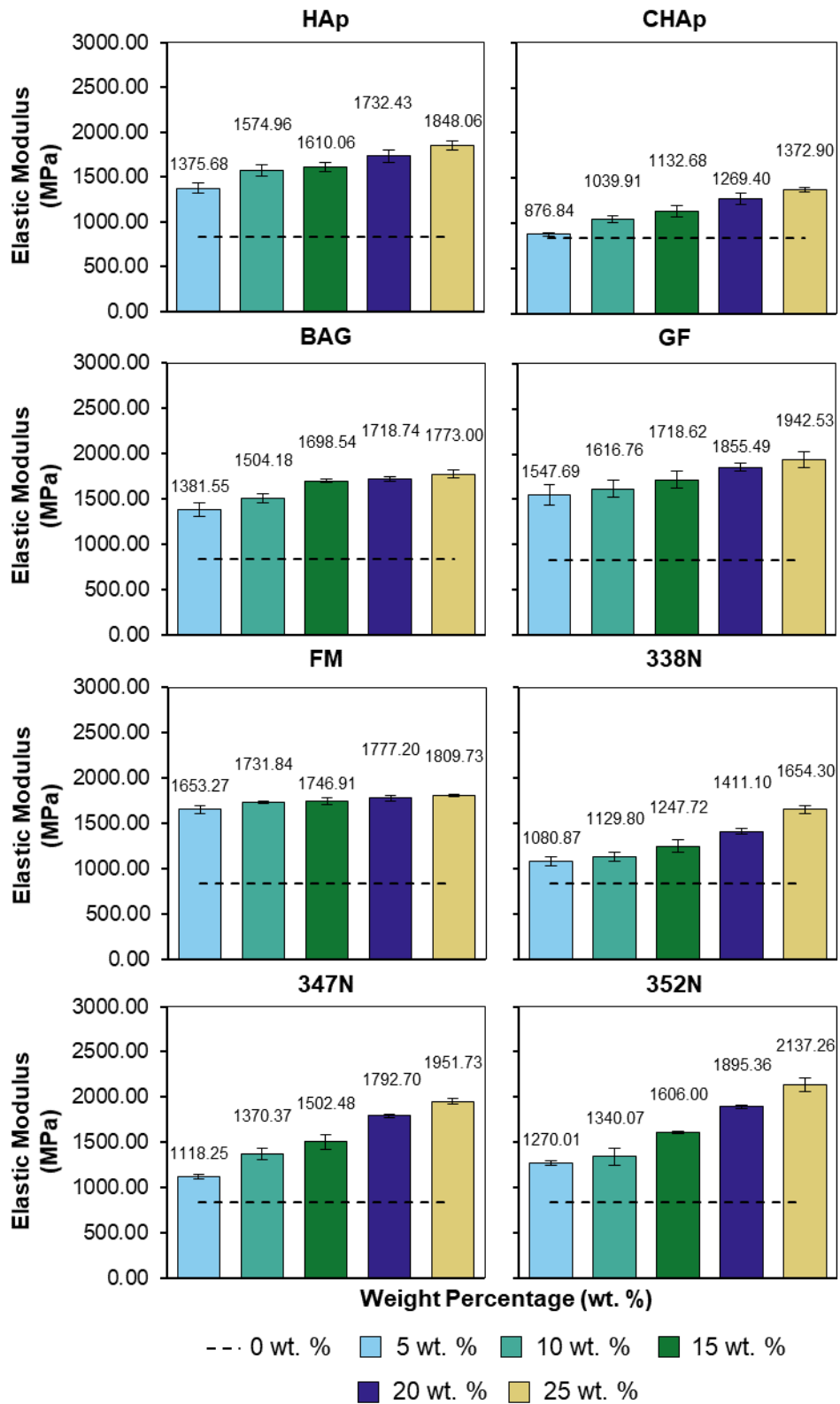
Figure 7.16: Mean elastic modulus of the developed composite photopolymers. 0 wt. % shown in all graphs at 833.82 MPa (± 18.07). Error bars presented as SD of the sample, $n = 8$.

Figure 7.17 shows the mean required forces to cut the developed composite photopolymers; the largest amount of force required was for the 0 wt. % photopolymer, 1.01 N (± 0.03). Of the composite photopolymers, 25 wt. % 352N required the least force to cut, 0.26 N (± 0.07), with 5 wt. % BAG requiring the most force, 0.89 N (± 0.08). As noted previously, a trend was seen as wt. % increased the force required decreased, statistical analysis supported this trend, as a significant difference was seen between the wt. % in individual material groups, however, between materials no significant difference was seen, except for 5-15 wt. % BAG and 5-10 wt. % GF.
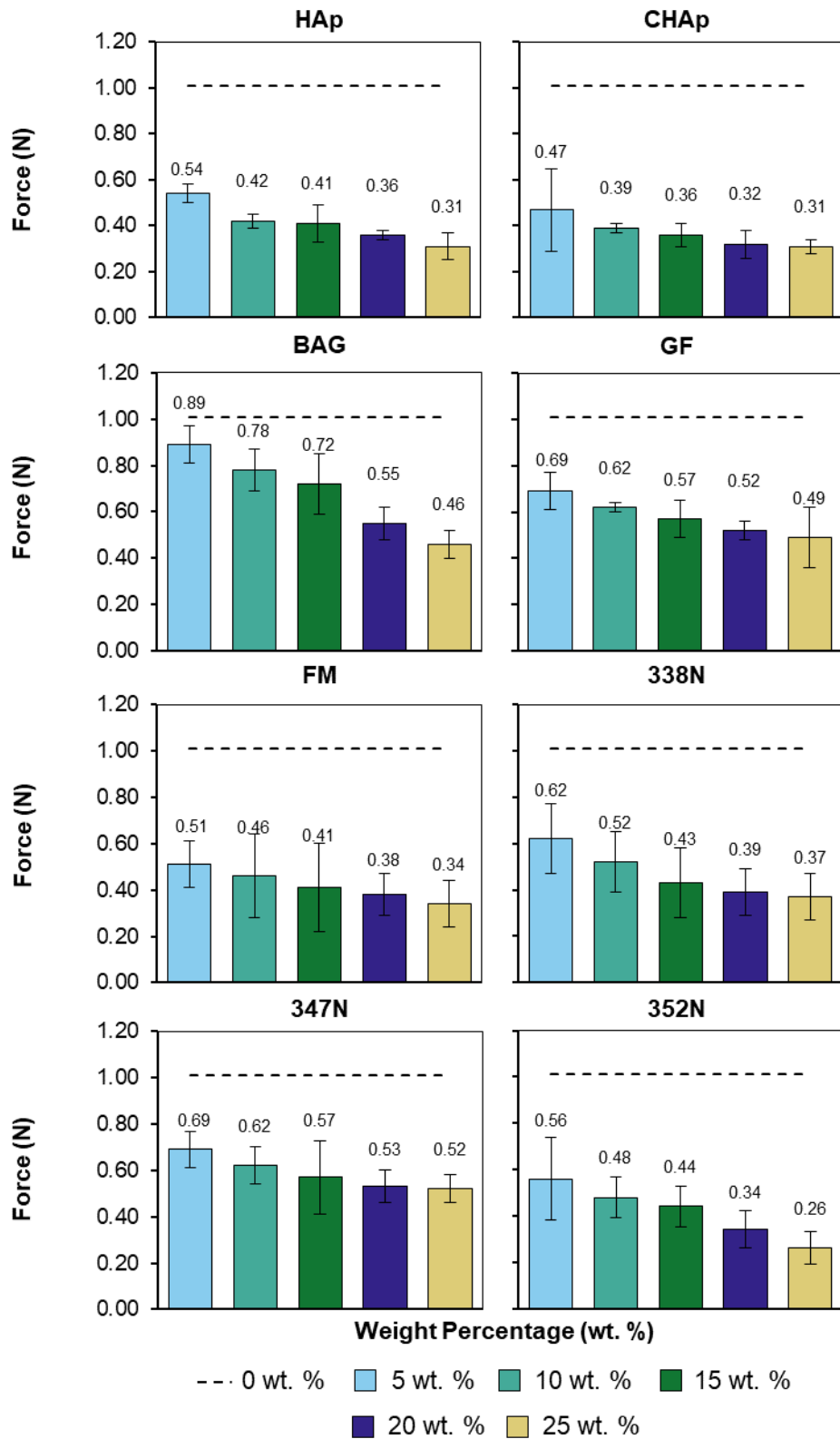
Figure 7.17: Mean force required to cut the developed composite photopolymers. 0 wt. % shown in all graphs at 1.01 N (± 0.03). Error bars presented as SD of the sample, $n = 8$.

Once materials were identified to match that of extracted enamel and dentine closely, the materials were printed separately and fixed together with the selected enamel resin; these were then imaged using XMT (Figure 7.18) and SEM (Figure 7.19) to examine the interface. Figure 7.18 clearly shows void within the interface of the enamel and dentine materials; this is also seen in Figure 7.19.B.
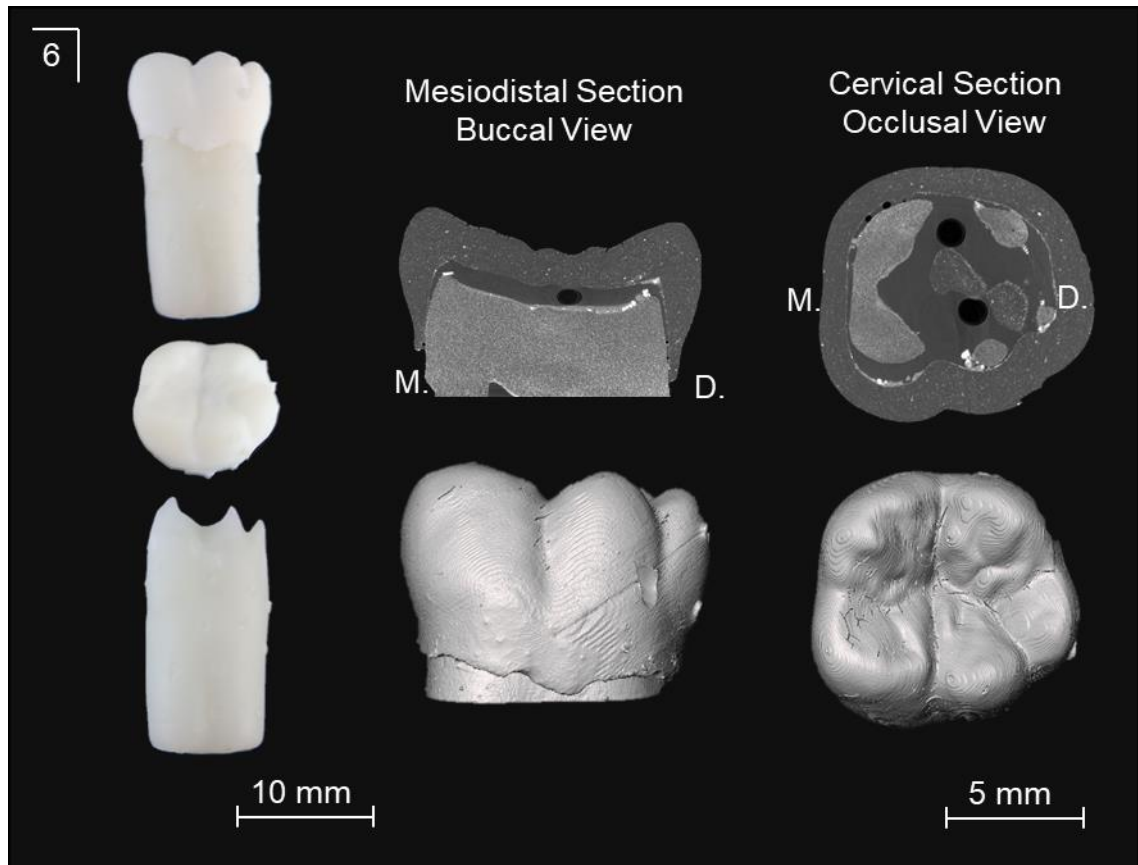
Figure 7.18: Mandibular first molar printed using 25 wt. % HAp and 25 wt. % GF.
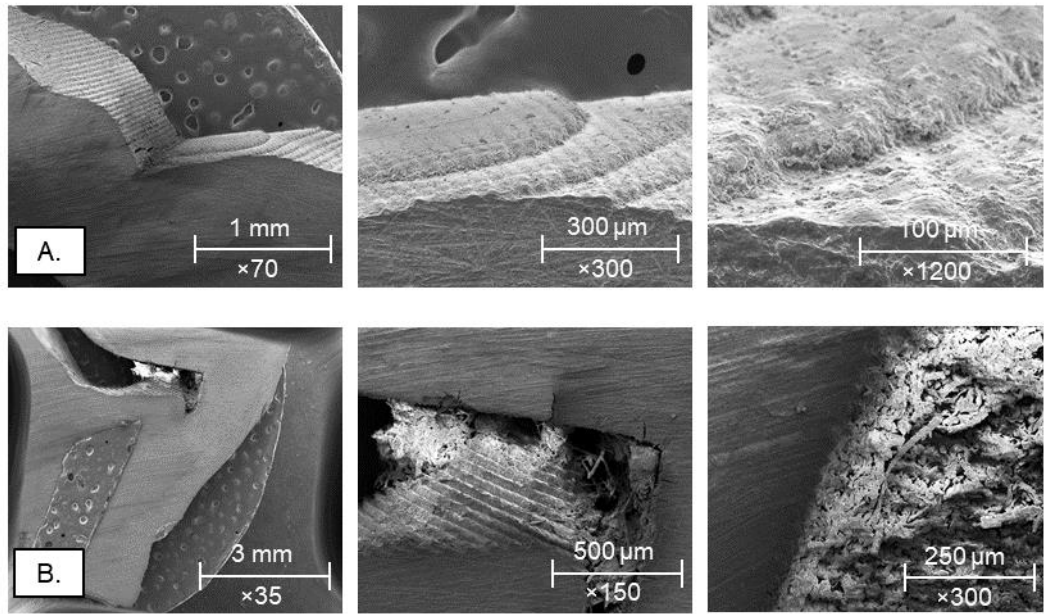
Figure 7.19: SEM images of the printed molar, 25 wt. % HAp and 25 wt. % GF. A. Occlusal surface. B. A void within the interface.

Results from the clinician cutting force experiment (Figure 7.20) showed the same trend seen prior in Section 4.3, and more force was used compared when using the automatic stage set-up. From the results, it can be established that the largest force seen when cutting was the 20 wt. % CHAp enamel with the 10 wt. % 352N dentine in the Z-axis, 1.79 N ($\pm$ 1.31), the least amount of force observed was when cutting 25 wt. % HAp enamel with the 5 wt. % CHAp dentine in the Y-axis direction, 1.09 N ($\pm$ 1.09). It was found there was no significant difference between the 25 wt. % GF and 10 wt. % 352N dentine groups; however, there were significant differences between the other dentine groups.
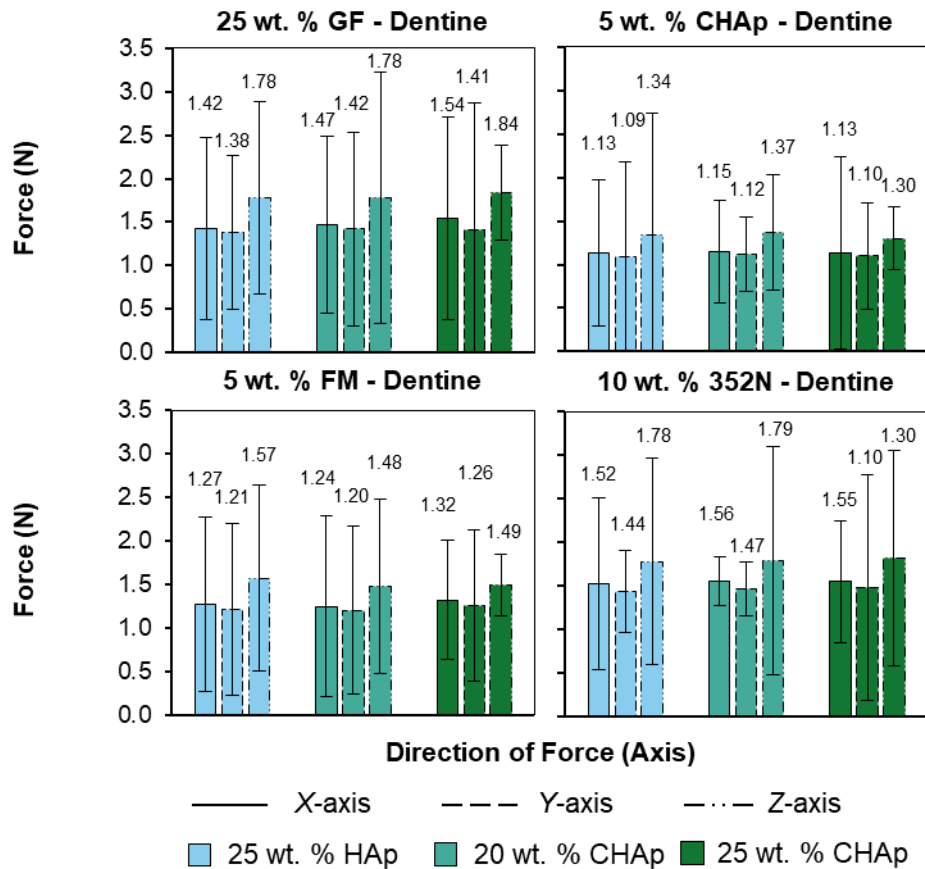
Figure 7.20: Mean force used by clinicians to cut composite photopolymers. Error bars presented as SD of the sample, *n* = 8.

7.4 Discussion

7.4.1 Composite Preparation

The selection of filler materials was based on conventional materials used in both dental research and the clinical setting. HAp has been previously reported to enhance mechanical properties in polymer composites, as well as CHAp, with evidence of CHAp being used in other commercial artificial teeth, as previously reported in Section 4.3 (Figure 4.21). BAG is commonly added to dental composites due to its effect on the mechanical properties as well as its influence on apatite formation (Tiskaya *et al.*, 2019), GF is noted as helping to prevent warping and shrinkage within polymers (Shahid *et al.*, 2011) and FM has been shown to have machinability properties which are useful in the development of ceramic crowns (Rashwan *et al.*, 2019). The Vitadur ceramic is

commonly used in restorations, veneers and denture preparations as they enhance mechanical properties, and also been noted to improve machinability (Fons Font *et al.*, 2006).

Data recorded from the absorbance and reflectance measurements showed a mirrored trend when increasing wt. %. For absorbance (Figure 7.4), as wt. % was increased, the amount of UV light absorbed decreased; however, as wt. % increased, reflectance also increased (Figure 7.5), suggesting as more particulates were added into the photopolymer, less UV light was absorbed and was reflected instead. This is easily explained, as the introduction of particulates within the photopolymer acts as competitor to the photoinitiator, an extra surface for the UV light to reflect off rather than being absorbed into the photopolymer. This would also explain the increased setting time, as wt. % increases, with more UV light being reflected, it takes longer for the photoinitiator to begin the photopolymerisation process. Figure 7.21 shows the relationship between reflectance and setting time, showing a linear trend between all material groups.
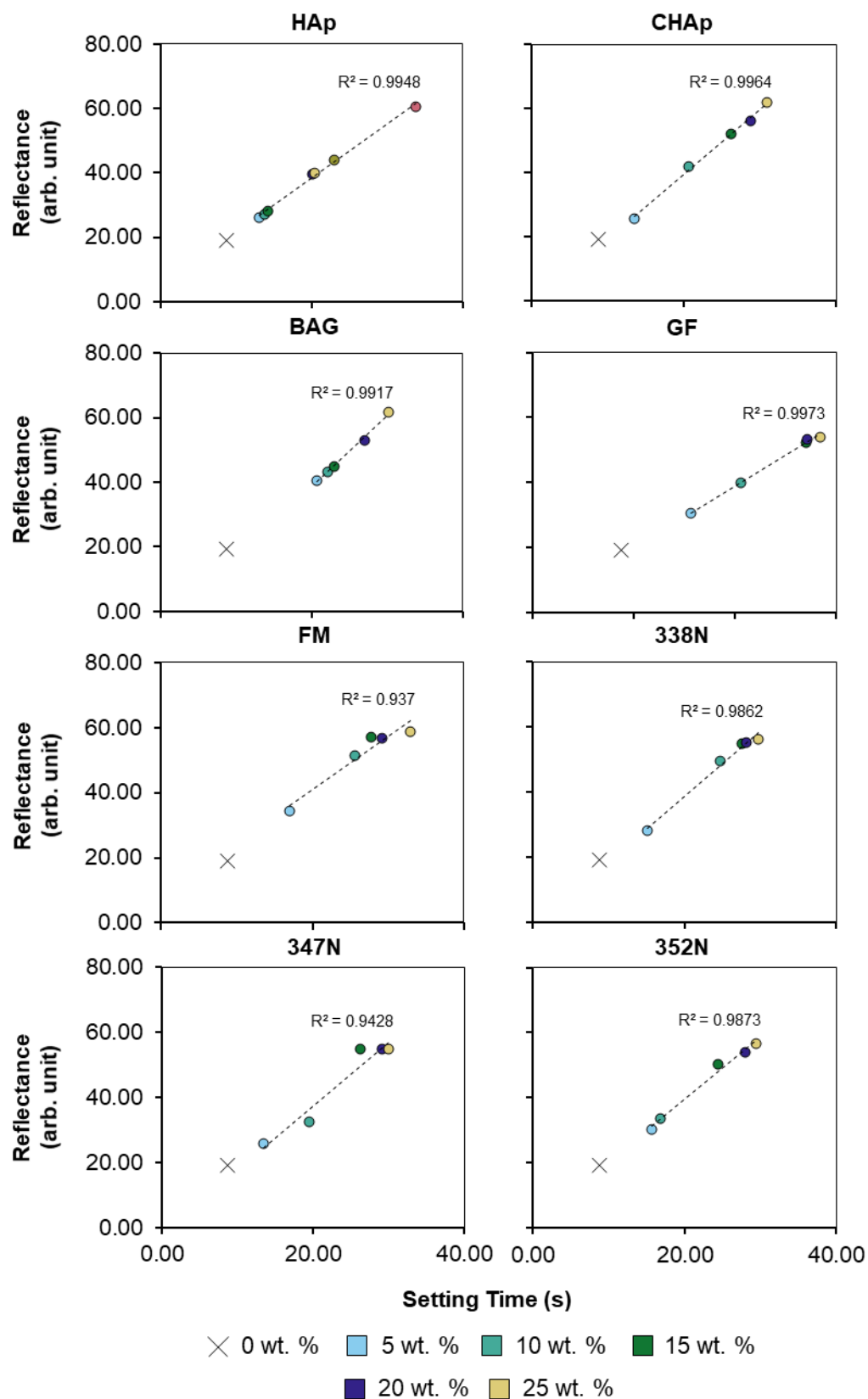
Figure 7.21: Reflectance plotted against setting time. A linear trendline was fitted, with the R^2 values referring to the data excluding 0 wt. % photopolymer.

The calculation of setting time allowed for the fine-tuning of curing settings for the composite photopolymers; with the specific settings tailored for each material and wt. % there were no difficulties in printing. Overall, however, this did increase printing times from 2 h to around 4-5 h. For the experiment, this was not an issue; however, when looking at a mass-producing point of view, the additional time means production cost also increases.

Figure 7.7 also demonstrated a positive correlation as wt. % increased the mean relative viscosity also increased. This can be explained by the presence of particulates aggregating and interacting preventing polymer flow, hence increasing the viscosity of the composite photopolymers, changing from Newtonian behaviour to non-Newtonian behaviour. Although measurements were recorded using the Zahn cup method, there is criticism of the use of this method and its inaccuracy; most literature recommends the use of a viscometer or a rheometer, for the measuring of viscosity (Harun *et al.*, 2009). However, for this experiment, the effect of an increased wt. % on viscosity was measured rather than obtaining absolute measurements for the viscosity of the photopolymers. This was proven useful, as when the photopolymers were prepared for printing, it was found that HAp composite photopolymers with a wt. % of > 30, proved incapable of printing, causing difficulties in the movement of the printing stage. These difficulties prevented a 50 μm gap between the print bed and the UV light, meaning inaccuracy in printing 50 μm resolution models. Therefore, it was decided to remove 30 wt. % and 35 wt. % from further testing.

7.4.2   Composite Testing

Particle size analysis showed that milling and sieving were successful in producing particle sizes below 38 μm (Figure 7.2); this was established as a crucial factor in printing the composites, as shown in Section 6.4.2. The XMT images (Figure 7.8-

Figure 7.10) also confirm not only the size of the particles but also the position and distribution of particles. Along with the SEM images (Figure 7.14), it can be seen that the majority of the particulates were up taken into the photopolymer and the space between the layers of the photopolymer (Figure 7.22).
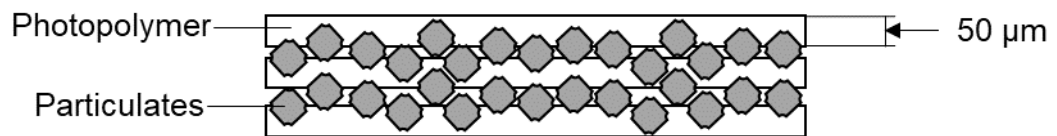
Figure 7.22: Diagram of the particulate position within the printed models.

Spectra collected through FTIR-ATR (Figure 7.12) and XRD (Figure 7.13) showed that filler material was present throughout the wt. %, with evidence of the filler material being observed around 10-15 wt. %. Although XRD spectra for the amorphous materials (BAG, GF, FM, 347N and 352N) was challenging to identify in the wt. %, the FTIR-ATR confirmed the presence of the materials. SEM (Figure 7.14) for the BAG at increasing wt. % showed an increased presence of spherical slab particulates, suggesting the increased wt. % was taken up into the 3D printed models. The SEM also confirmed the random placement of particulates as seen in the XMT. This random disbursement of particles has been noted previously to enhance mechanical properties (Eng *et al.*, 2017a; Eng *et al.*, 2017b), and within this study, an increase in hardness and Ē was observed as wt. % also increased.

In terms of hardness (Figure 7.15), the 0 wt. % photopolymer was recorded at 182.95 MPa ($\pm$ 10.84), in all instances of materials, the mean hardness increased with the introduction of particulate filler material, the biggest increase was seen in 5 wt. % 352N, with an increase of 383.92%, the lowest increase was seen in 5 wt. % BAG with a 15.65% increase. This was also seen in the measurements of Ē (Figure 7.16), 0 wt. % was recorded

at 833.82 MPa ($\pm$ 23.18), with the biggest increase from 0 to 5 w. % being FM, with an increase of 98.28%, and the smallest increase seen in CHAp with a 5.16% increase.

Figure 7.17 shows the required forces to cut the developed 3D printed materials, presenting the range of materials evaluated in this study as well as the different wt. % of reinforcement used to create the 3D printed composite teeth. A decrease in cutting force as the wt. % increase is observed across all samples. Of the 40 different compositions, three compositions closely matched ($\pm$ 0.02 N) the forces required to cut extracted enamel (0.31 N), specifically 25 wt. % HAp (0.31 N $\pm$ 0.06), 20 wt. % CHAp (0.32 N $\pm$ 0.06) and 25 wt. % CHAp (0.31 N $\pm$ 0.03). Four compositions closely matched ($\pm$ 0.02) the forces required to cut extracted dentine (0.49 N $\pm$ 0.15); 25 wt. % GF (0.49 N $\pm$ 0.13), 5 wt. % CHAp (0.47 N $\pm$ 0.18), 5 wt. % FM (0.51 N $\pm$ 0.10), and 10 wt. % Vitadur 352N (0.48 N $\pm$ 0.09).

As discussed previously in Section 6.4.2, this decrease in force as wt. % increases could be due to the increased presence of particulates and decreased amount of polymer, making the material more brittle than compared to 0 wt. %. From the hardness and $\bar{\text{E}}$ data, we can see that hardness is affected vastly more than $\bar{\text{E}}$ as wt. % increases, overall affecting the $\frac{H^3}{\bar{\text{E}}^2}$ ratio (mentioned in Section 4.4.3). Figure 7.23 shows the mean force required to cut the artificial teeth against the $\frac{H^3}{\bar{\text{E}}^2}$ ratio. A trend was observed for the composite teeth prepared in this study where increasing the wt. % resulted in a decrease in the cutting force, which was consistent across the range of material groups. Variations in data from the trend line are possible due to the presence of voids within the printed composites; however, analysis of the data in Figure 7.11 showed no significant difference in volume when comparing different material groups. One hypothesis was that the porosity was linked to the size of the particles (Figure 7.2); however, no correlation between particle size and porosity was noted. Distribution of particulates, however, could

be the reason in the variations. To prove this, more samples of the same wt. % and material should be imaged and analysed, a possible future experiment. 352N composites showed the biggest percentage decrease in force (53.57%) as wt. % increased, with GF composites showing the least change, 28.99%. Similar forces (± 0.02) seen between the 25 wt. % HAp, 20 wt. % CHAp, 25 wt. % CHAp, and extracted enamel. For extracted dentine, 25 wt. % GF, 5 wt. % CHAp, 5 wt. % FM, and 10 wt. % 352N had similar forces (± 0.02), as well as similar ratios. Our results, therefore, indicate that HAp, CHAp composites closely resemble enamel, whereas, GF, CHAp, FM, 352N composites require cutting forces that analogous to those required to cut through dentine.
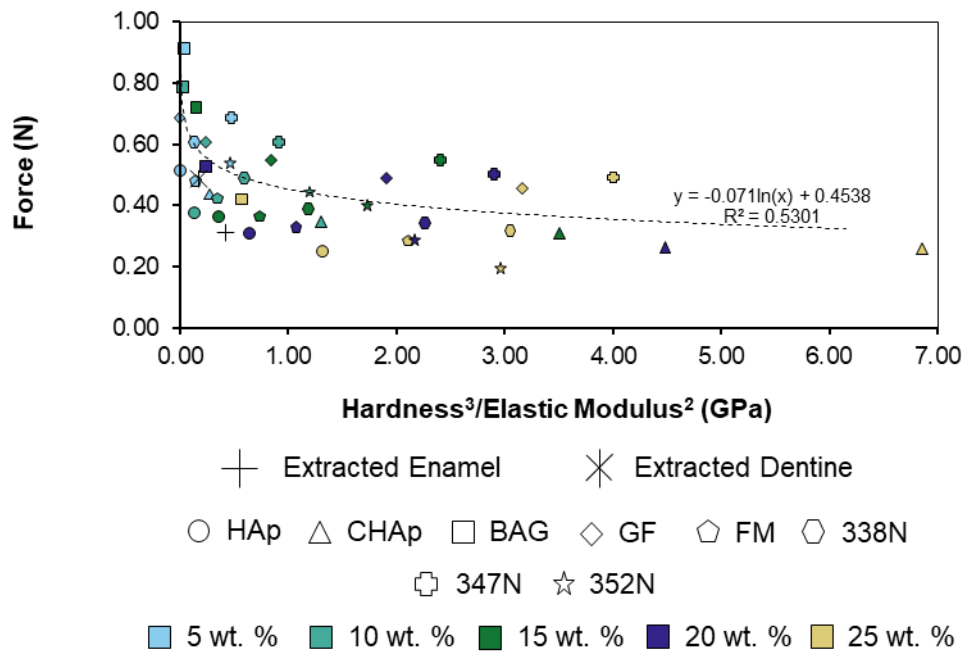
Figure 7.23: Average force required to cut composite teeth against $\frac{H^3}{\bar{E}^2}$. A logarithmic trendline was fitted, with the equations and R^2 values referring to the artificial teeth and extracted teeth values.

It is worth noting that the values do not match that as seen in Section 6.3, and were statistically significant, suggesting that geometry plays a part in the force cutting. Again, it is also worth noting that the sample shapes and sizes were different when measuring hardness and $\bar{E}$, explaining the difference in values.

7.4.3   Product Development

Once potential enamel and dentine analogues had been identified, the various enamel and dentine materials were mix and matched and combined to produce 12 different combinations. Each material was printed separately and fixed together with excess enamel material; the under-sizing of the dentine proved invaluable in fixing the materials together. However, from the XMT (Figure 7.18) and SEM images (Figure 7.19), there was evidence of large voids in the artificial enamel-dentine interface, due to pressure being released early before full curing took place, in future production, the enamel and dentine should be compressed together for longer to ensure complete curing has taken place. The addition of extra enamel material could be done incrementally on both structures before the enamel cap is placed on top; however, this would increase manufacturing time and lead to possible curing before assembly, meaning the enamel would not fix to the dentine.

From the clinician study, however, there were no apparent signs that the voids affected the force data being recorded. With the force data ranging from 1.09-1.44 N for the developed composites, extracted teeth ranged from 1.04-1.35 N and commercially available artificial teeth ranging from 2.20-3.71 N. The data between the three groups shows that the developed composites closely resemble that of extracted teeth than the commercial artificial teeth. Statistical analysis showed that there was no significant difference between the 25 wt. % GF and 10 wt. 352N dentine groups, however, there were differences recorded with the other dentine groups, suggesting that the dentine has a greater effect on the force required to cut than enamel. This finding is most likely because the dentine is the larger structure and more time is spent cutting this than the enamel structure which is 3-6 mm thick. However, differences between groups were negligible, the 5 wt. % CHAp dentine group overall recorded the closest match to extracted teeth. Although, there were no significant differences between the enamel groups within the 5

wt. % CHAp dentine, going forward, 20 wt. % HAp enamel would be the chosen material, as this requires the least amount of filler material to produce. In terms of manufacturing costs, this would be significant when looking into mass-producing these materials for creating mimetic artificial teeth for teaching and training.

7.5　Conclusions

In conclusion, the 3D printed composites produced from XMT imaging datasets using a range of particulate reinforcements also produced a range of cutting forces. Significantly, samples of HAp, CHAp and GF, CHAp, FM, 352 N required cutting forces that were comparable to enamel and dentine, respectively. A mechanical model previously introduced in Section 4.4.3 was shown to describe the relationship empirically between cutting force and the $\frac{H^3}{\bar{E}^2}$ ratio of mechanical properties, suggesting the importance of such a ratio over absolute material mechanical properties in defining a haptic response to cutting described from the mean cutting forces. Thus, 3D printed composite teeth that mimic the morphology, and the mechanical cutting response of extracted teeth were successfully produced. The next stage, however, would be to get feedback on these 3D printed teeth from clinicians and undergraduate dental students.

Chapter 8

Student's Perception of 3D Printed Models

This chapter explores the use of 3D printing and virtual reality as an educational tool, with a particular focus on students' thoughts and perception of the use of these tools in their education. Firstly, looking at how 3D printed models can be introduced and used in an undergraduate dental setting, in particular within anatomy and dental material modules. Secondly, investigating how students interact within a VR setting and how they feel this technology could be introduced into their education. Thirdly, asking students their opinions and feedback on the 3D printed artificial teeth developed in this project using the materials that closely resemble that of extracted enamel and dentine (Chapter 7).

This experimental work utilises published work from another author, the virtual tooth model published on Sketchfab by Davis (2018) when discussing VR. Permission was obtained from the author before use in this study.

8.1   Introduction

As mentioned previously, SBME is an established method used to ensure students and clinicians acquire the necessary skills needed for safe clinical practice (O'Brien *et al.*, 2016). This is an invaluable teaching skill in both the medical and dental field, as it allows participants to practise procedural skills in a realistic environment with no risk to patients. As discussed previously (Section 2.2), in undergraduate dentistry, this is typically carried out by dissections, prosections and the use of artificial teeth in phantom heads; however, as previously discussed, there are drawbacks to these techniques (Topp, 2004).

Anatomical models are also utilised in teaching anatomy; however, the limitation of these models is that they do not display anatomical difference (Sugand *et al.*, 2010). Therefore, the use of extracted teeth is seen as the gold standard, however, as discussed previously, recently, numbers of extracted teeth available to dental schools are in decline, so dental schools opt for artificial teeth, typodonts, which are typically mounted in a simulated head (phantom head) (Abu Eid *et al.*, 2013). Yet, although this method is utilised in dental schools, as this project has suggested and within previous literature (Abu Eid *et al.*, 2013; Al-Sudani & Basudan, 2016) students have difficulties in performing procedures on these artificial teeth due to the lack of realism and the increased force required to cut these. Therefore, the suggestion proposed in this project was a 3D printed alternative made from materials with similar cutting force than that of extracted enamel and dentine.

The use of 3D printing allows for clinical cases and situations to be replicated in a safe environment, and this is a useful tool in particular for clinicians, as it allows for the interaction of an individual patient's anatomy in a real environment multiple times. The literature on the use of 3D printing in SBME is growing, in particular, more recently Reymus *et al.* (2018) produced an available workflow for dental educational institutions with access to CBCT and 3D printing facilities to create resin teeth for endodontic teaching purposes. The authors asked the students the advantages of using these teeth compared to extracted teeth; the students rated the availability of these teeth higher (89%) over fairness due to standardisation (82%), more comfortable to practise all endodontics (67%) and hygiene (43%). Although the students recognised the advantages of producing teeth via 3D printing, the authors failed to ask the students their perceptions of these teeth, and whether they preferred these teeth compared to current artificial teeth their school used.

In another study, Hanafi *et al.* (2020) produced a modular 3D printed dental training model composing of 3D printed and extracted teeth, all for endodontic training.

Using a similar method that was outlined in Reymus *et al.* (2018), the authors collected CBCT data of a human skull and converted it into a .stl file; they then produced a lower jaw model with removable teeth which was presented to 68 students to perform root canal treatment on both the 3D printed teeth and the extracted teeth. The procedure was then subsequently evaluated, and it was found that overall, 85% of the teeth had acceptable treatment; however, the authors do not specify if this was on the 3D printed models or the extracted teeth. After carrying out the procedure, students were asked their perceptions on the model, and the overall consensus was that the students highly rated the training model despite it being more demanding, due to the lack of full visibility when placed within the phantom head. Overall, 96% of the students said they felt better prepared for the clinical situation and recommended the models' use in pre-clinical training and teaching. The authors concluded that the perceptions of the students were vital in evaluating this 3D printed model.

As well as 3D printing, VR has also emerged at the same time, often seen as competing technologies, VR offers a more virtual teaching method compared to the physical constraints of 3D printing (Redwood *et al.*, 2017). However, Erolin (2019) stated that although VR offers students a more in-depth learning experience (being able to manipulate and visualise more in 3D), the technology is expensive and quite in-effective for large study groups. The author recommended a combined teaching method of both 3D printing and VR to counteract the drawbacks of each technology.

Therefore, this study aims to provide students with 3D printed and VR models and to evaluate the perception of these technologies and whether they would recommend the use within pre-clinical teaching and training.

8.2 Materials and Methods

8.2.1 Model Preparation

All models (3D printed or VR) were prepared as outlined previously in Section 3.3, using data collected from extracted teeth. Models were modified in Meshlab and Autodesk Meshmixer before being exported to the appropriate slicing software (Section 3.3.1). All deciduous teeth were provided under ethical approval obtained from Queen Mary Research Ethics Committee (QMREC2011/62).

8.2.2 Questionnaire Design

All questionnaires were provided after participation was undertaken with either the 3D printed models or the VR set-up. Questionnaires provided were comprised of closed and open questions with Likert scale questions. Participants were informed before taking the questionnaires, that involvement was voluntarily, and that data was being collected for the purpose of research within this project.

8.2.2.1 Deciduous Tooth Anatomy

114 students (50 first year, 21 second year, 19 third year, 18 fourth year and 6 fifth year) undertaking a deciduous anatomy lecture were provided with natural deciduous teeth, and their enlarged 3D printed equivalents, the students were asked if they could identify the teeth and were then provided with a questionnaire asking them to rate the 3D printed models. The questionnaire presented to the students can be found in Appendix B.

8.2.2.2 Virtual Tooth Anatomy

The VR demonstration took place over two days (22nd-23rd June 2019) at the Institute of Dentistry Open Day, where 103 participants took part in the online questionnaire hosted on SurveyMonkey (SVMK Inc., USA). Participants included

undergraduate and postgraduate students as well as professionals, who all took part in the VR demonstration and were then asked to fill in the online questionnaire either with the laptop provided or at a later date using a QR code provided. The cut-off point for any submission was the 30th June 2019. The questionnaire presented to the participants can be found in Appendix B.

8.2.2.3   3D Printed Typodont Evaluation

Ten third-year undergraduate dental students were asked to evaluate the developed multi-material typodont, with the evaluation being carried out blind. Students were presented with two artificial teeth, a mandibular right first molar from Frasaco and a mandibular left first molar printed with the developed materials. Both teeth were nail varnished to prevent students from knowing which tooth was which; the teeth were subsequently labelled A and B. The teeth were mounted to a lower jaw model and students were asked to perform a Class I cavity preparation using a high-speed diamond bur on both teeth. The students were given no time constraints, and once completed, were asked to fill out a questionnaire. The questionnaire presented to the students can be found in Appendix B.

The evaluation of the 3D printed typodonts was limited to ten third-year undergraduate dental students due to the COVID-19 pandemic. Initially the study was designed to include more participants and focus groups to gather more feedback, however, the study was restricted to a questionnaire-based evaluation and limited contact with the participants.

8.3 Results

8.3.1 Deciduous Tooth Anatomy

XMT datasets were converted into 3D printed models utilising the methods outlined in 3.3. Eight different deciduous teeth were scanned and printed, including teeth with roots and reabsorbed roots; these were then scaled up to six times its original size, and were given to students and staff, along with extracted deciduous teeth. Figure 8.1 shows the models that were given to both students and staff.

Figure 8.1: 3D printed deciduous tooth models to a scale factor of six. *Top (Left to Right)* – Maxillary second molar, mandibular first molar, maxillary second molar, maxillary lateral incisor. *Bottom (Left to Right)* – Mandibular canine, mandibular first molar, maxillary canine, maxillary central incisor.

Overall, 127 participants took part in the questionnaire, 13 members of staff, 50 first year, 21 second year, 19 third year, 18 fourth year and 6 fifth-year undergraduate dental students. Figure 8.2 shows the responses that were received from the questionnaires and the distribution of answers between the different participants.

Question one (Figure 8.2.A) focussed on whether the participants would use the models given again, overall, 98% of participants said they would use the models again, with 2% responding no. The 2% was made up of one second-year student and one third-year student.

Question two (Figure 8.2.B) asked if the participants knew if the models were 3D printed, the majority of the responses were no, they were not aware (61%) with 39% of the participants aware the models were 3D printed.

Question three (Figure 8.2.C) was regarding the larger size of the models and whether the participants found it easier to understand and identify parts of the anatomy. The consensus from across the participants was that they strongly agreed with the statement (47%), 35% agreed, 10% neutral and 8% disagreeing with the statement (6% disagree, 2% strongly disagree).

Question four (Figure 8.2.D) was looking at the advantage of being able to hold and move the models freely (extracted deciduous teeth had to be handled with gloves), in understanding the anatomy. 62% of the participants strongly agreed with the statement, a further 32% agreed, 3% were neutral, and 5% disagreed (1% disagree, 2% strongly disagree).

Question five (Figure 8.2.E) was the statement "I could easily identify what the models were", the response with the largest percentage was 'agree' with 39%, neutral with 33%, 'strongly agree' with 25% and disagree with 3%, 'strongly disagree' recorded 0%.

Question six (Figure 8.2.F) directly compared the models with extracted deciduous teeth and asked the participants whether they preferred to use the models over

the extracted teeth. The answer with the largest response was neutral with 33%, 'agree' with 29%, 'strongly agree' 25%, 'disagree' with 10% and 'strongly disagree' with 3%.

Question seven (Figure 8.2.G) asked the participants what they liked most about the models; the question itself was open, allowing participants to add their own opinions. Five distinct answers came back from the participants; the models were cleaner than the extracted teeth (3%), the models had a high level of detail (25%), the size of the models (64%), the range of teeth on offer, for example, the use of teeth with reabsorbed roots (3%) and the shape of the teeth were considered to be realistic (3%). 3% of the participants opted not to answer the question.

Similar to question seven, question eight (Figure 8.2.H) asked the participants what they liked least about the models, again the question was open. Seven distinct answers were recorded; the models were cleaner than the extracted teeth (1%), the models lacked detail (17%), the models were too small (3%), the colour of the models, the participants asking for realistic colouring and shading (20%), more range of teeth, many participants asked for the permanent dentition to be printed as well (12%), some participants believed the shape was not realistic (8%) and that the models were too fragile (4%). 35% of the participants chose not to answer the question.

Question nine (Figure 8.2.I) wanted to know what the participants would change about the models. The answers that came back were similar to that of question eight's, with the participants saying they would change; the level of detail, asking for information on the model, i.e. why it was extracted? (11%), the size of the models, asking for larger sizes (7%), the colour of the models, more realistic colouring and shading (35%), more variety of teeth available (9%), more realistic shape (2%) and realistic scaling (1%). 35% chose not to answer the question.

Would you use the models provided again?
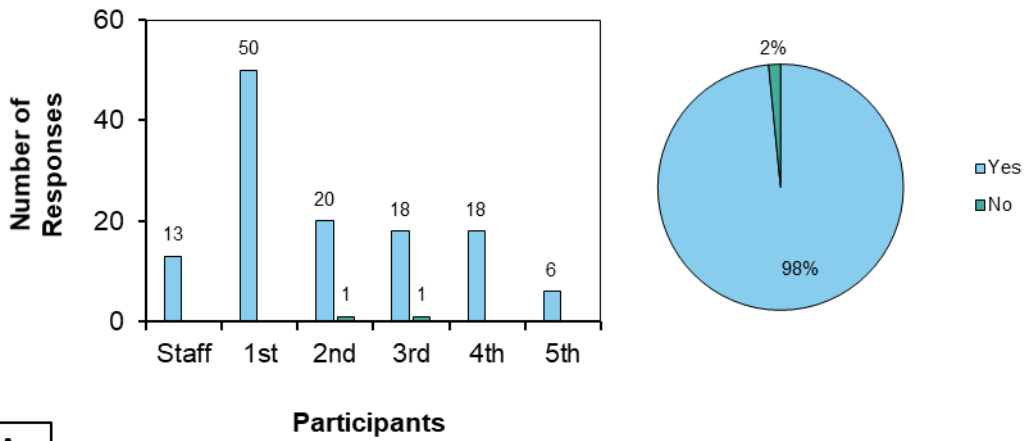
A.

Did you know that the models used in the session were 3D printed?
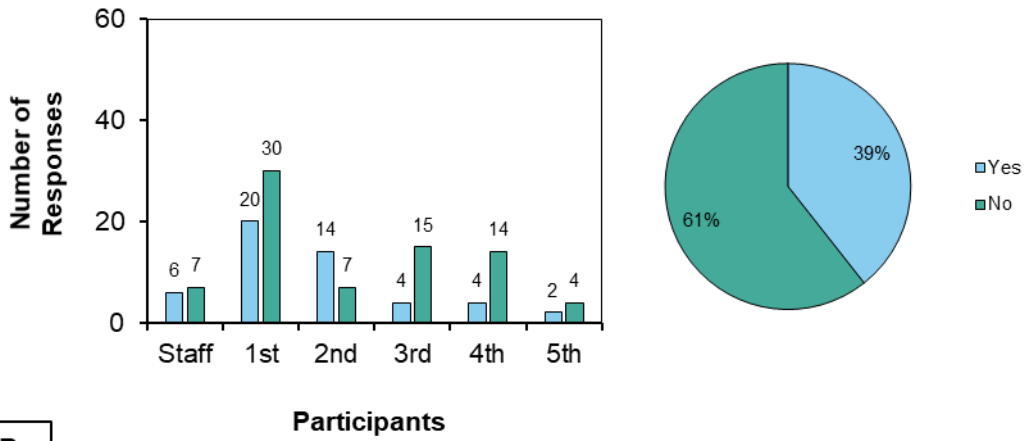
B.

The larger size of the models made it easier to understand the anatomy

C.

257
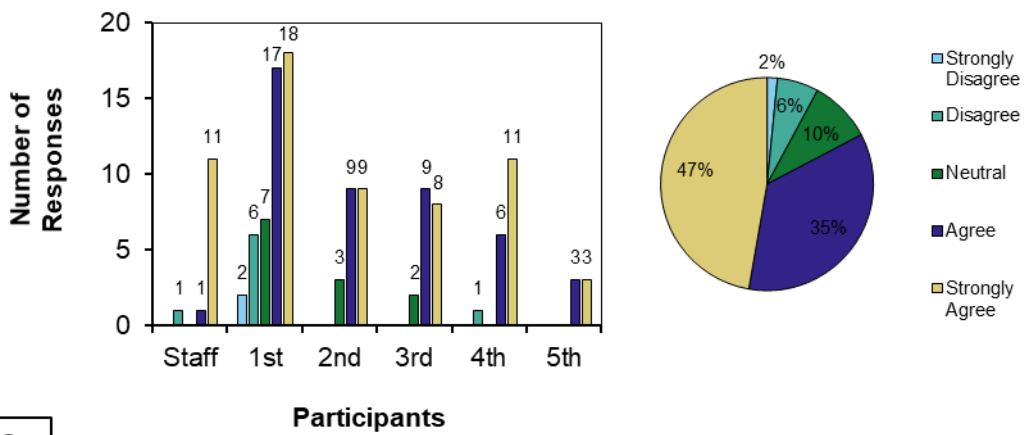
The ability to hold and move the models made it easier to understand the anatomy
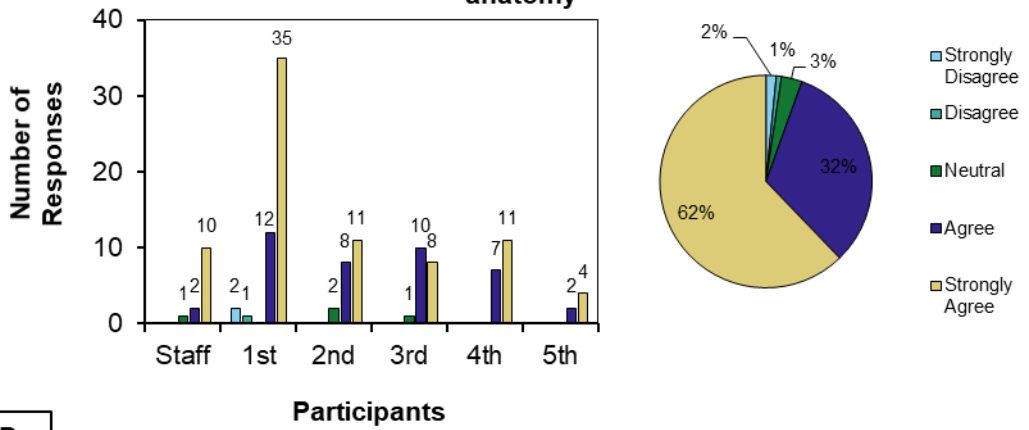
D.

I could easily identify what the models were
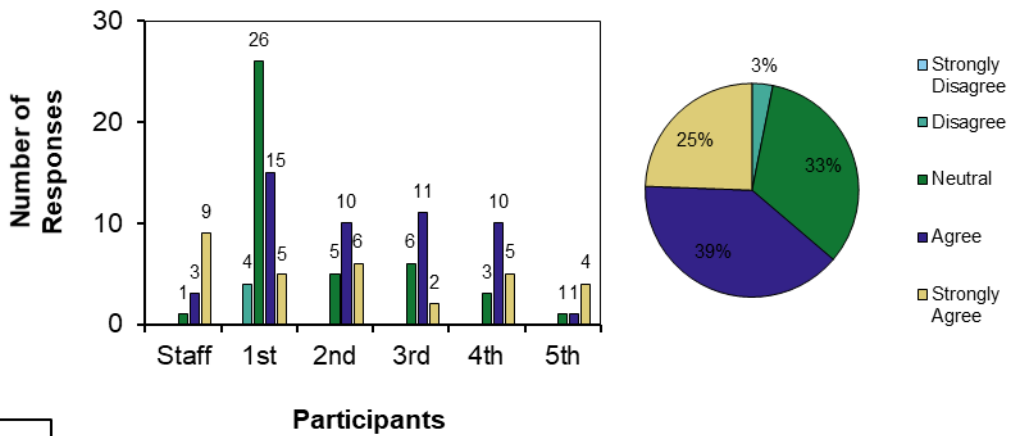
E.

I prefer to use the models compared to extracted teeth
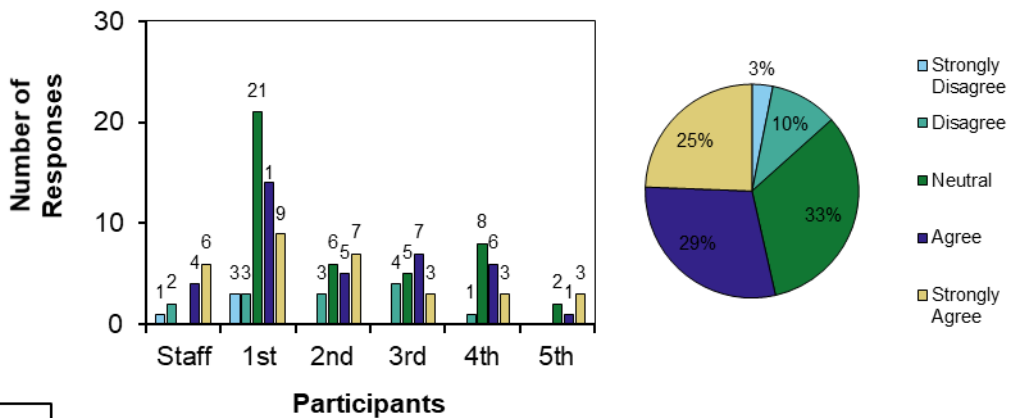
F.

What did you like the most about the models?
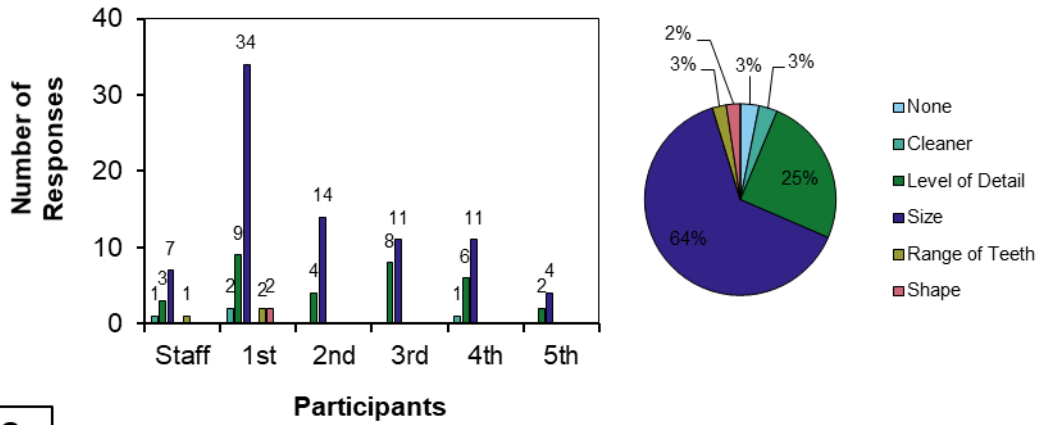
G.

What did you like the least about the models?

H.

259
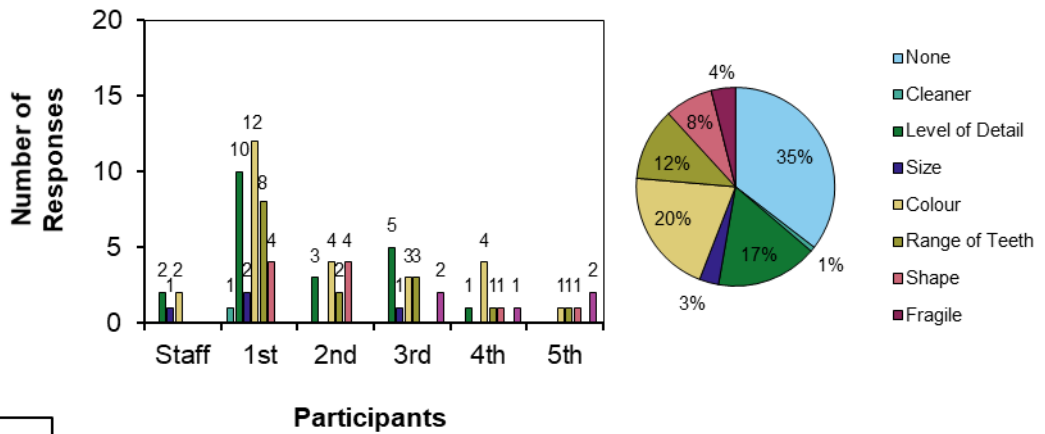
If any, what changes would you make to the models?
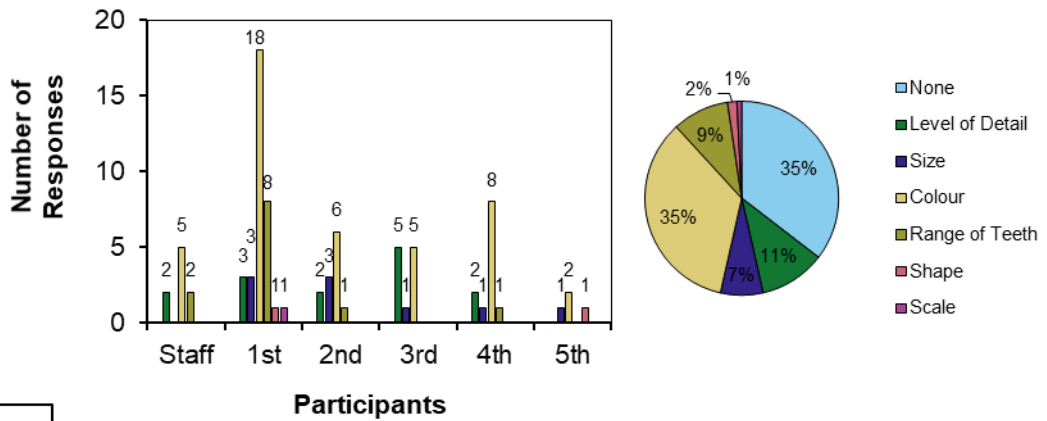
I.

Figure 8.2: Responses from the deciduous tooth model questionnaire. A. Would you use the models provided again? B. Did you know that the models used in the session were 3D printed? C. The larger size of the models made it easier to understand the anatomy. D. The ability to hold and move the models made it easier to understand the anatomy. E. I could easily identify what the models were. F. I prefer to use the models compared to extracted teeth. G. What did you like the most about the models? H. What did you like the least about the models? I. If any, what changes would you make to the models?

Question 10 of the questionnaire was left for any further comments, with many of the participants taking the chance to say they liked the models and also reiterating what they said in questions eight and nine.

8.3.2 Virtual Tooth Anatomy

Figure 8.3 shows the different views and points of interest of the VR tooth demonstration, where participants were taken with the demonstrator providing background information to each specific location.
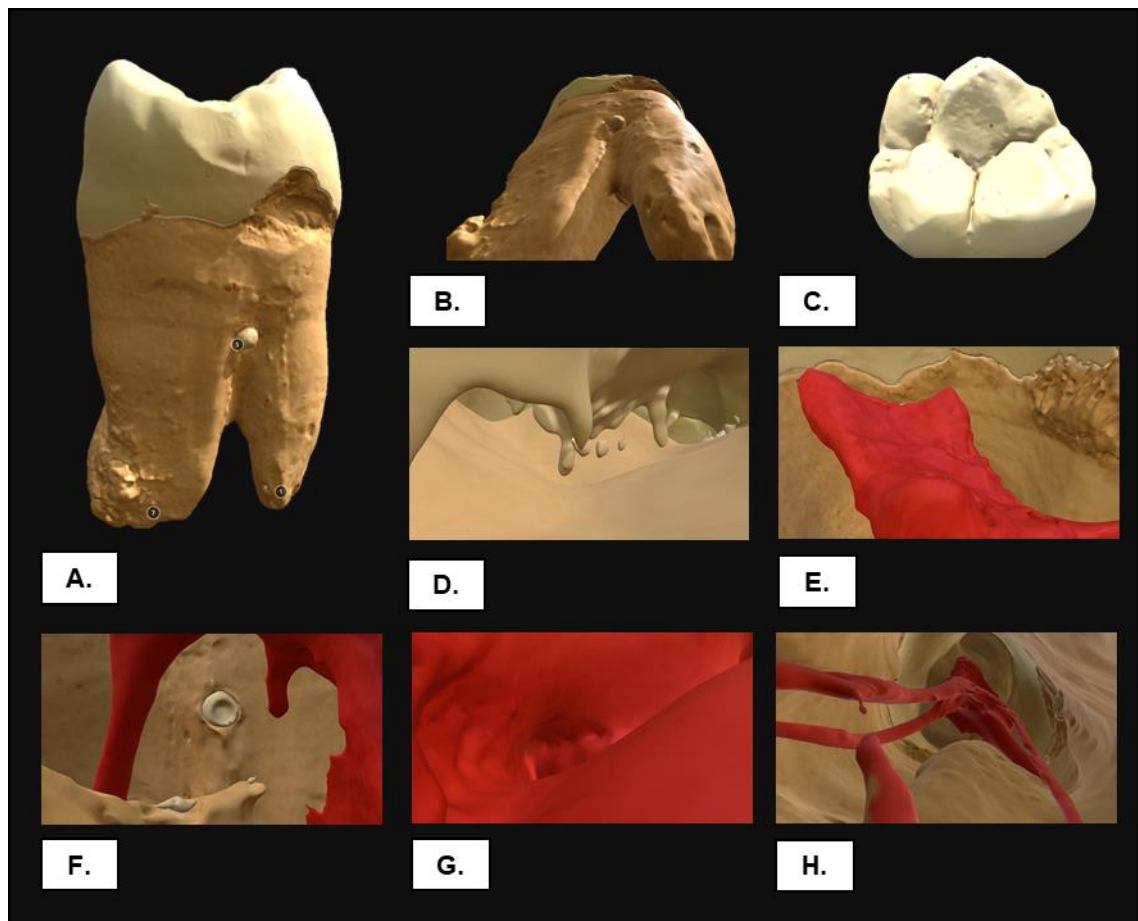
Figure 8.3: Views from the VR tooth demonstration developed by Davis (2018). A. View of the whole tooth model. B. View from the access canal of the root. C. View from the occlusal surface. D. View from inside the enamel. E. View from the dentine. F. View of an enamel pearl. G. View from inside the pulp chamber. H. View from the root apex.

Figure 8.4 shows the responses from the participants of the VR tooth demonstration; overall 103 took part in the questionnaire, question one asked the participants at which stage of education they were, the breakdown of the 103 participants were; 8 at GCSE stage, 64 at A-Level/BTEC stage, 16 were undergraduates, 7 were postgraduates, and 8 were qualified clinicians/professionals.

Question two (Figure 8.4.A) asked the participants if, before this demonstration, had they ever experience VR before, 52% of the participants had, with 48% of the participants first time being the tooth demonstration.

Question three (Figure 8.4.B) asked the participants on a scale of excellent to poor how would they rate the VR experience. 68% of all participants rated the experience excellent, with 27% rating is very good and 5% rating it good. None of the participants rated the experience fair or poor.

Question four (Figure 8.4.C) was regarding how informative the participants found the demonstration, rating from extremely information to not at all informative. 59% said they found the demonstration extremely information, 37% very information and 4% somewhat informative. None of the participants rated the demonstration not so or not at all informative.

Question five (Figure 8.4.D) looked at the comfortability of the headset, asking participants if they found the headset extremely comfortable to not at all comfortable. 58% found the headset extremely comfortable, 28% said very comfortable, and 14% said somewhat comfortable. None of the participants rated the headset, not so or not at all comfortable.

Question six (Figure 8.4.E) asked the participants if there was anything they liked most about the demonstration; the question was open to allow participants to add their own answers. 14% of the participants said they enjoyed the size of the tooth, and 19% said they enjoyed the detail of the model. 67% chose not to answer the question.

Question seven (Figure 8.4.F) asked where there was anything the participants liked least about the demonstration, again the question was left open for participants to add their own answers. 3% said there was not enough detail within the model, 3% said the colours were unrealistic, 4% were unhappy to queue for the demonstration, and 6% found the transition from one area of interest to another uncomfortable. 84% of participants chose not to answer the question.

Following on from question seven, question eight (Figure 8.4.G) asked if the participants what improvements should be made to the demonstration. 4% said they wanted more written details about the area of interest, 6% suggested a second headset, 4% recommended the introduction of sounds to the experience, and 5% suggested using realistic colouring. 81% of participants chose not to answer the question.

The final question, question nine (Figure 8.4.H) asked if the experience was made available online for free, would they recommend the tooth model, 100% of the participants said they would recommend the experience to others.

A.

B.
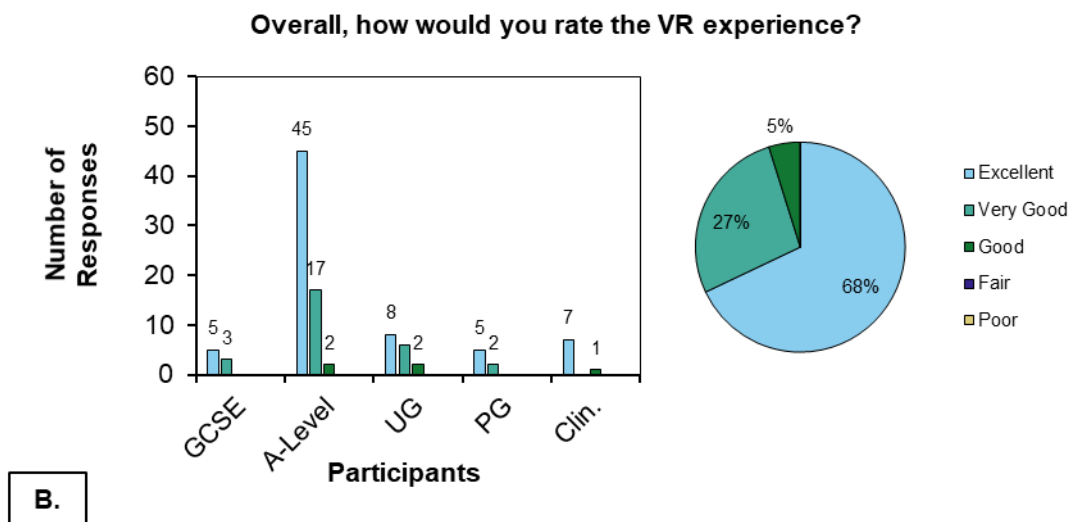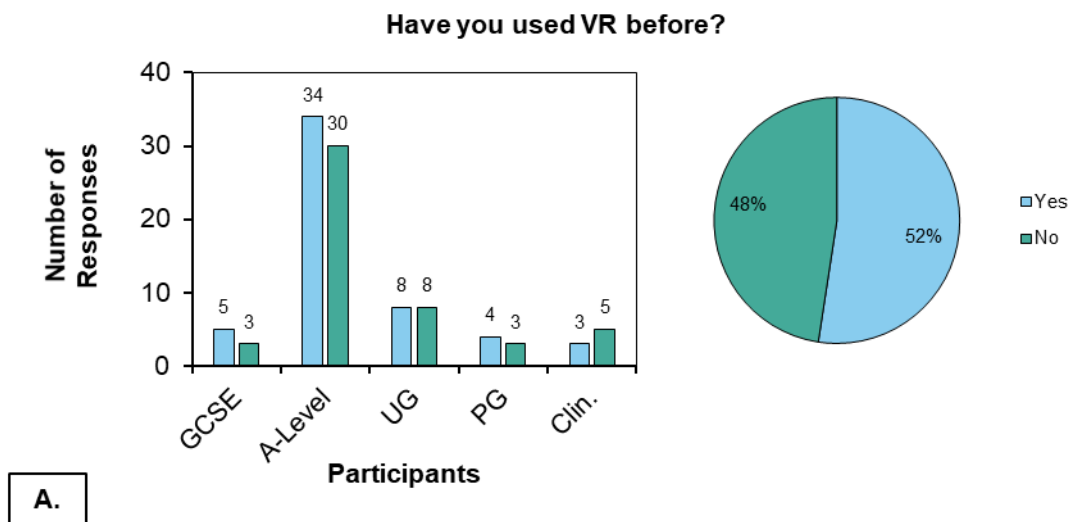
How informative did you find the VR experience?
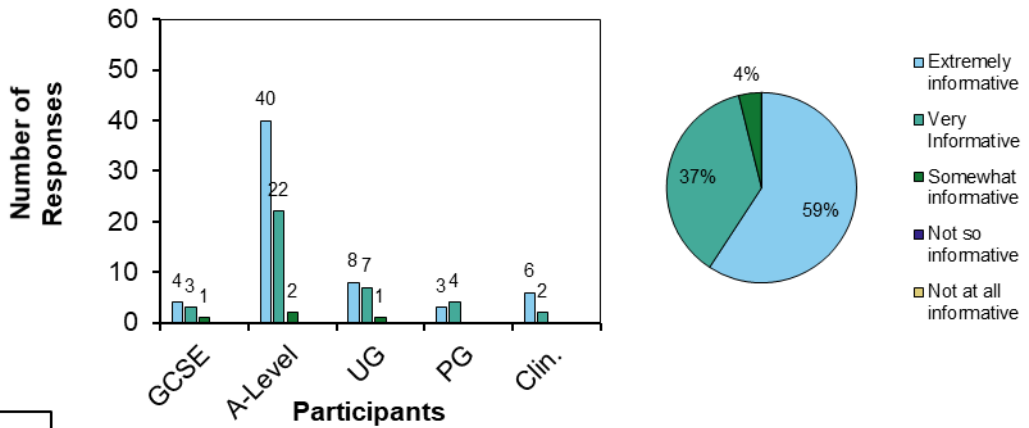
C.

How comfortable did you feel using the VR headset?
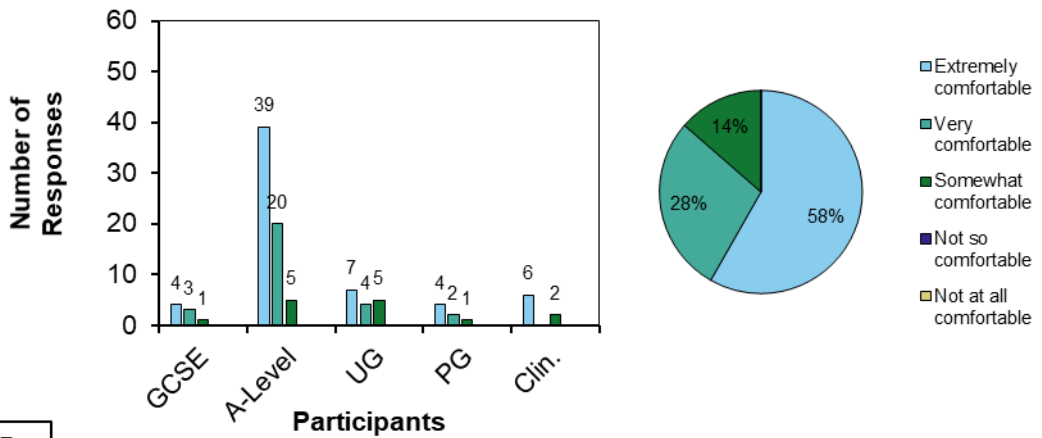
D.

Was there anything you liked the most about the VR experience?

E.
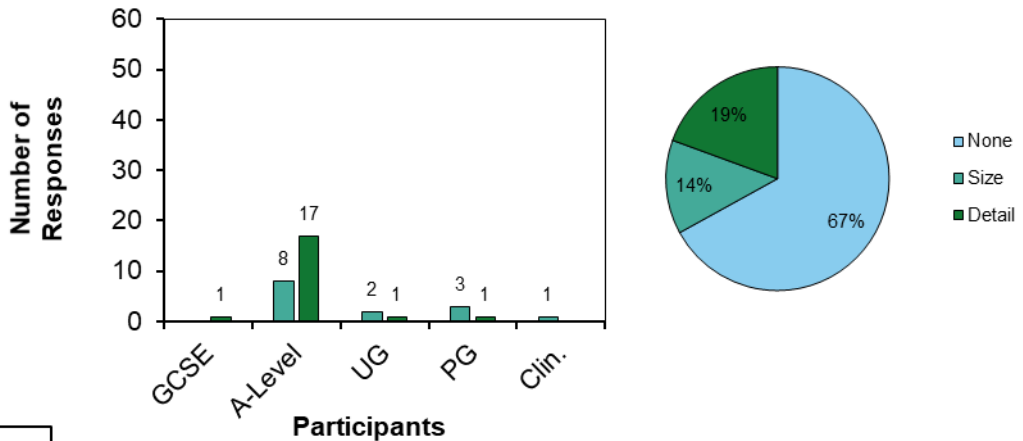
Was there anything you liked least about the VR experience?

F.

What improvements would you make?

G.

Finally, if this experience was available free online, would recommend to others?

H.
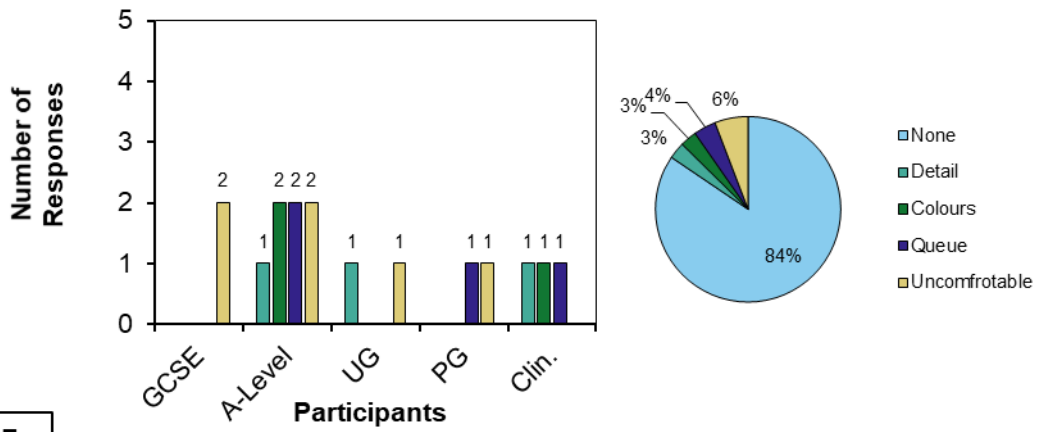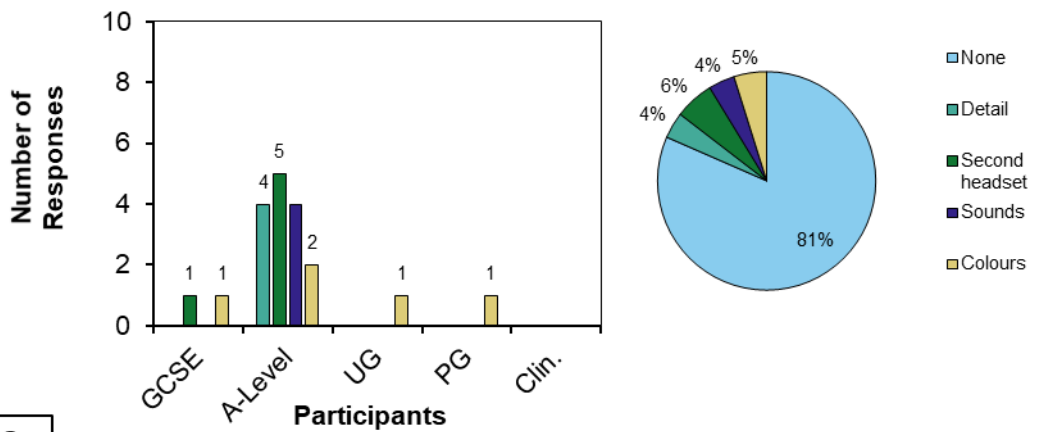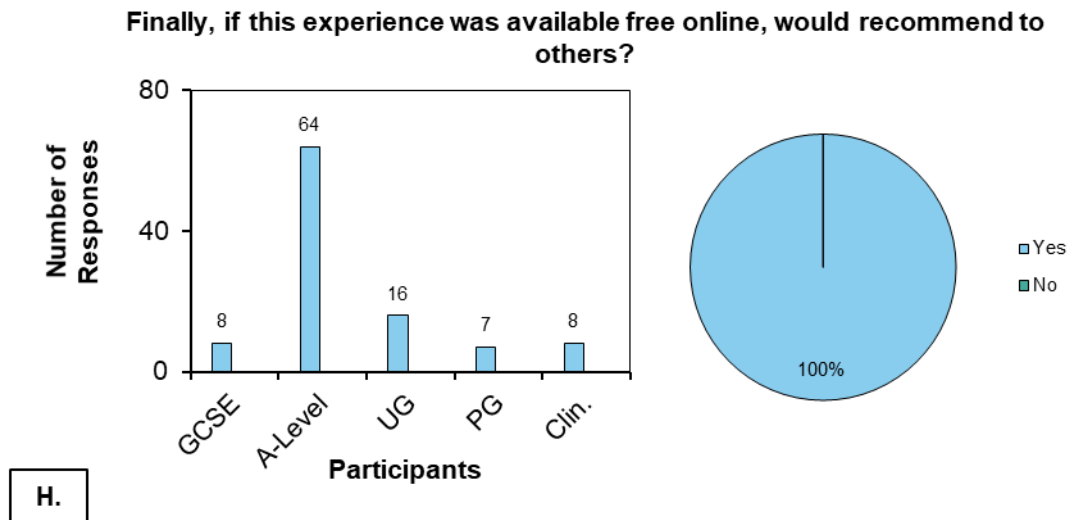
Figure 8.4: Responses from the VR tooth demonstration questionnaire. A. Have you used VR before? B. Overall, how would you rate the VR experience? C. How informative did you find the VR experience? D. How comfortable did you feel using the VR headset? E. Was there anything you liked the most about the VR experience? F. Was there anything you liked least about the VR experience? G. What improvements would you make? H. Finally, if this experience was available free online, would you recommend to others?

Similar to the questionnaire in Section 8.2.2.1, space was added at the end of the questionnaire to allow participants to add any further comments regarding the experience. Answers included how much they enjoyed the demonstration with others reiterating what they stated in questions eight and nine.

8.3.3   3D Printed Typodont Evaluation

The 3D printed composite typodonts were redesigned to have a Frasaco base to attach the 3D printed teeth to a Frasaco lower jaw model. Both mandibular first molars were painted with nail varnish as to ensure students were unable to identify the Frasaco and 3D printed typodonts and were then presented with both teeth attached to a lower jaw model (Figure 8.5). Students were then asked to perform a Class I cavity preparation and afterwards were presented with a questionnaire.
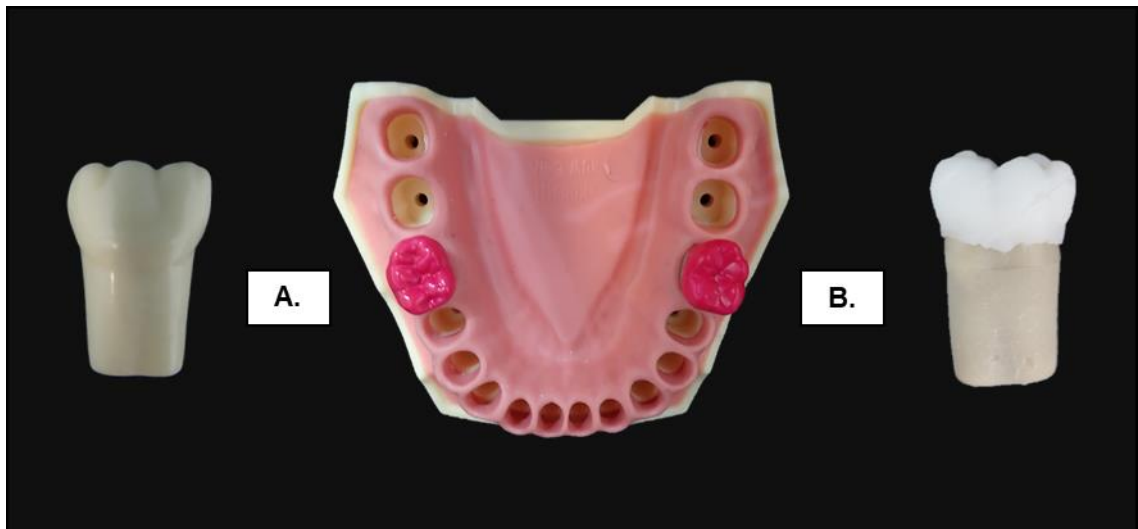
Figure 8.5: Mandibular first molars mounted in a lower jaw model. A. Mandibular right first molar (Frasaco typodont). B. Mandibular left first molar (3D printed typodont).

The questionnaire was given to 10 third-year undergraduate students who were asked to compare the developed 3D printed typodont with a Frasaco typodont. All students answered the questionnaires after performing a cavity preparation of both artificial teeth.

Question one (Figure 8.6.A) asked the participants which tooth was easier to cut, 100% of the participants stated that the tooth labelled B (3D printed tooth) was the easiest to cut.

Question two (Figure 8.6.B) asked the students to rate the tooth labelled A on a scaled of 1 to 10 on how the tooth compared to an extracted tooth when cutting, 1 being not at all and 10 being exactly the same. From the 10 responses, an average rating of 2.3 ($\pm$ 0.75) was acquired.

Question three (Figure 8.6.C) was the same as question two but asked students about the tooth labelled B, from the 10 responses, an average rating of 6.1 ($\pm$ 0.99) was acquired.

Question four (Figure 8.6.D) asked the participants which tooth they would prefer to use in the future, with the possibility of answering tooth A, tooth B or neither. Overall, 70% answered tooth B, with 30% answering neither, 0% answered tooth A.

Which tooth was easier to cut?
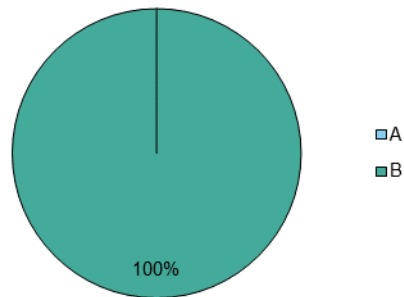
A.

On a scale of 1-10 how did tooth A compare to a real tooth in terms of cutting.

B.
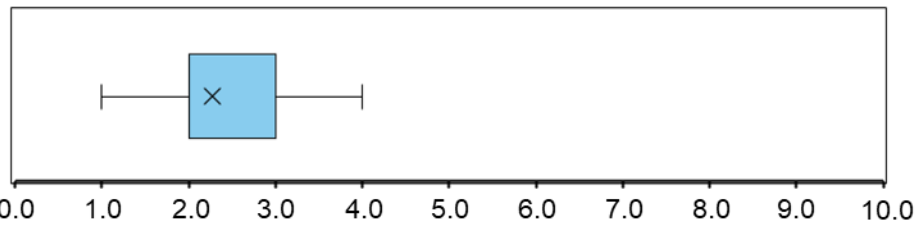
On a scale of 1-10 how did tooth B compare to a real tooth in terms of cutting.
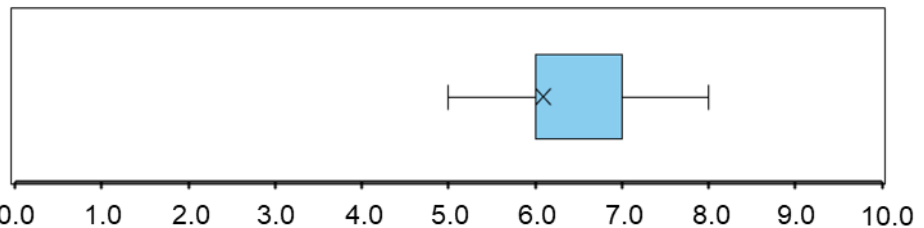
C.

Which tooth would you prefer to practise on in the future?
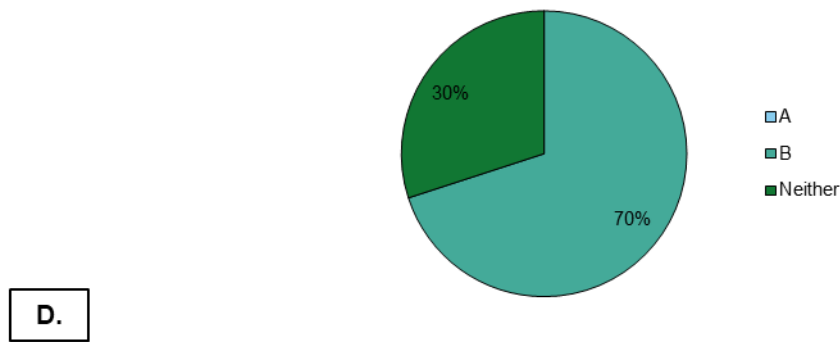
D.

Figure 8.6: Responses from the 3D printed typodont questionnaire. A. Which tooth was easier to cut? B. On a scale of 1-10, how did tooth A compare to a real tooth in terms of cutting? (1 = Not at all. 10 = Exactly the same). C. On a scale of 1-10, how did tooth B compare to a real tooth in terms of cutting? (1 = Not at all. 10 = Exactly the same). D. Which tooth would you prefer to practise on in the future?

Question five asked the participants, "if any, what improvements would you make to either of the teeth? If something specific to a particular tooth, please label which tooth you are referring to". The majority of the participants chose not to answer the question; however, two of the three participants that answered 'neither' for question four, wrote that they would prefer to use real extracted teeth in the future compared to artificial teeth.

8.4 Discussion

The use of tooth replicas is well established in dental education; however, there is a lack of 3D printed and VR models commonly used within dental schools (Hanafi *et al.*, 2020). Recent studies have established multiple routes in which these current technologies can be introduced, in this study we looked at the perceptions of students and how they interacted with 3D printed and VR models in an educational setting.

8.4.1 Deciduous Tooth Anatomy

Based on the feedback from the participants, overall, the students found the deciduous tooth models useful in understanding the anatomy. Deciduous teeth were

chosen due to their small and intricate anatomy, and it was hypothesised that if students were presented with larger models, then students would find it easier to identify the intricate anatomy of deciduous teeth. From the results 82% of the participants (47% strongly agree, 35% agree) found that the larger sizes helped to better understand the anatomy of deciduous teeth, with 94% (62% strongly agree, 32% agree) attributing the ability to hold and move the models to understand the anatomy better. Traditionally extracted deciduous teeth can be as small as 10 mm in length (or shorter if the roots are reabsorbed), making it challenging to identify key features, and being extracted, using extracted teeth have a potential risk of infection for students; therefore, PPE should be worn, and contact with the teeth is kept to a minimum. The ability to hold and feel the teeth helped to understand key features better and help to identify the teeth. Gadaleta *et al.* (2019) explored the use of 3D printed temporal bone as a tool for surgery simulation, the models themselves were manufactured in PLA, and the authors noted that surgeons benefitted more from the ability to hold and manipulate the models compared to studying from a textbook.

Question six asked whether the participants could easily identify the models; 39% of the responses agreed that they could easily identify the teeth; the second-highest response was 33% who neutral from the statement. The majority of the 'neutral' response came from the first-year cohort, and this can be easily explained by the fact the students were asked to identify these teeth from only experiencing a handful of deciduous anatomy classes. As the students' progress, in particular, the second to fourth-year students 'agree' with the statement compared to 'neutral' and with staff and fifth-year students answering 'strongly agree' compared to 'agree' and 'neutral', this is most likely due to extra years of training on deciduous teeth compared to the models themselves. However, due to the inconsistent sample sizes throughout the different levels of education, it is difficult to

conclude; moreover, in future studies, the sample size should be kept similar throughout the different levels of training to compare responses more accurately.

When asked about what the participants liked most about the models, size came out on top (64%), with this being the top response from all different stages of education, this response would corroborate the answers from question three. When asked, the participants stated that the colour was the thing that they liked least (20%) about the models, the models were prepared using a single colour resin, with 35% asking for different colouring and shading as an improvement, the addition of colour would be beneficial in immediately identifying problems such as cavities, however for future use of these models, colour can be artificially added to try and replicate realistic colouring as seen in Xiao *et al.* (2014). The second most common response was level of detail (17%), asking for more information regarding the teeth, for this study no additional information was given as the deciduous teeth were anonymised as per the requirements of the ethical approval. Despite this, for future reference, a QR code (2D barcode) could be added to the models, allowing students to scan the models that would redirect them to a site that had more information on the teeth, identifying critical parts of the anatomy as well as offering information on the reason for extraction. This recommendation could easily be paired with the technology seen in Section 8.2.2.2, allowing students to view the model in VR or AR and explore the anatomy in more depth.

Despite positive feedback on the enlarged models, and participants agreeing (25% strongly agree, 29% agree) that they would prefer to use the models over extracted teeth, the largest response was 33% 'neutral', suggesting that although students and staff liked the model, the use of extracted deciduous teeth is still essential in learning anatomy. This is a common perception amongst students found in multiple studies; Al-Sudani & Basudan (2016); Reymus *et al.* (2018); Hanafi *et al.* (2020). Although students could see the benefits of using alternatives such as 3D printed models over extracted teeth, the

consensus is that extracted teeth were still the 'gold standard' in learning anatomy as this offers the most realistic SBME, compared to artificial models. Allowing students to better understand and contextualise the anatomy.

8.4.2   Virtual Tooth Anatomy

From the online questionnaire, a total of 103 responses were recorded, with the majority of the participants being at A-level/BTEC level of education (62%), the event in which the demonstration was held was at an open day for prospectus students wishing to do undergraduate Dentistry at QMUL.

It is worth noting that the VR demonstration was used to access students' perceptions about the technology, this study was not used to evaluate its effectiveness compared to the 3D printed models discussed in the other studies.

It was found that 67% of the participants that had used a VR headset before the demonstration was more likely to answer extremely or very comfortable for question five (Figure 8.4.D). Suggesting a level of competency and comfortability when having previous experience with VR, when discussing with participants after the demonstration, the ones that answered, 'somewhat comfortable', explained that this was referring to the transition between areas of interest. It was decided before the demonstration that participants would be directed around the tooth by the demonstrator controlling via a keyboard rather than a handheld controller given to participants. This was to ensure, participants with no prior experience with VR would accidentally change settings which were controllable via the handheld controller.

It was found when participants were given the option of adding their answers to questions; a vast majority chose not to answer, question six (67%), question seven (84%) and question eight (81%). This is a common occurrence when participants are asked to

write answers rather than simply select a response (Boynton & Greenhalgh, 2004; Insight & Feedback Team, 2018). However, despite the significant 'none' response, the feedback regarding the VR demonstration was seen as generally positive, with 100% saying they would recommend the model to colleagues if made freely available online. Like the 3D printed deciduous models, participants rated size and level of detail when referring to aspects that they liked most about the demonstration. When asked about the elements they liked least about the demonstration, participants wanted to know more details regarding the tooth that the model was based on and the lack of realistic colouring, all responses similar to that obtained from the 3D printed deciduous teeth. Therefore, participants suggested more description be added to the numbered points that were used to navigate the users. This could easily be adapted for future demonstrations, as well as receiving input from clinicians on identifying critical aspects of the tooth. Other suggestions, included adding sounds to the model, sounds that would correspond to the material that they were standing on, currently, this level of editing is not available with the Sketchfab website; however, this could be a potential addition soon.

Other studies within the literature have shown positive feedback when using VR in a dental setting, but issues with availability and access are seen as an issue (Gottlieb *et al.*, 2011; de Boer *et al.*, 2015). In 2015, the University of Dundee's School of Dentistry published virtual models, created 3D interactive dental models on the website Sketchfab[2], to positive reception from students. These 3D interactive models have replaced traditional printed handouts and books by installing a computer at each station within the dissection room to provide bespoke dissection guides (Erolin, 2019). However, Erolin (2019) notes that typically, students, do not have access to high-end VR and AR set-ups at home, making the models challenging to be used in self-directed study. Despite this, VR and AR

---

[2] https://sketchfab.com/DundeeDental/models

have been shown increased interactivity and enjoyment amongst students (Moro *et al.*, 2017). Despite the demonstration being used as an outreach tool for dental anatomy rather than an undergraduate teaching tool, the responses from students show that students would be willing to use the technology again, possibly as a teaching method.

8.4.3   3D Printed Typodont Evaluation

When evaluating the students' opinions of the developed 3D printed artificial teeth, Frasaco artificial teeth were chosen as a comparison due to its use within the Institute of Dentistry at QMUL. The 3D printed typodont was manufactured to look like the Frasaco tooth and then both typodonts were painted, to ensure the evaluation was done blind and to ensure no bias. Ten third-year students were asked to take part in the questionnaire and to prepare Class I cavities in each tooth; third-year students were chosen due to their availability and their experience with preparing a Class I cavity (a skill learnt in the first year). It is suspected that different years groups may possibly have different views of the 3D printed typodonts, and for future studies it is recommended a wide range of different participants are used to get a more complete and accurate evaluation, however, despite COVID-19 restrictions, ten third-year students were able to participate, an ideal group of candidates because of their 'safe beginners' status.

The students stated that the 3D printed tooth was easier to cut, and when likened to extracted teeth, the 3D printed tooth ranked higher (6.1 ± 0.99) compared to the Frasaco tooth (2.3 ± 0.75). This vast difference in tactile similarity, it most likely due to the amount of force needed to cut the tooth, as previously established in Section 4.3 and Section 7.3. With extracted enamel requiring 0.31 N (± 0.12), Frasaco enamel requiring 0.69 N (± 0.21) and the 3D printed enamel requiring 0.36 N (± 0.03), this difference in force is reflected into the students' perception on ease of cutting as well as the tactile similarity between the extracted teeth and the 3D printed teeth.

274

Overall, 70% of students said they would be happy to use the 3D printed typodonts again in future simulated practises, 20% said they would prefer to use extracted teeth in future simulations, suggesting that extracted teeth are still a popular choice amongst students. However, due to the small sample size used in the feedback, it is difficult to conclude a final suggestion that these typodonts could be used as a replacement for Frasaco teeth, more feedback, as well as comparison to other commercially available artificial teeth, is required, before conclusions can be drawn. Future studies would focus on larger sample sizes; however, initial results show a promising perception from students when using the developed 3D printed teeth.

As mentioned previously (Section 8.2.2.3), the study was restricted by the COVID-19 pandemic, meaning access to participants was restricted to ten third-year undergraduates and a questionnaire-based study. Initially the study had intended to take focus groups from all years (first to fifth) to receive more in-depth feedback, to better understand how the students perceived the 3D printed typodonts and how they compared to the traditional artificial teeth they currently use. Following on from the students, the dental educators would be asked to evaluate the models, although this work was not carried out in this study, it will be recommended for future work (Section 9.2). However, if the other groups had been used it is assumed their perceptions would be different, for example, first-year students with no operative dental experience may struggle to use either the commercial or 3D printed typodont. Whereas a fifth-year may have a bias towards using all artificial teeth, after years of practice, or would be able to tell the difference between the commercial product or 3D printed typodont.

8.5   Conclusion

In conclusion, the need for an alternative to extracted teeth and dissections is required. Although artificial teeth and anatomical models offer a solution, there are many

limitations to these methods. The use of 3D printing and VR overcome these limitations, in particular to anatomical variety, and initial feedback gathered from this study, shows a willingness from students and staff to use these new innovative technologies. In terms, of tactile similarity, the developed 3D printed artificial teeth received positive initial feedback; however, a more extensive study needs to be conducted before the use of these teeth can be introduced in the teaching and training of undergraduate dental students.

Chapter 9

General Conclusions and Recommendations

This chapter is an overall summary of the conclusions drawn in Chapters 4, 5, 6, 7 and 8, reviewing what has been achieved throughout this study, as well as recommending future work to be carried out, based on what has been completed so far.

9.1 Conclusion

In summary, within this study, the tactile feedback when cutting extracted and artificial teeth were established, offering insight as to why students are 'unsatisfied' with commercial typodonts. A novel technique was devised to measure the force when cutting teeth, utilising an automatic set-up as well as using clinicians to cut the teeth. The findings showed that more force was required to cut the commercial typodonts compared to the extracted teeth; this was demonstrated in both the automatic and clinician experiments. With the clinician and non-clinician experiment, more than double the force was required to cut the artificial teeth; this was the case for both clinicians and non-clinicians demonstrating this was not resultant on biasedness. These initial findings helped to form the basis of how developed composites should compare and how typodonts could be improved, to give students a more realistic simulation.

An open-source method of converting XMT datasets into workable virtual 3D models was established and later used when creating 3D printed models and VR models of extracted teeth. The technique developed is like that used previously in other literature, and it was suggested that the accuracy when producing 3D printed models was dependent on multiple factors including the choice of 3D printing technology, highlighting the importance of correct parameter settings.

From the results of the initial composite material testing, it was found that either SLA or DLP was the most appropriate 3D printing techniques for developing a material suitable for cutting with a high-speed dental handpiece. FFF or SLS printed materials were deemed unsuitable due to their difficulties in cutting; however, in previous literature, it was found that these models may offer alternative SBME models. Although not suitable to be used as a haptic model, SLS produces high quality and accurate models that could be vital in teaching, whereas FDM offers a range of materials that could produce models with novel features (colour-changing structures, dissolvable structures).

The development of a 3D printable material reinforced with dental materials proved successful in recreating similar tactile feedback when cutting, this similarity in cutting force was seen to be based on the relationship between hardness and $\bar{E}$ rather than the mechanical properties individually. This 'brittleness' relationship suggested that the more brittle a material was, the less force was required to fracture the material. This mechanical relationship, as well as shape and geometry of the specimen, helped to recreate haptically similar materials. Typodonts were successfully created that both mimicked morphology and mechanical cutting responses, based on HAp and CHAp materials.

Students' perceptions of 3D printed, and VR models were investigated, and typically students perceived these models positively, suggesting their future use within dental education along with suggested improvements from the students. Initial feedback of the 3D printed typodonts suggested students favoured the 3D printed teeth over a commercial product, forming the basis for future studies involving a larger sample size and these developed typodonts.

9.2 Recommended Future Work

- The study was limited by the sample size of the final feedback for the developed typodonts, therefore, a future study involving a larger cohort of students as well as education providers to establish the suitability of the 3D printed teeth in dental education. Additionally, to also explore other procedures such as crown preparations and endodontic treatment.

- Although initially mentioned and investigated, the development of endodontic SBME models utilising the developed 3D printed typodonts should be explored. The addition of a hydrogel pulp would help to establish a realistic SBME model and the ability to modify the pulp anatomy through editing software would help to develop varying degrees of difficulties for students.

- The use of the Formlabs Ceramic Resin in Section 6.3, initially showed force feedback not too dissimilar to that of extracted tissue, more similar forces could be obtained through a firing process. The resin is intended to be fired within a furnace; a process designed to burn off much of the polymer leaving the ceramic particles behind. This process, in theory, should make the material more brittle, and in return, should decrease the force required to cut. This process could also be investigated for the materials developed within this study.

- The aesthetics of the 3D printed typodonts were not thoroughly investigated; therefore, a future recommendation would be to explore the possibility of introducing artificial colouring and shading to recreate a realistic aesthetic. The addition of a thin varnish or glaze to enamel could help to provide a more 'porcelain' effect to the enamel structure.

- Initial feedback of the 3D printed and VR models was positive and demonstrated students' willingness to use the technologies again; future studies could

investigate the effect of utilising these models on students' performance and whether the models help students to learn.

List of References

Abu Eid, R., Ewan, K., Foley, J., Oweis, Y., & Jayasinghe, J. (2013). Self-directed study and carving tooth models for learning tooth morphology: perceptions of students at the University of Aberdeen, Scotland. *Journal of Dental Education, 77*(9), 1147-1153.

ADEE. (2016). SIGT-02: 'Biomedical Sciences in Dentistry: Developing a Contemporary Core Curriculum'.

Ahmed, F. (2011). *Multiscale Quantitative Imaging of Human Femoral Heads Using X-ray Microtomography.* (PhD), Queen Mary University of London, London.

Ahmed, M. (2010). *X-ray Microtomography Study of Carious Dentine and a Comparison of its Removal by Three Techniques.* (PhD), Queen Mary University of London, London.

Ahmed, M., Davis, G. R., & Wong, F. S. L. (2012). X-Ray Microtomography Study to Validate the Efficacies of Caries Removal in Primary Molars by Hand Excavation and Chemo-Mechanical Technique. *Journal of Caries Research, 46*(6), 561-567.

Al-Khayyat, F. (2018). Tooth Morphology and How to Identify. In Queen Mary University of London (Ed.). London, UK: QMUL.

Al-Sudani, D. I., & Basudan, S. O. (2016). Students' Perceptions of Pre-Clinical Endodontic Training with Artificial Teeth Compared to Extracted Human Teeth. *European Journal of Dental Education, 21*(4), e72-e75.

Al Qahtani, S. J., Hector, M. P., & Liversidge, H. (2010). The London Atlas of Human Tooth Development and Eruption. *American Journal of Physical Anthropology, 142*, 481-490.

Al Shwaimi, E., & Narayanaraopeta, U. (2014). Effect of time on electronic working length determination with a novel endodontic module in preclinical endodontic training. *Saudi Journal of Medicine and Medical Sciences, 2*(37).

Allen, L. K., Bhattacharyya, S., & Wilson, T. D. (2015). Development of an interactive anatomical three-dimensional eye model. *Anatomical Sciences Education, 8*(3), 275-282.

Amin, M., Zulla, R., Gaudet-Amigo, G., Patterson, S., Murphy, N., & Ross, S. (2017). Dental Students' Perceptions of Learning Value in PBL Groups with Medical and Dental Students Together versus Dental Students Alone. *Journal of Dental Education, 81*(1), 65-74.

Amini, S., & Miserez, A. (2013). Wear and abrasion resistance selection maps of biological materials. *Acta Biomaterialia, 9*, 7895-7907.

Angjellari, M., Tamburri, E., Montaina, L., Natali, M., Passeri, D., Rossi, M., & Letizia Terranova, M. (2017). Beyond the Concepts of Nanocomposites and 3D Printing: PVA and Nanodiamonds for Layer-by-layer Additive Manufacturing. *Materials and Design, 119*, 12-21.

Angker, L., Swain, M. V., & Kilpatrick, N. M. (2005). Characterising the micro-mechanical behaviour of the carious dentine of primary teeth using nano-indentation. *Journal of Biomechanics, 38*(7), 1535-1542.

Arai, S., Tsunoda, S., Kawamura, R., Kuboyama, K., & Ougizawa, T. (2017). Comparison of crystallization characteristics and mechanical properties of poly(butylene terephthalate) processed by laser sintering and injection molding. *Materials & Design, 113*, 214-222.

ASTM International. (2015). Additive manufacturing - General principles - Terminology. In *ISO/ASTM 52900:2015*.

Atwell, C. (2017). 3D Printing and VR: A New Spin on Design and Manufacturing. Retrieved from http://www.machinedesign.com/3d-printing/3d-printing-and-vr-new-spin-design-and-manufacturing

Avery, J. K., & Chiego, D. J. (2006). *Essentials of Oral Histology and Embryology: a clinical approach*. Missouri, USA: Elsevier.

Aziz, M. A., McKenzie, J. C., Wilson, J. S., Cowie, R. J., Ayeni, S. A., & Dunn, B. K. (2002). The human cadaver in the age of biomedical informatics. *The Anatomical Record, 269*(1), 20-32.

Bacali, C., Badea, M., Moldovan, M., Sarosi, C., Nastase, V., Baldea, I., . . . Constantiniuc, M. (2019). The Influence of Graphene in Improvement of Physico-Mechanical Properties in PMMA Denture Base Resins. *Materials, 12*(14), 1-13.

Bacro, T. R., Gebregziabher, M., & Ariail, J. (2013). Lecture recording system in anatomy: possible benefit to auditory learners. *Anatomical Sciences Education, 6*(6), 376-384.

Baghdady, M. T., Carnaham, H., Lam, E. W., & Woods, N. N. (2014). Dental and dental hygiene students' diagnostic accuracy in oral radiology: effect of diagnostic strategy and instructional method. *Journal of Dental Education, 78*(9), 1279-1285.

Bakr, M. M., Thompson, C. M., & Massadig, M. (2017). Anatomical sciences: A foundation for a solid learning experience in dental technology and dental prosthetics. *Anatomical Sciences Education, 10*(4), 395-404.

Balooch, G., Marshall Jr, G. W., Marshall, S. J., Warren, O. L., Asif, S. A. S., & Balooch, M. (2004). Evaluation of a new modulus mapping technique to investigate microstructural features of human teeth. *Journal of Biomechanics, 37*(8), 1223-1232.

Becker, A. (2012). *Orthodontic Treatment of Impacted Teeth*. Sussex, UK: Wiley & Sons Ltd.

Bera, O., Pilić, B., Pavličević, J., Jovičić, M., Holló, B., Mészáros Szécsényi, K., & Špirkova, M. (2011). Preparation and thermal properties of polystyrene/silica nanocomposites. *Thermochimica Acta, 515*(1-2), 1-5.

Berkovitz, G. R. H., & Moxham, B. J. (2009). *Oral Anatomy, Histology and Embryology*. Sussex, UK: Elsevier.

Bernabe, E., & Sheiham, A. (2014). Tooth loss in the United Kingdom--trends in social inequalities: an age-period-and-cohort analysis. *PLOS ONE, 9*(8), e104808.

Bertram Broberg, K. (1999). Physical and Engineering Aspects of Fracture. In *Cracks and Fracture* (pp. 544-623). Dublin, Ireland: Elesiver.

Beuselinck, L., Govers, G., Poesen, J., Degraer, G., & Froyen, L. (1998). Grain-Size Analysis by Laser Diffractometry: comparison of the sieve-pipette method. *Catena, 32*, 193-208.

Bitter, K., Gruner, D., Wolf, O., & Schwendicke, F. (2016). Artificial Versus Natural Teeth for Preclinical Endodontic Training: a randomized controlled trial. *Journal of Endodontics, 42*(8).

Black, G. V. (1904). *A Work on Operative Dentistry; the technical procedures in filling teeth*. Woodstock, Illinois: Medico-Dental Publishing Company.

Bogacki, R. E., Best, A., & Abbey, L. M. (2004). Equivalence study of a dental anatomy computer-assisted learning program. *Journal of Dental Education, 68*(8), 867-871.

Bortolotto, C., Eshja, E., Peroni, C., Orlandi, M. A., Bizzotto, N., & Poggi, P. (2015). 3D Printing of CT Dataset: Validation of an Open Source and Consumer-Available Workflow. *Journal of Digital Imaging, 29*, 14-21.

Boyde, A. (1964). *The Structure and Development of Mammalian Enamel.* (PhD), University of London, London, UK.

Boyde, A. (1980). Electron microscopy of the mineralizing front. *Metabolic Bone Disease and Related Research*, 69-78.

Boyde, A. (1989). Enamel. In B. K. B. Berkovitz, A. Boyde, R. M. Frank, H. J. Hohling, B. J. Moxham, J. Nalbandian, & C. H. Tonge (Eds.), *Handbook of Microscopic Anatomy*. Berlin, Germany: Springer-Verlag.

Boyde, A. (1998). Cross-Striations Revisited: Backscattered Electron Imaging of Human and Equine Enamel Mineralisation. *Connective Tissue Research, 38*, 43.

Boyde, A. (2003a). Improved digital SEM of cancellous bone: scanning direction of detection, through focus for in-focus and sample orientation. *Journal of Anatomy, 202*(1), 183-194.

Boyde, A. (2003b). The real response of bone to exercise. *Journal of Anatomy, 203*(1), 173-189.

Boyde, A. (2007). Microstructure of Enamel. In D. J. Chadwick & G. Cardew (Eds.), *Ciba Foundation Symposium 205*. Sussex, UK: Wiley & Sons Ltd.

Boyde, A., & Jones, S. J. (1996). Density of Mineralisation of Lumber Vertebral Body Bone by Digital Backscattered Electron (BSE) Imaging. *Bone, 19*(3 Supplement), 132S.

Boynton, P. M., & Greenhalgh, T. (2004). Selecting, Designing, and Developing your Questionnaire. *British Medical Journal, 328*, 1312-1315.

Brand, R. W., & Isselhard, D. E. (2014). *Anatomy of Orofacial Structures: A comprehensive Approach* (Seventh ed.). Missouri, USA: Elsevier Inc.

Brennan, D. S., & Spencer, A. J. (2005). The role of dentist, practice and patient factors in the provision of dental services. *Community Dentistry and Oral Epidemiology, 33*(3), 181-195.

Burde, A.-V., Constantiniuc, M., & Campian, R.-S. (2015). Applications of RepRap Three-Dimensional Printers in Dentistry - A Literature Review. *International Journal of Medical Dentistry, 5*(1), 37-43.

Burk, D. T., Lee, L. M., & Lambert, H. W. (2013). Embryology and histology education in North American dental schools: the Basic Science Survey Series. *Journal of Dental Education, 77*(6), 744-756.

Bustamante, S., Bose, S., Bishop, P., Klatte, R., & Norris, F. (2014). Novel Application of Rapid Prototyping for Simulation of Bronchoscopic Anatomy. *Journal of Cardiothoracic and Vascular Anaesthesia, 28*(4), 1122-1125.

Cameron, J. R., & Skofronick, J. G. (1978). *Medical Physics*. New York: John Wiley & Sons.

Cantín, M., Munoz, M., & Olate, S. (2015). Generation of 3D tooth models based on three-dimensional scanning to study the morphology of permanent teeth. *International Journal of Morphology, 33*(2), 782-787.

Cevik, P., & Yildirim-Bicer, A. Z. (2016). The Effect of Silica and Prepolymer Nanoparticles on the Mechanical Properties of Denture Base Acrylic Resin. *Journal of Prosthodontics, 27*(8), 763-770.

Cherukara, G. P., Davis, G. R., Seymour, K. G., Zou, L., & Samarawickrama, D. Y. D. (2005). Dentin Exposure in Tooth Preparation for Porcelain Veneers: A Pilot Study. *Journal of Prosthetic Dentistry, 94*, 414-420.

Chhaya, M. P., Poh, P. S. P., Balmayor, E. l. R., van Griensven, M., Schantz, J.-T., & Hutmacher, D. W. (2015). Additive manufacturing in biomedical sciences and the need for definitions and norms. *Expert Review of Medical Devices, 12*(5), 537.

Chua, C. K., Chou, S. M., & Wong, T. S. (1998). A study of the state-of-the-art rapid prototyping technologies. *The International Journal of Advanced Manufacturing Technology, 14*, 146-152.

Chun, K. J., Choi, H. H., & Lee, Y. J. (2014). Comparison of mechanical property and role between enamel and dentin in the human teeth. *Journal of Dental Biomechanics, 5*, 1-7.

Clements, J. L., Tantbirojn, D., Versluis, A., & Cagna, D. R. (2018). Do denture processing techniques affect the mechanical properties of denture teeth? *The Journal of Prosthetic Dentistry, 120*(2), 246-251.

Cochrane, N. J., Anderson, P., Davis, G. R., Adams, G. G., Stacey, M. A., & Reynolds, E. C. (2012). An X-ray microtomographic study of natural white-spot enamel lesions. *Journal of Dental Research, 91*(2), 185-191.

Cohen, S. R., Apter, N., Jesse, S., Kalinin, S., Barlam, D., Peretz, A. I., & Ziskind, D. (2010). AFM investigation of mechanical properties of dentin. *Israel Journal of Chemistry, 48*(2), 65-72.

Collingwood, J., Bruce, M., & McIlwaine, C. (2019). *A reproducible approach to model simulated molar occlusal caries for student teaching and assessment using innovative technology.* Paper presented at the Association for Dental Education in Europe, Berlin, Germany.

Collys, K., Slop, D., Cleymaet, R., Coomans, D., & Michotte, Y. (1992). Load dependency and reliability of microhardness measurements on acid-etched enamel surfaces. *Dental Materials, 8*(5), 332-335.

Corcione, C. E., Gervaso, F., Scalera, F., Montagna, F., Sannino, A., & Maffezzoli, A. (2017). The feasibility of printing polylactic acid–nanohydroxyapatite composites using a low-cost fused deposition modeling 3D printer. *Journal of Applied Polymer Science, 134*(13), 1-10.

Corcione, C. E., Scalera, F., Gervaso, F., Montagna, F., Sannino, A., & Maffezzoli, A. (2018). One-step solvent-free process for the fabrication of high loaded PLA/HA composite filament for 3D printing. *Journal of Thermal Analysis and Calorimetry, 134*(1), 575-582.

Costello, J. P., Oliveri, L. J., Krieger, A., Thabit, O., Marshall, B., Yoo, S. J., . . . Nath, D. S. (2014a). Utilizing Three-Dimensional Printing Technology to Assess the Feasibility of High-Fidelity Synthetic Ventricular Septal Defect Models for Simulation in Medical Education. *World Journal for Pediatric and Congenital Heart Surgery, 5*(3), 421-426.

Costello, J. P., Oliveri, L. J., Su, L., Krieger, A., Alfares, F., Thabit, O., . . . Nath, D. S. (2014b). Incorporating Three-Dimensional Printing into a Simulation-based Congenital Heart Disease and Critical Care Training Curriculum for Resident Physicians. *Congenital Heart Disease, 10*(2), 185-190.

Cowpe, J., Plasschaert, A., Harzer, W., WVinkka-Puhaka, H., & Walmsley, A. D. (2010). Profile and competences for the graduating European dentist–update 2009. *European Journal of Dental Education, 14*(4), 193-202.

Craig, R. G., & Peyton, F. A. (1958). The microhardness of enamel and dentin. *Journal of Dental Research, 37*(4), 661-668.

Craig, R. G., Peyton, F. A., & Johnson, D. W. (1961). Compressive Properties of Enamel, Dental Cements, and Gold. *Journal of Dental Research, 40*(5), 936-945.

Crawford, J. M., Adami, G., Johnson, B. R., Knight, G. W., Knoernschild, K., Obrez, A., . . . Licari, F. W. (2007). Curriculum restructuring at a North American dental school: rationale for change. *Journal of Dental Research, 71*(4), 524-531.

Cresswell-Boyes, A. J. (2015). *Building Complex Cartilage-Like Structures Using 3D Bioprinting.* (MSc Nanomedicine), Swansea University, Swansea.

Cresswell-Boyes, A. J., Barber, A. H., Mills, D., Tatla, A., & Davis, G. R. (2018a). Approaches to 3D Printing Teeth from X-Ray Microtomography. *Journal of Microscopy, 272*(3), 207-212.

Cresswell-Boyes, A. J., Mills, D., Davis, G. R., & Boyde, A. (2018b). L2 Bone Quality in Osteoporosis: BIOMED 1 Revisited. *Orthopaedic Proceedings: a supplement to The Bone & Joint Journal, 100-B*(Supplement 14), 76.

Cunnigham, R., Narra, S., Montgomery, C., Beuth, J., & Rollett, A. D. (2017). Synchrotron-Based X-ray Microtomography Characterization of the Effect of the Processing Variables on Porosity Formation in Laser Power-Bed Additive Manufacturing of Ti-6Al-4V. *Journal of Materials, 62*, 1-10.

Cunningham, C., Scheuer, L., Blacks, S., & Liversidge, H. (2016). Chapter 6: Dentition. In *Developmental Juvenile Osteology* (Second ed.). Oxford: Academic Press.

Curnier, F. (2010). Teaching dentistry by means of virtual reality - the Geneva project. *International Journal of computerized dentistry, 13*(3), 251-263.

Cuy, J. L., Mann, A. B., Livi, K. J., Teaford, M. F., & Weihs, T. P. (2002). Nanoindentation mapping of the mechanical properties of human molar tooth enamel. *Archives of Oral Biology, 47*(4), 281-291.

D'Souza, R. N., Bachman, T., Baumgardner, K. R., Butler, W. T., & Litz, M. (1995). Characterization of cellular responses involved in reparative dentinogenesis in rat molars. *Journal of Dental Research, 74*(2), 702-709.

David, O. T., Szuhanek, C., Tuce, R. A., David, A. P., & Leretter, M. (2017). Polylactic Acid 3D Printed Drill Guide for Dental Implants Using CBCT. *Revista De Chimie, 68*(2), 341-342.

Davis, G. R. (1994). The Effect of Linear Interpolation of the Filtered Projections on Image Noise in X-ray Computed Tomography. *Journal of X-Ray Science and Technology, 4*(3), 191-199.

Davis, G. R. (2018). Upper Left Second Molar. In. https://sketchfab.com/3d-models/upper-left-second-molar-cd766135210449ad87110dbeefa93af0: Sketchfab.

Davis, G. R., & Elliott, J. C. (1997). X-ray microtomography scanner using time-delay integration for elimination of ring artefacts in the reconstructed image. *Nuclear Instruments & Methods in Physics Research, 394*, 157-162.

Davis, G. R., & Elliott, J. C. (2003). High Definition X-ray Microtomography using a Conventional Impact X-ray Source. *Journal de Physique IV (Proceedings), 104*(1), 131-134.

Davis, G. R., Evershed, A. N. Z., Elliott, J. C., & Mills, D. (2010, August). *Quantitative X-ray microtomography with a conventional source.* Paper presented at the SPIE Optical Engineering + Applications, San Diego, USA.

Davis, G. R., Evershed, A. N. Z., & Mills, D. (2013). Quantitative High Contrast X-Ray Microtomography for Dental Research. *Journal of Dentistry, 41*, 475-482.

Davis, G. R., Jain, N., & Elliott, J. C. (2008, 18th September). *A modelling approach to beam hardening correction.* Paper presented at the Proc. SPIE 7078, Developments in X-Ray Microtomography VI, 70781E, San Diego, USA.

Davis, G. R., Mills, D., & Anderson, P. (2018). Real-time observations of tooth demineralization in 3 dimensions using X-ray microtomography. *Journal of Dentistry, 69*(Feb.), 88-92.

Davis, G. R., & Wong, F. S. L. (1996). X-Ray Microtomography of Bones and Teeth. *Physiological Measurement, 17*, 121-146.

Dawood, A., Marti Marti, B., Sauret-Jackson, V., & Darwood, A. (2015). 3D Printing in Dentistry. *British Dental Journal, 219*, 521-529.

de Boer, I. R., Lagerweiji, M. D., Wesselink, P. R., & Vervoorn, J. M. (2015). Evaluation of the appreciation of virtual teeth with and without pathology. *European Journal of Dental Education, 19*(2), 87-94.

Dearment, A. (2013). Bioprinting on Horizon for 3-D Printing. *Drug Store News, 35*(12), 6-8.

Demiriz, L., Bodrumlu, E. H., Icen, M., & Durmuslar, M. C. (2016). Evaluation of the accuracy of cone beam computed tomography on measuring impacted supernumerary teeth. *The Journal of Scanning Microscopies, 38*(6), 579-584.

DeSimone, J. (2015). What if 3D Printing was 100x Faster? *TED2015*.

Dickson, K. A., & Stephens, B. W. (2015). It's all in the mime: Actions speak louder than words when teaching the cranial nerves. *Anatomical Sciences Education, 8*(6), 584-592.

Doney, E., Krumdick, L. A., Diener, J. M., Wathen, C. A., Chapman, S. E., Stamile, B., . . . Leevy, W. M. (2013). 3D Printing of Preclinical X-ray Computed Tomographic Data Sets. *Journal of Visualized Experiments*, 1-6.

dos Luz, D., de Ourique, F., Scarparo, R. K., Vier-Pelisser, F. V., Morgental, R. D., Waltrick, S. B., & de Figueiredo, J. A. (2015). Preparation time and perceptions of Brazilian specialists and dental students regarding simulated root canals for endodontic teaching: a preliminary study. *Journal of Dental Education, 79*(1), 56-63.

Doube, M., Kłosowski, M. M., Arganda-Carreras, I., Cordelières, F. P., Dougherty, R. P., Jackson, J. S., . . . Shefelbine, S. J. (2010). BoneJ: Free and extensible bone image analysis in ImageJ. *Bone, 47*(6), 1076-1079.

Douglas, R. D., Hopp, C. D., & Augustin, M. A. (2014). Dental students' preferences and performance in crown design: conventional wax-added versus CAD. *Journal of Dental Education, 78*(12), 1663-1672.

Dowker, S. E. P., Davis, G. R., & Elliott, J. C. (1997). X-ray microtomography: Nondestructive three-dimensional imaging for in vitro endodontic studies. *Oral Surgery, Oral Medicine, Oral Pathology and Oral Radiology, 83*(4), 510-516.

Dowker, S. E. P., Elliott, J. C., Davis, G. R., Wilson, R. M., & Cloetens, P. (2004). Synchrotron X-Ray Microtomographic Investigation of Mineral Concentrations at Micrometre Scale in Sound and Carious Enamel. *Caries Research, 38*(6), 514-522.

Doyle, W. M. (1992). Principles and Applications of Fourier Transform Infrared (FTIR) Process Analysis. *Process Control and Quality, 2*, 11-41.

Dummer, P. M. (1991). Comparison of Undergraduate Endodontic Teaching Programmes in the United Kingdom and in some dental schools in Europe and the United States. *International Endodontic Journal, 24*(1), 169-177.

Elias, K., Amis, A. A., & Setchell, D. J. (2003). The magnitude of cutting forces at high speed. *The Journal of Prosthetic Dentistry, 89*(3), 286-291.

Elliott, A. (1969). *Infra-red spectra and structure of organic long-chain polymers.* London: Edward Arnold Ltd.

Elliott, J. C., Anderson, P., Gao, X. J., Wong, F. S. L., Davis, G. R., & Dowker, S. E. P. (1994). Application of scanning microradiography and x-ray microtomography to studies of bones and teeth. *Journal od X-ray Science and Technology, 4*(2), 102-117.

Elliott, J. C., Bollet-Quivogne, F., Anderson, P., Dowker, S. E. P., Wilson, R. M., & Davis, G. R. (2005). Acidic demineralization of apatites studied by scanning X-ray microradiography and microtomography. *Mineralogical Magazine, 69*(5), 643-652.

Elliott, J. C., Davis, G. R., Anderson, P., Wong, F. S. L., Dowker, S. E. P., & Mercer, C. E. (1997). Application of Laboratory Microtomography to the Study of Mineralized Tissues. *Anales de Quimica, 93*(1), 77-82.

Elliott, J. C., & Dover, S. D. (1982). X-Ray Microtomography. *Journal of Microscopy, 126*(2), 211-213.

Eng, H., Maleksaeedi, S., Yu, S., Choong, Y. Y. C., Wiria, F. E., Kheng, R. E., . . . Tham, H. P. (2017a). Development of CNTs-filled photopolymer for projection stereolithography. *Rapid Prototyping Journal, 23*(1), 129-136.

Eng, H., Maleksaeedi, S., Yu, S., Choong, Y. Y. C., Wiria, F. E., Tan, C. L. C., . . . Wei, J. (2017b). 3D Stereolithography of Polymer Composites Reinforced with Orientated Nanoclay. *Procedia Engineering, 216*, 1-7.

England, G. (2018). Calculator for Conversion between Vickers Hardness Number and SI Units MPa and GPa. Retrieved from https://www.gordonengland.co.uk/hardness/hvconv.htm

Erolin, C. (2019). Interactive 3D Digital Models for Anatomy and Medical Education. In P. M. Rea (Ed.), *Biomedical Visualisation* (Vol. 2, pp. 1-16). Switzerland: Springer.

Evershed, A. N. Z. (2013). *A Multi-Material Approach to Beam Hardening Correction and Calibration in X-Ray Microtomography.* (PhD), Queen Mary University of London, London.

Evershed, A. N. Z., Mills, D., & Davis, G. R. (2012, 17th October). *Multi-species Beam Hardening Calibration Device for X-ray Microtomography.* Paper presented at the SPIE Optical Engineering + Applications, San Diego, USA.

Farah, R. A., Swain, M. V., Drummond, B. K., Cook, R., & Atieh, M. (2010). Mineral density of hypomineralised enamel. *Journal of Dentistry, 38*(1), 50-58.

Farré-Guasch, E., Wolff, J., Helder, M. N., Schulten, E. A. J. M., Forouzanfar, T., & Klein-Nulend, J. (2015). Application of Additive Manufacturing in Oral and Maxillofacial Surgery. *Journal of Oral and Maxillofacial Surgery, 73*, 2408-2418.

Fasel, J. H. D., Beinemann, J., Schaller, K., & Gailoud, P. (2013). A Critical Inventory of Preoperative Skull Replicas. *Annals of THe Royal College of Surgeons of England, 95*(6), 401-404.

Feldkamp, L. A., Davis, L. C., & Kress, J. W. (1984). Practical Cone-Beam Algorithm. *Journal of the Optical Society of America A-Optics Image Science and Vision, 1*(6), 612-619.

Field, M. J., & Jeffcoat, M. K. (1995). Dental education at the crossroads: a report by the Institute of Medicine. *Journal of the American Dental Association (1939), 126*(2), 191-195.

Fons Font, A., Solá Ruiz, M. F., Granell Ruíz, M., Labaig Rueda, C., & Martinínez González, A. (2006). Choice of ceramic for use in treatments with porcelain laminate veneers. *Clinical Dentistry, 11*, e297-e302.

Fultz, B., & Howe, J. M. (2012). *Transmission Electron Microscopy and Diffractometry of Materials*. Berlin, Germany: Springer-Verlag Berlin Heidelberg.

Gadaleta, D., Huang, D., Rankin, N., Hsue, V., Sakkal, M., Bovenzi, C., . . . Ku, B. (2019). 3D printed temporal bone as a tool for otologic surgery simulation. *American Journal of Otolaryngology*.

Garrett, P. H., Faraone, K. L., Patzelt, S. B., & Keaser, M. L. (2015). Comparison of Dental Students' Self-Directed, Faculty, and Software-Based Assessments of Dental Anatomy Wax-Ups: A Retrospective Study. *Journal of Dental Education, 79*(12), 1437-1444.

Gavrila, L., Balan, A., Murariu, A., Sandu, A. V., & Savin, C. (2016). In vitro Study Regarding the Effect of Various Commercial Remineralizing Products on Primary and Permanent Teeth Dentine Caries Lesions. *Revista De Chimie, 67*(11), 2228-2230.

GDC. (2020). *Preparedness for Practice of UK Graduates: Report 2020*. Retrieved from https://www.gdc-uk.org/docs/default-source/research/preparedness-for-practice.pdf?sfvrsn=104075d9_12

Ghali, S. R., Katti, G., Shahbaz, S., & Katti, C. (2018). Cone Beam Computed Tomography: A Boon for Maxillofacial Imaging. *Journal of Indian Academy of Oral Medicine & Radiology, 29*(1), 30-34.

Goh, G. D., Yap, Y. L., Agarwala, S., & Yeong, W. Y. (2018). Recent Progress in Additive Manufacturing of Fiber Reinforced Polymer Composite. *Advanced Materials Technologies, 4*(1), 1-22.

Goldberg, M., & Smith, A. J. (2004). Cells and extracellular matrices of dentin and pulp: a biological basis for repair and tissue engineering. *Critical Reviews in Oral Biology & Medicine, 15*(1), 13-27.

Goldman, L. W. (2007). Principles of CT and CT Scanning. *Journal of Nuclear Medicine Technologists, 35*(3), 115-128.

Goodridge, R. D., Shofner, M. L., Hague, R. J. M., McClelland, M., Schlea, M. R., Johnson, R. B., & Tuck, C. J. (2011). Processing of a Polyamide-12/carbon nanofibre composite by laser sintering. *Polymer Testing, 30*(1), 94-100.

Gottlieb, R., Lanning, S. K., Gunsolley, J. C., & Buchanan, J. A. (2011). Faculty Impressions of Dental Students' Performance With and Without Virtual Reality Simulation. *Journal of Dental Education, 75*(11), 1443-1451.

Gould, D. J., Clarkson, M. J., Hutchins, B., & Lambert, H. W. (2014). How neuroscience is taught to North American dental students: results of the Basic Science Survey Series. *Journal of Dental Education, 78*(3), 437-444.

Gross, B. C., Erkal, J. L., Lockwood, S. Y., Chen, C., & Spence, D. M. (2014). Evaluation of 3D Printing and Its Potential Impact on Biotechnology and the Chemical Sciences. *America Chemical Society: Analytical Chemistry, 86*(1), 3240-3253.

Grzesik, W. J., & Narayanan, A. S. (2002). Cementum and Periodontal Wound Healing and Regeneration. *Critical Reviews in Oral Biology & Medcine, 13*(6), 474-484.

Guessasma, S., Zhang, W., Zhu, J., Belhabib, S., & Nouri, H. (2015). Challenges of Additive Manufacturing Technologies from an Optimisation Perspective. *International Journal for Simulation and Multidisciplinary Design Optimization, 6*(A9), 1-13.

Gunther, D., Heymel, B., Gunther, J. F., & Ederer, I. (2014). Continuous 3D-Printing for Additive Manufacturing. *Rapid Prototyping Journal, 20*(4), 320-327.

Gutiérrez-Salazar, M. P., & Reyes-Gasga, J. (2003). Microhardness and Chemical Composition of Human Tooth. *Materials Research, 6*(3), 367-373.

Guttman, G. D. (2003). The current status of the anatomical sciences curriculum in U.S. and Canadian dental schools. *Journal of Dental Education, 67*(3), 375-379.

Habelitz, S., Marshall, S. J., Marshall Jr, G. W., & Balooch, M. (2001). Mechanical properties of human dental enamel on the nanometre scale. *Archives of Oral Biology, 46*(2), 173-183.

Hanafi, A., Donnermeyer, D., Schäfer, E., & Bürklein, S. (2020). Perception of a modular 3D print model in undergraduate endodontic education. *International Endodontic Journal*.

Harryson, O. L. A., Hosni, Y. A., & Nayfeh, J. F. (2007). Custom-designed orthopedic implants evaluated using finite element analysis of patient-specific computed tomography data: femoral-component case study. *BMC Musculoskeletal Disorders, 8*(91), 1-10.

Harun, W. S. W., Sharif, S., Idris, M. H., & Kadirgama, K. (2009). Characteristic studies of collapsibility of ABS patterns produced from FDM for investment casting. *Materials Research Innovations, 13*(3), 340-343.

Hassan, R., Caputo, A. A., & Bunshah, R. F. (1981). Fracture Toughness of Human Enamel. *Journal of Dental Research, 60*(4), 820-827.

He, L.-H., Yin, Z.-H., van Vuuren, L. J., Carter, E. A., & Liang, X.-W. (2013). A natural functionally graded biocomposite coating—human enamel. *Acta Biomaterialia, 9*(5), 6330-6337.

Hendee, W. R. (1995). X Rays in Medicine. *Physics Today, 48*(11), 51-56.

Hillson, S. (2014). *Tooth Development in Human Evolution and Bioarchaeology*. UK: Cambridge University Press.

Hochman, J. B., Kraut, J., Kazmerik, K., & Unger, B. J. (2014). Generation of a 3D Printed Temporal Bone Model with Internal Fidelity and Validation of the Mechanical Construct. *Otolaryngology - Head and Neck Surgery, 150*(3), 448-454.

Höhne, C., Schwarzbauer, R., & Schmitter, M. (2020). Introduction of a new teaching concept for crown preparation with 3D printed teeth. *European Journal of Dental Education*, e1-e9.

Howell, P. G. T., & Boyde, A. (2002). Volumes From Which Calcium and Phosphorus X-Rays Arise in Electron Probe Emission Microanalysis of Bone: Monte Carlo Simulation. *Calcified Tissue International, 72*(6), 745-749.

Hughes, A. J., DeBuitleir, C., Soden, P., O'Donnchadha, B., Tansey, A., Abdulkarim, A., . . . Hurson, C. J. (2017). 3D Printing Aids Acetabular Reconstruction in Complex Revision Hip Arthroplasty. *Advances in Orthopedics, 183*(1), 1-7.

Huotilainen, E., Jaanimets, R., Valášek, J., Marcián, P., Salmi, M., Tuomi, J., . . . Wolff, J. (2014). Inaccuracies in additive manufactured medical skull models caused by the DICOM to STL conversion process. *Journal of Cranio-Maxillofacial Surgery, 42*(5), e259-e265.

Ibrahim, D., Broilo, T., L;, Heitz, C., De Oliveira, M. G., De Olivira, H. W., Nobre, S. M. W., . . . Silva, D. N. (2009). Dimensional error of selective laser sintering, three-dimensional printing and PolyJet[TM] models in the reproduction of mandibular anatomy. *Journal of Cranio-Maxillofacial Surgery, 37*(3), 167-173.

Insight & Feedback Team. (2018). Writing an Effective Questionnaire. In NHS England (Ed.), (Vol. 06): Publications Gateway.

Ivanova, T. I., Frank-Kamenetskaya, O. V., Kol'tsov, A. B., & Ugolkov, V. L. (2001). Crystal Structure of Calcium-Deficient Carbonated Hydroxyapatite. Thermal Decomposition. *Journal of Solid State Chemistry, 160*(2), 340-349.

Iwamoto, N., & Ruse, N. D. (2002). Fracture Toughness of Human Dentin. *Journal of Biomedical Materials Research Part A, 66A*(3), 507-512.

Jantarat, J., Palamara, J. E. A., Lindner, C., & Messer, H. H. (2002). Time-dependent properties of human root dentin. *Dental Materials, 18*(6), 486-493.

Jelle, B. P., Nilsen, T. N., Hovde, P. J., & Gustavsen, A. (2012). Accelerated Climate Aging of Building Materials and their Characterization by Fourier Transform Infrared Radiation Analysis. *Journal of Building Physics, 36*, 99-112.

Jeng, Y.-R., Lin, T.-T., Hsu, H.-M., Chang, H.-J., & Shieh, D.-B. (2011). Human enamel rod presents anisotropic nanotribological properties. *Journal of the Mechanical Behaviour of Biomedical Materials, 4*(4), 515-522.

Jin, Y., & Fu, J. Z. (2015). Support Generation for Additive Manufacturing Based on Sliced Data. *The International Journal of Advanced Manufacturing Technology, 80*(9), 2041-2052.

Johnson, E. O., V;, C. A., & Troupis, T. G. (2012). Modernization of an anatomy class: From conceptualization to implementation. A case for integrated multimodal-multidisciplinary teaching. *Anatomical Sciences Education, 5*(6), 354-366.

Kak, A. C., & Slaney, M. (2001). *Principles of Computerized Tomographic Imaging*. Philadelphia: Society of Industrial and Applied Mathematics.

Kassebaum, N. J., Bernabe, E., Dahiya, M., Bhandari, B., Murray, C. J., & Marcenas, W. (2014). Global Burden of Severe Tooth Loss: A Systematic Review and Meta-analysis. *Journal of Dental Research, 93*(7 Supp.), 20s-28s.

Ketcham, R. A., & Carlson, W. D. (2001). Acquisition, optimization and interpretation of X-ray computed tomographic imagery: applications to the geosciences. *Computers & Geosciences, 27*(4), 381-400.

Khatoon, B., Hill, K. B., & Walmsley, A. D. (2014). Dental students' uptake of mobile technologies. *British Dental Journal, 216*(12), 669-673.

Khoo, Z. X., Teoh, J. E. M., Liu, Y., Chua, C. K., Yang, S., An, J., . . . Yeong, W. Y. (2015). 3D Printing of Smart Materials: a review on recent progressed in 4D printing. *Virtual and Physical Prototyping, 10*(3), 103-122.

Kilistoff, A. J., Mackenzie, L., D'Eon, M., & Trinder, K. (2013). Efficacy of a step-bystep carving technique for dental students. *Journal of Dental Education, 77*(1), 63-67.

Killough, S. A., Lundy, F. T., & Irwin, C. R. (2009). Substance P expression by human dental pulp fibroblasts: a potential role in neurogenic inflammation. *Journal of Endodontics, 35*(1), 73-77.

Kinney, J. H., Balooch, M., Marshall, G. W., & Marshall, S. J. (1999). A micromechanics model of the elastic properties of human dentine. *Archives of Oral Biology, 44*(10), 813-822.

Kishen, A., Ramamurty, U., & Asundi, A. (2000). Experimental studies on the nature of property gradients in the human dentine. *Journal of Biomedical Materials Research, 51*(4), 650-659.

Klueber, K. M. (2003). Neuroanatomy for the dentist in the twenty-first century. *Journal of Dental Education, 67*(3), 366-369.

Kodaka, T., Bebari, K., Yamada, M., & Kuroiwa, M. (1992). Correlation between microhardness and mineral content in sound human enamel. *Caries Research, 26*(2), 139-141.

Kondo, S., Tamura, Y., Bawden, J. W., & Tanase, S. (2001). The immunohistochemical localization of Bax and Bcl-2 and their relation to apoptosis during amelogenesis in developing rat molars. *Archives of Oral Biology, 46*, 557-568.

Kondrashova, T., De Wan, D., Briones, M. U., & Kondrashov, P. (2016). Integration of ultrasound imaging into pre-clinical dental education. *European Journal of Dental Education.*

Kontoyannis, C. G., & Vagenas, N. V. (2000). Calcium Carbonate Phase Analysis Using XRD and FT–Raman Spectroscopy. *The Analyst, 125*(2), 251-255.

Kumar, S., Hofmann, M., Steinmann, B., Foster, E. J., & Weder, C. (2012). Reinforcement of Stereolithographic Resins for Rapid Prototyping with Cellulose Nanocrystals. *ACS Applied Materials & Interfaces, 4*(10), 5399-5407.

Lacruz, R. S., Habelitz, S., Wright, J. T., & Paine, M. L. (2017). Dental Enamel Formation and Implications for Oral Health and Disease. *Physiological Reviews, 97*, 939-993.

Lam, M. T., Knwon, S. R., Qian, F., & Denehy, G. E. (2015). Evaluation of an Innovative Digital Assessment Tool in Dental Anatomy. *The Journal of Contemporary Dental Practice, 16*(5), 366-371.

Landi, E., Gelotti, G., Logroscino, G., & Tampieri, A. (2003). Carbonated hydroxyapatite as bone substitute. *Journal of European Ceramic Society, 23*(15), 2931-2937.

Larnpotang, S., Lizdas, D., Rajon, D., Luria, I., Gravenstein, N., Bisht, Y., . . . Robinson, A. (2013). *Mixed simulators: Augmented physical simulators with virtual underlays*. Paper presented at the Virtual Reality (VR), 2013 IEEE, Lake Buena Vista, Florida, USA.

Lau, S. K., & Leung, N. K. Y. (2015). *Opportunities and Impacts of Additive Manufacturing: a literature review*. Paper presented at the International Conference on Electronic Business (ICEB).

Laycock, S. D., Bell, G. D., Mortimore, M., Corps, N., & Finkle, I. (2012). Combining X-Ray Micro-CT Technology and 3D Printing for the Digital Preservation and Study of a 19th Century Cantonese Chess Piece with Intricate Internal Structure. *ACM Journal on Computing and Cultural Heritage, 5*(6), 131-137.

Lee, J. Y., An, J., & Chua, C. K. (2017). Fundamentals and applications of 3D printing for novel materials. *Applied Materials Today, 7*, 120-133.

Lee, K. Y., Cho, J. W., Chang, N. Y., Chae, J. M., Kang, K. M., Kim, S. C., & Cho, J. H. (2015). Accuracy of Three-Dimensional Printing for Manufacturing Replica Teeth. *Korean Journal of Orthodontics, 45*, 217-225.

Lees, S., & Rollins Jnr, F. R. (1972). Anisotropy in hard dental tissues. *Journal of Biomechanics, 5*(6), 557-564.

Lefebvre, L., Geremillard, L., Chevalier, J., Zenati, R., & Bernache-Assolant, D. (2008). Sintering behaviour of 45S5 bioactive glass. *Acta Biomaterialia, 4*(6), 1894-1903.

Lertichirakarn, V., Palamara, J. E. A., & Messer, H. H. (2001). Anisotropy of Tensile Strength of Root Dentin. *Journal of Dental Research, 80*(2), 453-456.

Lesot, H., Smith, A. J., Tziafas, D., Begue-Kirn, C., Cassidy, A., & Ruch, J. V. (1994). Biologically active molecules and dental tissue repair: a comparative review of reactionary and reparative dentinogenesis with induction of odontoblast differentiation in vitro. *Cell Materials, 4*, 199-218.

Lewis, R. (1997). Medical applications of synchrotron radiation x-rays. *Physics in Medicine & Biology, 42*(7), 1213-1243.

Lider, V. V. (2017). X-ray Microscopy. *Physics Uspekhi, 60*(2), 187-203.

Linde, A., & Goldberg, M. (1993). Dentinogenesis. *Critical Reviews in Oral Biology & Medicine, 4*(5), 679-728.

Liu, Y. F., Xu, L. W., Zhu, H. Y., & Liu, S. S. Y. (2014). Technical Procedures for Template-Guided Surgery for Mandibular Reconstruction Based on Digital Design and Manufacturing. *BioMedical Engineering Online, 13*(63), 1-15.

Lone, M. (2018). *Innovative strategies for teaching anatomy to dental students.* (Ph.D.), University College Cork, Cork.

Low, I. M. (2004). Depth-Profiling of Crystal Structure, Texture, and Microhardness in a Functionally Graded Tooth Enamel. *Journal of the American Ceramic Society, 87*(1), 2125-2131.

Loyaga-Rendon, P. G., Takahashi, H., Hayakawa, I., & Iwasaki, N. (2007). Compositional characteristics and hardness of acrylic and composite resin artificial teeth. *The Journal of Prosthetic Dentistry, 98*(2), 141-149.

Lunt, R. C., & Law, D. B. (1974). A review of the chronology of eruption of deciduous teeth. *The Journal of the American Dental Association, 89*(4), 872-879.

Macluskey, M., Durham, J., Bell, A., Cowpe, J., Crean, S. J., Dargue, A., . . . Thomson, P. (2012). A national survey of UK final year students' opinion of undergraduate oral surgery teaching. *European Journal of Dental Education, 16*(1), 205-212.

Maddox, M., Felibus, A., Lee, B., Wang, J., Thomas, R., & Silberstein, J. (2015). Evolution of 3-D Physical Models of Renal Malignancies Using Multi-Material 3-D Printers. *The Journal of Urology, 193*(4S), 242.

Magne, P. (2015). A new approach to the learning of dental morphology, function, and esthetics: the "2D-3D-4D" concept. *The International Journal of Esthetic Dentistry, 10*(1), 32-47.

Mahoney, E. K., Holt, B. A., Swain, M., & Kilpatrick, N. M. (2000). The hardness and modulus of elasticity of primary molar teeth: an ultra-micro-indentation study. *Journal of Dentistry, 28*(8), 589-594.

Mahoney, E. K., Rohanizadeh, R., Ismail, F. S. M., Kilpatrick, N. M., & Swain, M. V. (2004). Mechanical properties and microstructure of hypomineralised enamel of permanent teeth. *Biomaterials, 25*(20), 5091-5100.

Manapat, J. Z., Mangadlao, J. D., Tiu, B. D. B., Tritchler, G. C., & Advincula, R. C. (2017). High-Strength Stereolithographic 3D Printed Nanocomposites: Graphene Oxide Metastability. *ACS Applied Materials & Interfaces, 9*(11), 10085-10093.

Manogue, M., McLoughlin, J., Christersson, C., Delap, E., Lindh, C., Schoonheim-Klein, M., & Plasschaert, A. (2011). Curriculum structure, content, learning and assessment in European undergraduate dental education–update 2010. *European Journal of Dental Education, 15*(3), 133-141.

Maroof, M. A., Mahboubi, A., Noorzad, A., & Safi, Y. (2020). A new approach to particle shape classification of granular materials. *Transportation Geotechnics, 22*(e100296), 1-13.

Mashiko, T., Otani, K., Kawano, R., Konno, T., Kaneko, N., Ito, Y., & Watanabe, E. (2014). Development of Three-Dimensional Hollow Elastic Model for Cerebral Aneurysm Clipping Simulation Enabling Rapid and Low Cost Prototyping. *World Neurosurgery, 83*(3), 351-361.

McCaul, L. K., Jenkins, W. M., & Kay, E. J. (2001). The reasons for extraction of permanent teeth in Scotland: a 15-year follow-up study. *British Dental Journal, 190*(12), 658-662.

McHanwell, S. (2015). Teaching Anatomical Sciences to Dental Students. In L. K. Chan & W. Pawlina (Eds.), *Teaching Anatomy: A Practical Guide* (First ed.). New York, USA: Springer International.

McHanwell, S., Atkinson, M., Davies, C., Dyball, R., Morris, J., Ockleford, C., . . . Wilton, J. (2007). Adding 'common sense' to 'the need to know' in anatomy teaching. *Journal of Anatomy, 210*(5), 615-616.

McHarg, J., & Kay, E. J. (2008). The Anatomy of a New Dental Curriculum. *British Dental Journal, 204*(11), 635-638.

Meredith, N., Sherriff, M., Setchell, D. J., & Swanson, S. A. V. (1996). Measurement of the microhardness and young's modulus of human enamel and dentine using an indentation technique. *Archives of Oral Biology, 41*(6), 539-545.

Mironow, V., Viscounti, R. P., Kasyanov, V., Forgacs, G., Drake, C. J., & Markwald, R. R. (2009). Organ Printing: Tissue Spheroids as Building Blocks. *Biomaterials, 30*(12), 2164-2174.

Miserez, A., Li, Y., Waite, J. H., & Zok, F. (2007). Jumbo squid beaks: Inspiration for design of robust organic composites. *Acta Biomaterialia, 3*, 139-149.

Mitov, G., Dillschneider, T., Abed, M. R., Hohenberg, G., & Pospiech, P. (2010). Introducing and evaluating MorphoDent, a Web-based learning program in dental morphology. *Journal of Dental Education, 74*(10), 1133-1139.

Mitsouras, D., Liacouras, P., Imanzadeh, A., Gai, T., Kumamaru, K. K., George, E., . . . Rybicki, F. J. (2015). Medical 3D Printing for the Radiologist. *Radiographics, 35*(7), 1965-1988.

Miyazaki, T., Yamasaki, N., Tsuchiya, T., Matsumoto, K., Takagi, K., & Nagayasu, T. (2015). Airway Stent Insertion Simulated with a Three-Dimensional Printed Airway Model. *Annals of Thoracic and Cardiovascular Surgery, 99*(1), 21-23.

Moradian-Oldak, J., & Paine, M. L. (2010). Mammalian Enamel Formation. In A. Sigel, H. Sigel, & R. K. O. Sigel (Eds.), *Biomineralization: From Nature to Application, 1*. Sussex, UK: Wily & Sons Ltd.

Moro, C., Stromberga, Z., Raikos, A., & Stirling, A. (2017). The effectiveness of virtual and augmented reality in health sciences and medical anatomy. *Anatomical Sciences Education, 10*(6), 549-559.

Mould, R. F. (1995). The early history of X-ray diagnosis with emphasis on the contributions of physics 1895-1915. *Physics in Medicine & Biology, 40*, 1741-1787.

Mousavi, R., Miri, T., Cox, P. W., & Fryer, P. J. (2007). Imaging food freezing using X-ray microtomography. *International Journal of Food Science and Technology, 42*(6), 714-727.

Moxham, B. J. (2012). What is best for the teaching of gross anatomy? *Journal of Anatomy, 221*(1), 73-96.

Moxham, B. J., Plaisant, O., & Pais, D. (2015). The place of neuroanatomy in the curriculum. *European Journal of Anatomy, 19*(2), 215-228.

Moxham, B. J., Plaisant, O., Smith, C. F., Pawlina, W., & McHanwell, S. (2014). An approach toward the development of core syllabuses for the anatomical sciences. *Anatomical Sciences Education, 7*(4), 302-311.

Muller, F., Naharro, M., & Carlsson, G. E. (2007). What are the prevalence and incidence of tooth loss in the adult and elderly population in Europe?',. *Clinical Oral Implants Research, 18 Supp.*(3), 2-14.

Musson, D. (2010). *Adrenomedullin in Dental Tissues.* (Ph.D.), University of Birmingham, Birmingpham.

Nadershahi, N. A., Bender, D. J., Beck, L., & Alexander, S. (2013). A case study on development of an integrated, multidisciplinary dental curriculum. *Journal of Dental Education, 77*(6), 679-687.

Nagasawa, S., Yoshida, T., Tamura, K., Yamazoe, M., Hayano, K., Arai, Y., . . . Ito, M. (2010). Construction of database for three dimensional human tooth models and its ability for education and research - Carious tooth models. *Dental Materials, 29*(2), 132-137.

Nakada, T., Akiba, T., Inagakis, T., & Morikawa, T. (2014). Thoracoscopic Anatomical Subgmentectomy of the Right S2b + S3 using a 3D Printing Model with Rapid Prototyping. *Interactive Cardiovascular and Thoracic Surgery, 19*, 696-698.

Nanci, A. (2012). *Ten Cate's Oral Histology* (Eighth ed.). Missouri, USA: Elsevier.

Nassri, M. R., Carlik, J., da Silva, C. R., Okagawa, R. E., & Lin, S. (2008). Critical Analysis of Artificial Teeth for Endodontic Teaching. *Journal of Applied Oral Science, 16*(1), 43-49.

Ng, Y. L., Mann, V., Rahbaran, S., Lewsey, J., & Gulabivala, K. (2008). Outcome of primary root canal treatment: systematic review of the literature -- Part 2. Influence of clinical factors. *International Endodontic Journal, 41*(1), 6-31.

Ngo, H. (2010). Glass-Ionomer Cements as Restorative and Preventative Materials. *Dental Clinics of North America, 54*(3), 551-563.

Nnodium, J. O. (1990). Learning human anatomy: by dissection or from prosections? *Medical Education, 24*(4), 389-395.

O'Brien, E. K., Wayne, D. B., Barsness, K. A., McGaghie, W. C., & Barsuk, J. H. (2016). Use of 3D Printing for Medical Education Models in Transplantation Medicine: a Critical Review. *Current Transplantation Reports, 3*, 109-119.

O'Reilly, M. K., Reese, S., Herlihy, T., Geoghegan, T., Cantwell, C. P., Feeney, R. N. M., & Jones, J. F. X. (2016). Fabrication and Assessement of 3D Printed Anatomical Models of the Lower Limb for Anatomical Teaching and Femoral Vessel Access Training in Medicine. *Anatomical Sciences Education, January/February*, 71-79.

Obrez, A., Briggs, C., Buckman, J., Goldstein, L., Lamb, C., & Knight, W. G. (2011). Teaching clinically relevant dental anatomy in the dental curriculum: description and assessment of an innovative module. *Journal of Dental Education, 75*(6), 797-804.

Olowo-Ofayoku, A., & Moxham, B. J. (2014). Comparisons between the attitudes of medical and dental students toward the clinical importance of gross anatomy and physiology. *Clinical Anatomy (New York), 27*(7), 976-987.

Onuki, H., & Elleaume, P. (2002). *Undulators, Wigglers and Their Applications*. London: CRC Press.

Oropallo, W., & Piegl, L. A. (2015). Ten Challenges in 3D Printing. *Engineering with Computers, 32*(1), 135-148.

Park, S., Wang, D., H;, Zhang, D., Romberg, E., & Arola, D. (2008). Mechanical properties of human enamel as a function of age and location in the tooth. *Journal of Materials Science: Materials in Medicine, 19*(6), 2317-2324.

Park, S. E., & Howel, T. H. (2015). Implementation of a flipped classroom educational model in a predoctoral dental course. *Journal of Dental Education, 79*(5), 563-570.

Pauwels, R., Stamatakis, H., Bosmans, H., Bogaerts, R., Jacobs, R., Horner, K., & Tsiklakis, K. (2011). Quantification of metal artifacts on cone beam computed tomography images. *Clinical Oral Implants Research, 24*(A100), 94-99.

Perry, S., Bridges, S. M., & Burrow, M. F. (2015). A review of the use of simulation in dental education. *Simulation in Healthcare, 10*(1), 31-37.

Peyrin, F., Salome, M., Nuzzo, S., Cloetens, P., Laval-Jeantet, A. M., & Baruchel, J. (2000). Perspectives in three-dimensional analysis of bone samples using synchrotron radiation microtomography. *Cellular and Molecular Biology, 46*(1089-1102).

Pope, J. (1998). Diagnostic X-Rays. In *Medical Physics: Imaging* (pp. 28-47). Harlow, UK: Pearson Education Limited.

Postma, T. C., & White, J. G. (2017). Students' perceptions of vertical and horizontal integration in a discipline-based dental school. *European Journal of Dental Education, 21*(2), 101-107.

Preis, V., Hahnel, S., Behr, M., & Rosentritt, M. (2018). Contact Wear of Artificial Denture Teeth. *Journal of Prosthetic Research, 62*(2), 252-257.

Qualtrough, A. J., Whitworth, J. M., & Dummer, P. M. (1999). Preclinical Endodontology: an international comparison. *International Endodontic Journal, 32*(1), 406-414.

Queiroz, P. M., Oliveira, M. L., Groppo, F. C., Haiter-Neto, F., & Freitas, D. Q. (2017). Evaluation of metal artefact reduction in cone-beam computed tomography images of different dental materials. *Clinical Oral Investigations, 22*(1), 419-423.

Quinn, G. D. (2007). *Fracture Toughness of Ceramics by the Vickers Indentation Crack Length Method: A Critical Review.* Paper presented at the Cocoa Beach Conference of the American Ceramic Society, Cocoa Beach FL, USA.

Rafai, N., Lemos, L. N., Hawari, A., Gerhardt-Szép, S., & Classen-Linke, I. (2016). Anatomy meets dentistry! Linking anatomy and clinical practice in the preclinical dental curriculum. *BMC Medical Education, 16*(1), 305.

Rashwan, M., Cattell, M. J., & Hill, R. H. (2019). The effect of barium content on the crystallization and microhardness of barium fluormica glass-ceramics. *Journal of the European Ceramic Society, 39*(7), 2259-2565.

Redwood, B., Schoffer, F., & Garret, B. (2017). *The 3D Printing Handbook: Technologies, design and applications.* Amsterdam: Coers & Roest.

Redwood, C. J., & Townsend, G. C. (2011). The dead center of the dental curriculum: changing attitudes of dental students during dissection. *Journal of Dental Education, 75*(10), 1333-1344.

Reid, S. A., & Boyde, A. (1987). Changes in the mineral density distribution in human bone with age: image analysis using backscattered electrons in the SEM. *Journal of Bone and Mineral Research, 2*(1), 13-22.

Rengier, F., Mehndiratta, A., von Tengg-Kobligk, H., Zechmann, C. M., Unterhinninghoden, R., Kauczor, H. U., & Giesel, F. L. (2010). 3D Printing Based on Imaging Data: Review of Medical Applications. *International Journal of Computer Assisted Radiology, 5*, 335-341.

Reymus, M., Fotiadou, C., Kessler, A., Heck, K., Hickel, R., & Diegritz, C. (2018). 3D Printed Replicas for Endodontic Education. *International Endodontic Journal, 52*(1), 123-130.

Richardson-Hatcher, A., Hazzard, M., & Ramirez-Tanez, G. (2014). The cranial nerve skywalk: A 3D tutorial of cranial nerves in a virtual platform. *Anatomical Sciences Education, 7*(6), 469-478.

Robinson, C., Shore, R. C., Brookes, S. J., Strafford, S., Wood, S. R., & Kirkham, J. (2000). The Chemistry of Enamel Caries. *Critical Reviews in Oral Biology & Medicine, 11*(4), 481-495.

Rosario, A. M. C., Moreno, S., & Molina, R. (2010). Characterization of Vermiculite by XRD and Spectroscopic Techniques. *Earth Sciences Research Journal, 13*(2), 108-118.

Roy, S., & Basu, B. (2008). Mechanical and tribological characterization of human tooth. *Materials Characterization, 59*(6), 747-756.

Russias, J., Saiz, E., Nalla, R. K., Gryn, K., Ritchie, R. O., & Tomsia, A. P. (2006). Fabrication and mechanical properties of PLA/HA composites: A study of in vitro degradation. *Materials Science and Engineering: C, 26*(8), 1289-1295.

Sakuragi, T. (2014). Stereolithographic Biomodelling of Pulmonary Hilum by Multislice Computed Tomography Imaging. *European Journal of Cardio-Thoracic Surgery, 46*(1), 143.

Salajan, F. D., Mount, G. J., & Prakki, A. (2015). An Assessment of Students' Perceptions of Learning Benefits Stemming from the Design and Instructional Use of a Web3D Atlas. *Electronic Journal of e-Learning, 13*(2), 120-137.

Salazar, A., Rico, A., Rodríguez, J. R., Escudero, J. S., Seltzer, R., & Cutillas, F. M. d. l. E. (2014). Fatigue crack growth of SLS polyamide 12: Effect of reinforcement and temperature. *Composites Part B: Engineering, 59*, 285-292.

Salmi, M., Paloheimo, K. S., Tuomi, J., Wolff, J., & Mäkitie, A. (2013). Accuracy of Medical Models Made by Additive Manufacturing (Rapid Manufacturing). *Journal of Cranio-Maxillo-Facial Surgery, 41*, 603-609.

Salmoria, G. V., Ahens, C. H., Fredel, M., Soldi, V., & Pires, A. T. N. (2005). Stereolithography somos 7110 resin: mechanical behavior and fractography of parts post-cured by different methods. *Polymer Testing, 24*(2), 157-162.

San Diego, J. P., Newton, T., Quinn, B. F. A., Cox, M. J., & Woolford, M. J. (2013). Levels of Agreement Between Student and Staff Assessments of Clinical Skills in Performing Cavity Preparation in Artificial Teeth. *European Journal of Dental Education*.

Sarment, D. (2013). *Cone Beam Computed Tomography : Oral and Maxillofacial Diagnosis and Applications*. Chichester, UK: Wiley.

Saygin, N. E., Giannobile, W. V., & Somerman, M. J. (2000). Molecular and cell biology of cementum. *Periodontology 2000, 24*(1), 73-98.

Schmauss, D., Schmitz, C., Bigdeli, A. K., Weber, S., Gerber, N., Beiras-Fernandez, A., . . . Sodian, R. (2012). Three-Dimensional Printing of Models for Preoperative Planning and Simulation of Transcatheter Valve Replacement. *Annals of Thoracic and Cardiovascular Surgery, 93*(2), 31-33.

Schmitz, J. E., Teepe, J. D., Hu, Y., Smith, C. E., Fajardo, R. J., & Chun, Y. H. P. (2014). Estimating mineral changes in enamel formation by ashing/BSE and microCT. *Journal of Dental Research, 93*(3), 256-262.

Schonwetter, D. J., Gareau-Wilson, N., Cunha, R. S., & Mello, I. (2016). Assessing the Impact of Voice-Over Screen-Captured Presentations Delivered Online on Dental Students' Learning. *Journal of Dental Education, 80*(2), 141-148.

Schroeter, C. (1959). Practical application of tooth morphology. *Journal of Prosthetic Dentistry, 9*(5), 867-873.

Schultz, E., & Felix, R. (1980). Fan-beam computerized tomography systems with rotating and with stationary detector arrays ('third' and 'fourth' generation). *Medical Progress Through Technology, 7*(4), 169-181.

Schuurman, W., Harimaulyo, E. B., Gawlitta, D., Woodfield, T. B., Dhert, W. J., Van Weeran, P. R., & Malda, J. (2016). Three-Dimensional Assembly of Tissue-Engineered Cartilage Constructs Results in Cartilaginous Tissue Formation Without Retainment of Zonal Characteristics. *Journal of Tissue Engineering and Regenerative Medicine, 10*(4), 315-324.

Sclater, N. (2010). E-Learning in the Cloud. *International Journal of Virtual and Personal Learning Environments, 1*(1), 10-19.

Seibert, J. (2004). X-Ray Imaging Physics for Nuclear Medicine Technologists. Part 1: Basic Principles of X-Ray Production. *Journal of Nuclear Medicine Technologists, 32*(3), 139-147.

Seibert, J., & Boone, J. M. (2005). X-Ray Imaging Physics for Nuclear Medicine Technologists. Part 2: X-Ray Interactions and Image Formation`. *Journal of Nuclear Medicine Technologists, 33*(1), 3-18.

Senatov, F. S., Niaza, K. V., Zadorozhnyy, M. Y., Maksimkim, A. V., Kaloshkin, S. D., & Estrin, Y. Z. (2016). Mechanical properties and shape memory effect of 3D-printed PLA-based porous scaffolds. *Journal of Mechanical Behaviour of Biomedical Materials, 57*, 139-148.

Seredin, P., Kashkarov, V., Lukin, A., Ippolitov, Y., Julian, R., & Doyle, S. (2013). Local study of fissure caries by Fourier transform infrared microscopy and X-ray diffraction using synchrotron radiation. *Journal of Synchrotron Radiation, 20*(1), 705-710.

Shahid, S., Patel, M. P., Hill, R. G., Sidhu, S., Buarki, A., & Braden, M. (2011). *Flake Glass Dental Composites.* Paper presented at the IADR, Tampa, Florida, USA.

Shigli, K., Agrawal, N., Nair, C., Sajjan, S., Kakodkar, P., & Hebbal, M. (2016). Use of PowerPoint presentation as a teaching tool for undergraduate students in the subject of gerodontology. *Journal of Indian Prosthodontics Society*.

Siesler, H. W., & Holland-Moritz, K. (1980). *Infrared and Raman Spectroscopy of Polymers*. New York, USA: Marcel Dekker Inc.

Silva, N. R. F. A., Witek, L., Coelho, P. G., Thompson, V. P., Rekow, E. D., & Smay, J. (2011). Additive CAD/CAM Process for Dental Prostheses. *Journal of Prosthodontics, 20*, 93-96.

Simmer, J. P., Richardson, A. S., Hu, Y., Smith, C. E., & Hu, J. C. C. (2012). A post-classical theory of enamel biomineralization...and why we need one. *International Journal of Oral Science, 4*, 129-134.

Smith, C. F., Finn, G. M., Stewart, J., & McHanwell, S. (2016). Anatomical Society core regional anatomy syllabus for undergraduate medicine: the Delphi process. *Journal of Anatomy, 228*(1), 2-14.

Snelling, J., Sahai, A., & Ellis, H. (2003). Attitudes of medical and dental students to dissection. *Clinical Anatomy (New York), 16*(2), 165-172.

Spears, I. R., Van Noort, R., Crompton, R. H., Cardew, G. E., & Howard, I. C. (1993). The Effects of Enamel Anisotropy on the Distribution of Stress in a Tooth. *Journal of Dental Research, 72*(11), 1526-1531.

Spottiswoode, B. S., van den Heever, J., Chang, Y., Engelhardt, S., Du Plessis, A., Nicolls, F., . . . Gretschel, A. (2012). Preoperative Three-Dimensional Model Creation of Magnetic Resonance Brain Images as a Tool to Assist Neurosurgical Planning. *Stereotactic and Functional Neurosurgery, 91*(3), 162-169.

Staines, M., Robinson, W. H., & Hood, J. A. A. (1981). Spherical indentation of tooth enamel. *Journal of Materials Science, 16*(9), 2551-2556.

Stanford, J. W., Paffenbarger, G. C., Kumpula, J. W., & Sweeney, W. T. (1958). Determination of some compressive properties of human enamel and dentin. *The Journal of the American Dental Association, 57*(4), 487-495.

Stock, S. R. (1999). X-ray microtomography of materials. *International Materials Reviews, 44*(4), 141-164.

Stone, J., Candela, B., Alleuia, V., Fazili, A., Richards, M., Feng, C., . . . Ghazi, A. (2015). A Novel Technique for Simulated Surgical Procedures using 3D Printing Technology. *The Journal of Urology, 193*(4S), 270.

Sugand, K., Abrahams, P., & Khurana, A. (2010). The anatomy of anatomy: a review for its modernization. *Anatomical Sciences Education, 3*(2), 83-93.

Suvinen, T. I., Messer, L. B., & Franco, E. (1998). Clinical simulation in teaching preclinical dentistry. *European Journal of Dental Education, 2*(1), 25-32.

Suzuki, M., Ogawa, Y., Kawano, A., Hagiwara, A., Yamaguchi, H., & Ono, H. (2004). Rapid Prototyping of Temporal Bone for Surgical Training and Medical Education. *Acta Otolaryngol, 124*(4), 400-402.

Swanwick, T., Forrest, K., & O'Brien, B. C. (2018). *Understanding Medical Education: Evidence, Theory, and Practice*. Oxford: Wiley Blackwell.

Taft, R. M., Kondor, S., & Grant, G. T. (2011). Accuracy of rapid prototype models for head and neck reconstruction. *The Journal of Prosthetic Dentistry, 106*(6), 399-408.

Tam, M. D., Latham, T., Brown, J. R. I., & Jakeways, M. (2014). Use of a 3D Printed Hollow Aortic Model to Assist EVAR Planning in a Case with Complex Neck Anatomy: Potential of 3D Printing to Improve Patient Outcome. *Journal of Endovascular Therapy, 21*(5), 760-762.

Tam, M. D., Laycock, S. D., Brown, J. R. I., & Jakeways, M. (2013). 3D Printing of an Aortic Aneurysm to Facilitate Decision Making and Device Selection for Endovascular Aneurysm Repair in Complex Neck Anatomy. *Journal of Endovascular Therapy, 20*(6), 863-867.

Tan, H., Yang, K., Wei, P., Zhang, G., Dimitriou, D., Xu, L., . . . Luo, X. (2015). A Novel Preoperative Planning Technique Using a Combination of CT Angiography and Three-Dimensional Printing for Complex Toe-to-Hand Reconstruction. *Journal of Reconstructive Microsurgery, 31*(5), 369-377.

Tchorz, J. P., Brandl, M., Ganter, P. A., Karygianni, L., Polydorou, O., Vach, K., . . . Altenburger, M. J. (2015). Pre-Clinical Endodontic Training with Artificial Instead of Extracted Human Teeth?: does the type of exercise have an influence on clinical endodontic outcomes? *International Endodontic Journal, 48*, 888-893.

Thomas, D. J., & Claypole, T. C. (2016). 3-D Printing. In J. Izdebska & S. Thomas (Eds.), *Printing on Polymers - Fundamentals and Applications* (pp. 293-305). United States of America: Elsevier.

Tiskaya, M., Al-eesa, N. A., Wong, F. S. L., & Hill, R. G. (2019). Characterization of the bioactivity of two commercial composites. *Dental Materials, 35*(12), 1757-1768.

Topp, K. S. (2004). Prosection vs. dissection, the debate continues: Rebuttal to Granger. *The Anatomical Record Part B: The New Anatomist, 281B*(1), 12-14.

Trautz, O. R., Klein, E., Fessenden, E., & Addelston, H. K. (1953). The interpretation of the X-ray diffractograms obtained from human dental enamel. *Journal of Dental Research, 32*, 420-431.

Tsukamoto, Y., Fukutani, S., Shin-Ike, T., Kubota, T., Sato, S., Suzuki, Y., & Mori, M. (1992). Mineralized nodule formation by cultures of human dental pulp-derived fibroblasts. *Archives of Oral Biology, 37*(12), 1045-1055.

Tunchel, S., Blay, A., Kolerman, R., Mijiritsky, E., & Awad Shibli, J. (2016). 3D Printing/Additive Manufacturing Single Titanium Dental Implants: A Prospective Multicenter Study with 3 Years of Follow-Up. *International Journal of Dentistry*, 1-9.

Tziafas, D., Smith, A. J., & Lesot, H. (2000). Designing new treatment strategies in vital pulp therapy. *Journal of Dentistry, 28*(2), 77-92.

Uskokovic, V. (2012). Biomineralization and Biomimicry of Tooth Enamel. In P. Vallittu (Ed.), *Non-Metallic Biomaterials for Tooth Repair and Replacement* (First ed.). Cambridge, UK: Woodhead Publishing.

van Dalen, G., Blonk, H., van Aalst, H., & Hendriks, C. L. L. (2003). 3-D Imaging of Foods using X-ray Microtomography. *Imaging & Microscopy, 3*, 18-21.

Vuchkova, J., Maybury, T., & Farah, C. S. (2012). Digital interactive learning of oral radiographic anatomy. *European Journal of Dental Education, 16*(1), e79-87.

Walker, A. (2013). 3D Printing for Dummies: How do 3D printers work? Retrieved from http://www.independent.co.uk/life-style/gadgets-and-tech/features/3d=printing-for-dummies-how-to-do-3d-printers-work-8668937.html

Wallen, E. S., Schulein, T. M., & Johnson, L. A. (1997). A computer program to aid in visual concept development in dentistry. *Computer Methods and Programs in Biomedicine, 52*(2), 105-115.

Wang, R. Z., & Weiner, S. (1998). Strain–structure relations in human teeth using Moiré fringes. *Journal of Biomechanics, 31*, 135-141.

Waran, V., Narayanan, V., Karuppiah, R., Owen, S. L. F., & Aziz, T. (2014). Utility of Multimaterial 3D Printers in Creating Models with Pathological Entities to Enhance the Training Experience of Neurosurgeons. *Journal of Neurological Surgery, 120*(2), 489-492.

Wassif, H. (2007). *Application of x-ray microtomography to studies of model dental caries systems.* (PhD), Queen Mary University of London, London.

Watson, R. A. (2014). A Low-Cost Surgical Application of Additive Fabrication. *Journal of Surgical Education, 71*(1), 14-17.

Weber, A. L. (2001). History of Head and Neck Radiology: Past, Present, and Future. *Radiology, 218*(1), 15-24.

Wedl, J. S., Schoder, V., & Friedrich, R. E. (2004). Tooth eruption times of permanent teeth in male and female adolescents in Niedersachsen. *Archiv fur Kriminologie, 213*(3-4), 84-91.

White, T. D., & Folkens, P. A. (2005). *The Human Bone Manual*. Oxford, UK: Academic Press.

Willems, G., Celis, J. P., Lambrechts, P., Braem, M., & Vanherle, G. (1993). Hardness and Young's modulus determined by nanoindentation technique of filler particles of dental restorative materials compared with human enamel. *Journal of Biomedical Materials Research, 27*(6), 747-755.

Willmott, N. S., Wong, F. S. L., & Davis, G. R. (2007). An X-Ray Microtomography Study on the Mineral Concentration of Carious Dentine Removed during Cavity Preparation in Deciduous Molars. *Caries Research, 41*(2), 129-134.

Wong, F. S. L., Elliott, J. C., Anderson, P., & Davis, G. R. (1995). Three Dimensional Mineral Distribution in the Dentine of a Rat Incisor Measured by X-ray Microtomography. *Journal of Dental Research, 74*(1), 849.

Wong, F. S. L., Elliott, J. C., Davis, G. R., & Anderson, P. (2000). X-ray microtomographic study of mineral distribution in enamel of mandibular rat incisors. *Journal of Anatomy, 196*(3), 405-413.

Wong, F. S. L., Willmott, N. S., & Davis, G. R. (2006). Dentinal carious lesion in three dimensions. *International Journal of Paediatric Dentistry, 16*(6), 419-423.

Wright, E. F., & Hendricson, W. D. (2010). Evaluation of a 3-D interactive tooth atlas by dental students in dental anatomy and endodontics courses. *Journal of Dental Education, 74*(2), 110-122.

Xiao, K., Zardawi, F., van Noort, R., & Yates, J. M. (2014). Developing a 3D Colour Image Reproduction System for Additive Manufacturing of Facial Prostheses. *International Journal of Advanced Manufacturing Technology, 70*, 2043-2049.

Yan, J., Taskonak, B., & Mecholsky Jr., J. J. (2009). Fractography and Fracture Toughness of Human Dentin. *Journal of the Mechanical Behaviour of Biomedical Materials, 2*, 478-484.

Yang, G., Kabel, J., Rietbergen, B. V., Odgaard, A., Huiskes, R., & Cown, S. C. (1998). The Anisotropic Hooke's Law for Cancellous Bone and Wood. *Journal of Elasticity, 53*(2), 125-146.

Yeung, J. C., Fung, K., & Wilson, T. D. (2011). Development of a computer-assisted cranial nerve simulation from the visible human dataset. *Anatomical Sciences Education, 4*(2), 92-97.

Zadpoort, A. A., & Malda, J. (2017). Additive Manufacturing of Biomaterials, Tissues, and Organs. *Annals of Biomedical Engineering, 45*(1), 1-11.

Zaytsev, D., & Panfilov, P. (2015). Anisotropy of the mechanical properties of human dental enamel. *Materials Letters, 159*, 428-431.

Zhang, L. G., Fisher, J. P., & Leong, K. W. (2015). *3D Bioprinting and Nanotechnology in Tissue Engineering and Regenerative Medicine*. Oxford: Elsevier.

Zhang, Y. R., Du, W., Zhou, Z. D., & Yu, H. Y. (2014). Review of Research on the Mechanical Properties of the Human Tooth. *International Journal of Oral Sciences, 6*, 61-69.

Zheng, Q., Xu, H., Song, F., Zhang, L., Zhou, X., Shao, Y., & Huang, D. (2013). Spatial distribution of the human enamel fracture toughness with aging. *Journal of Mechanical Behaviour of Biomedical Materials, 26*, 148-154.

Ziskind, D., Hasday, M., Cohen, S. R., & Wagner, H. D. (2011). Young's modulus of peritubular and intertubular human dentin by nano-indentation tests. *Journal of Structural Biology, 174*(1), 23-30.

Zopf, A. A., Hollister, S. J., Nelson, M. E., Ohye, R. G., & Green, G. E. (2013). Bioresorbable Airway Splint with a Three-Dimensional Printer. *The New England Journal of Medicine, 368*(21), 2043-2045.

Zou, W., Hunter, N., & Swain, M. V. (2011). Application of Polychromatic μCT for Mineral Density Determination. *Journal of Dental Research, 90*(1), 18-30.

Appendix A Supplementary Material

XMT Scanning Parameters

Table A shows the parameters used when imaging particular samples with MuCAT2, providing information on the length of scan, number of projections, number of blocks, voxel size (resolution), voltage and current.

Table A: Scanning settings used for XMT.

Figure	Scan Time	No. of Proj.	No. of Blocks	Vox. Size (μm)	Voltage (keV)	Current (μA)
Figure 4.5	26 h 51 min	1503	3	15.0	90	180
Figure 4.6	2 h 5 min	603	1	30.0	40	405
Figure 4.7	2 h 22 min	963	1	30.0	40	405
Figure 4.8	2 h 11 min	675	1	30.0	40	405
Figure 4.9	2 h 11 min	675	1	30.0	40	405
Figure 4.10	2 h 11 min	675	1	30.0	40	405
Figure 4.11	2 h 35 min	705	1	30.0	40	405
Figure 5.3	24 h 11 min	909	3	15.0	90	180
Figure 5.4	18 h 55 min	711	3	15.0	90	180
Figure 5.5	18 h 55 min	711	3	15.0	90	180
Figure 5.6	26 h 34 min	999	3	15.0	90	180
Figure 5.7	17 h 57 min	675	3	15.0	90	180
Figure 5.8	60 h 12 min	1755	2	15.0	90	180
Figure 5.9	46 h 8 min	1305	2	15.0	90	180
Figure 5.10	36 h 2 min	1305	3	15.0	90	180
Figure 5.12[*]	1 h 40 min	675	1	30.0	40	405
Figure 5.13[*]	1 h 57 min	909	1	30.0	40	405
Figure 5.16[*]	2 h 43 min	901	1	30.0	40	405
Figure 5.17	3 h 42 min	1017	1	30.0	90	180
Figure 7.8[*]	15 h 52 min	1701	2[†]	10.0	90	180
Figure 7.9[*]	15 h 52 min	1701	2[†]	10.0	90	180

Figure 7.10[*]	15 h 52 min	1701	2[†]	10.0	90	180
Figure 7.18	15 h 52 min	1701	2	10.0	90	180
Figure C	1 h 35 min	639	1	30.0	90	180
Figure D	1 h 35 min	639	1	30.0	90	180
Figure E	1 h 35 min	639	1	30.0	90	180
Figure F	1 h 35 min	639	1	30.0	90	180
Figure G	1 h 35 min	639	1	30.0	90	180
Figure H	1 h 35 min	639	1	30.0	90	180
Figure I	1 h 35 min	639	1	30.0	90	180
Figure J	1 h 35 min	639	1	30.0	90	180
Figure M[‡]	34 h 54 min	2223	3	30.0	90	180

[*] = The figure contains multiple datasets in which the same XMT settings were used.
[†] = Block scanning was not carried out; the same block was imaged twice with the resulting data being averaged to produce a high contrast dataset.
[‡] = Samples were imaged together in groups of four.

Topography of FFF Printed Tooth

SEM was also carried out on the surface of a FFF printed mandibular first molar (Figure 5.13) to demonstrate the topography of the printed surface as well as to understand the layer adhesion. It can be seen in Figure A that there are defined layers, meaning the Ra would be higher (as shown in Figure 5.14).
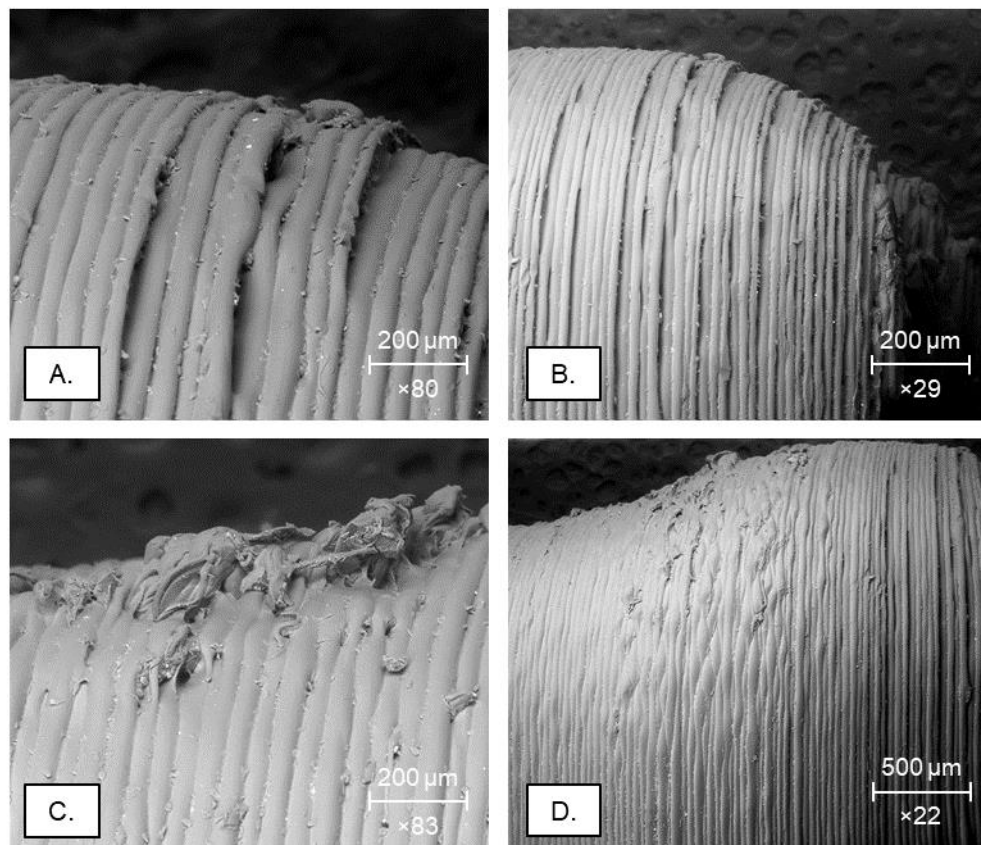

Figure A: SEM images of an FFF printed mandibular first molar. A. Distal cusp surface. B. Occlusal surface. C. Neck, distal side. D. Buccal view.

Hydrogel Pulp

Utilising work carried out in Cresswell-Boyes (2015), a hydrogel pulp was created to give a realistic simulation for the 3D printed typodonts. The hydrogel was a mixture of 6% Type B Bovine Gelatin (Sigma-Aldrich, Merck, Germany) and 5% Alginic Acid Sodium Salt Powder (Sigma-Aldrich, Merck, Germany) with the rest made up of distilled water and a few drops of red food colouring (Dr. Oetker, Germany). The constituents were placed within a falcon tube (50 ml) and placed within the rocking incubator at 37°C to allow for complete dissolution. The mixture was then centrifuged at 3000 rpm at 4°C for 6 min (Eppendorf 22 62 355-9, Eppendorf Ltd., UK), to remove any air bubbles. The mixture was then injected into the 3D printed model via an access canal (Figure B), 0.2 mol of calcium chloride (Sigma-Aldrich, Merck, Germany) was added to crosslink the alginate present within the hydrogel.
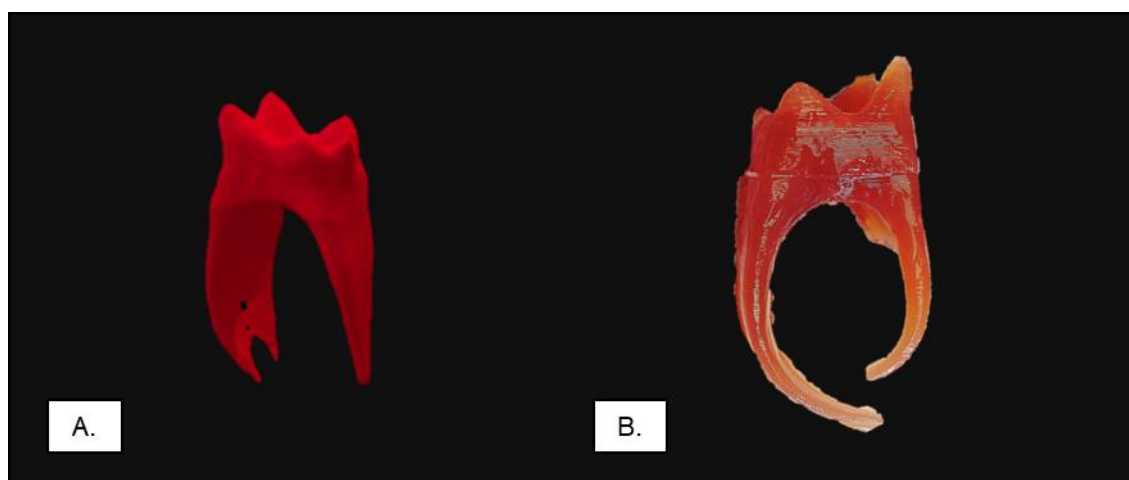

Figure B: The synthetic pulp manufactured from a hydrogel. A. 3D rendering of the pulp. B. Hydrogel pulp.

Due to the low molarity of the calcium chloride, the crosslinking only took place on the exposed surface of the synthetic pulp, meaning once the pulp was exposed through cutting, the hydrogel would flow, to simulate the exposure of the pulp. This synthetic pulp was presented given to students and received positive feedback. No study was carried on the pulp, however.

Deciduous Teeth XMT Dataset

XMT was utilised to capture high-resolution datasets of deciduous teeth used in Chapter 8. The datasets are presented in Figure C – Figure J.
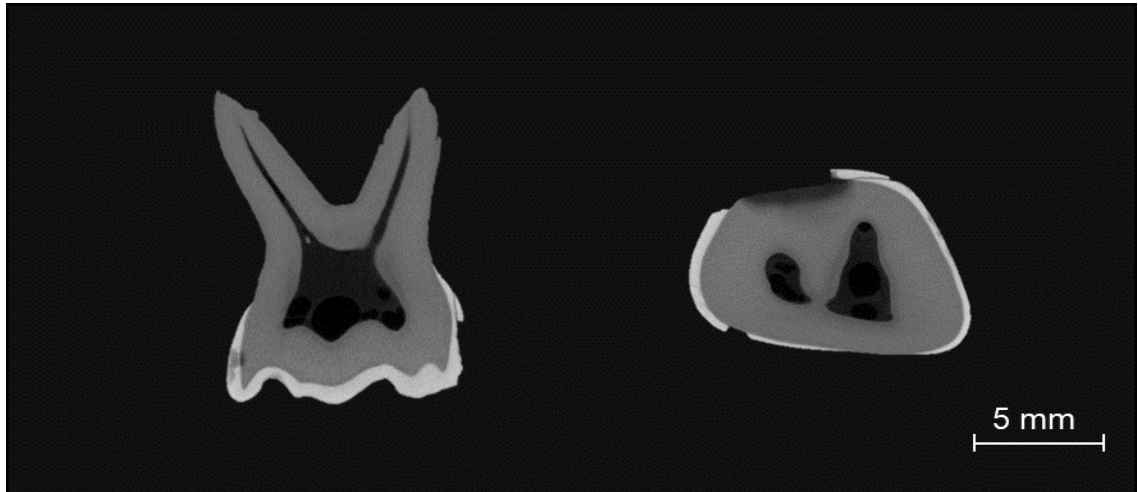

Figure C: XMT of an extracted deciduous maxillary second molar.
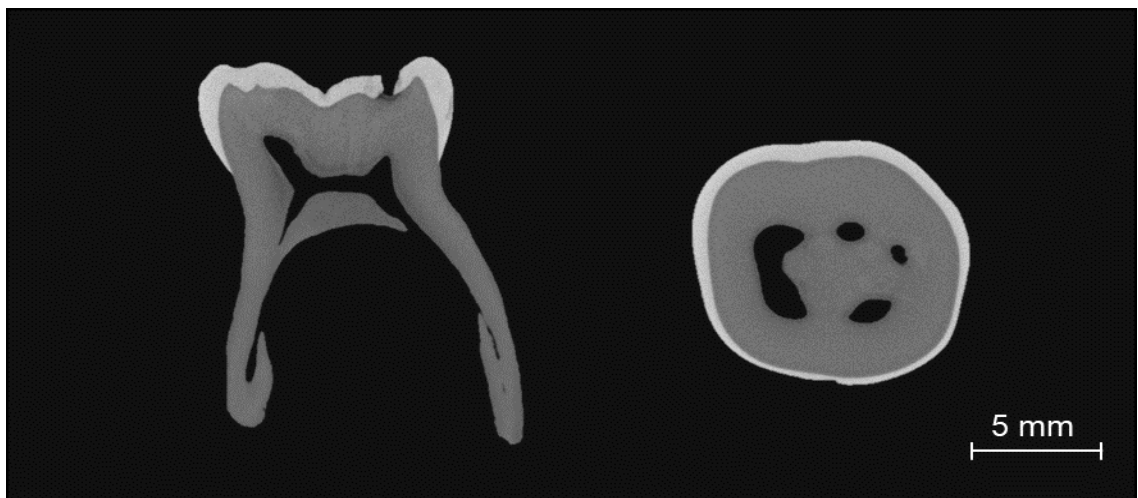

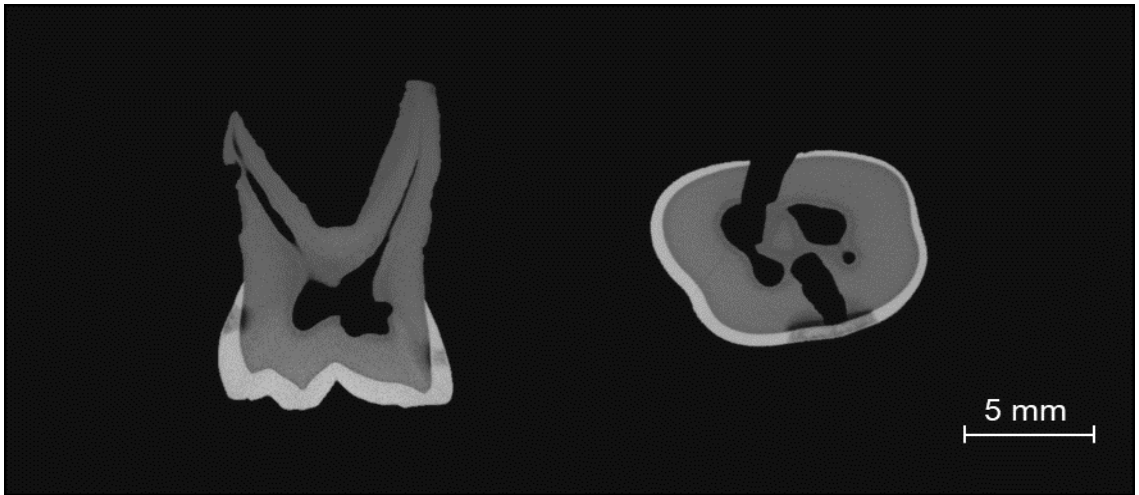Figure D: XMT of an extracted deciduous mandibular first molar.

Figure E: XMT of an extracted deciduous maxillary second molar.

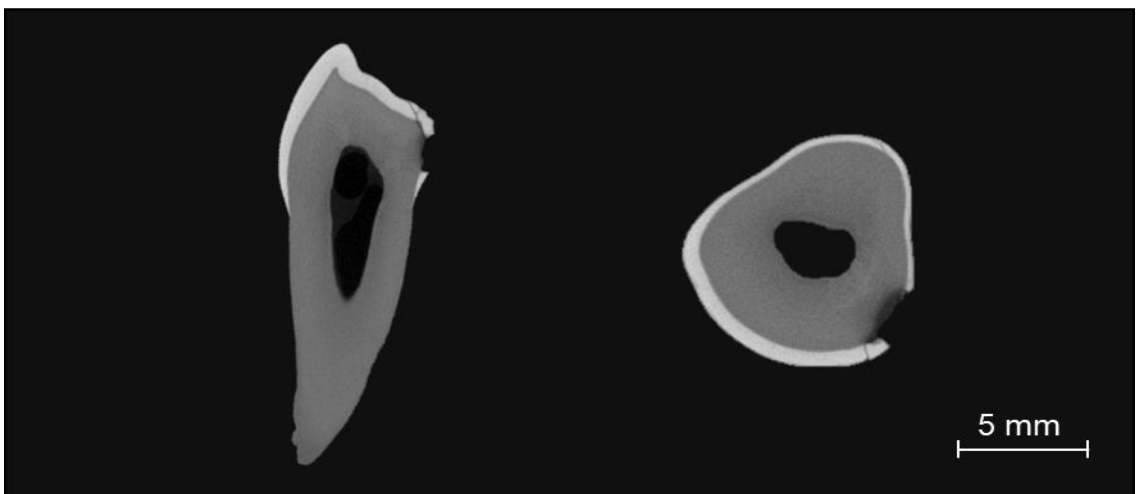Figure F: XMT of an extracted deciduous maxillary lateral incisor.

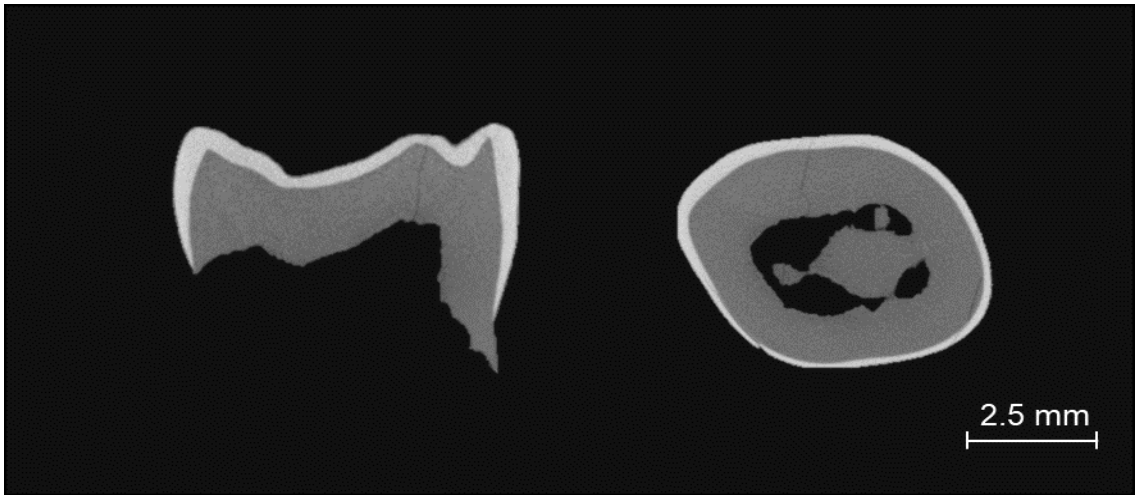Figure G: XMT of an extracted deciduous mandibular canine.

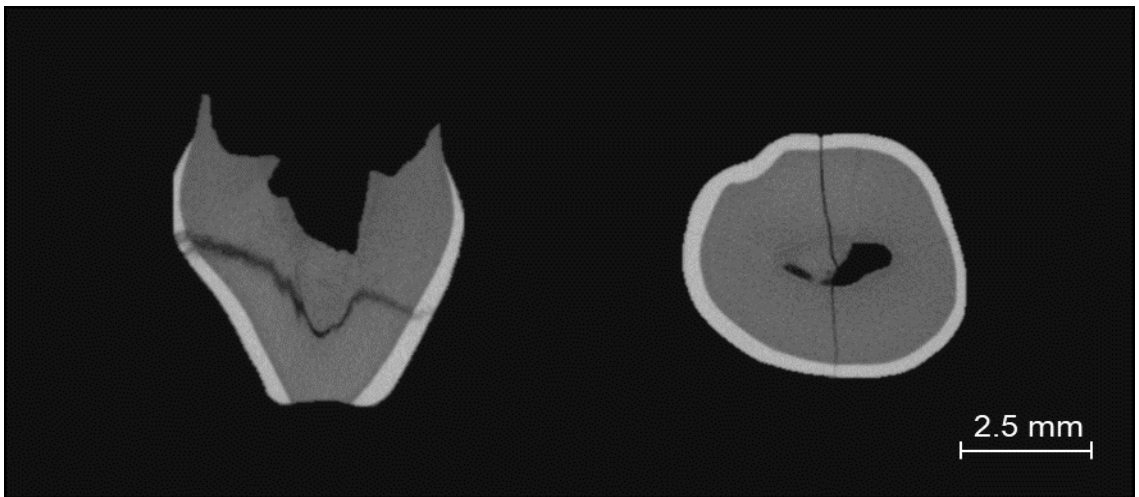Figure H: XMT of an extracted deciduous mandibular first molar.

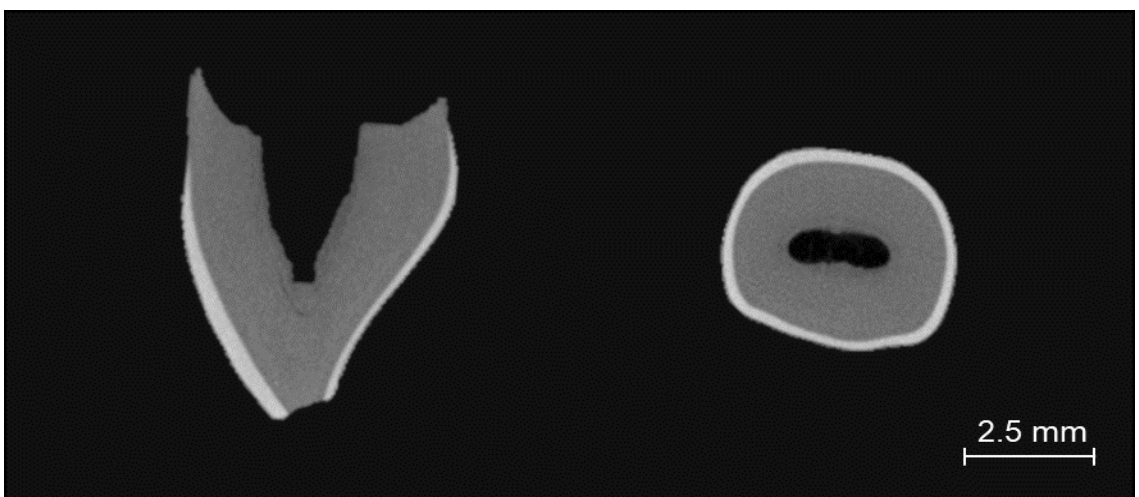Figure I: XMT of an extracted deciduous maxillary canine.

Figure J: XMT of an extracted deciduous maxillary central incisor.

Dental Materials Models

Two models were created for a dental materials questionnaire, the first model, a model for impression materials, was created from multiples datasets (Section 5.3), which were modified to produce one model file. This model was printed using white PLA and the Wanhao Duplicator i3, printing resolution was 100 μm, and each model took around 3 h to print (Figure K). The second model, a composite filling model, was made from two materials, transparent and opaque white resin (Formlabs) and was made from a segmented dataset (Figure 4.5), using the Formlabs Form 2, the enamel and dentine were printed separately at a 50 μm layer height and took around 2 h to print each structure (Figure L).

Ten second-year undergraduate dental students were asked about the opinions regarding either the models used in impression materials or composite filling. Students were undergoing a practical session in a Dental Materials module; the students had to identify the impression material that had the highest detail once an impression was taken of the 3D printed model. Students were also asked to fill the artificial cavity created on the second model with composite incrementally; this session was designed to teach students how to apply filling composites.
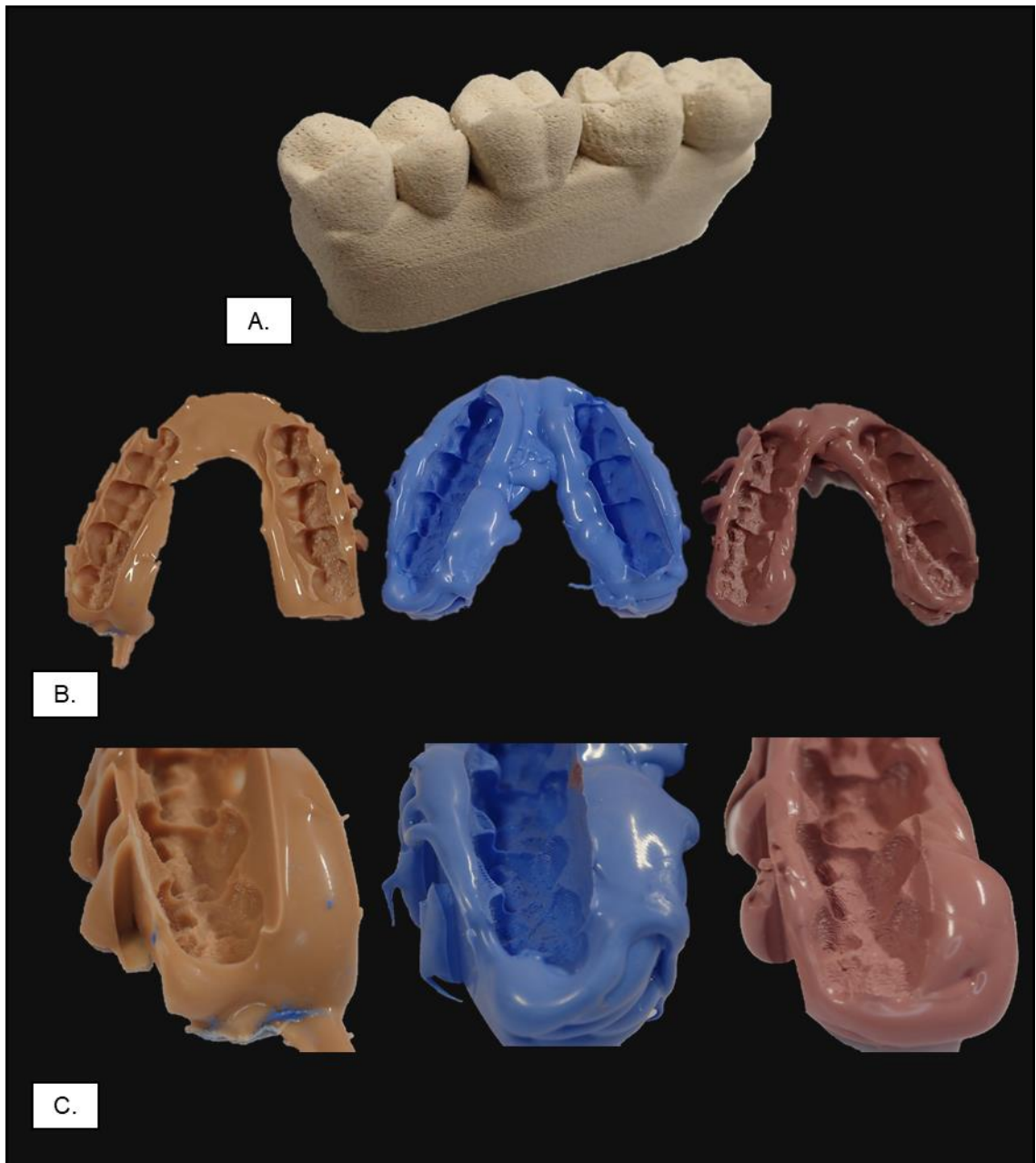
Figure K: Impression material model made from multiple datasets. A. Impression model. B. Three types of impression material after taking an impression with the model. C. Close up image of the three types of impression material after taking an impression with the model.

Figure L: Composite filling model. *Left to Right* - Full model, enamel structure, dentine structure.

Students perceptions of the models were positive, and each agreed that they would use the models again in a practical session.

Vertebrae Models

Vertebrae samples from a study carried out by Boyde & Jones (1996), were imaged using XMT as part of an updated visualisation study (Cresswell-Boyes *et al.*, 2018b). Using the method outlined in Section 3.3, XMT datasets of the vertebrae were 3D printing (using a Wanhao Duplicator i3 and wood-PLA) and optimised for VR (Figure M). The study was carried out to help better understand the datasets in 3D, a list of the vertebrae samples optimised for VR can be found in Appendix C.
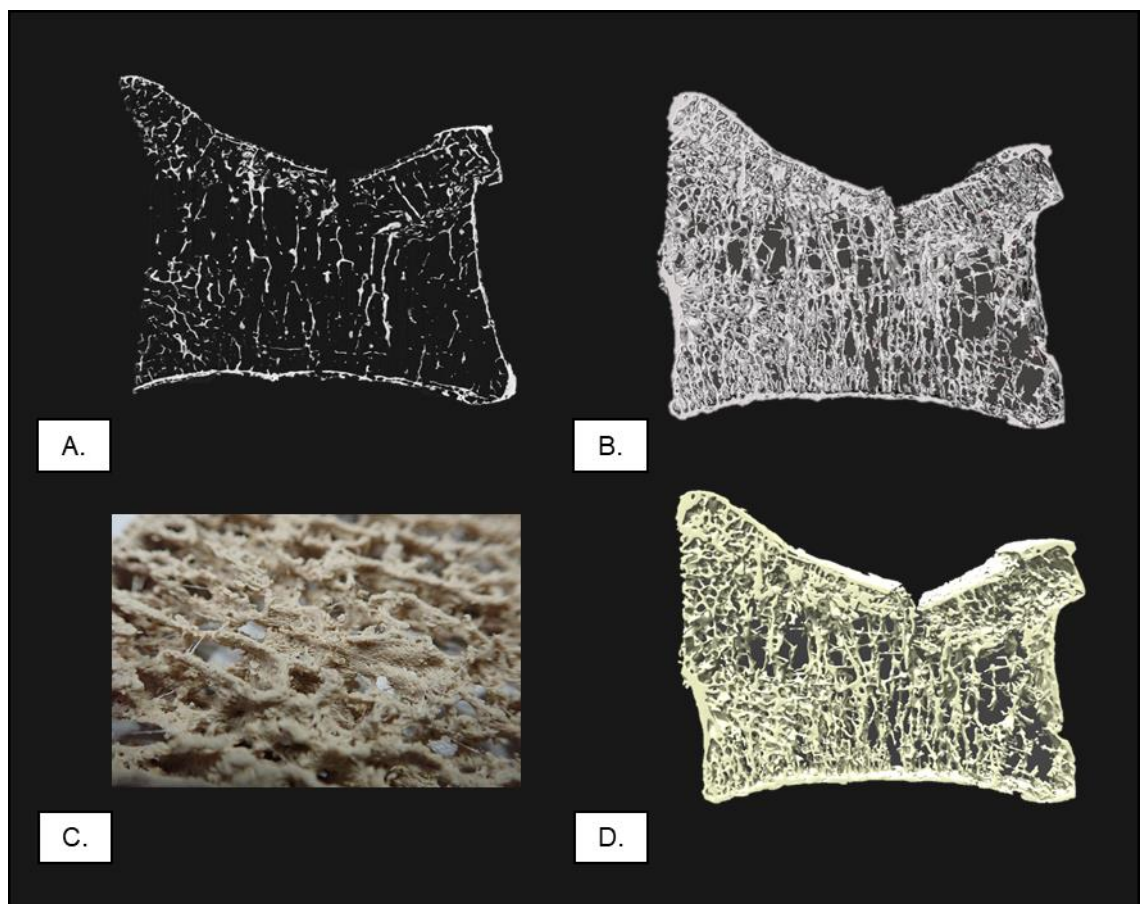

Figure M: A second lumbar (L2) vertebrae specimen. A. XMT reconstruction. B. 3D rendering. C. 3D printed model made using wood-PLA. D. VR rendering as viewed in Sketchfab.

Appendix B Questionnaires

Model Questionnaire

Degree: _____ Module: _____ Year of _____ Date: _____
Study:

1. Would you use the models provided again?

Yes ☐ No ☐

2. Did you know that the models used in the session were 3D printed?

Yes ☐ No ☐

Please answer the following statements using the scale below.

Scale	Strongly Disagree (**1**)	Disagree (**2**)	Neutral (**3**)	Agree (**4**)	Strongly Agree (**5**)

3. The larger size of the models made it easier to understand the anatomy.

1 ☐ 2 ☐ 3 ☐ 4 ☐ 5 ☐

4. The ability to hold and move the models made it easier to understand the anatomy.

1 ☐ 2 ☐ 3 ☐ 4 ☐ 5 ☐

5. I could easily identify what the models were.

1 ☐ 2 ☐ 3 ☐ 4 ☐ 5 ☐

6. I prefer to use the models compared to extracted teeth.

1 ☐ 2 ☐ 3 ☐ 4 ☐ 5 ☐

7. What did you like the most about the models?

_____

8. What did you like the least about the models?

_____

9. If any, what changes would you make to the models?

_____

10. Any other comments?

_____

Figure N: Questionnaire for the 3D printed deciduous models.

VR Questionnaire

1. At which stage of education are you?

GCSE ☐   A-Level ☐   Undergrad. ☐   Postgrad. ☐   Professional ☐

2. Have you used VR before?

Yes ☐   No ☐

3. Overall, how would you rate the VR experience?

Excellent ☐   Very Good ☐   Good ☐   Fair ☐   Poor ☐

4. How informative did you find the VR experience?

Extremely informative ☐   Very informative ☐   Somewhat informative ☐   Not so informative ☐   Not at all informative ☐

5. How comfortable did you feel using the VR headset?

Extremely comfortable ☐   Very comfortable ☐   Somewhat comfortable ☐   Not so comfortable ☐   Not at all comfortable ☐

6. Was there anything you liked most about the VR experience?

_____

7. Was there anything you liked least about the VR experience?

_____

8. What improvements would you make?

_____

9. Finally, if this experience was available free online, would you recommend to others?

Yes ☐   No ☐

10. Any other comments?

_____

Figure O: Questionnaire for the VR tooth demonstration.

Typodont Questionnaire

1. Which tooth was easier to cut?

A ☐   B ☐

2. On a scale of 1-10, how did tooth A compare to a real tooth in terms of cutting?
(1 = Not at all. 10 = Exactly the same)

  1   **2**   **3**   **4**   **5**   **6**   **7**   **8**   **9**   **10**

3. On a scale of 1-10, how did tooth B compare to a real tooth in terms of cutting?
(1 = Not at all. 10 = Exactly the same)

  1   **2**   **3**   **4**   **5**   **6**   **7**   **8**   **9**   **10**

4. Which tooth would you prefer to practice on in the future?

_____

5. Any other comments?

_____

Figure P: Questionnaire for the 3D printed typodonts.

Appendix C Digital Resources

Tooth Models

Extracted Mandibular First Molar – Feb. 2018
https://www.thingiverse.com/thing:2770645

Artificial Mandibular First Molar – Feb. 2018
https://www.thingiverse.com/thing:2770647

Mandibular Left First Molar – Jan. 2019
https://sketchfab.com/3d-models/mandibular-left-first-molar-d8f3f2d2411445fea96d2b1073966b5c

Human Deciduous Tooth – Jan. 2019
https://sketchfab.com/3d-models/human-deciduous-tooth-e3ed96462ca64ba6b4818b2417f93227

Deciduous Mandibular Molar – Jan. 2019
https://sketchfab.com/3d-models/deciduous-mandibular-molar-ac1e514160dd4a57aad01f9da3c3eb8d

Deciduous Maxillary Central Incisor – Jan. 2019
https://sketchfab.com/3d-models/deciduous-maxillary-central-incisor-7a086d86c9724fcdb49b4cc21d69b759

Deciduous Maxillary Canine – Jan. 2019
https://sketchfab.com/3d-models/deciduous-maxillary-canine-e0cda705d9b74d2db34e3b45b129f730

Class I Cavity Preparation – Apr. 2018
https://sketchfab.com/3d-models/class-i-cavity-preparation-cad27d2bc0ca446e93ac4dc7121c2206

Force Measurements

Class 1 Cavity Preparation #1 – Apr. 2018
https://www.youtube.com/watch?v=qppUBAnAWu0&t=17s

Class 1 Cavity Preparation #2 – Apr. 2018
https://www.youtube.com/watch?v=IQgiDBQJZVU

Class 1 Cavity Preparation #3 – Apr. 2018
https://www.youtube.com/watch?v=282Te8GF-fQ&t=13s

Class 1 Cavity Preparation #4 – Apr. 2018
https://www.youtube.com/watch?v=vtEz3Eyd8vQ&t=6s

Class 1 Cavity Preparation #5 – Apr. 2018
https://www.youtube.com/watch?v=eDYMZPjw_4U

Vertebrae Models

Vertebrae Sections – Jan. 2019
https://sketchfab.com/alexjcb/collections/vertebrae-sections

Appendix D Published Work

1. Cresswell-Boyes, A. J., Barber, A. H., Mills, D., Tatla, A., & Davis, G. R. (2018). Approaches to 3D Printing Teeth from X-Ray Microtomography. Journal of Microscopy, 272(3), 207-212.

2. Cresswell-Boyes, A. J., Mills, D., Davis, G. R., & Boyde, A. (2018). L2 Bone Quality in Osteoporosis: BIOMED 1 Revisited. Orthopaedic Proceedings: a supplement to The Bone & Joint Journal, 100-B(Supplement 14), 76.

Approaches to 3D printing teeth from X-ray microtomography

A.J. CRESSWELL-BOYES* [iD], A.H. BARBER†, D. MILLS*, A. TATLA‡ & G.R. DAVIS* [iD]

Dental Physical Sciences, Institute of Dentistry, Francis Bancroft Building, Queen Mary University of London, London, E1 4NS, U.K.

†*School of Engineering, London South Bank University, London, SE1 0AA, U.K.*

‡*GlaxoSmithKline, St George's Avenue, Weybridge, KT13 0DE, U.K.*

Summary

Artificial teeth have several advantages in preclinical training. The aim of this study is to three-dimensionally (3D) print accurate artificial teeth using scans from X-ray microtomography (XMT). Extracted and artificial teeth were imaged at 90 kV and 40 kV, respectively, to create detailed high contrast scans. The dataset was visualised to produce internal and external meshes subsequently exported to 3D modelling software for modification before finally sending to a slicing program for printing. After appropriate parameter setting, the printer deposited material in specific locations layer by layer, to create a 3D physical model. Scans were manipulated to ensure a clean model was imported into the slicing software, where layer height replicated the high spatial resolution that was observed in the XMT scans. The model was then printed in two different materials (polylactic acid and thermoplastic elastomer). A multimaterial print was created to show the different physical characteristics between enamel and dentine.

Introduction

A distinct need for hands-on preclinical training before treatment of a patient has been widely acknowledged within dental education (Qualtrough *et al.*, 1999). Throughout the years, numerous techniques have been created to teach students to perform different dental treatments. Artificial teeth are widely used and replicated with transparent resins in which the pulp chamber and root canals are distinguishable with different colours (Nassri *et al.*, 2008). Despite this use of artificial teeth, extracted human teeth remain one of the most popular and accurate samples used during preclinical endodontic training. Both artificial and extracted teeth have advantages and disadvantages, with the common practice using a combination of artificial root canal models and extracted human

teeth during preclinical training (Dummer, 1991).The disadvantages of using extracted teeth include the possibility of cross-infection, being potentially infectious to students, the unavailability of these teeth and anatomical variability of extracted teeth, meaning valid assessment for students is not uniform (Tchorz *et al.*, 2015). The benefits of artificial teeth include no risk of infection, availability in large quantities, and validation of assessment through their uniformity (Bitter *et al.*, 2016), tailoring to offer anatomical challenges and 3D printing into training models for simulation-based medical education (SBME) (San Diego *et al.*, 2013). However, based on previous studies, students reported artificial teeth as unsatisfactory because of a perceived lack of realism of these teeth, offering them a nonrealistic simulation to practice on, compared to natural teeth. Despite the reported difficulties, students recognised the advantages and suggested improvements, such as varying geometry, to include real-life imperfections of teeth such as caries (Al-Sudani & Basudan, 2016).

Previous literature studies have shown the ability to convert tomography files into viable 3D printed training models (O'Brien *et al.*, 2016) in order to support the concept of 3D printing artificial teeth. In Longfield *et al.* (2015), computed tomography (CT) scans were taken of 6-month-old patient's temporal bone for a low-cost training method in paediatric surgery and therefore provides a technique for creating realistic 3D datasets. In this study, we present a method of collecting structural biological data and converting into a 3D model, using open source software. The emphasis at this stage of the study is to focus on the geometry of the tooth, with future work looking into mimicking the mechanical properties of the tooth.

Materials and methods

X-ray microtomography

A natural mandibular first molar and a plastic replica (Fábrica de Sorrisos, Brazil) were selected as specimens to demonstrate the transition from XMT to 3D print. The specimens were

Correspondence to: A.J. Cresswell-Boyes, Dental Physical Sciences, Institute of Dentistry, Francis Bancroft Building, Queen Mary University of London, Mile End Road, London E1 4NS, UK. Tel: +44 207 882 5966; fax: +44 20 7882 7979; e-mail address: a.cresswell-boyes@qmul.ac.uk
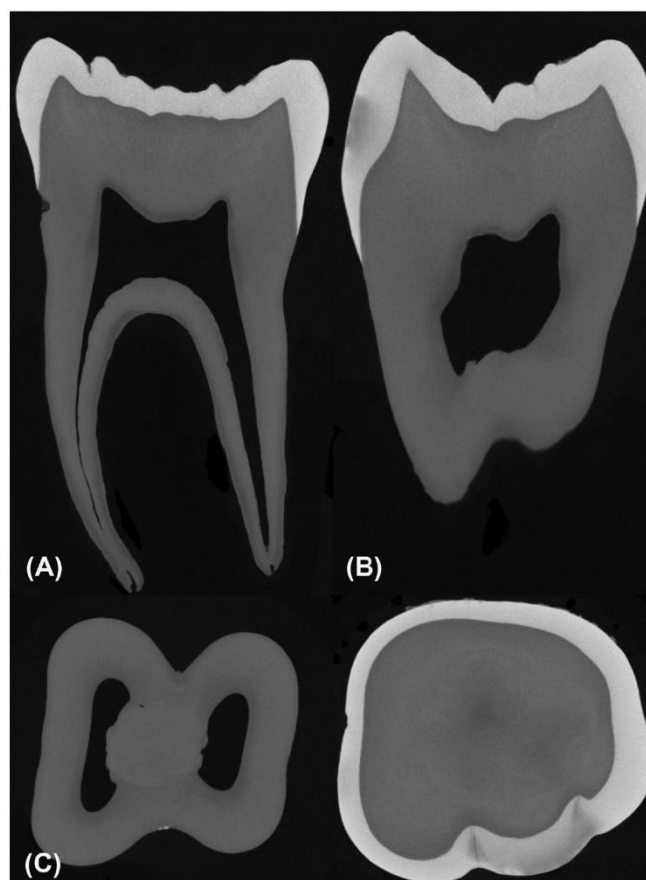
Fig. 1. Slices of natural mandibular first molar (A) mesiodistal section, exposing the buccal and lingual aspect of the pulp cavity, (B) buccolingual section, exposing the medial and distal aspect of the pulp cavity and (C) transverse section midroot and occlusal.

scanned using the 'in-house' TDI (time delay integration) X-ray microtomography scanner (MuCAT-2) at Queen Mary University of London (QMUL), developed by Davis & Elliott (2003). The system uses a charge-coupled detector (CCD) camera (Spectral Instruments, Tucson, Arizona, USA) with a 60 μm thick columnar caesium iodide scintillator (Applied Scintillation Technologies, Ltd., Cambridge, UK) (Davis & Elliott, 2003; Davis *et al.*, 2013). The natural tooth was scanned at 15 μm voxel size at 90 kV, 180 μA, 1503 projections were taken within 3 blocks,[1] whereas the plastic tooth was scanned at 40 kV, 405 μA, 675 projections within a single block. Time taken for the scans was 26 h 52 min and 5 h 8 min, respectively. The projections were reconstructed using a modified Feldkamp cone-beam back-projection algorithm (Feldkamp

et al., 1984). Following reconstruction, the files produced were 'trimmed' to produce single-byte voxel data containing only the cuboid of interest.

Visualisation

Tomview (Version 1.1, QMUL, 2003–2018), a tomography visualisation software specific to MuCAT-2, was used to view 2D slices through the trimmed volume (*.tom file) in any of the three orthogonal planes (XY, XZ and YZ). Tomview was used to create a metadata file (*.pvl.nc file) that was exported to Drishti (Version 2.6.3; ANU Vizlab, 2016), which is a multiplatform, open source volume exploration and presentation tool, written for visualising tomography datasets from various scanning technologies and different tomography file formats. Using Drishti, a mesh was generated in the form of a polygon file format (*.ply), which was opened using Meshlab (Version
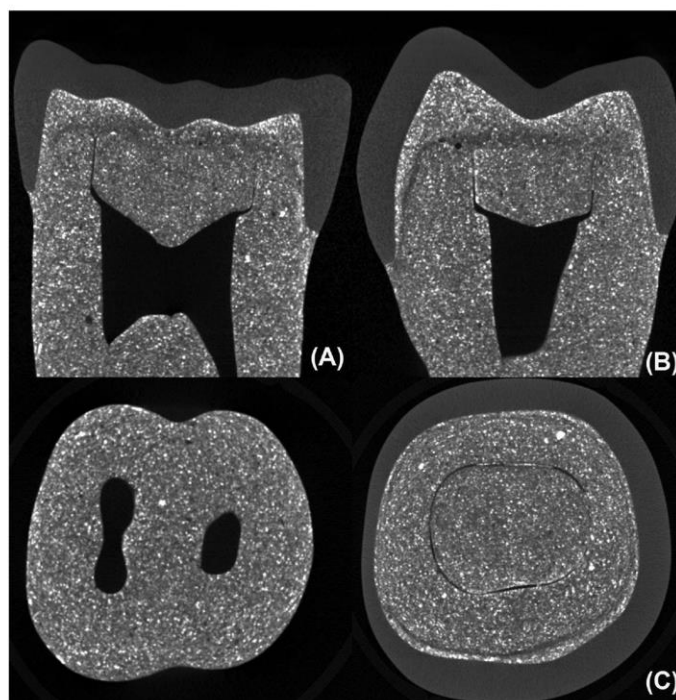
---

[1] Area of view for the camera of 501 slices and 675 slices for the extracted and artificial tooth, respectively.

Fig. 2. Slices of artificial mandibular first molar (A) mesiodistal section, exposing the buccal and lingual aspect of the pulp cavity, (B) buccolingual section, exposing the medial and distal aspect of the pulp cavity and (C) transverse section trunk and occlusal.

2016.12; ISTI-CNR, 2016). The 3D mesh was modified and manipulated in Meshlab to remove any unwanted or excess material or imperfections.

3D printing

The model file was exported as a *.stl file format with ASCII[2] coding into Cura (Version 2.3.1; Ultimaker, 2016). Cura is a 3D printer slicing application, in which parameters are set and a 3D visualisation of each layer is provided. This information is exported into a G-code file format and fed into the 3D printer. An open-source fused deposition modelling (FDM) 3D printer (Duplicator i3, Wanhao, China), read the numerical control programming language of the G-code to deposit a determined amount of material in a specific location. Modifications were made to the printer in the form of a Bowden extruder (Landry, 2016) (Flexion[TM], Diabase Engineering, USA), designed to increase the resolution of the 3D printer from 60 to 50 μm. Filaments used for the printing included a hard white polylactic acid (PLA) (3D Prima, Sweden) and flexible thermoplastic elastomer (TPE) (FFF World, Spain).

---

[2] American Standard Code for Information Interchange.

Results

A variety of images reconstructed from XMT volume datasets are shown in Figures 1 and 2. Figures 1 and 2 show both the natural and artificial mandibular molar at different cross-sectional planes, visualising difference in structure and material. Further details of the specimens are given in the figure captions. Figure 3 demonstrates the result of the 3D surface rendering that is applied to the reconstructed volume datasets achievable in the open-source software. This rendering is required to provide discrete surfaces that can be exported effectively to the 3D printer.

Three models were produced to demonstrate the ability to convert tomography files to 3D prints. Two prints were produced from PLA, for both natural and artificial tooth structures (Fig. 4A), whereas the third print was an assembled model made from the harder PLA representative of enamel and TPE for the dentine and pulp cavity (Fig. 4B).

Discussion

The nondestructive 3D imaging of teeth provides a basis for SBME, using the data for the teaching of dental morphology, operative dentistry, and endodontics (Dowker *et al.*, 1997). Combining this 3D imaging technology with recent advances

Fig. 3. Rendered surface images of both natural and artificial mandibular first molar (A) viewed in Drishti and (B) viewed in Meshlab.

Fig. 4. 3D printed mandibular first molar (A) both natural and artificial molar in PLA and (B) natural molar in multiple materials, PLA for enamel, TPE for dentine and pulp cavity.

in modelling and computational power provides the ability to manipulate biological image datasets and export to physical models using complementary 3D printing. Such an approach is appropriate for applications in teaching where physical models for training can be produced and modified on demand. Physical outputs are expected to be further enhanced using virtual reality/augmented reality for SBME, in which sensory feedback is received from simulated environments (Dowker *et al.*, 1997; Wang *et al.*, 2015). However, virtual reality is currently underdeveloped and has only recently become available in the consumer market, unlike 3D printing with desktop printers now widely available.
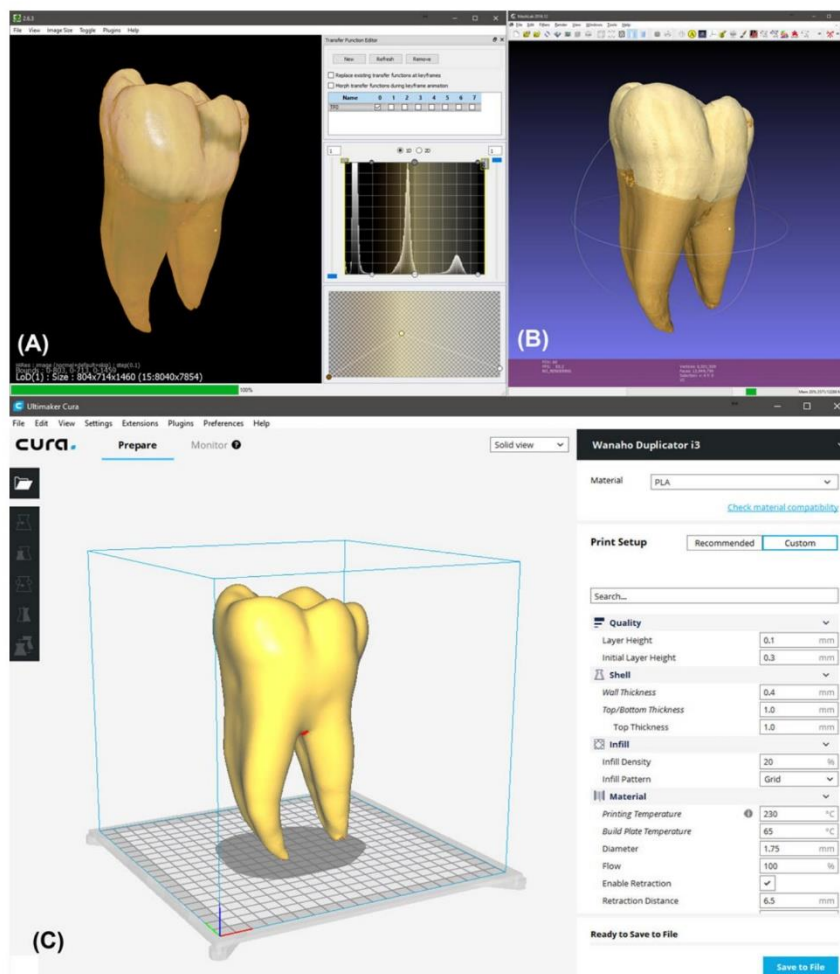
Fig. 5. Screenshots of the open-source software used to convert tomography files to 3D print (A) rendering of the 3D surface in Drishti, (B) rendering of the 3D surface in Meshlab, with the ability to manipulate file to the desired final product and (C) slicing view in Cura, with the ability to edit layer settings.

XMT produces a high-resolution scan of the teeth, both extracted and artificial, which were easily converted into workable 3D models using multiple software (Drishti, Meshlab) (Fig. 5). The specimens' datasets can be uploaded to a free access database for downloading to be used in 3D printing (websites such as Thingiverse[3,4]; www.thingiverse.com) and/or virtual reality (Sketchfab; www.sketchfab.com). Both data collected from extracted teeth and artificial teeth showed the internal and external geometry, with the artificial tooth being scanned as a comparison to show whether the anatomy differs from natural teeth. In the example of the artificial tooth, the internal geometry showed differences in the structure between

the enamel and dentine with different types of resin used to distinguish this (Fig. 2).

Drishti allows the isolation of different meshes, such as enamel, dentine and pulp. The isolation of different meshes allowed for the ability to print each structure separately and with different materials. With Meshlab, the meshes can be edited, changing the dimensions, and changing the number of triangles and vertices, which in turn alters the resolution of the model and the size of the model file. This combination of programs proved effective in altering the tooth datasets and could be a possible pathway to use in future conversion of XMT data to *.stl files.

The software program Cura was used to divide the meshed data into slices (dependent on layer thickness) and allows

---

[3] Extracted tooth; www.thingiverse.com/thing:2770645.

[4] Artificial tooth; www.thingiverse.com/thing:2770647.

finite control over the final product, as more parameters can be set and changed compared to other slicing programs. Cura is also compatible with most commercially available 3D printers, making it an ideal choice for exporting the meshed data to a physical output. The XMT data of the artificial tooth was used to produce replicas in white PLA that contained both internal and external structures. The choice of only using one material to recreate the artificial tooth was to prove the concept of translating data into a physical model. The XMT data of the extracted tooth was used to create various models using white PLA. The models proved that it was possible to use a cost-effective 3D printer and produce from XMT data, physical 3D models, but at a lower resolution. Specifically, the MuCAT-2 system has a spatial resolution of around 13 μm whereas the Wanhao Duplicator i3 (with Flexion$^{\text{TM}}$ extruder) can only produce a resolution of around 50 μm, thus indicating that the high definition from the imaging was not captured in the physical output. The ability to create multiple meshes for the internal anatomy was taken advantage of, as a multimaterial print was created, using PLA as the enamel, and the flexible TPE as the dentine and pulp, to primitively demonstrate the different mechanical properties of real enamel and dentine. The use of dual extrusion would allow for a simultaneous print using multiple materials. However, the print made of a range of parts allows for dismantling which could be a valuable tool in teaching students tooth anatomy especially the different structures that make up a tooth. More advanced multimaterial 3D printing technology is however available, but at a much higher cost, compared to the Duplicator i3.

Conclusions

We have demonstrated 3D models of a tooth, manufactured from tomography files generated from XMT, using various open-source programs. The approach is generic and provides a workflow for 3D printed physical outputs from high-resolution nondestructive XMT scans of biological specimens. This workflow could prove to be invaluable for SBME to exploit the availability of desktop 3D printers, as well as free-access databases that contain tomographic files. Future work following on from this study will aim to mimic the properties of natural teeth using 3D printing. Such an approach has been exploited from XMT imaging bone structures and provided mechanical analogies using multimaterial 3D printing (Parwani *et al.*, 2017) but has not been translated into teeth.

Conflict of interest

The authors declare no potential conflicts of interest with respect to the authorship and/or publication of this article.

References

Al-Sudani, D.I. & Basudan, S.O. (2016) Students' perceptions of preclinical endodontic training with artificial teeth compared to extracted human teeth. *Euro. J. Dental Educ.* **21**(4), e72–e75.

Bitter, K., Gruner, D., Wolf, O. & Schwendicke, F. (2016) Artificial versus natural teeth for preclinical endodontic training: a randomized controlled trial. *J. Endod.* **42**(8), 1212–1217.

Davis, G.R. & Elliott, J.C. (2003) High definition x-ray microtomography using a conventional impact x-ray source. *J. Phys. IV (Proc.)* **104**(1), 131–134.

Davis, G.R., Evershed, A.N.Z. & Mills, D. (2013) Quantitative high contrast x-ray microtomography for dental research. *J. Dentist.* **41**, 475–482.

Dowker, S.E.P., Davis, G.R., Elliott, J.C. & Wong, F.S.L. (1997) X-ray microtomography: 3-dimensional imaging of teeth for computer-assisted learning. *Euro. J. Dental Educ.* **1**, 61–65.

Dummer, P.M. (1991) Comparison of undergraduate endodontic teaching programmes in the United Kingdom and in some dental schools in Europe and the United States. *Int. Endod. J.* **24**(1), 169–177.

Feldkamp, L.A., Davis, L.C. & Kress, J.W. (1984) Practical cone-beam algorithm. *J. Opt. Soc. Am. A – Optics Image Sci. Vis.* **1**(6), 612–619.

Landry, T. (2016) Extruders 101: a crash course on an essential component of your 3D printer. Retrieved from https://www.matterhackers.com/articles/extruders-101:-a-crash-course-on-an-essential-component-of-your-3d-printer, accessed January 20, 2018.

Longfield, E.A., Brickman, T.M. & Jeyakumar, A. (2015) 3D printed pediatric temporal bone: a novel training model. *Otolog. Neurotol.* **36**(5), 793–795.

Nassri, M.R., Carlik, J., da Silva, C.R., Okagawa, R.E. & Lin, S. (2008) Critical analysis of artificial teeth for endodontic teaching. *J. Appl. Oral Sci.* **16**(1), 43–49.

O'Brien, E.K., Wayne, D.B., Barsness, K.A., McGaghie, W.C. & Barsuk, J.H. (2016) Use of 3D printing for medical education models in transplantation medicine: a critical review. *Curr. Transpl. Rep.* **3**, 109–119.

Parwani, R., Curto, M., Kao, A.P., Rowley, P.J., Pani, M., Tozzi, G. & Barber, A.H. (2017) Morphological and mechanical biomimetic bone structures. *ACS Biomater. Sci. Eng.* **10**(1021), 1–7.

Qualtrough, A.J., Whitworth, J.M. & Dummer, P.M. (1999) Preclinical endodontology: an international comparison. *Int. Endod. J.* **32**(1), 406–414.

San Diego, J.P., Newton, T., Quinn, B.F.A., Cox, M.J. & Woolford, M.J. (2013) Levels of agreement between student and staff assessments of clinical skills in performing cavity preparation in artificial teeth. *Euro. J. Dental Educ.* **18**(1), 58–64.

Tchorz, J.P., Brandl, M., Ganter, P.A., Karygianni, L., Polydorou, O., Vach, K., Hellwig, E. & Altenburger, M.J. (2015) Pre-clinical endodontic training with artificial instead of extracted human teeth?: Does the type of exercise have an influence on clinical endodontric outcomes? *Int. Endod. J.* **48**, 888–893.

Wang, D., Li, T., Zhang, Y. & Hou, J. (2015) Survey on multisensory feedback virtual reality dental training systems. *Euro. J. Dent. Educ.* **20**(4), 248–260.

L2 BONE QUALITY IN OSTEOPOROSIS: BIOMED 1 REVISITED

A.J. Cresswell-Boyes, D. Mills, G.R. Davis, A. Boyde

As a part of the European Union BIOMED I study "Assessment of Bone Quality in Osteoporosis," Sixty-nine second lumbar vertebral body specimens (L2) were obtained post mortem from 32 women and 37 men (age 24–92 years). Our initial remit was to study variations in density of the calcified tissues by quantitative backscattered electron imaging (BSE-SEM). To this end, the para-sagittal bone slices were embedded in PMMA and block surfaces micro-milled and carbon coated. Many samples were re-polished to remove the carbon coat and stained with iodine vapour to permit simultaneous BSE imaging of non-mineralised tissues - especially disc, annulus, cartilage and ligament - uncoated, at 50Pa chamber pressure. We have now studied most of these samples by 30-µm resolution high contrast resolution X-ray microtomography (XMT), typically 72 hours scanning time, thus giving exact correlation between high resolution BSE-SEM and XMT. The 3D XMT data sets were rendered using Drishti software to produce static and movie images for visualisation and edification. We have now selected a set of the female samples for reconstruction by 3D printing - taking as examples the youngest, post-menopausal, oldest, best, worst, and anterior and central compression fractures and anterior collapse with fusion to L3 - which will be attached to the poster display. The most porotic cases were also the most difficult to reconstruct. A surprising proportion of elderly samples showed excellent bone architecture, though with retention of fewer, but more massive, load-bearing trabeculae.